

**Phthalocyanine-nanoparticle conjugates  
supported on inorganic nanofibers as  
photocatalysts for the treatment of biological  
and organic pollutants as well as for hydrogen  
generation**

A thesis submitted in fulfilment of the requirements for the degree of

**DOCTOR OF PHILOSOPHY**

**OF**

**RHODES UNIVERSITY**

**BY**

**SIVUYISIWE MAPUKATA**

**JULY 2021**

# DEDICATIONS

This thesis is dedicated to my beloved mother in heaven:

**Glory Nosisi Mapukata ♥**

*Ndinjenje ngumama....All her sacrifices, support and prayers*

*Ndiyabulela kakhulu MaTenza wam*

It is also dedicated to:

my father;

Griffiths Mvuyiswa Mapukata

as well as

my late paternal grandparents;

Nzima and Nowinile Mapukata

along with

my late maternal grandparents;

Joseph Mbhele and Diana Mbombo

and lastly to

*ooNkwali, ooTshezi, ooGaba ooMvubu nabo bonke*

*ookhokho bam, ndiyabulela ngeentsikelelo*

# ACKNOWLEDGEMENTS

*“Udumo malubekuye owenza iZulu nomhlaba, Amen!”*

To my supervisor; Distinguished Prof Nyokong, thank you for the inspiration, encouragement and guidance throughout my PhD studies. Thank you for the travelling opportunities and research ideas. Your patience, encouragement, tenacity and just overall aura have made me believe in the validity of my dreams and the will power to achieve whatever I put my mind to.

Thank you to Prof Scaiano, Dr Lanterna and their entire research group for the warm reception and supervision during my stay at the University of Ottawa, Canada. I sure learnt a lot. Thank you to Ms Cobus, Prof Mack and Dr Britton for always lending a helping hand. Thank you to Marvin and Papa Francis as well the entire Chemistry Department for the help with different instruments.

To my siblings; Mlungisi, Sakhise, Mbali and Indiphile Mapukata, thank you for cheering me on and always believing in me, you guys are beyond amazing. I'd also like to acknowledge the rest of my family with a special mention to granny Thandiwe Mbombo, Wendy Fipaza, Cikizwa Mbombo, Thulani Mbombo, Wongama Mbombo, Afrika Mbombo and Nonela James-Mbombo. Your support and encouragement has kept me going, *ndiyabulela kuni booTshezi, Nangamso.*

To all my S22 colleagues, thank you for the pleasant working environment and memories. Nobuhle Ndebele, Somila Dingiswayo, Tumi Nkhahle, Aviwe Magadla, Refilwe Matshitse and Robin Nxele, I appreciate you guys, thank you for your individual roles in making things a bit more bearable. To Nosimo Vena, Siwaphiwe Peteni and Zizo Mjonono, thank you for literally wiping away my tears when the going got tough and for always showing up for me. Khanyisa Nolusu, Olu Ngxube, Sinazo Somhlahlo and Sandiswa Nozintaba, your support has been amazing. Thank you to Drs Jali, Babu, Sekhosana, Managa, Kubheka, Sen, Osifeko and Kyremeh for the mentorship and support.

Lastly I'd like to acknowledge The National Research Foundation and Department of Science and Technology/Mintek for funding my studies.

.....I didn't know own strength!!

# ABSTRACT

This thesis reports on the synthesis, photophysicochemical and photocatalytic properties of various zinc phthalocyanines (Pcs). For enhanced properties and catalyst support, the reported Pcs were conjugated to different nanoparticles (NPs) through chemisorption as well as amide bond formation to yield Pc-NP conjugates. For increased catalyst surface area and catalyst reusability, the Pcs and some of their conjugates were also supported on electrospun inorganic nanofibers i.e. SiO<sub>2</sub>, hematite (abbreviated Hem and has formula  $\alpha$ -Fe<sub>2</sub>O<sub>3</sub>), ZnO and TiO<sub>2</sub> nanofibers. The effect that the number of charges on a Pc has on its antimicrobial activities was evaluated by comparing the photoactivities of neutral, octacationic and hexadecacationic Pcs against *S. aureus*, *E. coli* and *C. albicans*. The extent of enhancement of their antimicrobial activities upon conjugation (through chemisorption) to Ag NPs was also studied in solution and when supported on SiO<sub>2</sub> nanofibers. The results showed that the hexadecacationic complex **3** possessed the best antimicrobial activity against all three microorganisms, in solution and when supported on the SiO<sub>2</sub> nanofibers. Covalent conjugation of Pcs with carboxylic acid moieties (complexes **4-6**) to amine functionalised NPs (Cys-Ag, NH<sub>2</sub>-Fe<sub>3</sub>O<sub>4</sub> and Cys-Fe<sub>3</sub>O<sub>4</sub>@Ag) resulted in enhanced singlet oxygen generation and thus antibacterial efficiencies. Comparison of the photodegradation efficiencies of semiconductor nanofibers (hematite, ZnO and TiO<sub>2</sub>) when bare and when modified with a Pc (complex **6**) were evaluated. Modification of the nanofibers with the Pc resulted in enhanced photoactivities for the nanofibers with the hematite nanofibers being the best. Modification of the hematite nanofibers with two different Pcs i.e. monosubstituted (complex **5**) and an asymmetrical tetrasubstituted Pc (complex **6**) showed that complex **6** better enhanced the activity of the nanofibers. Evaluation of the hydrogen generation efficiencies of the bare and modified TiO<sub>2</sub> nanofibers calcined at different temperatures demonstrated that the anatase nanofibers calcined at 500 °C possessed the best catalytic efficiency. The efficiency of the TiO<sub>2</sub> nanofibers was enhanced in the presence of the Co and Pd NPs as well as a Pc (complex **7**), with the extent of enhancement being the greatest for the nanofibers modified with the Pd NPs. The reported findings therefore demonstrate the versatility of applications of Pcs for different water purification techniques when supported on different nanomaterials.

# Table of Contents

Title Page.....	i
Dedications.....	ii
Acknowledgements.....	iii
Abstract.....	iv
Table of Contents.....	v
List of Symbols.....	xii
List of Abbreviations.....	xiii
<b>Preamble.....</b>	<b>1</b>
<b>Chapter 1.....</b>	<b>2</b>
1. Introduction.....	3
1.1 Nanofibers .....	3
1.1.1 Electrospinning.....	3
1.1.2 Modification of electrospun nanofibers.....	5
1.1.3 Polymer free nanofibers.....	7
1.1.3.1 Silica nanofibers (SiO <sub>2</sub> NFs).....	8
1.1.3.2 Semiconductor based nanofibers.....	8
1.2 Nanoparticles (NPs).....	10
1.2.1 Silver nanoparticles (Ag NPs).....	11
1.2.2 Iron oxide magnetic nanoparticles (Fe <sub>3</sub> O <sub>4</sub> NPs).....	12
1.2.3 Bimetallic iron oxide-silver nanoparticles (Fe <sub>3</sub> O <sub>4</sub> @Ag NPs).....	13

1.2.4	Palladium nanoparticles (Pd NPs).....	13
1.2.5	Cobalt nanoparticles (Co NPs).....	14
1.3	Phthalocyanines (Pcs) .....	15
1.3.1	Synthesis of symmetrical and asymmetrical Pcs.....	16
1.3.2	Phthalocyanines studied in this thesis.....	18
1.3.3	Electronic Absorption Spectra of Pcs.....	24
1.3.4	Photophysical Parameters of Pcs.....	25
1.3.4.1	Fluorescence Quantum yields ( $\Phi_F$ ) and lifetimes ( $\tau_F$ ).....	27
1.3.4.2	Triplet Quantum yields ( $\Phi_T$ ) and lifetimes ( $\tau_T$ ).....	28
1.3.4.3	Singlet Oxygen Quantum yields ( $\Phi_\Delta$ ).....	29
1.3.5	Photocatalytic activities of Pcs studied in this work.....	31
1.3.5.1	Photodynamic Antimicrobial Chemotherapy (PACT).....	31
1.3.5.2	Photodegradation of organic water pollutants.....	34
1.3.5.3	Hydrogen generation.....	36
1.4	Aims of thesis.....	37
<b>Chapter 2.....</b>		<b>39</b>
2.	Experimental.....	40
2.1	Materials.....	40
2.1.1	Solvents.....	40
2.1.2	Reagents for synthesis of Pcs, NPs, NFs and their conjugates.....	40
2.1.3	Reagents for photophysical studies.....	41
2.1.4	Reagents used for photocatalytic applications.....	41

2.2 Equipment.....	42
2.3 Synthesis.....	51
2.3.1 Synthesis of Pcs (complexes <b>2-5</b> ).....	51
2.3.1.1 Synthesis of 2,9(10),16(17),23(24)-Tetrakis-(4'-(1',3'-N-dimethyl, 4'-6'-diaminopyrimidin-2'-ylthio))) phthalocyaninato zinc (II) ( <b>2</b> ), <b>Scheme 3.1</b> .....	51
2.3.1.2 Synthesis of 2,9(10),16(17),23(24)-Tetrakis-(4'-(1',3'-N-dimethyl, 4'-6'-(hexamethylaminopyrimidin-2'-ylthio))) phthalocyaninato zinc (II) ( <b>3</b> ), <b>Scheme 3.1</b>	52
2.3.1.3 Synthesis of 2-Mono-isophthalic acid-9(10),16(17),23 (24)- tri ( <i>tert</i> -butylphenoxy) phthalocyaninato zinc(II) ( <b>4</b> ), <b>Scheme 3.2</b> .....	52
2.3.1.4 Synthesis of 2-Mono-(5-oxy) isophthalic acid phthalocyaninato zinc(II) ( <b>5</b> ), <b>Scheme 3.2</b> .....	53
2.3.2 Synthesis and functionalisation of NPs.....	54
2.3.2.1 Synthesis of oleylamine capped Ag NPs (OLM-Ag NPs), <b>Scheme 3.3</b> .....	54
2.3.2.2 Synthesis of cysteamine functionalised Ag NPs (Cys-Ag NPs), <b>Scheme 3.4</b>	55
2.3.2.3 Synthesis of Fe <sub>3</sub> O <sub>4</sub> NPs (NH <sub>2</sub> -Fe <sub>3</sub> O <sub>4</sub> NPs), <b>Scheme 3.5</b> .....	55
2.3.2.4 Synthesis of cysteamine capped core-shell Fe <sub>3</sub> O <sub>4</sub> @Ag NPs (Cys-Fe <sub>3</sub> O <sub>4</sub> @Ag NPs), <b>Scheme 3.6</b> .....	56
2.3.3 Conjugation of NPs to Pcs.....	57
2.3.3.1 Conjugation of OLM-Ag NPs to complexes <b>1-3</b> <i>via</i> chemisorption, <b>Scheme 3.7</b> .....	57
2.3.3.2 Conjugation of Cys-Ag, NH <sub>2</sub> -Fe <sub>3</sub> O <sub>4</sub> and Cys-Fe <sub>3</sub> O <sub>4</sub> @Ag NPs to complexes <b>4-6</b> <i>via</i> amide bonds, <b>Scheme 3.8</b> .....	57

2.4	Fabrication of electrospun NFs.....	58
2.4.1	SiO <sub>2</sub> NFs.....	58
2.4.1.1	Bare SiO <sub>2</sub> NFs.....	58
2.4.1.2	<i>in situ</i> synthesis of Ag NPs onto SiO <sub>2</sub> NFs (Ag-SiO <sub>2</sub> NFs).....	59
2.4.1.3	Pc decorated SiO <sub>2</sub> NFs (Pc-SiO <sub>2</sub> NFs).....	59
2.4.1.4	Pc decorated Ag-SiO <sub>2</sub> NFs (Pc@Ag-SiO <sub>2</sub> NFs).....	60
2.4.2	Semiconductor NFs.....	60
2.4.2.1	Bare Hem NFs.....	60
2.4.2.2	Bare ZnO NFs .....	61
2.4.2.3	Bare TiO <sub>2</sub> NFs.....	61
2.4.2.4	Pc decorated semiconductor NFs.....	62
2.4.2.5	<i>in situ</i> synthesis of Pd NPs onto TiO <sub>2</sub> NFs .....	63
2.4.2.6	<i>in situ</i> synthesis of Co NPs onto TiO <sub>2</sub> NFs .....	63
2.5	Photocatalytic applications.....	64
2.5.1	PACT studies.....	64
2.5.2	Photodegradation studies.....	66
2.5.3	Hydrogen generation studies.....	66
	<b>Results and Discussion.....</b>	<b>67</b>
	<b>Publications.....</b>	<b>68</b>



<b>Chapter 3.....</b>	<b>70</b>
3.1 Phthalocyanines (Pcs).....	71
3.1.1 2,9(10),16(17),23(24)-Tetrakis-(4'-(1',3'-N-dimethyl, 4'-6'-diaminopyrimidin-2'-ylthio))) phthalocyaninato zinc (II) (2) and 2,9(10),16(17),23(24)-Tetrakis-(4'-(1',3'-N-dimethyl,4'-6'-(hexamethylaminopyrimidin-2'-ylthio))) phthalocyaninato zinc (II) (3).	71
3.1.2 2-Mono-isophthalic acid-9(10),16(17),23 (24)- tri ( <i>tert</i> -butylphenoxy) phthalocyaninato zinc(II) (4) and 2-Mono-(5-oxy) isophthalic acid phthalocyaninato zinc(II) (5).....	77
3.2 Nanoparticles (NPs) and conjugates.....	81
3.2.1 Nanoparticles.....	81
3.2.2 Chemisorption of complexes <b>1-3</b> to OLM-Ag NPs.....	84
3.2.2.1 Transmission Electron Microscopy (TEM).....	85
3.2.2.2 X-ray Diffraction (XRD).....	85
3.2.2.3 Ground state UV-vis spectroscopy.....	86
3.2.2.4 X-ray photoelectron spectroscopy (XPS).....	88
3.2.3 Covalent conjugation of complexes <b>4-6</b> to Cys-Ag, NH <sub>2</sub> -Fe <sub>3</sub> O <sub>4</sub> and Cys-Fe <sub>3</sub> O <sub>4</sub> @Ag NPs .....	91
3.2.3.1 Transmission Electron Microscopy (TEM).....	92
3.2.3.2 X-ray Diffraction (XRD).....	93
3.2.3.3 Ground state UV-vis spectroscopy .....	94
3.2.3.4 X-ray photoelectron spectroscopy (XPS).....	96

3.3 Loading of Pcs on NPs.....	97
3.4 Closing Remarks.....	98
<b>Chapter 4.....</b>	<b>99</b>
4. Characterisation of electrospun nanofibers .....	100
4.1 SiO <sub>2</sub> NFs.....	100
4.2 Semiconductor NFs.....	110
4.2.1 Hem NFs.....	110
4.2.2 ZnO NFs.....	117
4.2.3 TiO <sub>2</sub> NFs.....	120
4.3 Closing Remarks.....	130
<b>Chapter 5.....</b>	<b>131</b>
5.1 Fluorescence studies.....	132
5.1.1 Spectra.....	132
5.1.2 Quantum yields ( $\Phi_F$ ) and lifetimes ( $\tau_F$ ).....	133
5.2 Triplet Quantum yields ( $\Phi_T$ ) and triplet lifetimes ( $\tau_T$ ).....	135
5.3 Singlet oxygen quantum yields ( $\Phi_\Delta$ ).....	138
5.3.1 Comparative method .....	138
5.3.2 Absolute method.....	143
5.4 Closing Remarks.....	146

<b>Chapter 6</b> .....	<b>147</b>
6.1 Antimicrobial activity of Pcs and Pc-NP conjugates in solution.....	148
6.2 Antimicrobial activity of Pc/NP modified electrospun NFs .....	156
6.2.1 Antimicrobial activity on SiO <sub>2</sub> NFs.....	156
6.2.2 Antimicrobial activity on Hem NFs.....	164
6.3 Mechanism of PACT activity.....	165
6.4 Closing Remarks.....	168
<b>Chapter 7</b> .....	<b>169</b>
7.1 Photodegradation of Methyl Orange (MO).....	170
7.2 Mechanism of photodegradation.....	180
7.3 Closing Remarks.....	182
<b>Chapter 8</b> .....	<b>183</b>
8.1 Photo-induced hydrogen generation.....	184
8.2 Mechanism of sacrificial electron donor (SED) assisted hydrogen generation.	187
8.3 Closing Remarks.....	188
<b>Chapter 9</b> .....	<b>189</b>
9.1 Conclusions.....	190
9.2 Future work.....	191
<b>References</b> .....	<b>192</b>

# List of Symbols

$\Phi_{ADMA}$	ADMA Quantum Yield
$K_A$	Adsorption coefficient
$k$	Apparent reaction rate constant
$\tau_F$	Fluorescence Lifetime
$\Phi_F$	Fluorescence Quantum Yield
$t_{1/2}$	Half-life
$r_o$	Initial photocatalytic degradation rate
$C_o$	Initial concentration of pollutant
$I_{abs}$	Light intensity
$n$	Refractive index of sample solvent
$n_{std}$	Refractive index of standard solvent
$\Phi_{\Delta}$	Singlet Oxygen Quantum Yield
$\tau_T$	Triplet Lifetime
$\Phi_T$	Triplet Quantum Yield
$\alpha$	Absorption coefficient
$h$	Planck's constant,
$\nu$	Photon's frequency
$E_g$	Band gap energy
$k$	Proportionality constant

# List of Abbreviations

AA	Acetic acid
ADMA	Anthracene-9,10-bis-methylmalonate
APTES	(3-Aminopropyl)triethoxysilane
BET	Brunauer–Emmett–Teller
<i>C. albicans</i>	<i>Candida Albicans</i>
DBU	1,8-Diazabicyclo[5.4.0]undec-7ene
DCC	Dicyclohexylcarbodiimide
DCM	Dichloromethane
DMAE	Dimethylaminoethanol
DMSO	Dimethyl sulfoxide
DMF	N,N-Dimethylformamide
DPBF	1,3- Diphenylisobenzofuran
EDC	N,N'-dicyclohexylcarbodiimide
EDX	Energy Dispersive X-ray
<i>E. coli</i>	<i>Escherichia Coli</i>
EtOH	Ethanol
GC-TCD	Gas Chromatograph-Thermal Conductivity Detector
Hem	Hematite
HPLC	High performance liquid chromatography
<sup>1</sup> H NMR	Proton Nuclear Magnetic resonance
HOMO	Highest Occupied Molecular Orbital
IC	Internal conversion
ISC	Intersystem crossing
LUMO	Lowest Unoccupied Molecular Orbital

MALDI-TOF	Matrix- Assisted Laser Desorption Ionization- Time of Flight
MO	Methyl Orange
MNP	Metal Nanoparticles
MPc	Metallophthalocyanine
PBS	Phosphate Buffer Solution
Pc	Phthalocyanine
PVP	Polyvinylpyrrolidone
ROS	Reactive Oxygen Species
<i>S. aureus</i>	<i>Staphylococcus Aureus</i>
SED	Sacrificial Electron Donor
SEM	Scanning Electron Microscopy
SPR	Surface Plasmon Resonance
TCD	Tip to Collector Distance
TCSPC	Time-Correlated Single Photon Counting
TEM	Transmission Electron Microscopy
TEOS	Tetraethoxysilane
THF	Tetrahydrofuran
XRD	X-ray Diffraction
XPS	X-ray Photoelectron Spectroscopy

## **Preamble**

This thesis reports on the fabrication and characterisation of hybrid nanomaterials composed of various phthalocyanines that have been supported on nanofibers and nanoparticles. The composite nanomaterials are applied for water purification studies including the photoinactivation of microbes, photooxidation of organic pollutants and for the generation of hydrogen.

# Chapter 1

This chapter describes the basis of the thesis. It gives background on nanofibers, nanoparticles and phthalocyanines and how these nanomaterials can be conjugated to form hybrid visible light active nanocatalysts.



## 1. Introduction

The treatment of water contaminants (including bacteria and organic pollutants) is an area of importance due to the scarcity and hence increased demand for clean water. This thesis describes the fabrication, characterisation and application of various heterogeneous catalysts based on nanofibers (NFs) and nanoparticles (NPs) which have been modified with different phthalocyanines (Pcs). The fabrication of such organic-inorganic hybrid nanomaterials yields nanoconjugates with unique photophysicochemical properties and thus versatile applications.

### 1.1 Nanofibers (NFs)

Nanofibers are generally fibers with diameters in the nanometer range. They can be generated from different polymers and can have different physical properties and hence application potentials. The different NFs discussed in this work were all fabricated through electrospinning and used in varying water treatment applications.

#### 1.1.1 Electrospinning

Electrospinning; a technique that was developed in 1934 by Forhals, is used for the fabrication of continuous fibers with diameters in the nanometer to micrometer range through an electrically charged jet of polymer [1,2]. As depicted in **Figure 1.1**, the basic electrospinning components include a high voltage direct current power supply, a ground/rotating collector (an electrical conducting material) and a spinneret (typically a syringe needle) [3]. During the generation of the electrospun NFs, a high voltage is applied to a polymer fluid which is fed through the spinneret with the help of the syringe pump (controls the flow rate). The discharged polymer solution undergoes a whipping wherein the solvent evaporates and the stretched polymer fibers are deposited on the collector [3,4].

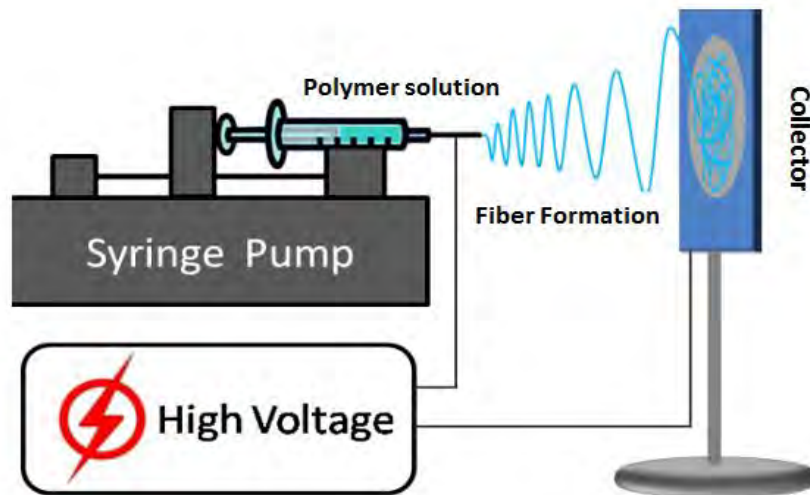


**Figure 1.1:** Schematic diagram of electrospinning setup [3]

The morphologies and diameters of electrospun NFs can be altered by modifying parameters including [5-7]:

- intrinsic properties of the polymer solution such as the type of polymer, solution viscosity, and solvent volatility.
- processing parameters including the strength of the applied electric field, solution flow rate, and tip to collector distance (TCD).

Variables such as humidity and temperature of the surroundings also contribute to the physical properties of the electrospun NFs [3].

Through experimental investigations, general relationships between these parameters and fiber morphologies have been elucidated. For instance, a higher voltage has been observed to lead to larger fiber diameters, a trend that is not necessarily monotonic. It has also been observed that the more viscous the polymer solution, the larger the fiber diameter [3].

Electrospun NFs commonly possess properties such as porosity, long length and higher surface areas hence they are used in numerous fields including tissue engineering scaffolds, protective clothing, filtration, and wound dressing amongst others [7-10].

In this work, the electrospun NFs are used as catalyst supports for phthalocyanines (Pcs), nanoparticles (NPs) and their respective conjugates for application in the photoinactivation of microbes, photodegradation of organic pollutants and for hydrogen generation studies.

### **1.1.2 Modification of electrospun nanofibers**

As demonstrated in **Table 1.1**, electrospun NFs have been used to embed a range of Pcs and NPs for use in different water purification applications [11-17]. This is to ensure catalyst recovery and hence reusability as well as cost effectiveness. The use of NFs also increases the catalyst surface area and in addition, embedding the photocatalysts in the NFs also ensures that they are protected from degradation and do not leach into the water, thereby further polluting it.

All the modified NFs in **Table 1.1** are derived from various polymers. The electrospun NFs reported in this work are however different from the commonly used ones as they are polymer free. This is achieved by calcination of the polymer of choice at high temperatures to yield purely inorganic NFs. The polymer therefore acts as sacrificial entity and aids in the generation of NFs from otherwise powdered or liquid materials. The calcination of the polymer is attractive in that it eliminates the possible shielding and suppression of the activity of the embedded catalysts. The polymer removal also ensures that there is direct contact and hence better interaction between the pollutants

and the catalyst without the polymer barrier. It is novel for Pcs to be embedded onto polymer-free NFs.

This work reports on the fabrication, characterisation and application of a range of polymer free NFs i.e. silica NFs as well as various semiconductor based NFs.

**Table 1.1:** Modified electrospun nanofibers for different water treatment applications

Catalysts	Polymer	Application	Ref.
InOCPc	Polyacrylonitrile	Degradation of Methyl Orange and Photoinactivation of <i>S. aureus</i>	11
LuTPPc	Polystyrene	Degradation of 4-Chlorophenol	12
Lead Pc	Polystyrene	Photoinactivation of <i>Escherichia coli</i>	13
ZnOCPc-Fe <sub>3</sub> O <sub>4</sub> conjugate	Polyamide-6	Degradation of Orange G	14
ZnTCPPc and ZnTAPPc	Polystyrene	Degradation of Orange G	15
Copper Pc	Polyacrylonitrile	Degradation of Rhodamine B	16
H <sub>2</sub> TPCPc	Polystyrene	Photoinactivation of <i>S. aureus</i>	17

**InOCPc** = In octacarboxy phthalocyanine, **LuTPPc** = Lu tetraphenoxy phthalocyanine, **ZnOCPc** = Zn octacarboxy phthalocyanine, **ZnTCPPc** = Zn tetracarboxyphenoxy phthalocyanine, **ZnTAPPc** = Zn tetraaminophenoxy phthalocyanine, **H<sub>2</sub>TPCPc** = free-base tetraphenylcarboxy phthalocyanine.

### 1.1.3 Polymer free nanofibers

Attractive properties of heterogeneous catalysts for water treatment include high surface areas, high activity, stability, cost effectivity, reusability and versatility, hence this work compares the properties and catalytic efficiencies of a range of polymer free NFs.

As demonstrated in **Table 1.2** [18-22], various polymer free NFs have been fabricated for various applications. In this work however, the synergistic interactions of the various NFs with different Pcs and NPs are explored for the first time. The NFs discussed in this work are applied in the presence of Pcs and NPs for a range of water purification based applications such as the degradation of water pollutants and antimicrobial studies amongst others to demonstrate their versatility and hence multi-functional purposes.

**Table 1.2:** Electrospun polymer free nanofibers and their various applications.

Type of Nanofiber	Application	Ref.
Alumina nanofibers	Methyl Orange adsorption	18
Cyclodextrin nanofibers	-	19
Tin oxide nanofibers	Detection of Triacetone triperoxide Precursors	20
Tantalum pentoxide fibers	-	21
Cesium tungstate	Photodegradation of Rhodamine B	22

### 1.1.3.1 Silica nanofibers (SiO<sub>2</sub> NFs)

Silica (SiO<sub>2</sub>) is one of the most abundant compounds in the earth's crust and it exists in crystalline (quartz) and amorphous (glass) form, both of which possess different properties [23]. Due to their attractive properties such as chemical and physical stability, biocompatibility as well as high surface areas, the fabrication and application of SiO<sub>2</sub> NFs for studies such as thermal energy storage and removal of organic pollutants have been reported [24-27]. These NFs are also good as catalyst supports as they are stable, difficult to destroy in solvents, easy to recycle, flexible and possess high-heat-resistance [28,29].

Herein the fabrication and characterisation of inorganic SiO<sub>2</sub> NFs is reported. This entails the combination of electrospinning with sol-gel process, followed by calcination. The NFs are also decorated with different Pcs and NPs for the first time with the aim of creating effective antibacterial and antifungal agents against *Staphylococcus Aureus* (*S. aureus*), *Escherichia Coli* (*E. coli*) and *Candida Albicans* (*C. albicans*), respectively.

### 1.1.3.2 Semiconductor based nanofibers

Over the years, research interest on semiconductor based photocatalysts has increased due to their versatile applications, including the photodegradation of organic waste, bacterial treatment, anticancer properties and water splitting [30-33]. Hematite (Hem), titanium dioxide (TiO<sub>2</sub>), and zinc oxide (ZnO) are the most commonly used of these photocatalysts due to their relatively low cost, good chemical and optical stability as well as their easy fabrication in a range of nanostructures such as nanowires, nanocombs and nanospheres etc. [34-36].

This thesis reports on the fabrication (through electrospinning followed by calcination), characterisation and applications of Hem, ZnO and TiO<sub>2</sub> NFs. These NFs are particularly attractive relative to the other semiconductor nanomaterials as they usually have small diameters (nano to micrometer scale) and high surface-to-volume ratios [37,38]. The limitation of some semiconductors however is that they tend to have wide band gaps of ~3.0 eV meaning their photoactivity is mainly under UV irradiation [39,40]. The sunlight reaching the earth's surface on the other hand contains less than 5% UV irradiation, thereby limiting the real life applications of these photocatalysts [41]. Hence this thesis discusses the fabrication of Hem, ZnO and TiO<sub>2</sub> NFs decorated with visible light active Pcs for the first time.

The conjugation of Pcs to iron oxide NPs has been reported before [42,43]. This work however reports for the first time on the fabrication and characterisation of Pc modified polymer free Hem NFs. This is done with the aim of creating dual purpose catalyst with high activity and that can be magnetically regenerated post-application. The photocatalytic activities of the Pc modified Hem NFs are evaluated for antibacterial studies against *S. aureus* and for the photodegradation of Methyl Orange (MO), an organic pollutant.

The conjugation of Pcs to ZnO NPs for enhanced photocatalytic activity has been reported before [44]. This thesis however reports on the fabrication and characterisation of Pc modified ZnO NFs for the first time. The photocatalytic activities of these NFs are discussed based on their efficiencies in the photodegradation of MO.

The conjugation of Pcs to TiO<sub>2</sub> NPs has also been reported before [45]. In this thesis however, the fabrication, characterisation and application of anatase and rutile TiO<sub>2</sub> NFs is discussed. Comparison of the catalytic efficiencies of the anatase and rutile

TiO<sub>2</sub> is also reported. The NFs are modified with NPs and Pcs and applied for the photodegradation of MO and the generation of hydrogen.

## 1.2 Nanoparticles (NPs)

Nanoparticles (NPs) are the building blocks of nanotechnology that in broadest terms signifies the understanding and controlling of properties of matter at dimensions of roughly 1–100nm [46]. Although small, NPs are mainly composed of three layers [47]:

- The surface layer, which may be functionalized with a variety of small molecules, metal ions, surfactants and polymers.

- The shell layer, which is chemically different material from the core in all aspects.

- The core, which is essentially the central portion of the NP and usually refers the NP itself.

Some of the main advantages of using NPs include their ability to target drugs to specific locations in the body, they can enhance aqueous solubility of other materials, they have tuneable properties and they have large surface areas, which allow for multiple functional groups to be added to their surfaces [48]. In addition, NPs can influence the photophysicochemical properties of a photosensitiser and they tend to exhibit size-related properties that differ significantly from those observed in fine particles or bulk materials [47,49]. The NPs that have been synthesised and are reported in this work are silver, iron oxide (Fe<sub>3</sub>O<sub>4</sub>), bimetallic iron oxide- silver, palladium and cobalt NPs. As shown in **Table 1.3** [50-63], these NPs have been used for various applications. This thesis however discusses the syntheses and role of the NPs in the enhancement of the photoactivities of the different Pcs; in solution (Ag, Fe<sub>3</sub>O<sub>4</sub> and bimetallic Fe<sub>3</sub>O<sub>4</sub>@Ag NPs) and when supported on NFs (Ag, Pd and Co



NPs). The different chemical bonds holding the NPs to the NFs and Pcs are also reported based on the different capping agents that are used. As shown in **Table 1.3** [60-63], the conjugation of the NPs with various Pcs also results in conjugates that have been used for photocatalytic applications.

**Table 1.3:** Various applications of the NPs and Pc-NP conjugates.

<b>NPs/ Pc-NP conjugates</b>	<b>Application</b>	<b>Ref.</b>
Silver NPs	Drug delivery, catalysis, wound dressing	<b>50-52</b>
Iron oxide magnetic NPs	Antibacterial agents, catalysis	<b>53,54</b>
Bimetallic iron oxide- silver NPs	Biosensors	<b>55</b>
Palladium NPs	Fuel cells, catalysis	<b>56,57</b>
Cobalt NPs	Biomedicine, catalysis	<b>58,59</b>
Pc-silver NP conjugate	Antimicrobial agents	<b>60,61</b>
Pc-iron oxide magnetic NP conjugate	Antimicrobial agents, catalysis	<b>11,62</b>
Pc- bimetallic iron oxide- silver NP conjugate	Antimicrobial agents	<b>63</b>

### 1.2.1 Silver nanoparticles (Ag NPs)

Silver nanoparticles (Ag NPs) are commonly used nanomaterials in various research areas due to their attractive properties including optical, electrical, and thermal stability, high electrical conductivity, and biological activity amongst others [64,65]. A variety of preparation techniques have been reported for the synthesis of silver NPs such as laser ablation, gamma irradiation, electron irradiation, microwave processing and biological synthetic methods [66-70].

This work reports on the fabrication of Ag NPs on the surface of SiO<sub>2</sub> NFs for catalyst support and reusability. This was conducted using the *in situ* chemical reduction, as the method allows for control of the particle size and morphology of the NPs [71]. The anchoring of Ag NPs on SiO<sub>2</sub> NFs is particularly attractive as the photoactive Ag<sup>+</sup> ions have been shown to exhibit sustained release from Ag NPs when they are immobilised on substrates, thereby providing prolonged catalytic effects [72].

Oleylamine capped Ag NPs were also fabricated and then conjugated to sulfur and nitrogen rich Pcs through chemisorption using Ag-N and Ag-S bonds. The conjugation of Ag NPs to uncharged Pcs has been reported to enhance their photophysicochemical and hence photocatalytic properties [60,61] (Table 1.3). In this work however, the conjugation of Ag NPs to cationic Pcs is reported for the first time. This was achieved through the thermal decomposition of silver acetate, a method that has been reported to yield monodispersed Ag NPs with controlled sizes [73]. The conjugation of cysteamine capped Ag NPs to Pcs with terminal carboxylic acid groups through amide bonds is also explored and reported. All of the Ag NP modified Pcs and NFs reported herein are applied for antimicrobial purposes.

### 1.2.2 Iron oxide magnetic nanoparticles (Fe<sub>3</sub>O<sub>4</sub> NPs)

Due to their superparamagnetism and high surface areas, research interest in magnetite nanoparticles (Fe<sub>3</sub>O<sub>4</sub> NPs) has increased [74]. Various methods have been reported for the synthesis of these NPs including co-precipitation, microemulsion, thermal decomposition, solvothermal and sonochemical techniques [75-79]. The Fe<sub>3</sub>O<sub>4</sub> NPs reported herein were synthesised using the co-precipitation method. This is because it is an easy method, uses less harmful materials, it has high productivity, short reaction times and controlled NP sizes [80].

This work reports on the conjugation of amine functionalised Fe<sub>3</sub>O<sub>4</sub> NPs to carboxylic acid functionalised Pcs through amide bonds to get magnetically retrievable photocatalysts. The effect of the conjugation on the photophysicochemical and antibacterial properties of the Pcs is studied and discussed. The conjugation of Pcs to Fe<sub>3</sub>O<sub>4</sub> NPs and their antibacterial behaviours have been reported before [11,62] (Table 1.3). In this work however, asymmetrical Pcs are investigated in such a study for the first time.

### 1.2.3 Bimetallic iron oxide- silver nanoparticles (Fe<sub>3</sub>O<sub>4</sub>@Ag NPs)

With the aim of combining the optical and photochemical properties of Ag NPs to the magnetic properties of Fe<sub>3</sub>O<sub>4</sub> NPs, bimetallic composite iron oxide- silver NPs were synthesised. This was achieved through the thermal decomposition of silver acetate on the surface of Fe<sub>3</sub>O<sub>4</sub> NPs. Although the fabrication of these NPs has not been explored much, they have been reported to possess an enhanced magneto-optic response relative to Ag and Fe<sub>3</sub>O<sub>4</sub> NPs alone [81].

The conjugation of these NPs to Pcs has been reported before [63] (Table 1.3). This thesis however reports for the first time on their conjugation to asymmetric Pcs. The effect of the conjugation on the photophysicochemical and antibacterial properties of the Pcs is studied and discussed.

### 1.2.4 Palladium nanoparticles (Pd NPs)

Palladium (Pd) is a rare and precious metal that belongs to the platinum group elements [82]. Pd NPs are largely employed as active catalysts due to their high surface area to volume ratio and high surface energy [83]. Several methods have been

developed for the synthesis of these NPs including microwave assisted, microemulsions, biosynthesis and sonochemical reduction [84-87].

This thesis however reports for the first time on the use of TiO<sub>2</sub> NFs to reduce Pd<sup>2+</sup> to Pd<sup>0</sup> thereby leading to the *in situ* formation of the NPs on the NFs. It is also the first time that Pcs are employed with Pd NPs. This is done with the aim of enhancing the photocatalytic efficiencies of the anatase and rutile TiO<sub>2</sub> NFs which is evaluated based on their abilities to promote the production of hydrogen from contaminated water.

### 1.2.5 Cobalt nanoparticles (Co NPs)

Cobalt is considered to be the first catalyst made from nonprecious metal with properties closely matching with those of the highly active platinum [88]. Cobalt NPs are particularly attractive due to their superparamagnetic nature and easy fabrication in different shapes and sizes [89,90]. Reported methods for the synthesis of Co NPs include microfluidics, microemulsion, biosynthesis and template based synthesis [91-94].

In this work, reduction of Co<sup>2+</sup> to Co<sup>0</sup> is conducted on the TiO<sub>2</sub> NFs leading to the *in situ* formation of the NPs on the surface of the NFs, a study that is conducted for the first time. It is also the first time that Pcs are employed with Co NPs. This is done with the aim of enhancing the photocatalytic efficiencies of the anatase and rutile TiO<sub>2</sub> NFs and comparing the findings to those obtained for the TiO<sub>2</sub> NFs modified with Pd NPs. The catalytic behaviour of the NFs modified with the Co NPs was also evaluated based on their abilities to promote the production of hydrogen from contaminated water.

### 1.3 Phthalocyanines (Pcs)

Phthalocyanines (Pcs) are structural analogues of other macrocyclic pigments such as porphyrins and were first characterized and documented by Linstead and co-workers [95]. They are synthetic tetrapyrrolic macrocycles containing four iminoisoindoline rings (connected via nitrogen atoms) with a conjugated 18  $\pi$ -electron system [96]. The central cavity of Pcs can accommodate numerous metals or metalloids, while various substituents can be incorporated to the outer hydrocarbon moieties on the non-peripheral ( $\alpha$ ) and peripheral ( $\beta$ ) positions as shown in **Figure 1.2**. According to nomenclature of tetrapyrroles [97],  $\alpha$ -substituents are located at the 1, 4, 8, 11, 15, 18, 22, and 25 positions on the Pc ring, while  $\beta$ -substituents are located at the 2, 3, 9, 10, 16, 17, 23, and 24 positions on the Pc ring.

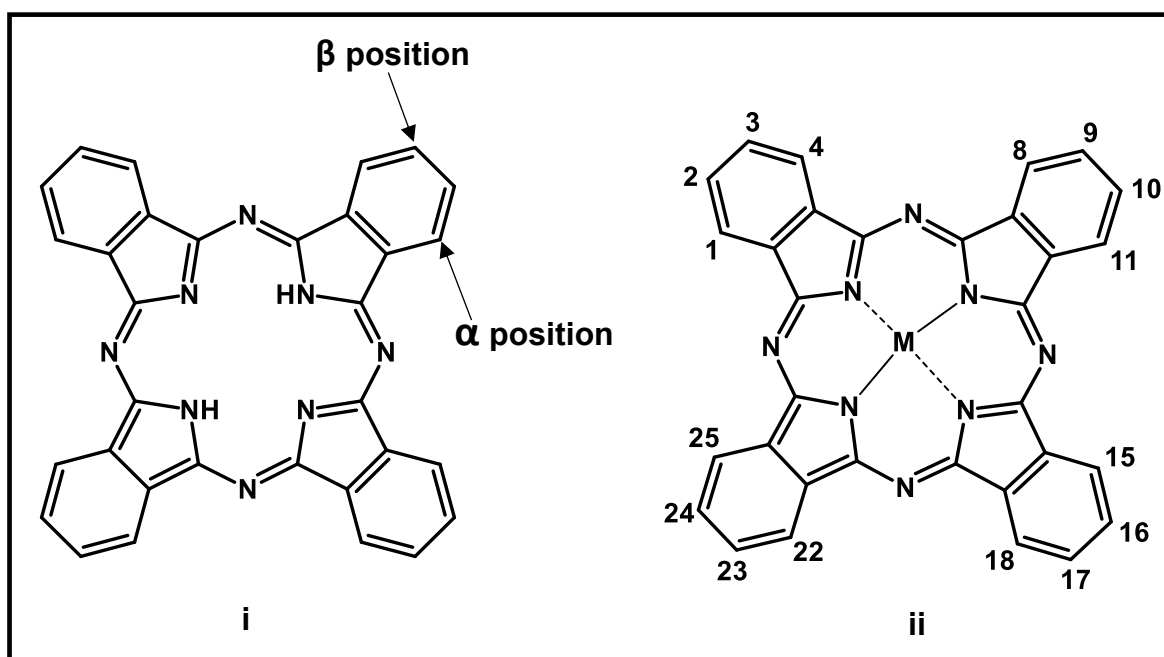
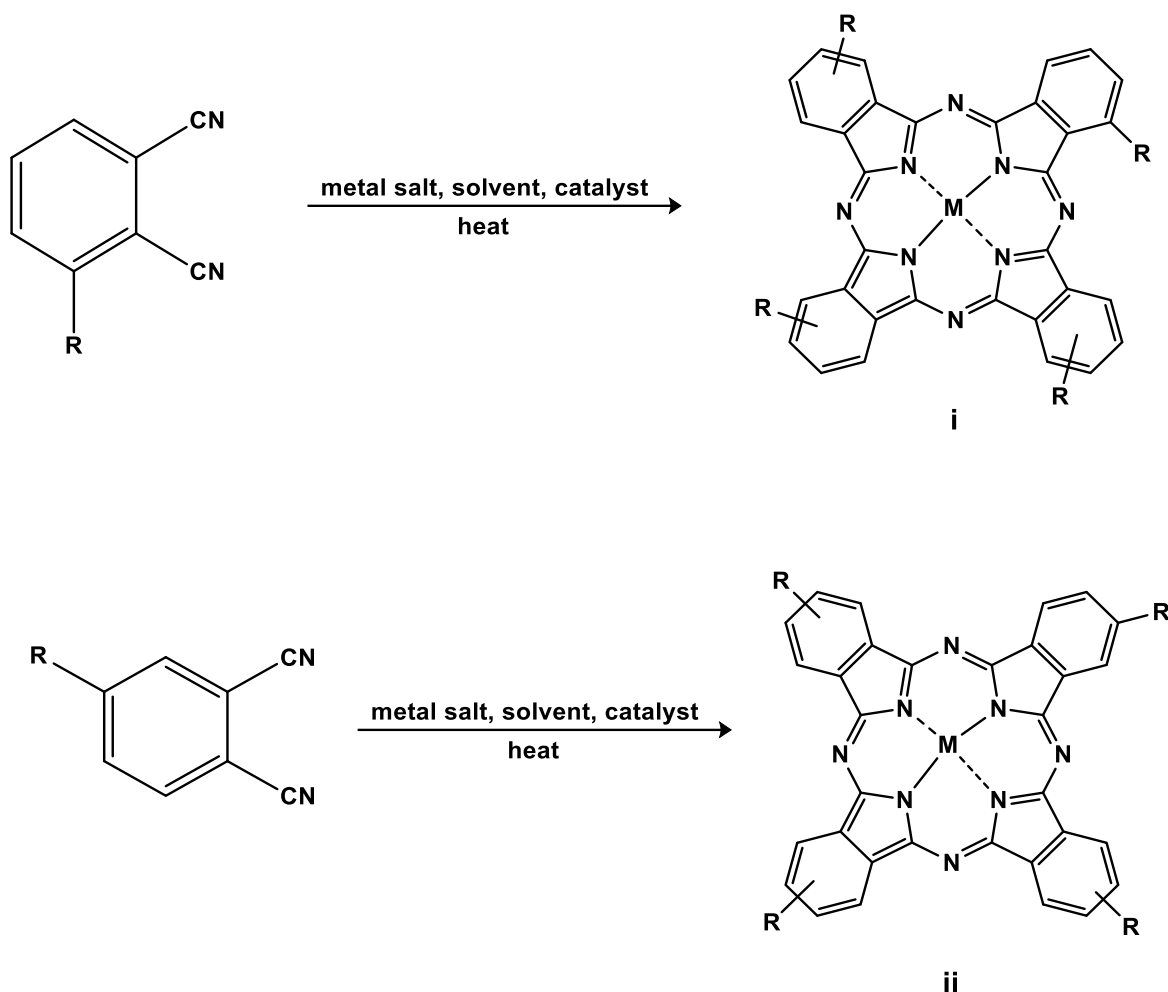


**Figure 1.2:** The molecular structures of (i) an unmetallated phthalocyanine (H<sub>2</sub>Pc) and (ii) a metallophthalocyanine (MPc).

The use of the different central metals and substituents allows for the generation of a wide range of Pc complexes with different properties and hence applications. Pcs generally possess attractive properties such as excellent visible/near infrared absorption, high chemical and thermal stability and the ability of generate singlet oxygen [98]. They have gained attention in diverse applications including nonlinear optics [99], photodynamic therapy of cancer [100], dye sensitised solar cells [101], water splitting [102], sensors [103], textile coloring [104] and corrosion inhibition [105] amongst others.

### 1.3.1 Synthesis of symmetrical and asymmetrical Pcs

Various routes have been reported for the synthesis of Pcs, all of which depend on the type of the desired Pc i.e. whether metallated or metal free, symmetrical or asymmetrical. The synthesis of Pcs can be achieved using different precursors including o-cyanobenzamide, o-dibromobenzene, diiminosoindole and phthalonitriles. The use of phthalonitriles is more popular due to ease of purification and high yields of the generated Pcs [106,107]. The synthesis of  $\alpha$  and  $\beta$ -tetrasubstituted Pcs would thus require the use of a 3-nitrophthalonitrile and 4-nitrophthalonitrile, respectively. The nitro groups of the phthalonitriles can then be modified to afford the desired substituted phthalonitriles for the synthesis of Pcs [108]. Symmetrically tetrasubstituted Pcs are synthesized by cyclotetramerization of monosubstituted phthalonitriles in the presence of a metal salt (in the case of metallophthalocyanines), a base such as 1,8-diazabicycloundec-7ene (DBU) or dimethylaminoethanol (DMAE) and a solvent such as quinoline and 1-pentanol [109,110], **Scheme 1.1**.



**Scheme 1.1:** The synthesis of tetrasubstituted MPcs from monosubstituted phthalonitriles at (i) non-peripheral ( $\alpha$ ) and (ii) peripheral ( $\beta$ ) positions. R represents the substituent of choice.

The cyclotetramerization of monosubstituted phthalonitriles to form tetrasubstituted Pcs results in a mixture of isomers with the molecular symmetry of  $C_{4h}$ ,  $C_{2v}$ ,  $C_s$  and  $D_{2h}$ . Although time consuming and resulting in low yields, these isomers have been reported to be separable using specially designed high performance liquid chromatographic (HPLC) columns [111].

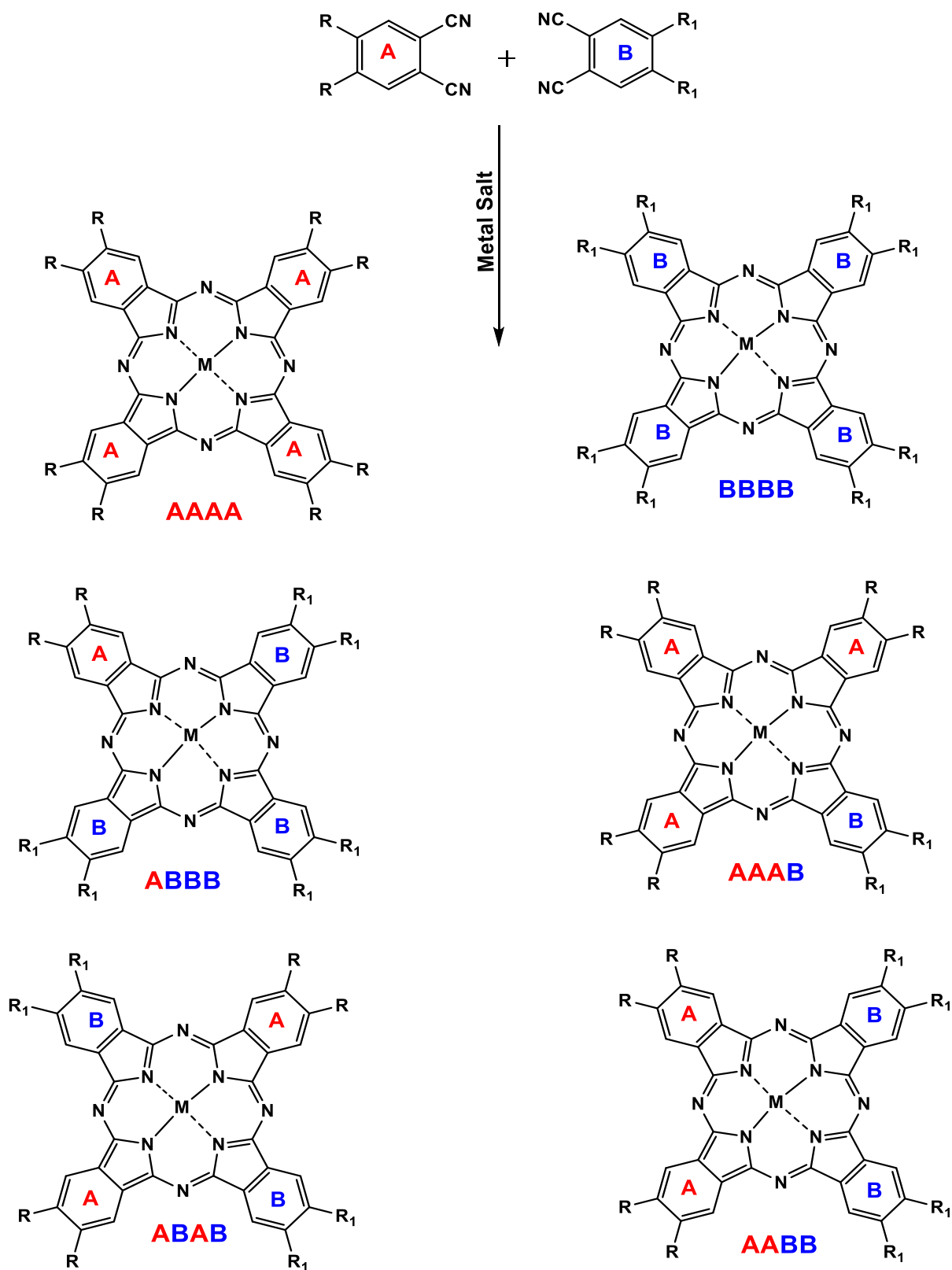
The synthesis of asymmetrical Pcs has been achieved using various methods including sub-phthalocyanine expansion and the conventional statistical condensation of two differently substituted phthalonitriles [112,113]. The statistical condensation approach was implemented for the synthesis of A<sub>3</sub>B-type asymmetrical Pcs in this work. These Pcs have three identical isoindole subunits and one different subunit. This method requires two differently substituted phthalonitriles which upon cyclising in the presence of a metal salt give six possible constitutional isomers with varying percentage yields, **Scheme 1.2** [114,115]. The six products can be chromatographically isolated to obtain the desired Pc.

### 1.3.2 Phthalocyanines studied in this thesis

This work reports on symmetrical and asymmetrical peripherally substituted Pcs with a zinc (Zn) central metal. The central metal of Pcs influences their photophysicochemical properties. Zn was particularly chosen for the Pcs reported in this thesis because it is diamagnetic and hence has a closed shell structure which results in enhanced photophysicochemical properties. In addition, as a heavy atom, Zn promotes intersystem crossing (ISC) of the excited dye to populate the triplet state, a phenomenon known as the heavy atom effect. ISC is mostly observed in atoms whose nuclei are large and enhances the kinetics of both radiative and non-radiative transitions between states with different spins [116,117]. Complexes **1, 6** and **7** have been reported before [118-120] while complexes **2-5** are novel, **Table 1.4**.

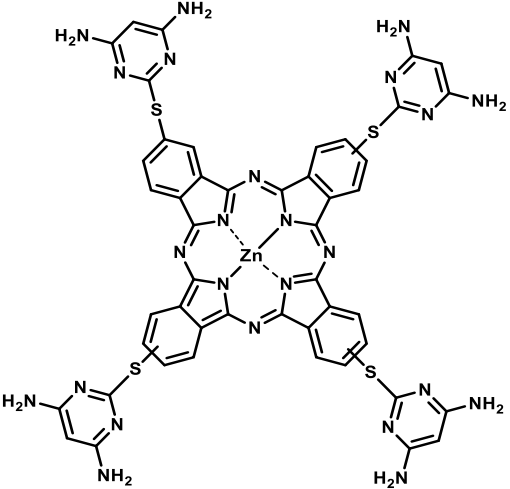
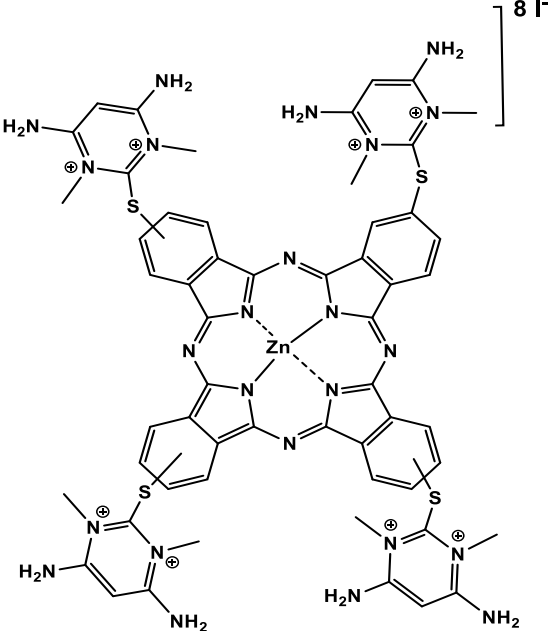
Please note: Complex **6** was reported as part of my MSc work, but has now been expanded to include NPs and NFs.

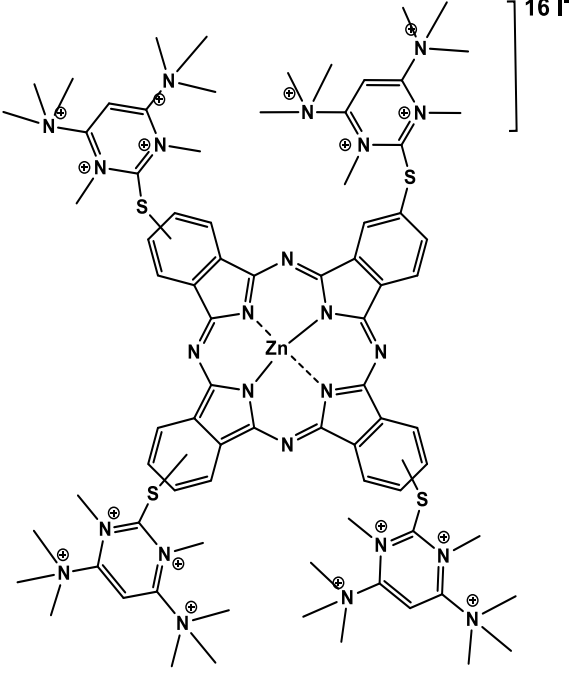
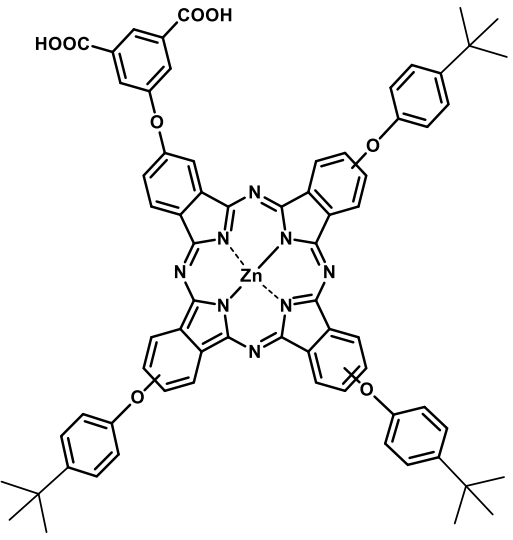


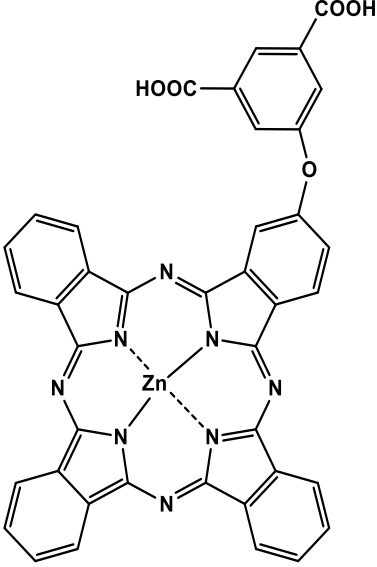
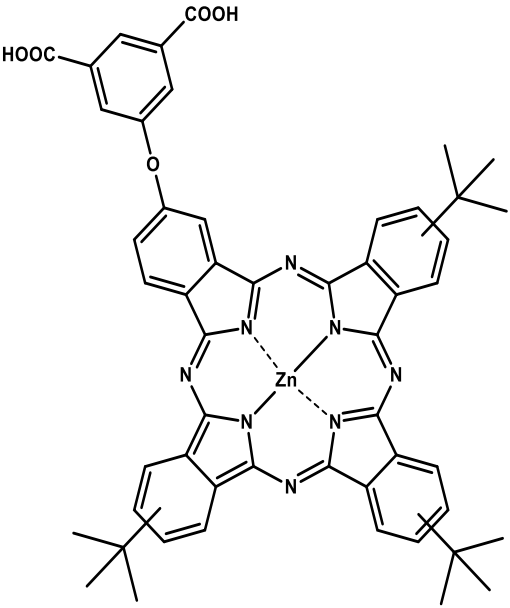


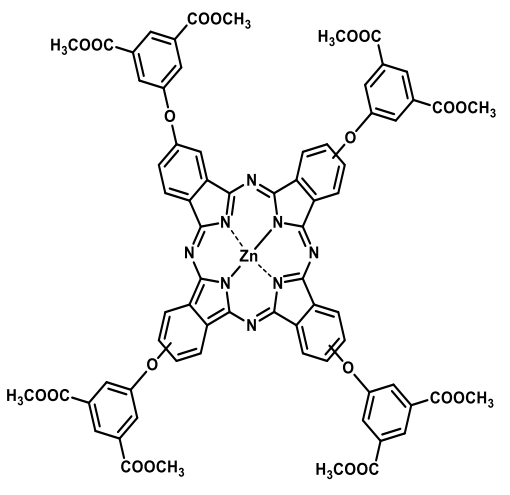
**Scheme 1.2:** Methods for the synthesis of unsymmetrical Pcs using the statistical condensation of phthalonitriles **A** and **B**.

**Table 1.4:** Phthalocyanine complexes used in this thesis

Pc structure and name	Support (NFs and / or NPs)	Application	Complex
 <p>2,9(10),16(17),23(24)-Tetrakis-(4'-(4'-6'-diaminopyrimidin-2'-ylthio)) phthalocyaninato zinc (II)</p>	<p><b>No NFs</b> OLM-Ag NPs <b>(Ag-N &amp; Ag-S bonds)</b></p> <hr/> <p><b>SiO<sub>2</sub> NFs</b> with <i>in situ</i> Ag NPs</p>	<p>Photodynamic Antimicrobial Chemotherapy of <i>S. aureus</i>, <i>E. coli</i> and <i>C. albicans</i></p>	<p><b>1</b> <b>[118]</b></p>
 <p>2,9(10),16(17),23(24)-Tetrakis-(4'-(1',3'-N-dimethyl, 4'-6'-diaminopyrimidin-2'-ylthio)) phthalocyaninato zinc (II)</p>	<p><b>No NFs</b> OLM-Ag NPs <b>(Ag-N &amp; Ag-S bonds)</b></p> <hr/> <p><b>SiO<sub>2</sub> NFs</b> with <i>in situ</i> Ag NPs</p>	<p>Photodynamic Antimicrobial Chemotherapy of <i>S. aureus</i>, <i>E. coli</i> and <i>C. albicans</i></p>	<p><b>2</b> <b>[NEW]</b></p>

 <p>2,9(10),16(17),23(24)-Tetrakis-(4'-(1',3'-N-dimethyl, 4'-6'-(hexamethylaminopyrimidin-2'-ylthio))) phthalocyaninato zinc (II)</p>	<p><b>No NFs</b></p> <p>OLM-Ag NPs</p> <p><b>(Ag-S bonds)</b></p>	<p>Photodynamic Antimicrobial Chemotherapy of <i>S. aureus</i>, <i>E. coli</i> and <i>C. albicans</i></p>	<p><b>3</b></p> <p><b>[NEW]</b></p>
<p><b>SiO<sub>2</sub> NFs</b></p> <p>with</p> <p><i>in situ</i> Ag NPs</p>			
 <p>2-Mono-isophthalic acid-9(10),16(17),23(24)- tri (<i>tert</i>-butylphenoxy) phthalocyaninato zinc(II)</p>	<p><b>No NFs</b></p> <p>Cys-Ag, NH<sub>2</sub>-Fe<sub>3</sub>O<sub>4</sub> and Cys-Fe<sub>3</sub>O<sub>4</sub>@Ag NPs</p> <p><b>(Amide bonds)</b></p>	<p>Photodynamic Antimicrobial Chemotherapy of <i>S. aureus</i></p>	<p><b>4</b></p> <p><b>[NEW]</b></p>
<p><b>Hem NFs</b></p> <p>No NPs</p>			

 <p>2-Mono-(5-oxy)isophthalic acid phthalocyaninato zinc(II)</p>	<p><b>No NFs</b></p> <p>Cys-Ag, NH<sub>2</sub>-Fe<sub>3</sub>O<sub>4</sub> and Cys-Fe<sub>3</sub>O<sub>4</sub>@Ag NPs</p> <p><b>(Amide bonds)</b></p>	<p>Photodynamic Antimicrobial Chemotherapy of <i>S. aureus</i></p>	<p><b>5</b></p> <p><b>[NEW]</b></p>
<p><b>Hem NFs</b></p> <p>No NPs</p>	<p>Photodynamic Antimicrobial Chemotherapy of <i>S. aureus</i></p>	<p>Photodegradation of Methyl Orange</p>	
 <p>2-[5-(phenoxy)-isophthalic acid] 9(10), 16(17), 23(24)-tris(tert-butyl)phthalocyaninato zinc(II)</p>	<p><b>No NFs</b></p> <p>Cys-Ag, NH<sub>2</sub>-Fe<sub>3</sub>O<sub>4</sub> and Cys-Fe<sub>3</sub>O<sub>4</sub>@Ag NPs</p> <p><b>(Amide bonds)</b></p>	<p>Photodynamic Antimicrobial Chemotherapy of <i>S. aureus</i></p>	
<p><b>Hem NFs</b></p> <p>No NPs</p>	<p>Photodynamic Antimicrobial Chemotherapy of <i>S. aureus</i></p>	<p>Photodegradation of Methyl Orange</p>	
<p><b>ZnO and TiO<sub>2</sub> NFs</b></p> <p>No NPs</p>	<p>Photodegradation of Methyl Orange</p>		

 <p data-bbox="87 739 670 806">2,9(10),16(17),23(24)-Tetra 5-(phenoxy)-isophthalic acid phthalocyaninato] Zinc (II)</p>	<p data-bbox="766 358 909 403"><b>TiO<sub>2</sub> NFs</b></p> <p data-bbox="813 425 861 470">with</p> <p data-bbox="694 492 989 537"><i>in situ</i> Pd and Co NPs</p>	<p data-bbox="1069 425 1372 470">Hydrogen generation</p>	<p data-bbox="1492 448 1524 492"><b>7</b></p> <p data-bbox="1468 515 1548 560"><b>[120]</b></p>
--	---	--	---

Complexes **1-3** were chosen based on them having nitrogen and sulfur moieties, thereby allowing for chemisorption of the Pcs on Ag NPs via Ag-N or Ag-S bonding [121]. In addition, complexes **2** and **3** are cationic, a trait that makes them good candidates for the photoinactivation of different kinds of microorganisms [122,123]. The antimicrobial activities of complexes **1-3** and their respective conjugates were evaluated in solution when they are alone and when conjugated to oleylamine capped Ag NPs as well as in solid state when they are supported on SiO<sub>2</sub> NFs. Although the synthesis and antibacterial studies of a hexadecacationic Pc (with different substituents) have been recently reported [124], this thesis reports for the first time on the photophysicochemical attributes of the hexadecacationic complex **3** when alone, when conjugated to Ag NPs and when supported on NFs. Complexes **4-6** were chosen based on their asymmetry as it has been reported that asymmetry in Pcs results in improved singlet oxygen quantum yields [125]. Complexes **4-6** also have carboxylic acid moieties which allow for their covalent conjugation to various NPs (Ag, Fe<sub>3</sub>O<sub>4</sub> and Fe<sub>3</sub>O<sub>4</sub>@Ag NPs) with amine groups for enhanced photophysicochemical properties

as observed before [126]. The carboxylic acid groups in complexes 4-6 also allow for anchoring of the Pcs to the surface of their respective NFs to provide intimate electronic coupling. The *tert*-butyl and carboxylic acid groups of complex 6 act as “push” and “pull” groups, respectively. This is important for light-harvesting systems wherein the photosensitizer possesses directionality which can be achieved by using electron donating (push) and electron withdrawing (pull) functional groups as substituents [127]. In addition, the bulky *tert*-butyl groups in complexes 4 and 6 cause increased solubility and reduce aggregation of the Pcs in solution. Complexes 4-6 and their respective conjugates were applied for antibacterial studies while complexes 5 and 6 were also applied for the photodegradation of MO when supported on different NFs. Lastly, complex 7 was chosen based on it being easily soluble in volatile solvents such as THF, making its adsorption onto the surface of TiO<sub>2</sub> NFs effortless. Complex 7 was used in the modification of different TiO<sub>2</sub> NFs for the generation of hydrogen.

### 1.3.3 Electronic Absorption Spectra of Pcs

The spectra of Pcs are influenced by numerous factors including the presence or absence of a central metal, the nature of the substituents, solvents and aggregation tendencies [128,129]. The Pcs reported in this work are all metallated and generally have similar spectra with two major distinct absorption bands as shown in **Figure 1.3**.

The Q band is the most intense peak and it is observed in the near infrared region, accompanied by vibronic bands (Qvib). The Gouterman’s four orbital model was used to explain the transitions that occur to give rise to the individual absorption bands. The Q band results from the  $\pi$ - $\pi^*$  transition from the ground state  $a_{1u}$  of the highest occupied molecular orbital (HOMO) to the doubly degenerate  $e_g$  of the lowest unoccupied molecular orbital (LUMO), **Figure 1.3** (insert) [130,131]. The B band (B<sub>1</sub>

and B<sub>2</sub> combined) is attributed to the  $\pi$ - $\pi^*$  transitions from a<sub>2u</sub> and b<sub>2u</sub> of the HOMO to the e<sub>g</sub> of the LUMO, **Figure 1.3** (insert) [132,133].

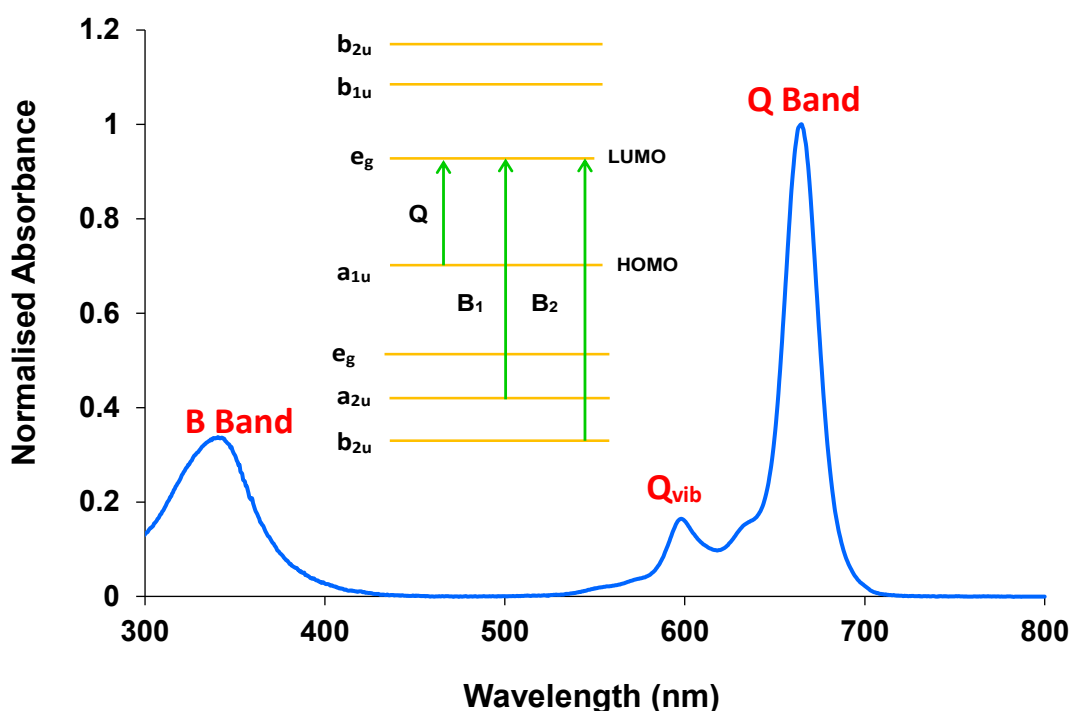


**Figure 1.3:** Example of ground state UV-vis spectrum of Pcs extrapolated from unpublished work. Insert = molecular orbital representation of electronic transition).

#### 1.3.4 Photophysical Parameters of Pcs

The photophysical properties of Pcs determine their applicability as photosensitizers in areas such as photocatalysis. These properties explain the changes that occur in quantum states of a molecule upon exposure to light wherein the chemical nature is unaltered. A Jablonski diagram such as that shown in **Figure 1.4** is commonly used to demonstrate the processes that occur when photosensitisers such as Pcs absorb light.

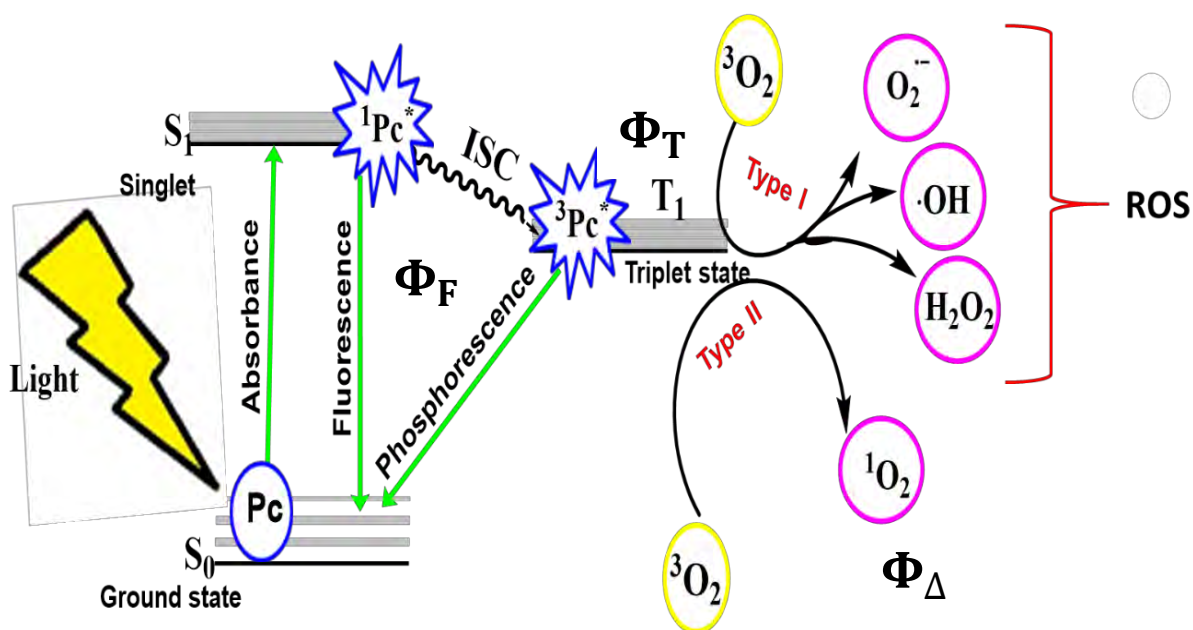


**Figure 1.4:** Modified Jablonski diagram showing the major photophysical parameters of Pcs.  $S_0$  = ground state,  $S_1$  = first excited singlet state,  $T_1$  = excited triplet state, ISC = intersystem crossing, ROS = reactive oxygen species.

Briefly, the Pc in its ground state ( $S_0$ ) absorbs light and is excited to the first excited singlet state ( $S_1$ ). The excited Pc can then dissipate energy either by spontaneous emission (fluorescence) back to the ground state ( $S_0$ ) or by intersystem crossing (ISC) to the excited triplet state ( $T_1$ ). The Pc can then transfer electrons (Type I) or energy (Type II) to ground state molecular oxygen ( $^3O_2$ ) thereby generating various reactive oxygen species (ROS) including singlet oxygen [134,135]. The singlet oxygen is the main active species in photosensitiser mediated photocatalysis [136]. Quantification of the major transitions i.e. fluorescence, population of the excited triplet state and the amount of singlet oxygen produced is therefore of importance as they determine the suitability of a Pc as a photosensitiser for photocatalytic applications. These



parameters are denoted as  $\Phi_F$ ,  $\Phi_T$ , and  $\Phi_\Delta$  for fluorescence, triplet and singlet oxygen quantum yields, respectively in **Figure 1.4**.

#### 1.3.4.1 Fluorescence Quantum yields ( $\Phi_F$ ) and lifetimes ( $\tau_F$ )

The fluorescence quantum yield ( $\Phi_F$ ) is a direct measure of the extent of conversion of absorbed light into emitted light through fluorescence [137].

The  $\Phi_F$  values of the Pcs in this work were determined using the comparative method [138] wherein their emission spectra were compared to that of a standard upon their excitation at the same wavelength. The  $\Phi_F$  was thus calculated using **Equation 1.1**:

$$\Phi_F = \Phi_{F(Std)} \frac{F A_{Std} n^2}{F_{Std} A n_{Std}^2} \quad 1.1$$

where  $F$  and  $F_{Std}$  represent the area under the fluorescence curves of the samples and standard respectively.  $A$  and  $A_{Std}$  are the absorbance values of the sample and standard at the excitation wavelength while  $n$  and  $n_{Std}$  are the refractive indices of the solvents used for the preparation of the sample and standard solutions, respectively.  $\Phi_{F(Std)}$  is the fluorescence quantum yield of the standard in a particular solvent. The standard used for  $\Phi_F$  quantification in organic solvents in this thesis is an unsubstituted zinc Pc (ZnPc) and its  $\Phi_{F(Std)}$  is provided in the relevant section in Chapter 5.

The fluorescence lifetime ( $\tau_F$ ) on the other hand shows the average time an excited molecule stays in the excited state before losing all its energy through fluorescence. It is directly proportional to the fluorescence quantum yield and is usually in the order of nanosecond ( $10^{-9}$  s). The  $\tau_F$  values of the Pcs reported in this work were determined using the time-correlated single photon counting (TCSPC) method [139].

### 1.3.4.2 Triplet Quantum yields ( $\Phi_T$ ) and lifetimes ( $\tau_T$ )

The triplet quantum yield ( $\Phi_T$ ) is the fraction of species that undergo radiationless decay through intersystem crossing from the excited singlet state to the excited triplet state [140].

Using ZnPc as the standard, the  $\Phi_T$  values of the Pcs reported in this work were determined based on the comparative method [141] as shown in **Equation 1.2**:

$$\Phi_T = \Phi_T^{\text{Std}} \frac{\Delta A_T \varepsilon_T^{\text{Std}}}{\Delta A_T^{\text{Std}} \varepsilon_T} \quad \mathbf{1.2}$$

where  $\Delta A_T$  and  $\Delta A_T^{\text{Std}}$  are the changes in the triplet state absorption of the samples and standard, respectively. The  $\Phi_T^{\text{Std}}$  is the triplet quantum yield of the ZnPc in a particular solvent and its value is provided in the relevant section in Chapter 5.  $\varepsilon_T$  and  $\varepsilon_T^{\text{Std}}$  are the triplet state extinction coefficients for the samples and the standard, respectively and they are determined using **Equations 1.3** and **1.4** respectively:

$$\varepsilon_T = \varepsilon_S \frac{\Delta A_T}{\Delta A_S} \quad \mathbf{1.3}$$

$$\varepsilon_T^{\text{Std}} = \varepsilon_S^{\text{Std}} \frac{\Delta A_T^{\text{Std}}}{\Delta A_S^{\text{Std}}} \quad \mathbf{1.4}$$

where  $\varepsilon_S$  and  $\varepsilon_S^{\text{Std}}$  are ground state molar extinction coefficients and  $\Delta A_S$  and  $\Delta A_S^{\text{Std}}$  are the changes in the singlet state absorptions of the Pcs and standard, respectively.

The triplet lifetime ( $\tau_T$ ) is the amount of time it takes for the excited triplet state to be depopulated by either transferring energy/ electrons to molecular oxygen or losing energy by phosphorescence. In this work it was quantified by exponential fitting of the kinetic curve using the ORIGIN 8 Software.

#### 1.3.4.3 Singlet Oxygen Quantum yields ( $\Phi_\Delta$ )

Singlet oxygen ( $^1O_2$ ) is a metastable oxidant that is produced through energy transfer from the excited triplet state of the Pcs to molecular oxygen [142]. It is the main active species in photosensitised treatment of organic pollutants and microbial inactivation [143,144].

Quantification of the generated singlet oxygen for all Pcs and their conjugates was determined using the chemical method as reported before [145]. This requires the use of singlet oxygen quenchers which react with singlet oxygen and are degraded in the process. The progress of the reaction is spectroscopically monitored over pre-determined time intervals.

In this work, 1, 3- diphenylisobenzofuran (DPBF) and anthracene-9,10-bis-methylmalonate (ADMA) were used as singlet oxygen quenchers in organic and aqueous media, respectively.

The singlet oxygen quantum yields were calculated using **Equation 1.5**:

$$\Phi_\Delta = \Phi_\Delta^{\text{Std}} \frac{R I_{\text{Abs}}^{\text{Std}}}{R^{\text{Std}} I_{\text{Abs}}} \quad \mathbf{1.5}$$

where  $\Phi_\Delta^{\text{std}}$  is the singlet oxygen quantum yield of the standard. The ZnPc is the commonly used standard in organic media while an aluminium sulfonated Pc

(AIPcSmix), which is a mixture of sulfonated Pc derivatives is the used standard in aqueous media. The  $\Phi_{\Delta}^{\text{std}}$  values are provided in the relevant section in Chapter 5.

$R$  and  $R^{\text{std}}$  are the rates of photobleaching of the singlet oxygen quencher in the presence of the sample and the standard, respectively.  $I_{\text{Abs}}$  and  $I_{\text{Abs}}^{\text{Std}}$  are the rates of absorption of light by the samples and standard, respectively and are defined by

**Equations 1.6 and 1.7:**

$$I_{\text{Abs}} = \frac{\alpha \cdot A \cdot I}{N_A} \quad \mathbf{1.6}$$

$$I_{\text{Abs}}^{\text{Std}} = \frac{\alpha \cdot A \cdot I}{N_A} \quad \mathbf{1.7}$$

where  $\alpha = 1-10^{-A(\lambda)}$ ,  $A(\lambda)$  is the absorbance of the sensitizer at the irradiation wavelength,  $A$  is the irradiated cell area ( $\text{cm}^2$ ),  $I$  is the intensity of light calculated using the wavelength of the Q band of the Pc (photons/ $\text{cm}^2 \text{ s}$ ) and  $N_A$  is Avogadro's constant.

Quantification of the  $\Phi_{\Delta}$  of Pcs (or conjugates) embedded in NFs was conducted using the absolute method due to lack of standards. The studies were carried out in an aqueous solution, using ADMA as a chemical quencher for singlet oxygen wherein its degradation was spectroscopically monitored at 380 nm [146].

The quantum yield of ADMA ( $\Phi_{\text{ADMA}}$ ) was calculated using **Equation 1.8**:

$$(\Phi_{\text{ADMA}}) = \frac{(C_0 - C_t)V_R}{I_{\text{Abs}} \cdot t} \quad \mathbf{1.8}$$

where  $C_0$  and  $C_t$  are the ADMA concentrations prior to and after irradiation, respectively;  $V_R$  is the solution volume;  $t$  is the irradiation time per cycle and  $I_{\text{Abs}}$  is defined above in **Equation 1.6**.

The absorbances used for **Equation 1.8** are those of the Pcs in the NFs and the light intensity measured refers to the light reaching the spectrophotometer cells. It is expected that some of the light may be scattered, hence the  $\Phi_{\Delta}$  values of the Pcs in the NFs are estimates. The singlet oxygen quantum yields ( $\Phi_{\Delta}$ ) were calculated using **Equation 1.9**:

$$\frac{1}{\Phi_{ADMA}} = \frac{1}{\Phi_{\Delta}} + \frac{1}{\Phi_{\Delta}} \cdot \frac{k_d}{k_a} \cdot \frac{1}{[ADMA]} \quad 1.9$$

where  $k_d$  is the decay constant of singlet oxygen and  $k_a$  is the rate constant for the reaction of ADMA with  $^1O_2$  ( $^1\Delta_g$ ). The intercept obtained from the plot of  $1/\Phi_{\Delta ADMA}$  versus  $1/[ADMA]$  gives  $\Phi_{\Delta}$ .

### 1.3.5 Photocatalytic activities of Pcs studied in this work

The ability of Pcs to absorb light and thus produce ROS (including singlet oxygen) as depicted in **Figure 1.4** makes them versatile in photo-induced processes. In this work, the photocatalytic activities of Pcs are reported based on their roles as antimicrobial agents, catalysts for the degradation of organic water pollutants such as dyes and hydrogen generation from contaminated water.

#### 1.3.5.1 Photodynamic Antimicrobial Chemotherapy (PACT)

Due to the rapid emergence and spread of drug-resistant microorganisms such as bacteria in healthcare and the community at large, urgency in the development of alternative treatment methods has been prompted [147]. Photodynamic antimicrobial chemotherapy (PACT) is a method of photoinactivation of microbes in the presence of a photosensitizer such as a Pc. Upon activation of the photosensitizer with light of

appropriate wavelength, and upon interaction with oxygen, the generated ROS (including singlet oxygen) result in photodamage and cell death [148,149]. This work reports on the PACT efficiencies of Pcs conjugated to NPs as well as when supported on bare and modified SiO<sub>2</sub> NFs as depicted in **Figure 1.5**.

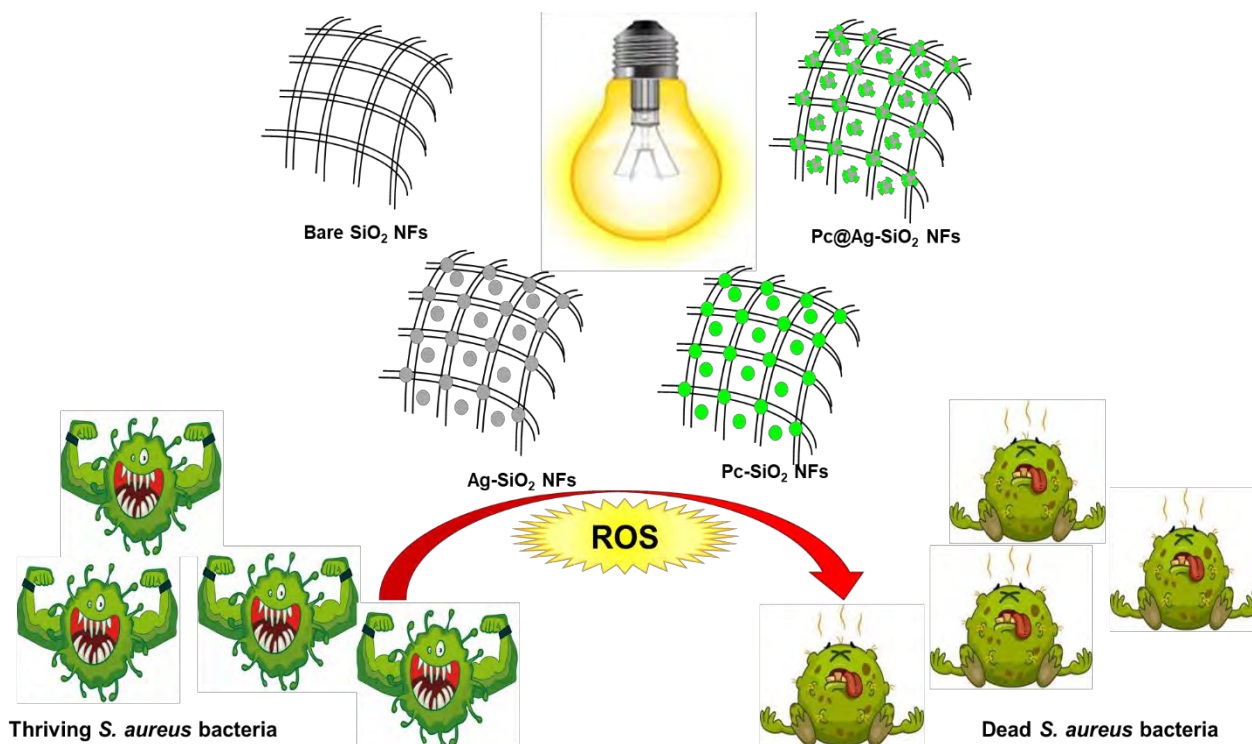


**Figure 1.5:** Illustration of the photoinactivation of bacteria using modified electrospun SiO<sub>2</sub> NFs. ROS = Reactive oxygen species.

The antibacterial activities of Pc modified Hem NFs are also reported. Neutral Pcs have been efficiently applied in the phototreatment of gram-positive bacteria while cationic Pcs are effective for both gram-positive and gram-negative bacteria [123,150]. As shown in **Figure 1.6**, gram-negative bacteria have a double lipid bilayer sandwiching the peptidoglycan layer plus an outer layer of lipopolysaccharide, resulting in a low degree of permeability while gram-positive bacteria possess a porous peptidoglycan layer and a single lipid bilayer [151,152].

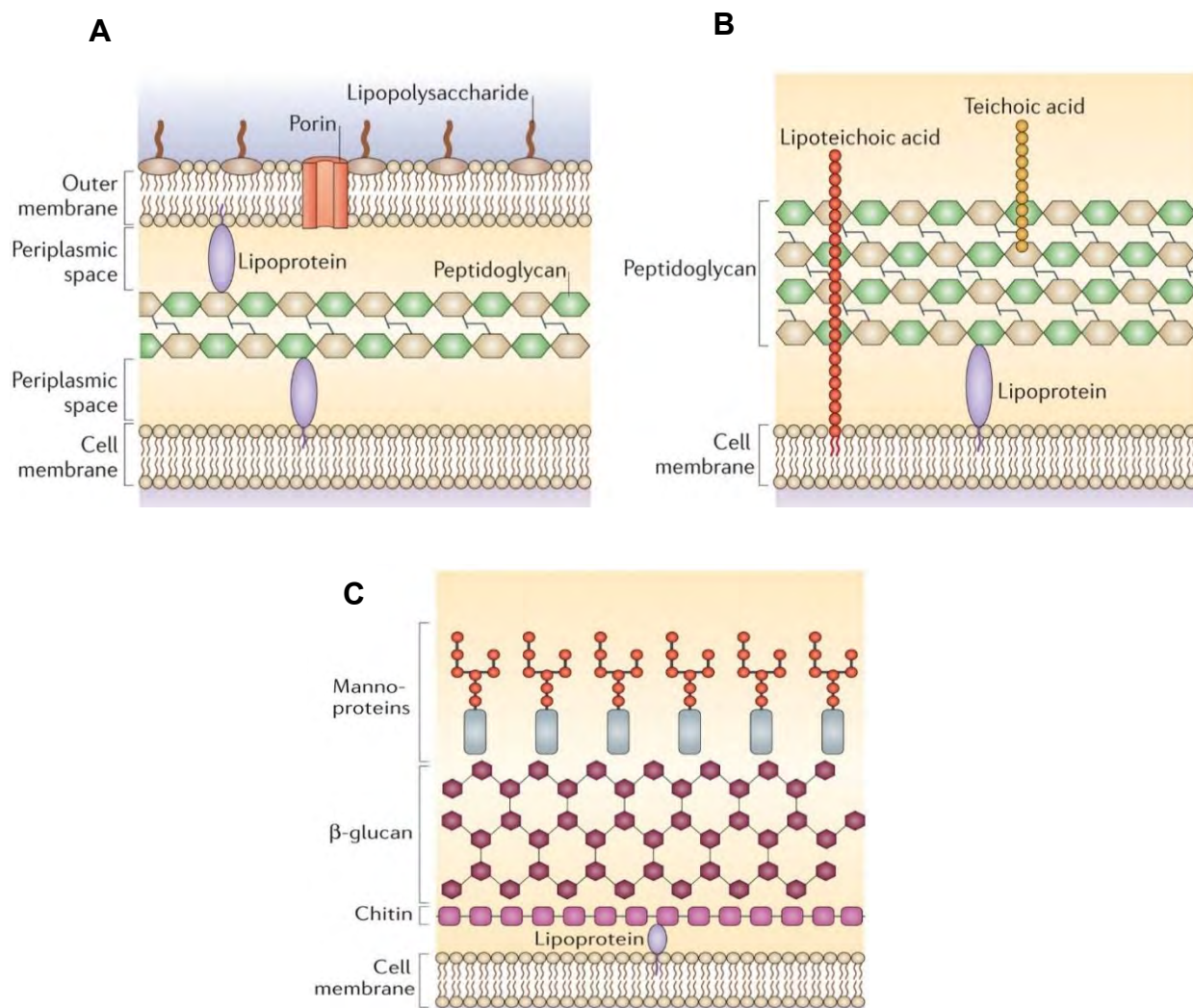


**Figure 1.6:** Cell wall structure of (A) gram-negative bacteria, (B) gram-positive bacteria, and (C) fungi [152].

Thus the membrane barrier of gram-negative prevents the uptake of anionic and neutral Pcs [153]. The PACT efficiencies of cationic Pcs against fungi have also been reported [154]. Fungi has a lipid bilayer and the polysaccharides; chitin,  $\beta$ -glucan and mannan (in the form of mannoproteins), **Figure 1.6** [152].

The conjugation of Pcs to NPs has been reported to enhance their singlet oxygen quantum yields and hence antimicrobial efficiencies [154,155]. This work therefore reports on the antimicrobial efficiencies of neutral and cationic Pcs when conjugated

to various NPs. As shown in **Table 1.3** [60-63], the antimicrobial efficiencies of Pcs when conjugated to different NPs have been reported before. These studies were however predominantly conducted with symmetrical Pcs unlike the asymmetrical complexes **4-6** that are conjugated to the same NPs and applied for PACT in this thesis. The effect of the number of charges a Pc has on its antimicrobial properties are also reported. This is done by comparing the antimicrobial properties of neutral, octacationic and hexadecacationic Pcs when alone and when conjugated to Ag NPs against gram-positive *S. aureus*, gram-negative *Escherichia coli* (*E. coli*) and *Candida albicans* (*C. albicans*) which is a fungus.

### 1.3.5.2 Photodegradation of organic water pollutants

Azo dyes are synthetic, water-soluble dyes possessing the characteristic azo (-N=N-) bond and they possess poor biodegradability due to their complex structures [156]. The azo bond determines the color of the dyes and is the most reactive moiety, usually undergoing oxidation leading to fading of the color of the dye solution upon degradation [157].

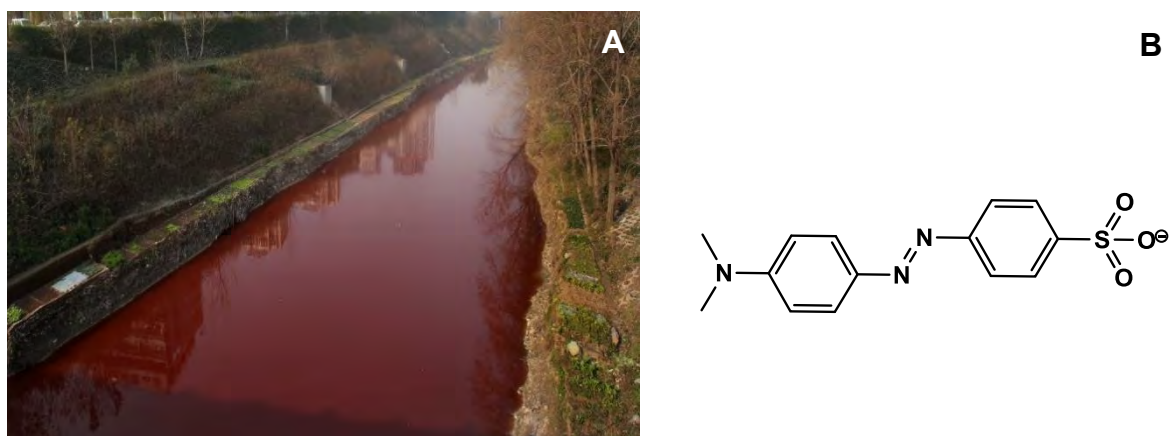


**Figure 1.7:** (A) Picture of azo-dye contaminated water (<https://edition.cnn.com/style/article/dyeing-pollution-fashion-intl-hnk-dst-sept/index.html>) and (B) structure of Methyl Orange.



These dyes are common water pollutants (**Figure 1.7A**) thereby compromising aquatic life, they are carcinogenic and potential genotoxic agents, hence the importance of devising means for effectively degrading them [**158,159**]. The azo dye studied as a model pollutant in this work is Methyl Orange (MO, **Figure 1.7B**). Methods including filtration, coagulation, precipitation and adsorption have been reported for the removal of azo dyes from water [**160-162**]. These methods however merely change the dye from one phase to another and are not destructive, making treatment of azo dyes costly due to the required retreatment [**163,164**], hence alternative methods are required. A comparison on the photocatalytic efficiencies of bare and Pc modified Hem, TiO<sub>2</sub> and ZnO NFs on MO photooxidation are reported as depicted in **Figure 1.8**.

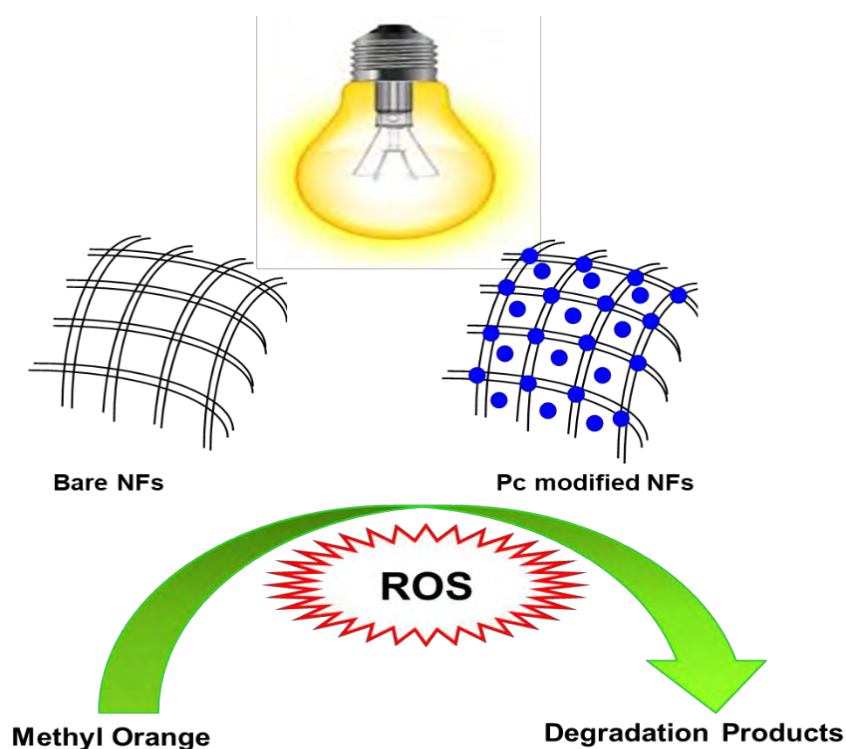


**Figure 1.8:** Diagrammatic representation showing the use of NFs for the degradation of MO.

### 1.3.5.3 Hydrogen generation

The global energy crisis and ongoing environmental issues have prompted extensive focus on producing hydrogen from water under solar light irradiation because for both concerns, hydrogen rich system would be beneficial [165]. Hydrogen has been identified as a clean, zero-emission energy source and environmentally-friendly alternative to traditional fossil fuels [166].

True water splitting entails breaking down water to form hydrogen and oxygen in the presence of a catalyst, such as  $\text{TiO}_2$ . Unfortunately, this process is rather inefficient [167,168]. Sacrificial electron donors (SEDs) are commonly used to improve the hydrogen generation at the expense of the consumption of the SEDs. A range of SEDs have been reported to be effective for this process [127,168]. In this work, 1% methanol is used as a SED. For the first time, Pc modified anatase and rutile  $\text{TiO}_2$  NFs are used for SED assisted generation of hydrogen. For comparison and enhancement of the catalytic efficiencies of the  $\text{TiO}_2$  NFs, they are also decorated with Co and Pd NPs. The catalytic efficiencies of the NFs were evaluated using different light intensities so as to optimise hydrogen generation conditions for the fabricated catalysts.

## 1.4 Aims of thesis

The work reports on the design of composite nanocatalysts for the treatment of microbes (bacteria and fungi) and organic water pollutants as well as for the generation of hydrogen.

The specific aims of the thesis include:

- Synthesis of phthalocyanine complexes **2-5**.
- Fabrication of polymer free SiO<sub>2</sub> nanofibers.
- Modification of the SiO<sub>2</sub> nanofibers with Ag nanoparticles and different phthalocyanines i.e. neutral, octacationic and hexadecacationic (complexes **1-3**) as well as their conjugates.
- Evaluation of antimicrobial efficiencies of phthalocyanine and nanoparticle modified SiO<sub>2</sub> nanofibers against *S. aureus*, *E. coli* and *C. albicans*.
- Evaluation and comparison of photophysicochemical and antimicrobial properties of phthalocyanines varying in number of charges (complexes **1-3**) in solution, before and after conjugation to OLM-Ag nanoparticles (*via* chemisorption).
- Synthesis and characterisation of amine functionalised Cys-Ag, NH<sub>2</sub>-Fe<sub>3</sub>O<sub>4</sub> and Cys-Ag@Fe<sub>3</sub>O<sub>4</sub> nanoparticles.
- Covalent conjugation of phthalocyanines (complexes **4-6**) to Cys-Ag, NH<sub>2</sub>-Fe<sub>3</sub>O<sub>4</sub> and Cys-Fe<sub>3</sub>O<sub>4</sub>@Ag nanoparticles *via* amide bond formation.
- Antimicrobial studies of phthalocyanine (complexes **4-6**)-nanoparticle conjugates against *S. aureus*.
- Fabrication and modification of polymer free Hem, ZnO and TiO<sub>2</sub> nanofibers.

- Evaluation of antimicrobial efficiencies of phthalocyanine (complexes **4-6**) modified Hem nanofibers.
- Evaluation and comparison of photodegradation efficiencies of phthalocyanine (complex **6**) modified Hem, TiO<sub>2</sub> and ZnO nanofibers.
- Evaluation of hydrogen generation efficiencies of phthalocyanine (complex **7**) and nanoparticle (Co and Pd) modified TiO<sub>2</sub> nanofibers.

# Chapter 2

This chapter gives details on the materials, instrumentation and experimental procedures implemented in the synthesis as well as characterisation and application of the nanomaterials.

## 2. Experimental

### 2.1 Materials

#### 2.1.1 Solvents

Deuterated dimethyl sulphoxide (DMSO-d<sub>6</sub>) and spectroscopic dimethyl sulphoxide (DMSO) were purchased from Merck. Ethyl acetate, N, N-dimethylformamide (DMF), tetrahydrofuran (THF), diethyl ether, chloroform, dichloromethane (DCM), acetonitrile, hexane, methanol, ammonia, toluene, absolute ethanol and hydrochloric acid (HCl) were purchased from SAARChem. Glacial acetic acid (AA) was purchased from Minema chemicals. Ultra-pure (Type 1) water was obtained from an Elga PURELAB Chorus 2 (RO/DI) system.

#### 2.1.2 Reagents for synthesis of Pcs, NPs, NFs and their conjugates

Zinc acetate dihydrate, polyvinylpyrrolidone (PVP, Mw = 1, 300, 000), titanium (IV) propoxide, ferric nitrate nonahydrate, iodomethane, dimethylaminoethanol (DMAE), N,N'-dicyclohexylcarbodiimide (DCC), N,N'-dimethylpyridin-4-amine (DMAP), 1,2-dicyanobenzene, cobalt nitrate hexahydrate, silver acetate, silver nitrate, diphenyl ether, oleic acid, oleylamine (OLM), cysteamine (Cys), tetraethoxysilane (TEOS), 3-aminopropyl-triethoxysilane (APTES) and ferrous chloride tetrahydrate were purchased from Sigma-Aldrich. Ferric chloride hexahydrate was purchased from Saarchem. Silicon substrates were purchased from Biotain Crystal Co., Ltd. Palladium (II) chloride (99%) was purchased from Alfa Aesar. Irgacure-907 (2-methyl-4'-(methylthio)-2-morpholinopropiophenone) was a gift from Ciba Specialty Chemicals. Sodium hydroxide pellets were purchased from Minema Chemicals. The syntheses of 2,9(10),16(17),23(24)-tetrakis-(4'-(4'-6'-diaminopyrimidin-2'-ylthio))) phthalocyaninato zinc (II) (1) [118], 2-[5-(phenoxy)-isophthalic acid] 9(10), 16(17), 23(24)-tris (*tert*-butyl)

phthalocyaninato zinc (II) (**6**) [119] and 2,9(10),16(17),23(24)-tetra 5-(phenoxy)-isophthalic acid phthalocyaninato] zinc (II) (**7**) [120] were conducted as reported in literature. The syntheses of dimethyl 5-(3,4-dicyanophenoxy) isophthalate [120,169] and 4-(4-*tert*-butylphenoxy phthalonitrile [170] have also been reported before.

### 2.1.3 Reagents for photophysicochemical studies

Anthracene-9,10-bis-methylmalonate (ADMA), unsubstituted zinc phthalocyanine (ZnPc) and 1,3- diphenylisobenzofuran (DPBF) were purchased from Sigma-Aldrich. AlPcSmix (a mixture of sulfonated aluminium Pcs) was synthesized according to literature [171].

### 2.1.4 Reagents used for photocatalytic applications

Titanium (IV) oxide (P25-TiO<sub>2</sub>) and Methyl Orange were purchased from Sigma-Aldrich. *Escherichia coli* (ATCC 25922) was obtained from Microbiologics USA. *Staphylococcus aureus* (ATCC 25923) and *Candida albicans* (ATCC 24433) were obtained from Davies Diagnostics, South Africa. Nutrient agar and bacteriological BBL Muller Hinton broth were purchased from Merck. Phosphate buffer saline (PBS) was prepared using appropriate quantities of sodium chloride and potassium chloride purchased from Minema chemicals as well as sodium hydrogen phosphate dihydrate and dipotassium hydrogen phosphate purchased from Riedel-de Haën.

## 2.2 Equipment

1. The ground state electronic absorption spectra were measured at room temperature on a Shimadzu UV-2550 spectrophotometer using a 1 cm pathlength cuvette in solution.
2. A Perkin Elmer Lambda 950 UV-vis spectrophotometer was used for the solid state spectra of the NFs.
3. Fluorescence emission and excitation spectra were obtained on a Varian Eclipse spectrofluorometer using a 1 cm pathlength quartz cuvette. The excitation spectra were all recorded at the wavelength of the emission.
4. Fluorescence lifetimes were measured using a time correlated single photon counting (TCSPC) (FluoTime 300, Picoquant GmbH) setup such as that depicted in **Figure 2.1**. The excitation source was a diode laser (LDH-P-670 driven by PDL 800-B, 670 nm, 20 MHz repetition rate, 44 ps pulse width, Pico quant GmbH). Fluorescence was detected under the magic angle with a peltier cooled photomultiplier tube (PMT) (PMA-C 192-N-M, Picoquant GmbH) and integrated electronics (PicoHarp 300E, Picoquant GmbH). A monochromator with a spectral width of 4 nm was used to select the required emission wavelength. The response function of the system, which was measured with a scattering Ludox solution (DuPont), had a full width at half-maximum (FWHM) of about 300 ns. The ratio of stop to start pulses was kept low (below 0.05) to ensure good statistics. The luminescence decay curve was measured at the maximum of the emission peak. The data was analyzed with the FluoFit Software program (Picoquant GmbH, Germany). The support plane approach was used to estimate the errors of the decay times.



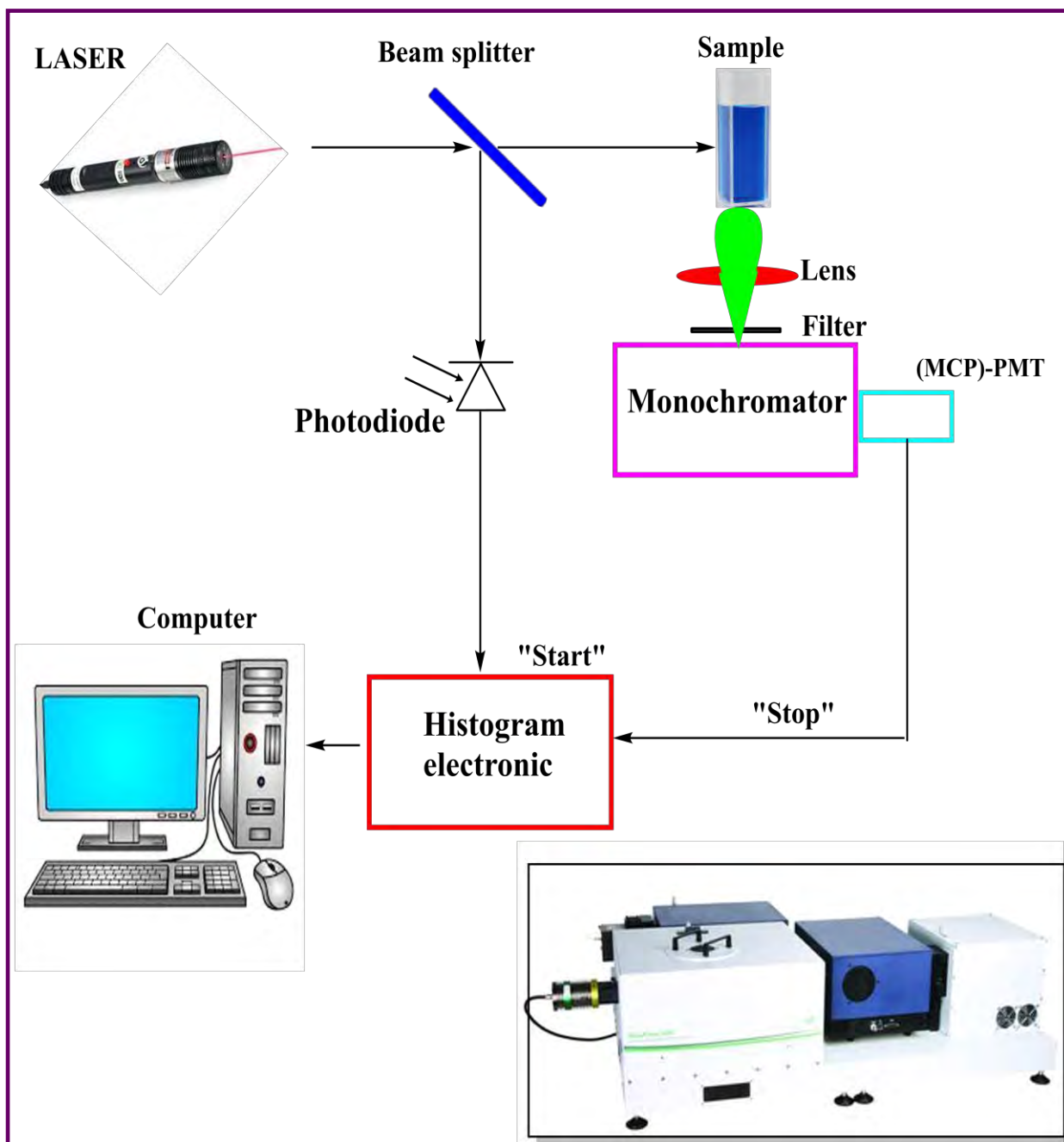


**Figure 2.1:** Schematic diagram of a TCSPC setup.

**(MCP)-PMT= (Multichannel plate detector)-Photomultiplier tube. Insert shows the actual TCSPC setup that was used.**

5. Energy dispersive X-ray spectroscopy (EDX) was done on an INCA PENTA FET coupled to the VAGA TESCAM using 20 kV accelerating voltage.

6. Mass spectral data were collected with a Bruker AutoFLEX III Smartbeam TOF/TOF Mass spectrometer operated in the positive mode using  $\alpha$ -cyano-4-hydroxycinnamic acid as the MALDI matrix.
7. Transmission electron microscopy (TEM) images for the NPs and conjugates were obtained using a ZEISS LIBRA<sup>®</sup> TEM.
8. Triplet state quantum yields were determined using a laser flash photolysis system consisting of an LP980 spectrometer with a PMT-LP detector and an ICCD camera (Andor DH320T-25F03). The signal from a PMT detector was recorded on a Tektronix TDS3012C digital storage oscilloscope. The excitation pulses were produced using a tunable laser system consisting of an Nd:YAG laser (355 nm, 135 mJ/4–6 ns) pumping an optical parametric oscillator (OPO, 30 mJ/3–5 ns) with a wavelength range of 420–2300 nm (NT-342B, Ekspla). The schematic representation of the setup is shown in **Figure 2.2**.

The solutions were prepared such that the sample and standard absorbance values were  $\sim 1.5$  at the Q band (to avoid aggregation effects) in 1 cm path length quartz cells. The solutions were deaerated using argon and then sealed. Lastly, the solutions were illuminated using an appropriate excitation wavelength i.e. the crossover wavelength of the sample and the standard at the Q band region is used. The triplet lifetimes were obtained by exponential fitting of the kinetic curves using OriginPro 8 software.

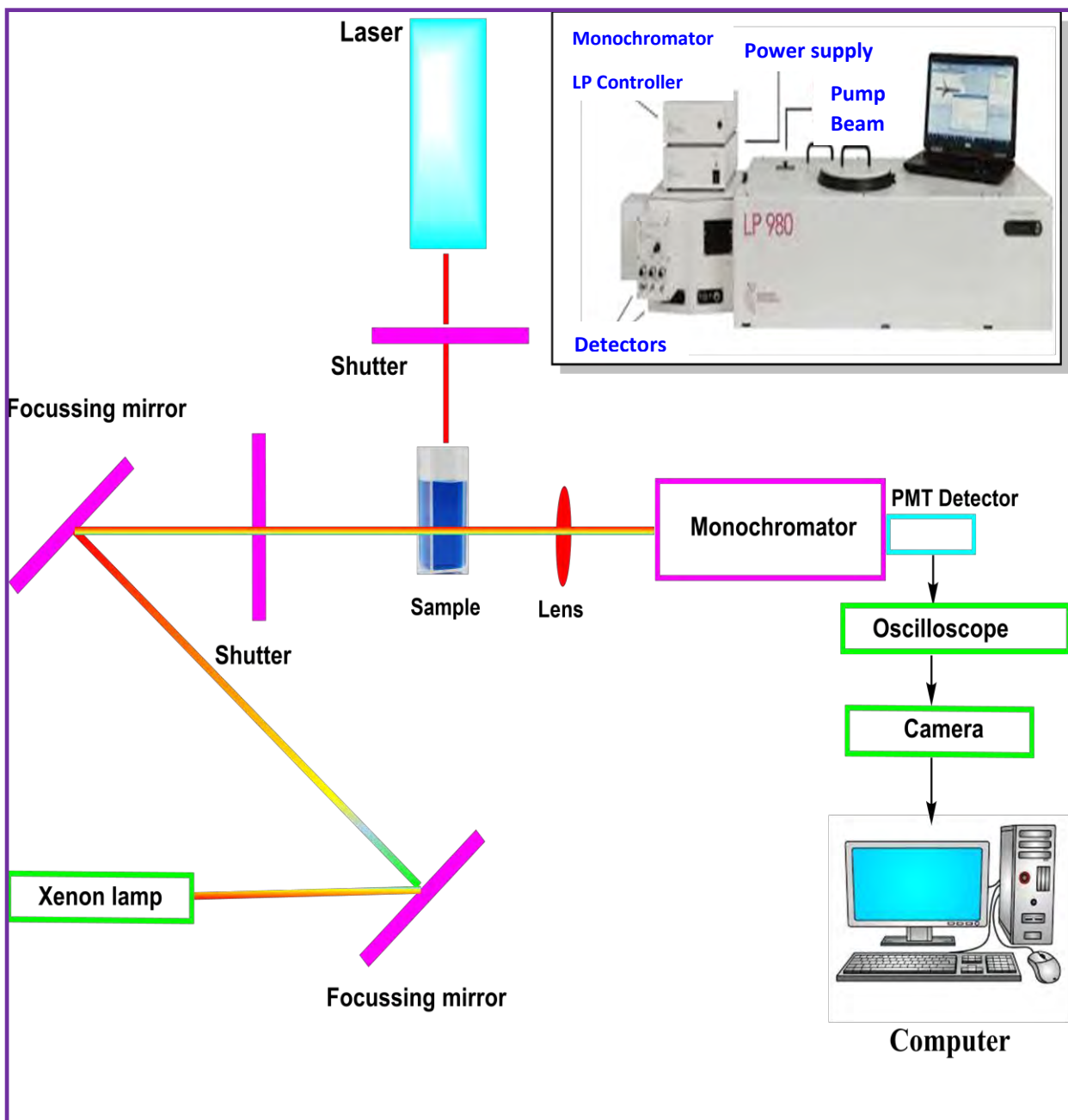


**Figure 2.2:** Schematic diagram of a LP980 laser flash photolysis setup.

**PMT = Photomultiplier tube. Insert shows the actual TCSPC setup that was used.**

9. Scanning electron microscopy (SEM) images of the electrospun NFs were examined using a scanning electron microscope (JOEL JSM 840 scanning electron microscope) at an accelerating voltage of 20 kV.

10. Nitrogen adsorption/desorption isotherms were carried out at 77 K using a Micrometrics ASAP 2020 Surface Area and Porosity Analyzer. Prior to each measurement, degasing was carried at room temperature for varying amounts of time, depending on sample. The Brunauer–Emmett–Teller (BET) method was employed to determine surface area and porosity. The BET surface area and total pore volume were calculated from the isotherms obtained.
11. A Metrohm Swiss 827 pH meter was used for all pH measurements.
12. The electrospun NFs were fabricated from the electrospinning setup shown in **Figure 2.3**. The setup consists of a high voltage source (Glassman High Voltage, Inc. series, 0-40 kV), a pump (Kd Scientific, KDS-100-CE) and a plastic syringe equipped with a steel needle with diameter of a 0.60 mm. A metallic plate covered with aluminium foil was as a ground collector for the NFs.

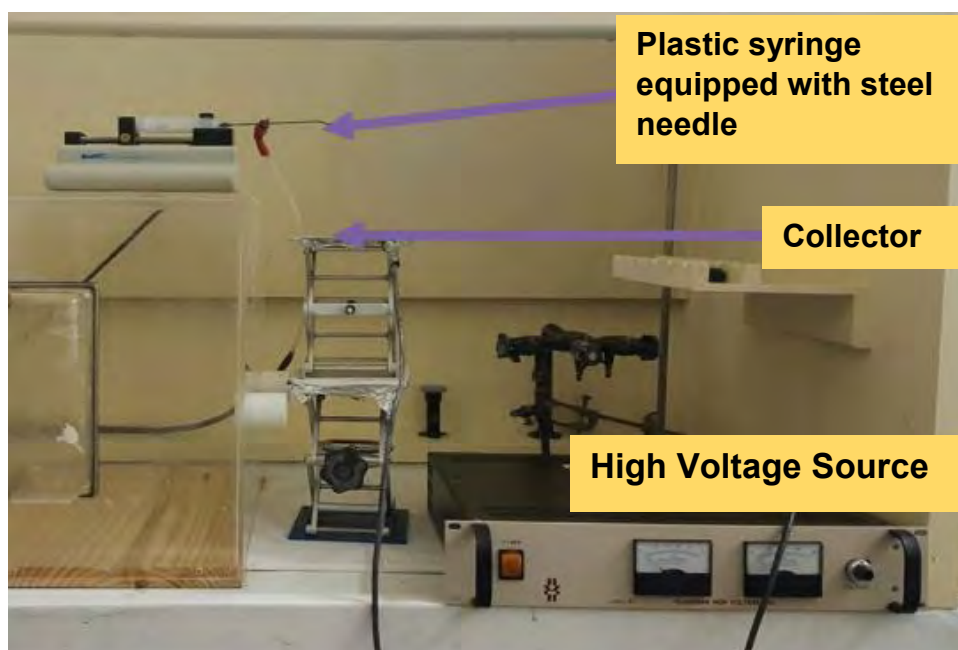


**Figure 2.3:** The electrospinning setup used in the fabrication of the NFs.

13. Calcination of all of the NFs was then was conducted in a Labotec Precision Furnace (SNOL 3/1100).
14. Elemental Analyses (CHNS) were done using a Vario-Elementar Microcube ELIII Series.
15. X-ray powder diffraction patterns were recorded on a Bruker D8 Discover equipped with a LynxEye detector, using CuK $\alpha$  radiation ( $\lambda = 1.5405 \text{ \AA}$ , nickel filter). Data were collected in the range from  $2\theta = 5^\circ$  to  $100^\circ$ , scanning at  $1^\circ \text{ min}^{-1}$  with a filter time-constant of 2.5 s per step and a slit width of 6.0 mm. Samples were placed on a zero background silicon wafer slide. The X-ray diffraction data were treated using Eva (evaluation curve fitting) software. Baseline correction was performed on each diffraction pattern.
16. X-ray photoelectron spectroscopy (XPS) analysis was done using a Kratos AXIS Ultra DLD, with Al (monochromatic) anode equipped with a charge neutraliser, supplied by Kratos Analytical. The following parameters were used: the emission was 10 mA, the anode (HT) was 15 kV and the operating pressure below  $5 \times 10^{-9}$  torr. A hybrid lens was used and resolution to acquire scans was at 160 eV pass energy in slot mode. The centre used for the scans was at 520 eV with a width of 1205 eV, with steps at 1 eV and dwell time at 100 ms. The high resolution scans were acquired using 80 eV pass energy in slot mode.
17. Time-of-flight-secondary ion mass spectrometer (TOF-SIMS) data were recorded with an ION TOF GmbH TOF SIMS 5–100 run in micro-raster mode. The raster area was  $3000 \mu\text{m} \times 3000 \mu\text{m}$ , and the sample was run in both positive and negative ion modes. The analyzer was set to a standard operating mode with a cycle time of 100  $\mu\text{s}$ ; the primary beam was a Bi $_3$  ion cluster gun with a current of 0.4 pA and an energy of 3000 eV (also termed as spectrometry mode). The Bi $_3$

cluster and electron flood gun were used to get a better ion signal from the sample. Charge compensation was used to account for the electron flood gun. The raw data were processed using the Surface Lab 6.5 software provided by ION TOF. Glassy carbon plates (Goodfellow, UK) of 1 × 1 cm and 2 mm thick were used as substrates for TOF-SIMS.

18. Raman spectroscopy was conducted on a Horiba Xplora TM Plus Raman Microscope configured with 785 nm (at 50  $\mu$ W) laser line at 100% power and data analyses were done using LabSpec 6 software.
19. Proton nuclear magnetic resonance spectra recorded on a Bruker AMX 600 MHz NMR spectrometer using tetramethylsilane (TMS) as an internal reference.
20. FT-IR spectra of the NFs were acquired using a Bruker® ALPHA FT-IR spectrometer with a universal attenuated total reflectance (ATR) sampling accessory.
21. The optical densities of the bacteria culture were determined using the LEDTECT 96 from LABXIM PRODUCTS. A vortex mixer and HERMLE Z233M-2 centrifuge from LASIEC were used to mix the bacterial suspension and for the harvesting of the bacterial cells, respectively.
22. Quantification of Pd, Co and Zn on the TiO<sub>2</sub> NFs was conducted with Inductively Coupled Plasma Optical Emission Spectrometry (ICP-OES), using an Agilent Vista Pro ICP Emission Spectrometer. Approximately 10 mg portions were accurately weighed in triplicates and digested with aqua regia. Solutions were further diluted and measured by ICP-OES wherein the respective emission lines obtained were used for quantification.

23. Irradiations for singlet oxygen determination were conducted using a general electric quartz lamp (300W), 600 nm glass (Schott) and water filters were used to filter off ultraviolet and far infrared radiations respectively. An interference filter of 670 nm with a band of 40 nm was placed in the light path just before the cell containing the sample. The intensity of the light reaching the cell was measured with a POWER MAX 5100 (Molelectron Detector Incorporated) power meter. A schematic representation of the setup is shown in **Figure 2.4**. Irradiations for photodegradation studies and PACT for the NFs were also conducted with the same setup but without any of the filters.

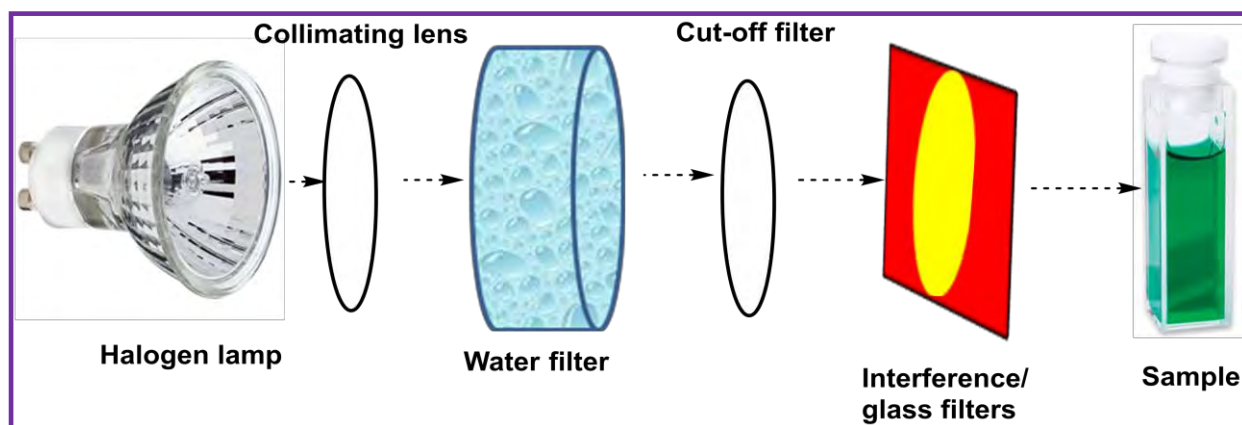


**Figure 2.4:** Schematic representation of photochemical setup.

24. Illumination for PACT studies in solution were carried out using the Modulight® Medical Laser system (ML) 7710-680 channel Turnkey laser system coupled with a 2 × 3 W channel at 680 nm, cylindrical output channels, aiming beam, integrated calibration module, foot/hand switch pedal, fiber sensors (subminiature version A) connectors and safety interlocks. The used illumination kit for PACT studies was a 127.75 × 85.05 mm 24 well plate. The setup is shown in **Figure 2.5**.

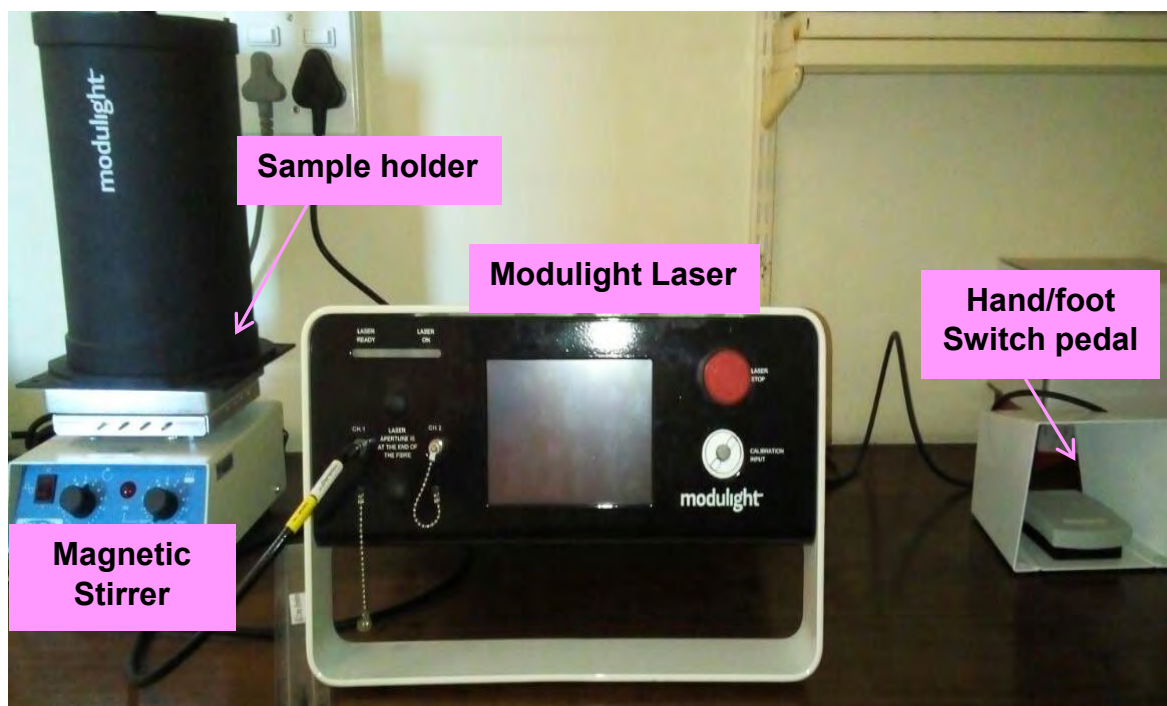


**Figure 2.5:** Laser setup used for PACT studies.

25. A Luzchem (LZC-4V) photoreactor fitted with UVA lamps was used for decoration of the TiO<sub>2</sub> NFs with the Pd and Co nanoparticles.
26. Photo-induced hydrogen generation was performed upon irradiation utilizing light-emitting diodes (LEDs) of 10 W from LedEngin centered at 368 or 630 nm.
27. Hydrogen detection was carried out in a Perkin Elmer, Claurus Gas Chromatograph coupled to Thermal Conductivity Detector (GC-TCD) using Argon as a carrier gas and a 5 Å Zeolite molecular sieves column.



## 2.3 Synthesis

### 2.3.1 Synthesis of Pcs (complexes 2-5)

As stated before, the syntheses of complexes **1**, **6** and **7** have been reported before [118-120]. The syntheses of the novel complexes **2-5** is explained below.

#### 2.3.1.1 Synthesis of 2,9(10),16(17),23(24)-Tetrakis-(4'-(1',3'-N-dimethyl, 4'-6'-diaminopyrimidin-2'-ylthio))) phthalocyaninato zinc (II) (**2**), Scheme 3.1

Complex **1** (0.100 g, 0.088 mmol) was dissolved in dry DMF (20 mL) followed by the addition of iodomethane (3.52 mmol, 0.2 mL). The solution was stirred while heating at 70 °C for 24 h under nitrogen atmosphere. The reaction mixture was then cooled to room temperature and complex **2** was precipitated out of the solution using diethyl ether. The formed precipitate was collected by centrifugation and washed several times with chloroform, ethyl acetate as well as ethanol and then dried overnight under a high vacuum fumehood.

Yield = 52%. UV-Vis (DMSO):  $\lambda_{\text{max}}/\text{nm}$  ( $\log \epsilon$ ): 687 (5.53), 620 (4.88), 353 (5.30). FT-IR ( $\nu_{\text{max}}/\text{cm}^{-1}$ ): 3304, 3150 (N-H stretch), 3007 (Aromatic C-H stretch), 2924, 2742 (Aliphatic C-H stretch), 1638 (C=N stretch), 1383 (C-H bend), 1143 (C-N stretch), 940 (C=C bend). MS MALDI-TOF ( $m/z$ ): Calculated: 157.04 Found: 159.44 [M+2H].  $^1\text{H}$  NMR (600 MHz, DMSO- $d_6$ ):  $\delta$ , ppm: 11.36 (s, 16H, NH<sub>2</sub>), 9.50 (s, 4H, Ar-H), 8.44 (s, 4H, Ar-H), 8.01 (d, 4H, Ar-H), 7.89 (d, 4H, Ar-H), 2.73 (s, 24H, Aliph-H).

**2.3.1.2 Synthesis of 2,9(10),16(17),23(24)-Tetrakis-(4'-(1',3'-N-dimethyl, 4'-6'-(hexamethylaminopyrimidin-2'-ylthio))) phthalocyaninato zinc (II) (3), Scheme 3.1**

Complex **1** (0.100 g, 0.088 mmol) was dissolved in dry DMF (20 mL) followed by the addition of iodomethane (7.04 mmol, 0.4 mL). The solution was stirred while heating at 70 °C for 72 h under nitrogen atmosphere. Iodomethane (7.04 mmol, 0.4 mL) was again added to the reaction after 24 h and 48 h of the ongoing reaction. The reaction mixture was then cooled to room temperature followed by the precipitation of complex **3** out of the solution using diethyl ether. The formed precipitate was collected by centrifugation and washed several times with chloroform, ethyl acetate as well as ethanol and then finally dried overnight under a high vacuum fumehood.

Yield = 29%. UV–Vis (DMSO):  $\lambda_{\text{max}}/\text{nm}$  ( $\log \epsilon$ ): 686 (4.88), 623 (4.31), 358 (4.96). FT-IR ( $\nu_{\text{max}}/\text{cm}^{-1}$ ): 3006 (Aromatic C-H stretch) 2946, 2730 (Aliphatic C-H stretch), 1619 (C=N stretch), 1478, 1395 (C-H bend), 940 (C=C bend). MS MALDI-TOF ( $m/z$ ): Calculated: 100.05, Found: 100.98.  $^1\text{H NMR}$  (600 MHz, DMSO- $d_6$ ):  $\delta$ , ppm: 8.01 (s, 4H, Ar-H), 7.96 (d, 4H, Ar-H), 7.88 (d, 4H), 7.79 (s, 4H), 3.10 (s, 72H), 2.71 (s, 24H).

**2.3.1.3 Synthesis of 2-Mono-isophthalic acid-9(10),16(17),23 (24)- tri (*tert*-butylphenoxy) phthalocyaninato zinc(II) (4), Scheme 3.2**

Dimethyl 5-(3,4-dicyanophenoxy) isophthalate (0.28 g, 0.83 mmol), *tert*-butylphenoxy phthalonitrile (0.80 g, 2.90 mmol) and zinc acetate dihydrate (0.45 g, 2.45 mmol) were weighed into a round bottomed flask followed by the addition of dimethylaminoethanol (DMAE, 5 mL). The mixture was stirred at 240 °C for 1 h under argon atmosphere. The temperature was then lowered to 180 °C and the reaction continued for a further 5 h. After cooling the reaction to room temperature, the obtained product was precipitated

out with methanol followed by column chromatography to isolate the derivative Pc of complex **4** (which has ester groups instead of carboxylic acid groups) using tetrahydrofuran (THF) and methanol as eluents. The obtained product was dried and hydrolysis of the ester groups to form carboxylic acid groups was conducted by dissolving the unhydrolysed Pc (0.2 g, 0.16 mmol) in THF (5 mL) followed by the addition of a 5 M NaOH solution in a round bottomed flask. The reaction was stirred at 80 °C for 24 h under reflux. THF was then evaporated from the reaction mixture and dilute HCl was added to the solution resulting in the formation of a precipitate which was then filtered off. Column chromatography was run to isolate complex **4** from some of the unhydrolysed Pc using dichloromethane (DCM) and methanol (9:1) as eluents. Yield: 15% (w/w). UV/Vis (DMSO):  $\lambda_{\text{max}}/\text{nm}$  ( $\log \epsilon$ ): 357 (4.44), 612 (4.19), 680 (4.86). Calc. for  $\text{C}_{70}\text{H}_{56}\text{N}_8\text{O}_8\text{Zn}$ : C 69.91, H 4.69, N 9.32; Found C 68.57, H 4.80, N 7.96. MS MALDI-TOF (m/z): Calculated: 1202.65, Found: 1202.80. IR [ $\nu_{\text{max}}/\text{cm}^{-1}$ ]: 3420 (O-H stretch), 2815 (Aliphatic C-H stretch), 1750 (C=O stretch), 1610 (C=C stretch), 1490 (C-C stretch), 1335 (C-N stretch).  $^1\text{H}$  NMR (600 MHz, DMSO):  $\delta$ , ppm: 9.56 (s, 2 H, COOH), 9.42–8.29 (m, 12 H, macrocycle-H), 8.22–7.78 (m, 15 H, phenyl-H), 1.57 (s, 18 H,  $\text{C}(\text{CH}_3)_3$ ), 1.05 (m, 9 H,  $\text{C}(\text{CH}_3)_3$ ).

#### **2.3.1.4 Synthesis of 2-Mono-(5-oxy) isophthalic acid phthalocyaninato zinc(II) (5), Scheme 3.2**

Dimethyl 5-(3,4-dicyanophenoxy) isophthalate (0.40g, 1.28 mmol), 1,2-dicyanobenzene (0.50 g, 3.90 mmol) and zinc acetate dihydrate (0.45 g, 2.45 mmol) were weighed into a round bottomed flask. Dimethylaminoethanol (DMAE, 5 mL) was then added to the flask and the mixture was stirred at 240 °C for 1 h under argon atmosphere. The temperature was then lowered to 180 °C and the reaction continued

overnight. The reaction mixture was cooled and the obtained product was then precipitated out with methanol followed by column chromatography to isolate the derivative Pc of complex **5** (which has ester groups) followed by its hydrolysis wherein the Pc (0.3 g, 0.38 mmol), THF (5 mL) and 5 M NaOH (1 mL) were stirred in a round bottomed flask at 80 °C for 24 h under reflux. The THF was evaporated from the reaction mixture and dilute HCl was added to the solution. The formed precipitate was then filtered off and column chromatography was used to isolate complex **5** using dichloromethane (DCM) and methanol (9:1) as eluents.

Yield: 32% (w/w). UV/Vis (DMSO):  $\lambda_{\text{max}}/\text{nm}$  ( $\log \epsilon$ ): 343 (4.35), 608 (4.25), 671 (5.05). Calc. for  $\text{C}_{40}\text{H}_{20}\text{N}_8\text{O}_5\text{Zn}$ : C 63.38, H 2.66, N 14.78; Found C 64.05, H 3.11, N 13.25. MS MALDI-TOF (m/z): Calculated: 756.08, Found: 756.25. IR [ $\nu_{\text{max}}/\text{cm}^{-1}$ ]: 3287 (O-H stretch), 1665 (C=C stretch), 1571 (C=C bend), 1360 (C-H bend), 1210 (C-N stretch), 920 (C=C bend).  $^1\text{H}$  NMR (600MHz, DMSO):  $\delta$ , ppm 9.42 (s, 2H, COOH), 9.11–8.29 (m, 15 H, Pc macrocycle-H), 8.00–7.25 (m, 3H, phenyl-H).

## **2.3.2 Synthesis and functionalisation of NPs**

### **2.3.2.1 Synthesis of oleylamine capped Ag NPs (OLM-Ag NPs), Scheme 3.3**

Synthesis of the OLM-Ag NPs was conducted as reported before [172]. Briefly, silver acetate (0.50 g, 3.00 mmol), oleylamine (2 mL) and toluene (50 mL) were refluxed at 115 °C while stirring overnight. The solution turned from yellow to a dark brown as the reaction proceeded. The solution was allowed to cool to room temperature followed by the addition of methanol (100 mL) which lead to the formation of a black precipitate. The precipitate was dissolved in hexane (10 mL) and the NPs were then re-precipitated with methanol (20 mL). The formed OLM-Ag NPs were air dried under an enclosed high vacuum fume hood.

### **2.3.2.2 Synthesis of cysteamine functionalised Ag NPs (Cys-Ag NPs), Scheme 3.4**

Synthesis of the Cys-Ag NPs was carried out as reported before [173,174] but with slight modification. Briefly, cysteamine (0.020 g, 0.26 mol) was then added to the already formed OLM-Ag NPs described above followed by stirring for another 2 h at 100 °C. The reaction mixture was then cooled to room temperature and the cysteamine functionalised Ag NPs were precipitated out of solution with ethanol under centrifugation. The NPs were washed several times with ethanol, followed by air drying of the formed precipitate under an enclosed high vacuum fume hood.

### **2.3.2.3 Synthesis of Fe<sub>3</sub>O<sub>4</sub> NPs (NH<sub>2</sub>-Fe<sub>3</sub>O<sub>4</sub> NPs), Scheme 3.5**

Synthesis of the NH<sub>2</sub>-Fe<sub>3</sub>O<sub>4</sub> NPs was conducted using the co-precipitation method as reported before [175]. Briefly, ferric chloride hexahydrate (1.08 g, 4.00 mmol) and ferrous chloride tetrahydrate (0.40 g, 2.00 mmol) were stirred in a flask containing water (40 mL) under nitrogen atmosphere. The solution was heated to 80 °C followed by the addition of ammonia (5 mL, 25 %) which resulted in the formation of a precipitate. The formed bare Fe<sub>3</sub>O<sub>4</sub> NPs were rinsed several times with deionised water then dispersed in ethanol (120 mL) followed by sonication for 15 min. Water (40 mL), ammonia (3 mL, 25 %) and tetraethoxysilane (TEOS, 2 mL) were then added to the solution followed by continuous stirring for 24 h. The precipitates were washed three times with deionized water and collected by centrifugation (15 000 rpm) resulting in Si-Fe<sub>3</sub>O<sub>4</sub> NPs. The formed Si-Fe<sub>3</sub>O<sub>4</sub> NPs were then functionalised with amine groups using previously reported methods [42] as follows: Si-Fe<sub>3</sub>O<sub>4</sub> NPs were added to a solvent mixture of DMF (12 mL) and toluene (8 mL) followed by stirring. APTES (1200 µL) was added dropwise into the solution and reaction was stirred for 24 h at

room temperature under a nitrogen gas flow. The formed  $\text{NH}_2\text{-Fe}_3\text{O}_4$  NPs were washed four times with toluene and collected with a magnet. The NPs were then air dried under an enclosed high vacuum fume hood.

#### **2.3.2.4 Synthesis of cysteamine capped core-shell $\text{Fe}_3\text{O}_4@Ag$ NPs (Cys- $\text{Fe}_3\text{O}_4@Ag$ NPs), Scheme 3.6**

Synthesis of the Cys- $\text{Fe}_3\text{O}_4@Ag$  NPs was conducted by adding the Si- $\text{Fe}_3\text{O}_4$  NPs (0.15 g), silver acetate (0.25 g, 1.50 mmol), diphenyl ether (20 g, 117 mmol), oleic acid (5 mL) and oleylamine (10 mL) in a round bottomed flask. The Si- $\text{Fe}_3\text{O}_4$  NPs were chosen instead of the bare  $\text{Fe}_3\text{O}_4$  NPs because silica has been reported to be a stabilizing surfactant, thereby preventing the alteration of the properties of the core  $\text{Fe}_3\text{O}_4$  NPs [176]. The mixture was heated at 200 °C, under argon gas flow for 5 h followed by the addition of cysteamine (0.020 g, 0.26 mol). The mixture was then stirred at a reduced temperature of 100 °C for another 5 h and then cooled to room temperature. Using ethanol, the NPs were precipitated out of solution followed by successive washing with ethanol. Cys- $\text{Fe}_3\text{O}_4@Ag$  NPs were then magnetically retrieved and air dried under an enclosed high vacuum fume hood.

### 2.3.3 Conjugation of NPs to Pcs

Complexes **1-3** were conjugated to the OLM-Ag NPs *via* chemisorption through Ag-N and Ag-S bonds. Complexes **4-6** on the other hand were conjugated to the Cys-Ag, NH<sub>2</sub>-Fe<sub>3</sub>O<sub>4</sub> and Cys-Fe<sub>3</sub>O<sub>4</sub>@Ag NPs through amide bond formation between the carboxylic acid moieties of the Pcs and the amine moieties of the NPs.

#### 2.3.3.1 Conjugation of OLM-Ag NPs to complexes 1-3 *via* chemisorption, Scheme 3.7

The conjugation of the Pcs to the OLM-Ag NPs was conducted *via* interaction between Ag and the nitrogen (and/or the sulfur) groups on the Pcs as reported before [116] wherein the Pcs replace the loosely bound OLM. Briefly, 5 mg of each of the Pcs was dissolved in DMF (10 mL) followed by the addition of a solution of the OLM-Ag NPs (2 mg in 5 mL chloroform) to each of the Pc solutions. The mixtures were allowed to react at 80 °C for 48 h under argon gas flow. After cooling to room temperature, methanol was added to each of the solutions and the Pc-NP conjugates were collected by centrifugation. The conjugates were washed further with methanol and ethanol and then dried under a high vacuum fume hood. The obtained conjugates for complexes **1**, **2** and **3** are denoted **1-Ag**, **2-Ag** and **3-Ag**, respectively.

#### 2.3.3.2 Conjugation of Cys-Ag, NH<sub>2</sub>-Fe<sub>3</sub>O<sub>4</sub> and Cys-Fe<sub>3</sub>O<sub>4</sub>@Ag NPs to complexes 4-6 *via* amide bonds, Scheme 3.8

The conjugation of complexes **4-6** to the different NPs was conducted as reported before for the conjugation of Ag NPs to Pcs [173] but with slight modifications. The method of conjugation using complex **4** as an example is explained. Briefly, complex **4** (0.02 g, 0.017 mmol) was weighed into three flasks and dissolved in DMF (2 mL). N,N'-dicyclohexylcarbodiimide (DCC) (0.017 g, 0.082 mmol) was then added to each

of the flasks followed by stirring for 48 h at room temperature. N,N'-dimethylpyridin-4-amine (DMAP) (0.010 g, 0.082 mmol) was then added to each of the reaction mixtures followed by the addition of the Cys-Ag NPs, NH<sub>2</sub>-Fe<sub>3</sub>O<sub>4</sub> NPs and Cys-Fe<sub>3</sub>O<sub>4</sub>@Ag NPs (0.01 g) to their respective flasks. The reaction mixtures were stirred for a further 48 h at room temperature so as to allow for amide bond formation between the NPs and Pc. The formed conjugates were precipitated out of solution with methanol and washed with ethanol followed by air drying under an enclosed high vacuum fume hood. The resulting conjugates are represented as **4-Ag**, **4-Fe<sub>3</sub>O<sub>4</sub>** and **4-Fe<sub>3</sub>O<sub>4</sub>@Ag** NPs, respectively. The same procedure was followed for complexes **5** and **6** and their conjugates are denoted as **5-Ag**, **5-Fe<sub>3</sub>O<sub>4</sub>**, **5-Fe<sub>3</sub>O<sub>4</sub>@Ag** NPs and **6-Ag**, **6-Fe<sub>3</sub>O<sub>4</sub>**, **6-Fe<sub>3</sub>O<sub>4</sub>@Ag** NPs, respectively.

## **2.4 Fabrication of electrospun NFs**

### **2.4.1 SiO<sub>2</sub> NFs**

The SiO<sub>2</sub> NFs reported herein were electrospun, calcined and then modified with Ag NPs and Pc complexes **1-3** using the procedures described below. Composite NFs containing both Pcs and Ag NPs were also prepared. The bare and modified NFs were then applied for antimicrobial studies.

#### **2.4.1.1 Bare SiO<sub>2</sub> NFs**

Preparation of the electrospun SiO<sub>2</sub> NFs was conducted as reported before [26]. Briefly, polyvinylpyrrolidone (PVP, 3.0 g) and TEOS (2.8 mL) were mixed in ethanol (24 mL) followed by stirring for 2 h at room temperature. The gelatation/hydrolysis of TEOS was then conducted by adding HCl (0.35 mL) dropwise into the solution followed by stirring for another 12 h at room temperature. The solution was then electrospun using an applied voltage of 12 kV, a tip to collector distance (TCD) of



16.0 cm and a flow rate of 2 mL/h to obtain a white fibrous mat on the aluminium foil which was used as the collector. The NFs were electrospun at a room temperature of 25.7 °C and room humidity of 53 %. The calcination of the NFs was then conducted wherein the fibrous mat was placed in

a furnace which was heated to 600 °C for 6 h at a heating rate of 5 °C/min with air flow in order to burn off all organic components of the nanofibers. Purely inorganic SiO<sub>2</sub> NFs were obtained and allowed to cool to room temperature.

#### **2.4.1.2 *in situ* synthesis of Ag NPs onto SiO<sub>2</sub> NFs (Ag-SiO<sub>2</sub> NFs)**

Grafting of Ag NPs on the surface of the bare SiO<sub>2</sub> NFs was conducted as reported before [177] but with slight modification. The SiO<sub>2</sub> NFs were immersed in 100 mL aqueous solution of 0.1 M AgNO<sub>3</sub> in a 250 mL round bottomed flask. A few drops of ammonia were added to the solution and the flask was then placed in an oil bath and heated at 90 °C for 1.5 h accompanied by magnetic stirring. The NFs were then washed with deionized water three times and dried at room temperature under a high vacuum fume hood in the dark for 24 h. The obtained SiO<sub>2</sub> NFs modified with Ag NPs are denoted Ag-SiO<sub>2</sub> NFs (**Table 4.1**).

#### **2.4.1.3 Pc decorated SiO<sub>2</sub> NFs (Pc-SiO<sub>2</sub> NFs)**

The Pc decorated NFs were fabricated by immersing the bare SiO<sub>2</sub> NFs in 75 μM of each of the Pc solutions in DMF (10 mL). The mixtures were stirred gently for 24 h at room temperature. The NFs were then rinsed with deionised water and then with ethanol. The obtained green NFs were then dried in an enclosed high vacuum fume hood. The NFs modified with complexes **1-3** are denoted **1-SiO<sub>2</sub>**, **2-SiO<sub>2</sub>** and **3-SiO<sub>2</sub>** NFs, respectively (**Table 4.1**).

#### 2.4.1.4 Pc decorated Ag-SiO<sub>2</sub> NFs (Pc@Ag-SiO<sub>2</sub> NFs)

Composite NFs composed of both the Ag NPs and the Pcs were fabricated through chemisorption (Ag-N, Ag-S) of the Pcs onto the surface of the *in situ* fabricated Ag NPs. Briefly, the Ag-SiO<sub>2</sub> NFs were immersed in 75 μM solutions of the complexes **1-3** in DMF for 96 h at room temperature. The NFs were rinsed with water, followed by drying under an enclosed high vacuum fume hood. The obtained NFs modified with complexes **1-3** are denoted **1@Ag-SiO<sub>2</sub>**, **2@Ag-SiO<sub>2</sub>** and **3@Ag-SiO<sub>2</sub>** NFs, respectively (**Table 4.1**).

#### 2.4.2 Semiconductor NFs

The fabrication of bare Hem NFs is reported and so is their modification with complexes **4-6**. In order to compare the photocatalytic activities of the ZnO and TiO<sub>2</sub> NFs to those of the Hem NFs, studies were conducted where the bare NFs were fabricated and calcined at the same temperature followed by modification with the same Pc (complex **6**). No NPs were added to any of these NFs. A separate batch of TiO<sub>2</sub> NFs was however also fabricated and calcined at different temperatures. It was modified with Pd and Co NPs as well as another Pc (complex **7**) for hydrogen generation studies.

##### 2.4.2.1 Bare Hem NFs

Fabrication of the polymer-free Hem NFs was conducted as reported before [**178**] but with modifications. Briefly, ferric nitrate nonahydrate (4.04 g, 10 mmol) was dissolved in a solvent mixture of ethanol (10 mL) and DMF (10 mL) while stirring for 10 min. PVP (2 g) was then added to the solution followed by further stirring for 4 h to form the spinning solution. The precursor solution was then loaded into a plastic syringe equipped with a stainless steel needle. The electrospinning setup was set to a voltage

of 13 kV, a tip to collector distance of 12.0 cm and a flow rate of 1 mL/h to obtain a yellow fibrous mat on the aluminium foil which was used as the collector. The NFs were electrospun at a room temperature of 26.3 °C and room humidity of 48 %. Calcination of the NFs was then conducted at 450 °C using a heating rate of 2 °C/min for 3 h in air to obtain purely inorganic Hem NFs. Due to their fragile nature, the NFs were then cast to 0.8 cm x 0.8 cm dimensions on glass slides before modification.

#### **2.4.2.2 Bare ZnO NFs**

The fabrication of the ZnO fibers was conducted as reported before [179] but with slight modification. Briefly, zinc acetate dihydrate (1.5 g) was dissolved in a solvent mixture of ethanol (15 mL) and DMF (5 mL) under magnetic stirring at room temperature. After 2 h of stirring, PVP (2.5 g) was added to the solution followed by continuous stirring for 6 h to obtain a homogenous viscous solution. The solution was loaded into a plastic syringe equipped with a stainless steel needle and connected to a high voltage power supply. A solution flow rate of 0.03 mL h<sup>-1</sup> and a voltage of 15.5 kV were administered with the distance between the needle tip and the collector being maintained at 20 cm. The recorded temperature and humidity in the room were 26.7 °C and 49%, respectively. The formed NFs were collected on the surface of silicon substrates clamped on top of a conductive aluminium collector and subsequently exposed to the air overnight for stabilization. The NFs were then calcined at 450 °C at a heating rate of 2 °C min<sup>-1</sup> for 3 h to obtain purely inorganic ZnO NFs.

#### **2.4.2.3 Bare TiO<sub>2</sub> NFs**

Fabrication of the TiO<sub>2</sub> NFs was conducted as reported before [180,181] but with slight modifications. A solution of glacial acetic acid (5 mL) and titanium (IV) propoxide (5 mL) was prepared and added to a solution of 10 % PVP (10 mL) in ethanol. The

resulting solution was stirred for 24 h and then loaded into a syringe equipped with a stainless steel needle, connected to a high voltage power supply. A voltage of 12.5 kV was applied between the needle and the stationary aluminium foil collector. The distance between the tip of the needle and the collector (TCD) was 12 cm and the applied flow rate was 1.5 mL/h (controlled using a syringe pump). The recorded temperature and humidity in the room in which the electrospinning was conducted were 24.7 °C and 49%, respectively. The collected NFs were left in open air for 2 h and then calcined at 450 °C at a heating rate of 2 °C min<sup>-1</sup> for 3 h to obtain purely inorganic TiO<sub>2</sub> NFs.

#### **2.4.2.4 Pc decorated semiconductor NFs**

Complex **6** was dissolved in a 1:1 solvent mixture of acetonitrile and ethanol in three separate reaction vessels to make 75 µM solutions. The Hem, ZnO and TiO<sub>2</sub> NFs were immersed in each of the Pc solutions overnight in sealed containers and left in the dark. Blue NFs were retrieved, washed with ethanol and then dried under a high vacuum fume hood. The resulting functionalised NFs are denoted **6-Hem**, **6-ZnO** and **6-TiO<sub>2</sub>** NFs. Since the Hem NFs were also modified with complexes **4** and **5**, the same procedure reported above was conducted but using DMF instead of acetonitrile and ethanol and the resulting NFs are denoted **4-Hem** and **5-Hem**, respectively (**Table 4.2**).

Due to the different properties of the phases that TiO<sub>2</sub> can exist in, a second batch of TiO<sub>2</sub> NFs was prepared using the same sample preparation and electrospinning technique reported above but in this case the electrospun NFs were calcined at temperatures of 500, 750 and 950 °C for 3 h instead. The obtained bare NFs calcined at 500, 750 and 950 °C are denoted as TiO<sub>2</sub>-500, TiO<sub>2</sub>-750 and TiO<sub>2</sub>-950, respectively

(Table 4.2). Modification of these NFs with complex 7 was conducted as reported above for complex 6 but instead using THF instead of acetonitrile and ethanol. The obtained Pc modified NFs for TiO<sub>2</sub>-500, TiO<sub>2</sub>-750 and TiO<sub>2</sub>-950 are denoted 7@TiO<sub>2</sub>-500, 7@TiO<sub>2</sub>-750 and 7@TiO<sub>2</sub>-950, respectively (Table 4.2). A comparative study of the photocatalytic properties of the fabricated NFs against the commercially available P25-TiO<sub>2</sub> was conducted thus the Pc modified P25-TiO<sub>2</sub> is denoted therefore 7@P25-TiO<sub>2</sub>. The NFs (and P25-TiO<sub>2</sub>) were also modified with Pd and Co NPs as discussed below.

#### 2.4.2.5 *in situ* synthesis of Pd NPs onto TiO<sub>2</sub> NFs

The formation of Pd NPs was conducted by the reduction of Pd<sup>2+</sup> under ultraviolet A (UVA) irradiation in the presence of the calcined TiO<sub>2</sub> NFs (TiO<sub>2</sub>-500, TiO<sub>2</sub>-750 or TiO<sub>2</sub>-950) and P25-TiO<sub>2</sub>. This was done following the protocols previously described [182] but with slight modifications. Each of the calcined NFs and P25-TiO<sub>2</sub> (500 mg) together with PdCl<sub>2</sub> (22 mg) were added to 20 mL water in separate reaction vessels followed by UVA irradiation in a photoreactor for 8 h. The NFs were then rinsed with water and dried overnight in a desiccator. Brown Pd decorated TiO<sub>2</sub> NFs were obtained and denoted Pd@TiO<sub>2</sub>-500, Pd@TiO<sub>2</sub>-750, Pd@TiO<sub>2</sub>-950 NFs and Pd@P25-TiO<sub>2</sub> (Table 4.2).

#### 2.4.2.6 *in situ* synthesis of Co NPs onto TiO<sub>2</sub> NFs

The formation of Co NPs on the surface of the TiO<sub>2</sub> NFs (and P25-TiO<sub>2</sub>) was conducted following the protocols previously described [183] but with slight modifications. Irgacure-907 (I-907) was used as a photoinitiator for the photochemical reduction of Co<sup>2+</sup> to Co NPs. Each of the calcined NFs and P25-TiO<sub>2</sub> (160 mg) were added to a 20 mL solution of 1 mM cobalt nitrate and 2 mM I-907 in argon-saturated

acetonitrile, followed by irradiation in a photoreactor for 2 h. The catalysts were then rinsed with water and left to dry overnight. Due to the instability of the Co NPs in the presence of oxygen, the otherwise black and paramagnetic Co NPs did not exhibit paramagnetic behaviour in the presence of air and resulted in grey/white Co decorated TiO<sub>2</sub> NFs which are denoted Co@TiO<sub>2</sub>-500, Co@TiO<sub>2</sub>-750, Co@TiO<sub>2</sub>-950 NFs and Co@P25-TiO<sub>2</sub>, respectively (**Table 4.2**).

## **2.5 Photocatalytic applications**

### **2.5.1 PACT studies**

The microorganisms were grown on agar plate according to the manufacturer's specifications to obtain individual colonies. The colonies were inoculated into nutrient broth and placed on a rotary shaker (~200 rpm) overnight at 37 °C (*E. coli* and *S. aureus*) or 30 °C (*C. albicans*). Aliquots of the culture were aseptically transferred to fresh broth (4 mL) and incubated at 37°C or 30°C to mid-logarithmic phase (absorbance ≈ 0.6 at 620 nm). The bacteria/fungal cultures in the logarithmic phase of growth were harvested through the removal of the broth culture by centrifugation for 15 min at 3000 rpm followed by washing using PBS three times. The bacteria/fungal cultures were diluted to 1/1000 using PBS to get a bacterial working stock solution of approximately 10<sup>6</sup> colony forming units (CFU) per mL.

The antimicrobial studies were carried out as reported before [184] but with slight modification. In all the experiments, the bacterial/fungal suspensions were incubated in an oven equipped with a shaker for 30 min in the dark at 37°C (bacteria) or 30°C (fungus). Half (3 mL) of the incubated bacterial/fungal suspensions were irradiated at the Q band maximum of the photosensitizers using the irradiation set-up described in **Section 2.2** and the other half kept in the dark. After irradiation, 100µL samples were

spotted on agar plates using a micropipette. The plates were inverted and incubated overnight. The experiments were done in triplicates. Complexes **1**, **2**, **4** and **5** and their conjugates are not soluble in water while complex **3** is partially soluble hence they were dissolved in DMSO (2%) and made up with PBS for PACT studies. Control experiments were also prepared for both light and dark toxicity studies wherein there was no Pc/conjugate in the bacterial/fungal solution.

The photoinactivation of the microorganisms using the SiO<sub>2</sub> and Hem NFs was conducted using previously reported procedures [13]. Briefly, the modified NFs were placed on agar plates inoculated with the microorganisms (150 µL). A set of agar plates containing the modified NFs and the bare NFs (used as control) were illuminated with light for 30 min. A similar set of agar plates were prepared but kept in the dark instead. All the plates were then incubated overnight at 37 °C for *S. aureus* and *E. coli* and 30 °C for *C. albicans*.

The antimicrobial efficiencies of the bare and modified NFs were evaluated by measuring the zones of inhibition for each of the NFs. Using a ruler, the length from the centre of the NFs to the edge of the area with no microbial growth were measured. Since experiments were conducted in triplicate, the average length (in millimeters) was calculated and recorded. The zone of inhibition can be directly related to the level of antimicrobial activity present in the sample i.e. the larger the zone of inhibition, the more potent the NF while smaller zones of inhibition can be an indication of the resistance of the microorganisms.

### **2.5.2 Photodegradation studies**

The photodegradation efficiencies of the bare and Pc modified semiconductor NFs (Hem, ZnO and TiO<sub>2</sub> NFs) were evaluated. The photodegradation of MO was carried out at pH 2.5 as it has been reported that the degradation of MO is enhanced in acidic conditions with pH ranges of 2-3 [185,186]. Spectral changes that occurred were monitored at 506 nm on a UV-vis spectrophotometer using 20 mg of the NFs. Kinetics calculations were then conducted to compare the manner and rates in which the pollutant degrades using the different catalysts. All the experiments were carried out under aerobic conditions using a range of pollutant concentrations.

### **2.5.3 Hydrogen generation studies**

The bare and modified TiO<sub>2</sub> NFs (and P25-TiO<sub>2</sub>) (10 mg) were suspended in 4 mL of 1% methanol aqueous solution under argon atmosphere and sealed in a crimp top vial followed by irradiation for 4 h. Samples of the headspace gas were then taken with a sample lock syringe and injected in the Gas Chromatograph-Thermal Conductivity Detector (GC-TCD) wherein the H<sub>2</sub> signal was detected at ~ 4.0 min. Quantification of H<sub>2</sub> was performed using the already reported calibration curve of the gas detection in the GC-TCD instrument.



# Results and Discussion

**Chapter 3:** Synthesis and Characterisation of Pcs, NPs and conjugates

**Chapter 4:** Fabrication and Characterisation of nanofibers

**Chapter 5:** Photophysical and photochemical parameters

**Chapter 6:** Antimicrobial studies

**Chapter 7:** Photooxidation of organic pollutants

**Chapter 8:** Hydrogen generation applications

## Publications

1. **Sivuyisiwe Mapukata**, Andrew S. Hainer, Anabel E. Lanterna, Juan C. Scaiano, Tebello Nyokong, Decorated titania fibers as photocatalysts for hydrogen generation and organic matter degradation, *J. Photochem. Photobiol. A: Chem.* 388 (2020)112185.
2. **Sivuyisiwe Mapukata**, Nnamdi Nwahara, Tebello Nyokong, The photodynamic antimicrobial chemotherapy of *Staphylococcus aureus* using an asymmetrical zinc phthalocyanine conjugated to silver and iron oxide based nanoparticles, *J. Photochem. Photobiol. A: Chem.* 402, (2020) 112813.
3. **Sivuyisiwe Mapukata**, Tebello Nyokong, Development of phthalocyanine functionalised TiO<sub>2</sub> and ZnO nanofibers for photodegradation of methyl orange, *New J. Chem.*44 (2020) 16340-16350.
4. **Sivuyisiwe Mapukata**, Jonathan Britton, Olawale L. Osifeko, Tebello Nyokong, The improved antibacterial efficiency of a zinc phthalocyanine when embedded on silver nanoparticle modified silica nanofibers, *Photodiagnosis Photodyn. Ther.* 33 (2021) 102100.
5. **Sivuyisiwe Mapukata**, Pinar Sen, Olawale L. Osifeko, Tebello Nyokong, The antibacterial and antifungal properties of neutral, octacationic, hexadecacationic Zn phthalocyanines when conjugated to silver nanoparticles, *Photodiagnosis Photodyn. Ther.* 35 (2021) 102361.
6. **Sivuyisiwe Mapukata**, Tebello Nyokong. The photocatalytic properties of a zinc phthalocyanine supported on  $\alpha$ -Fe<sub>2</sub>O<sub>3</sub> nanofibers against Methyl Orange and *Staphylococcus aureus*. Submitted to *J. Photochem. Photobiol. A: Chem.*

## Extra publications

7. Francis Chindeka, Philani Mashazi, Jonathan Britton, David O. Oluwole, **Sivuyisiwe Mapukata**, Tebello Nyokong, Fabrication of dye-sensitized solar cells based on push-pull asymmetrical substituted zinc and copper phthalocyanines and reduced graphene oxide nanosheets, J. Photochem. Photobiol. A: Chem. 399 (2020) 112612.

# Chapter 3

This chapter gives details on the syntheses and characterisation of the Pcs, NPs as well as their respective conjugates.

### 3.1 Phthalocyanines (Pcs)

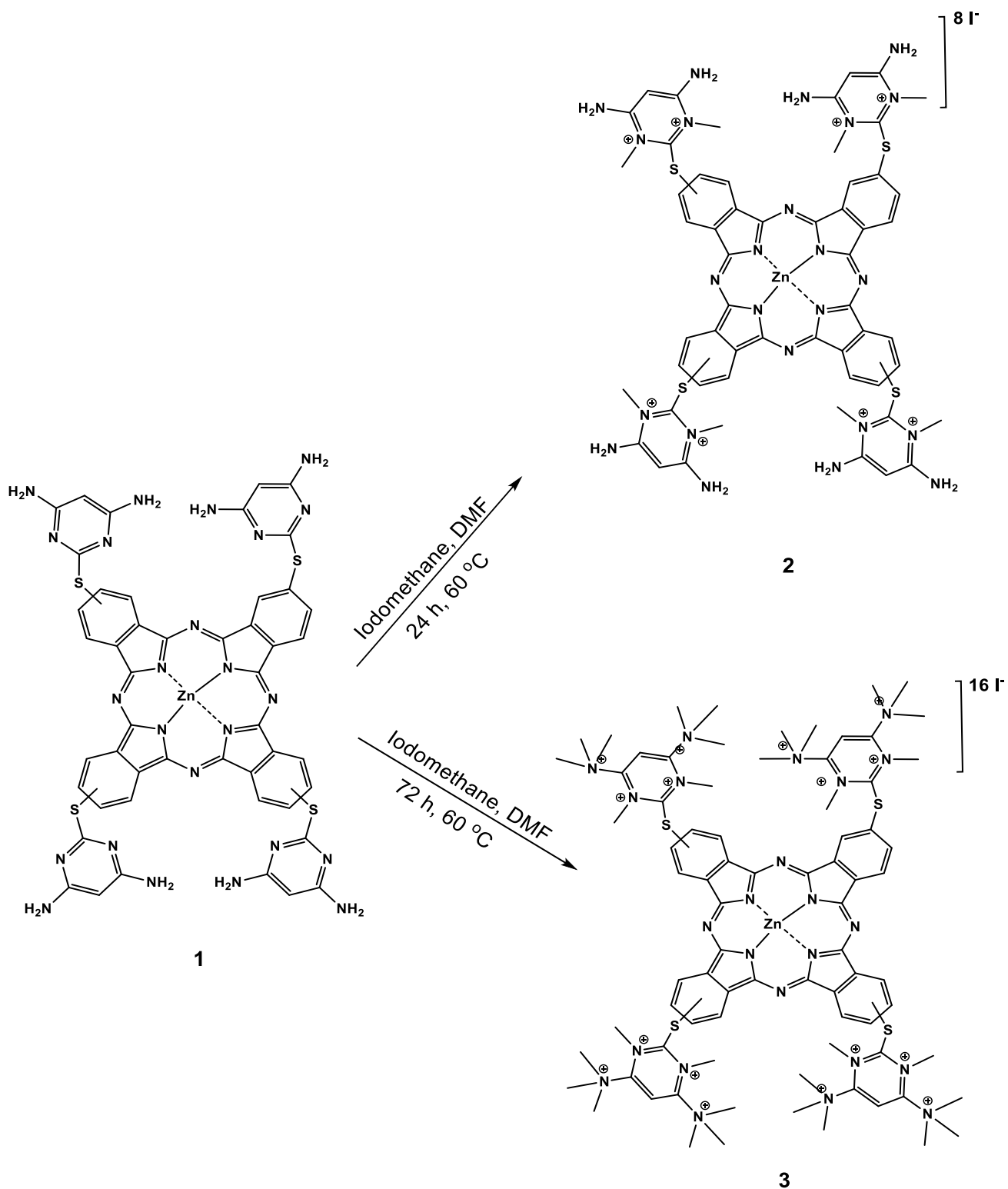
Since the syntheses of complexes **1**, **6** and **7** has been reported before [118-120], their characterisation will not be discussed. Discussions of the syntheses and characterisation of complexes **2-5** is however elaborated below.

Complexes **2** and **3** originate from the same Pc. They were both obtained from the quaternization of complex **1**. Discussions on their characterisations are therefore combined for comparative studies. Complexes **4** and **5** also only differ based on the former having *tert*-butylphenoxy groups hence their characterisation is also combined for comparative studies.

**3.1.1 2,9(10),16(17),23(24)-Tetrakis-(4'-(1',3'-N-dimethyl, 4'-6'-diaminopyrimidin-2'-ylthio))) phthalocyaninato zinc (II) (2) and 2,9(10),16(17),23(24)-Tetrakis-(4'-(1',3'-N-dimethyl,4'-6'-(hexamethylaminopyrimidin-2'-ylthio))) phthalocyaninato zinc (II) (3)**

**Scheme 3.1** demonstrates the quaternization of complex **1** to yield complexes **2** and **3** using varying amounts of iodomethane as the quaternizing agent at different reaction times. Using various spectroscopic techniques, characterisation of the novel cationic Pcs was conducted to confirm their structures.

As shown in **Figure 3.1**, the FT-IR spectrum of complex **2** shows peaks at 3304 and 3150  $\text{cm}^{-1}$  corresponding to the primary amine N-H stretch, thereby proving that the amine peaks of the Pc are not quaternized. These peaks are however not observed for complex **3** as it is completely quaternized. The FT-IR spectra also shows peaks attributed to the introduced methyl groups at 2924-2742  $\text{cm}^{-1}$  for complex **2** and 2946-2730  $\text{cm}^{-1}$  for complex **3**.



**Scheme 3.1:** Quaternization of complex **1** to yield complexes **2** and **3**.

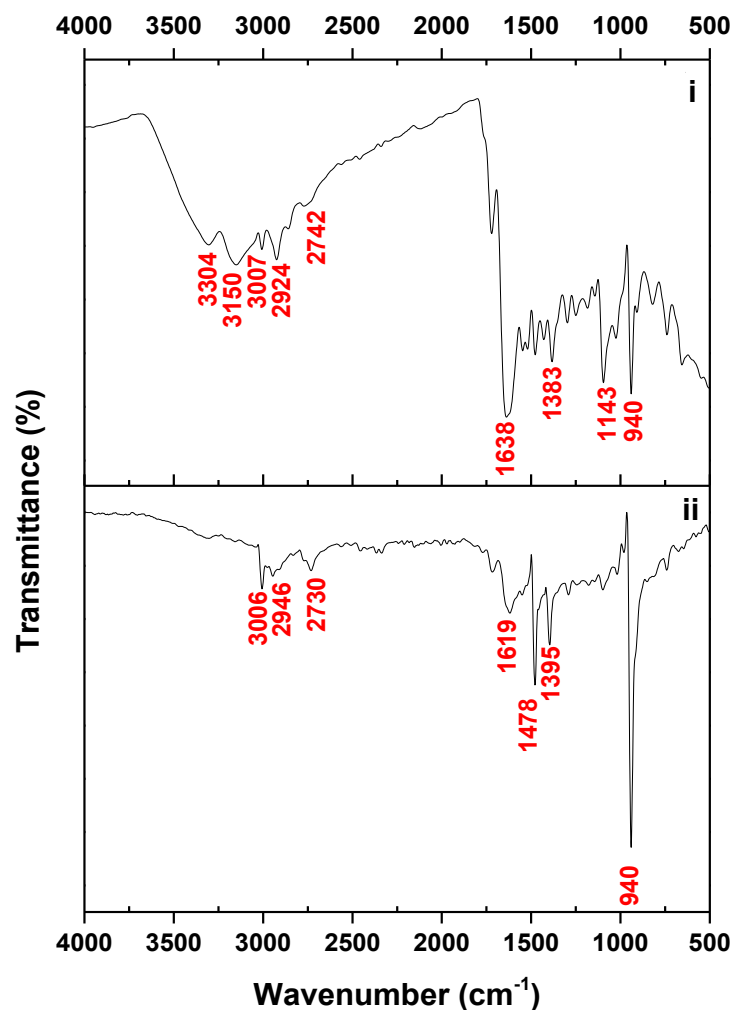


**Figure 3.1:** FT-IR spectrum complexes (i) **2** and (ii) **3**.

As shown in **Figure 3.2**, the MALDI-TOF spectra (run in positive mode) of complexes **2** and **3** show single peaks for each Pc with  $m/z$  of 159.44 and 100.98, respectively. These values correspond to the calculated  $m/z$  of the Pcs without the iodine atoms which balance the charges. This is therefore evidence of successful quaternization of complex **1** as no peaks associated with it are observed on either spectrum nor are there any other peaks that are unaccounted for.

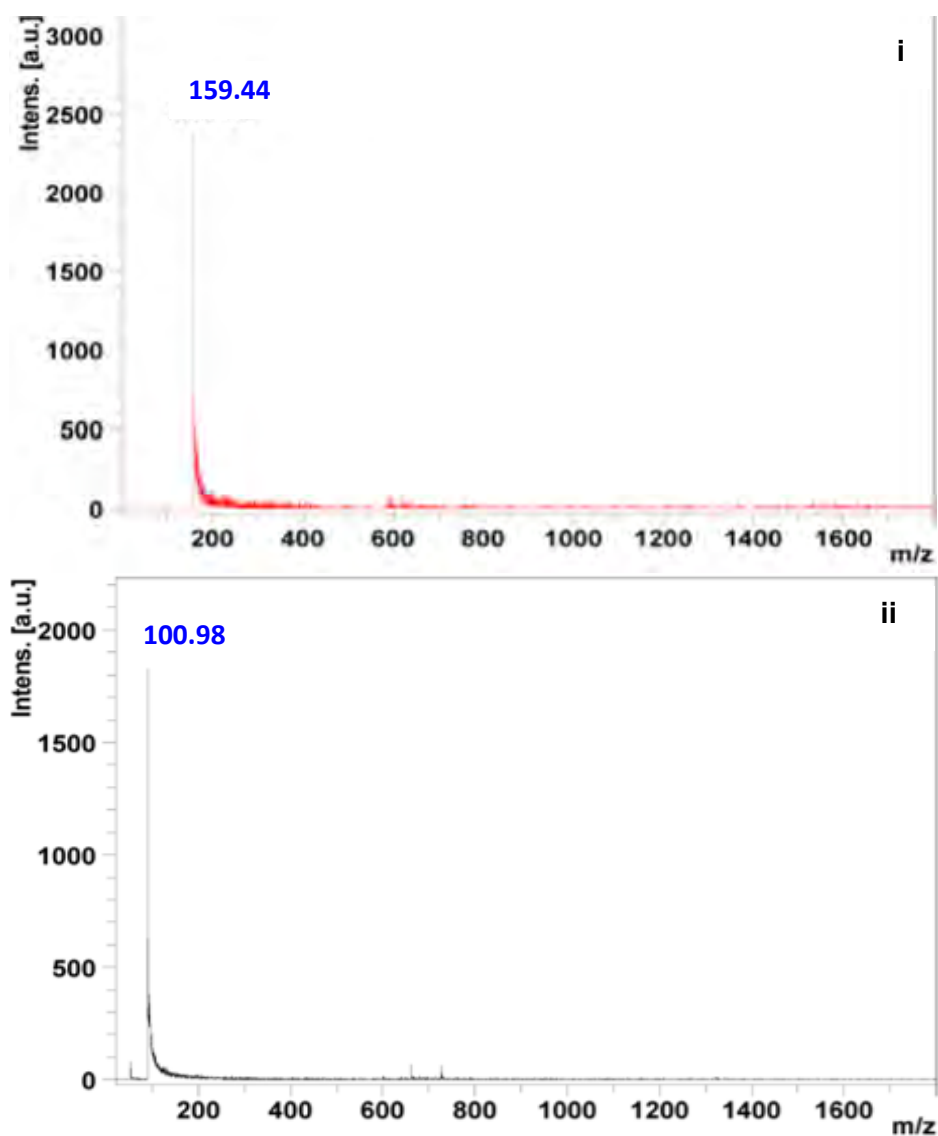


**Figure 3.2:** MALDI-TOF spectra of complexes (i) **2** and (ii) **3**.

Integration of the  $^1\text{H}$  NMR spectra of complexes **2** and **3** further confirmed their structures as all the expected protons were accounted for, thereby confirming their purity. The aromatic proton peaks were observed at 7.89-9.50 ppm for complex **2** and 7.79-8.01 ppm for complex **3**. The shift in the aromatic peaks between the two complexes is due to differences in their electron densities thereby proving that the Pc complexes have different structures. The ground state electronic absorption spectra



of complexes **2** and **3** in DMSO are shown in **Figure 3.3**. The spectra show the characteristic bands associated with monomeric metallated Pcs i.e. Q band accompanied by a vibronic band and B band. The Q bands for complexes **2** and **3** are observed at 687 and 686 nm, respectively (**Table 3.1**). The spectra of the cationic complexes **2** and **3** are thus slightly blue shifted relative to the neutral complex with a Q band at 689 nm [**118**], **Table 3.1**. The optical behaviour of complexes **2** and **3** was also analysed in 2% DMSO (in PBS) as that is the solvent mixture used in antimicrobial studies due to the poor solubility of complex **2** in water. As shown in **Figure 3.3 (insert)**, the Q bands are broad and split due to aggregation. It is typical of Pcs in aqueous media to form aggregates attributed to the  $\pi$ - $\pi$  stacking interactions of the aromatic rings of the Pcs [**187**].

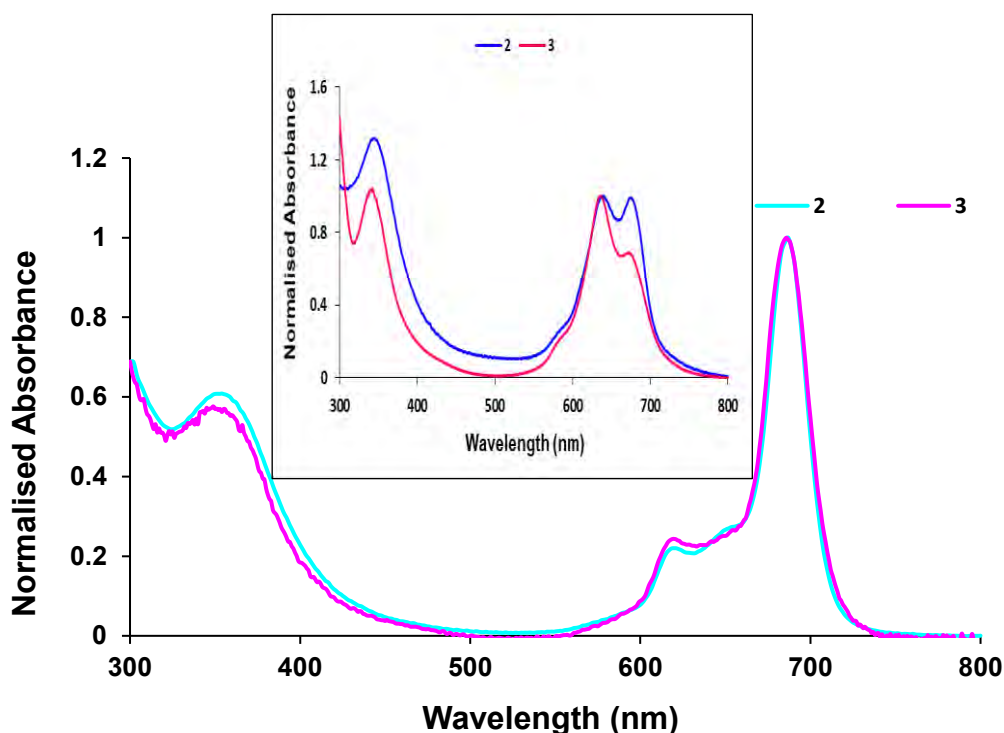


**Figure 3.3:** Ground state UV-vis spectra of complexes **2** and **3** in DMSO. Insert = Absorption spectra of complexes **2** and **3** in 2% DMSO (in PBS).

**Table 3.1:** The Q band absorbance values of the Pc complexes and their conjugates in DMSO.

<b>Pc/ conjugate</b>	<b>Q band (nm)</b>
Complex 1	689
1-Ag	689
Complex 2	687
2-Ag	687
Complex 3	686
3-Ag	686
Complex 4	680
4-Ag	682
4-Fe <sub>3</sub> O <sub>4</sub>	680
4-Fe <sub>3</sub> O <sub>4</sub> @Ag	681
Complex 5	671
5-Ag	671
5-Fe <sub>3</sub> O <sub>4</sub>	671
5-Fe <sub>3</sub> O <sub>4</sub> @Ag	671
Complex 6	676
6-Ag	676
6-Fe <sub>3</sub> O <sub>4</sub>	676
6-Fe <sub>3</sub> O <sub>4</sub> @Ag	676
Complex 7	680 <sup>a</sup>

Values in brackets were obtained in 2% DMSO (in PBS)

<sup>a</sup>Values in THF

### 3.1.2 2-Mono-isophthalic acid-9(10),16(17),23 (24)- tri (*tert*-butylphenoxy) phthalocyaninato zinc(II) (4) and 2-Mono-(5-oxy) isophthalic acid phthalocyaninato zinc(II) (5)

The synthetic routes for 2-mono-isophthalic acid-9(10),16(17),23 (24)- tri (*tert*-butylphenoxy) phthalocyaninato zinc(II) (4) and 2-mono-(5-oxy) isophthalic acid phthalocyaninato zinc(II) (5) are shown in **Scheme 3.2**. The cyclotetramerization of their respective phthalonitriles as well as the hydrolysis of their ester counterparts was confirmed with FT-IR. The FT-IR spectra of complexes **4** and **5** are shown in **Figure 3.4**.

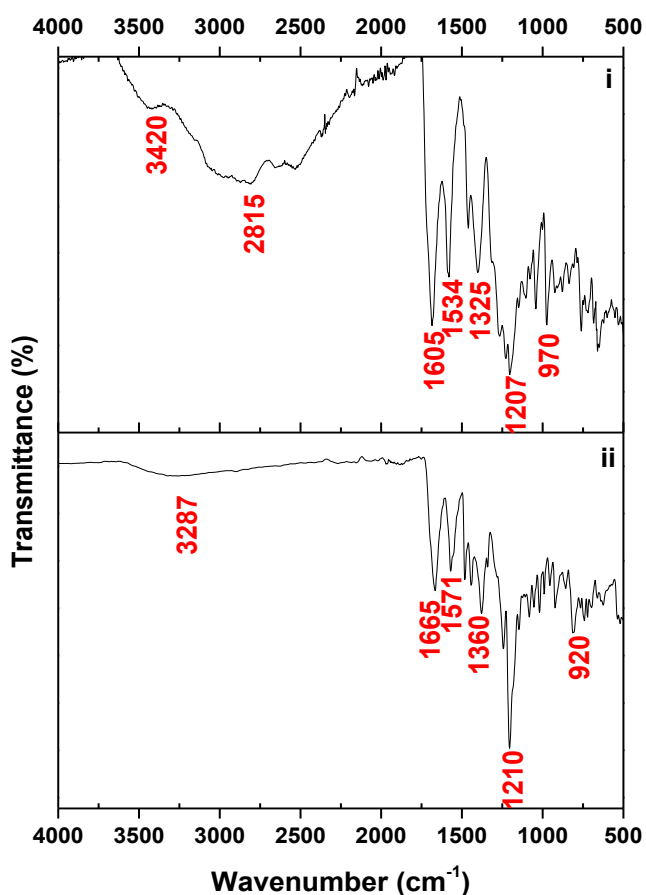
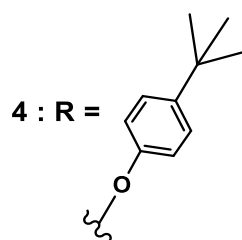
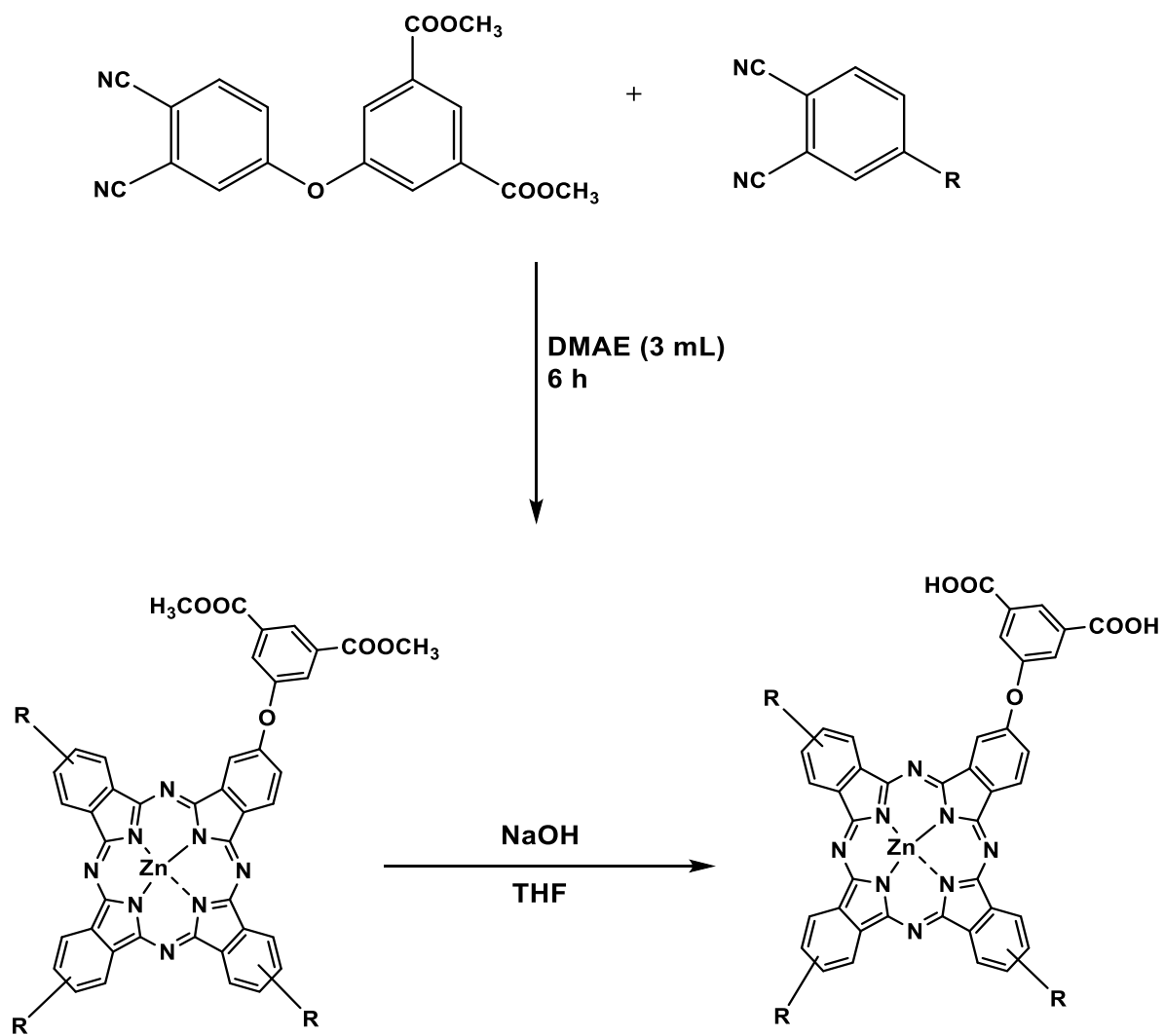


**Figure 3.4:** FT-IR spectra of complexes (i) **4** and (ii) **5**.



5: R = H

**Scheme 3.2:** Synthesis of complexes **4** and **5**.

The lack of C=N peaks at  $\sim 2200\text{ cm}^{-1}$  is an indication of complete cyclization of the phthalonitriles to form the ester substituted Pcs and the presence of -OH vibration peaks at values  $> 3200\text{ cm}^{-1}$  is an indication of efficient hydrolysis of the ester groups to form complexes **4** and **5** with carboxylic acid groups. In addition, complex **4** has a peak at  $2815\text{ cm}^{-1}$  due to the aliphatic hydrogens of the *tert*-butyl groups. These peaks are absent in complex **5** as it is monosubstituted which proves that the two Pcs have different functional groups and thus structures.

The MALDI-TOF spectra (run in positive mode) of complexes **4** and **5** are shown in **Figure 3.5**.

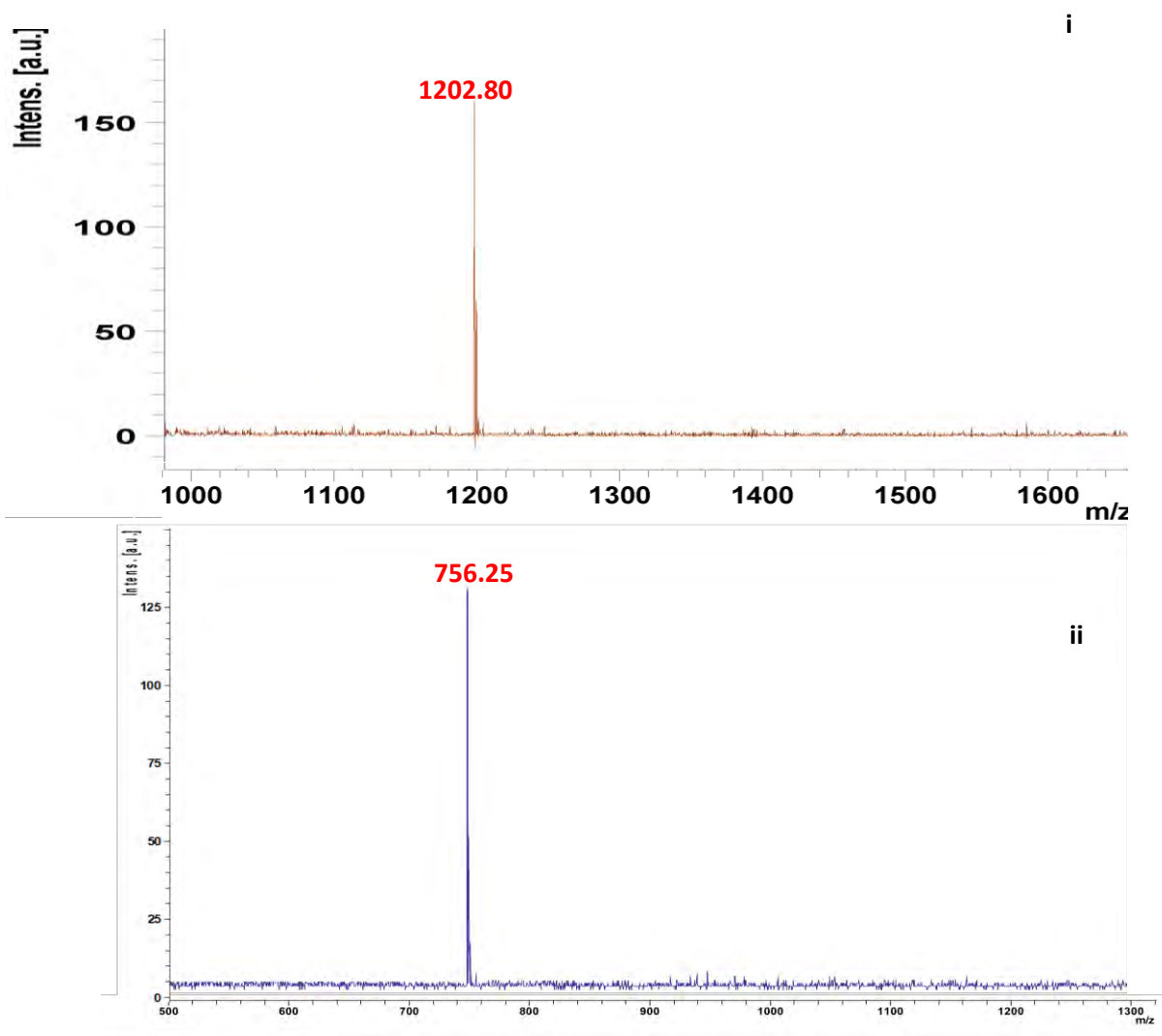


**Figure 3.5:** MALDI-TOF spectra of complexes (i) **4** and (ii) **5**.

The spectra show single peaks at 1202.80 and 756.25 for complexes **4** and **5**, respectively. These values correspond to the calculated  $m/z$  of the Pcs, which therefore serves as evidence of successful synthesis and purity of both complexes.

Integration of the  $^1\text{H}$  NMR spectra of both complexes **4** and **5** further confirmed their structures as all the expected protons were accounted for. Complex **4** has peaks at 1.05- 1.57 ppm due to the *tert*-butyl groups which were not observed for complex **5** thereby proving that the two Pcs have different structures.

The ground state electronic absorption spectra of complexes **4** and **5** in DMSO are shown in **Figure 3.6**. The spectra show that both complexes **4** and **5** also exhibit monomeric behaviour in DMSO with the Q bands observed at 680 and 671 nm, respectively (**Table 3.1**).

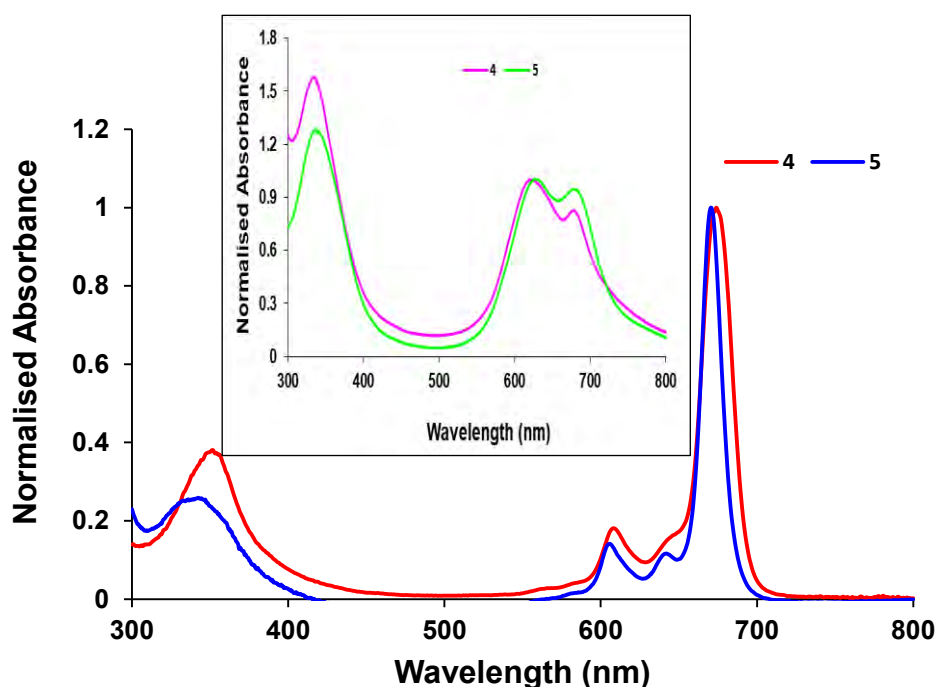


**Figure 3.6:** Ground state UV-vis spectra of complexes **4** and **5** in DMSO. Insert = Absorption spectra of complexes **4** and **5** in 2% DMSO (in PBS).

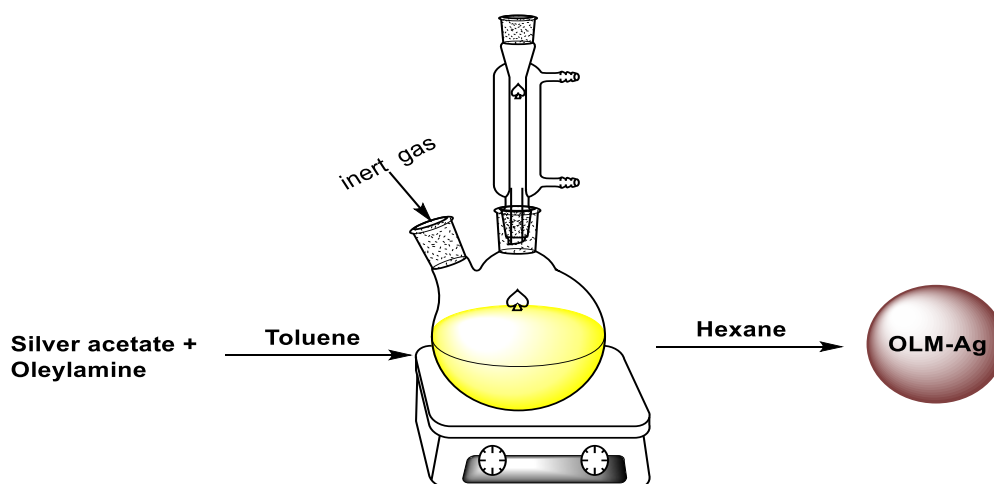
The blue shift of complex **5** can be attributed to the lack of electron donating *tert*-butyl groups that are present in complex **4**. Just as with complexes **2** and **3**, complexes **4** and **5** were also analysed in 2% DMSO (in PBS) due to their poor solubility in water. As shown in **Figure 3.6 (insert)**, both Pcs are aggregated in the solvent mixture.

## 3.2 Nanoparticles (NPs) and conjugates

### 3.2.1 Nanoparticles

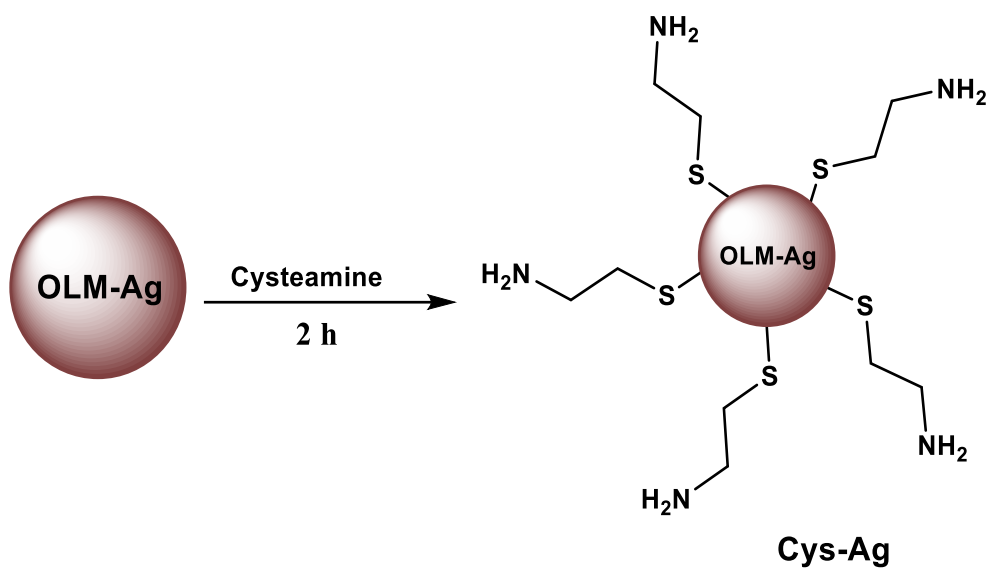
Various NPs were synthesised with the aim of conjugating them to Pcs for synergistic interactions and thus enhanced photophysicochemical properties. Characterisation of the conjugates was conducted using Transmission Electron Microscopy (TEM), X-ray Diffraction (XRD), Ground state UV-vis spectroscopy and X-ray photoelectron spectroscopy (XPS).

An illustrative representation of the synthetic route of the OLM-Ag NPs is demonstrated in **Scheme 3.3**. The OLM-Ag NPs were synthesised by reduction of silver acetate to form the NPs using oleylamine which also acts as the surfactant on the NPs. Further functionalisation of the NPs is not conducted as they are synthesised with the aim of conjugating them *via* chemisorption to complexes **1-3**.



**Scheme 3.3:** Synthesis of oleylamine capped Ag NPs (OLM-Ag NPs).

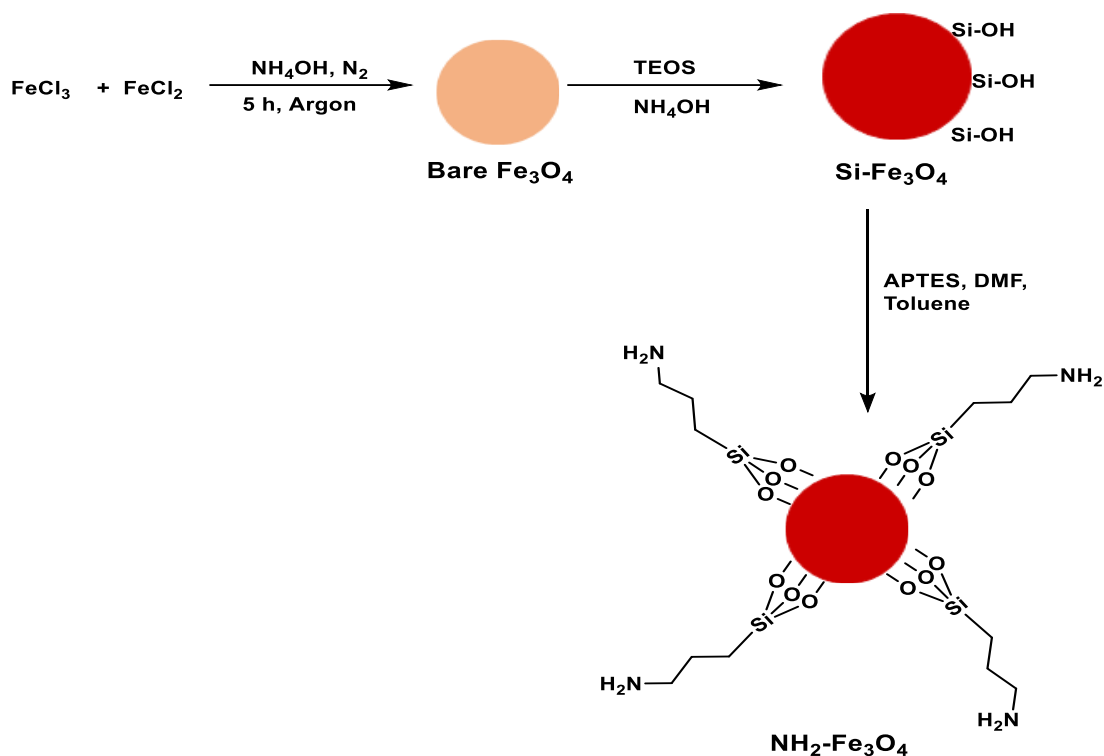
As demonstrated in **Scheme 3.4**, cysteamine was used to functionalise Ag NPs that had OLM as a surfactant to yield Cys-Ag NPs.



**Scheme 3.4:** Synthesis of cysteamine capped silver NPs (Cys-Ag NPs).

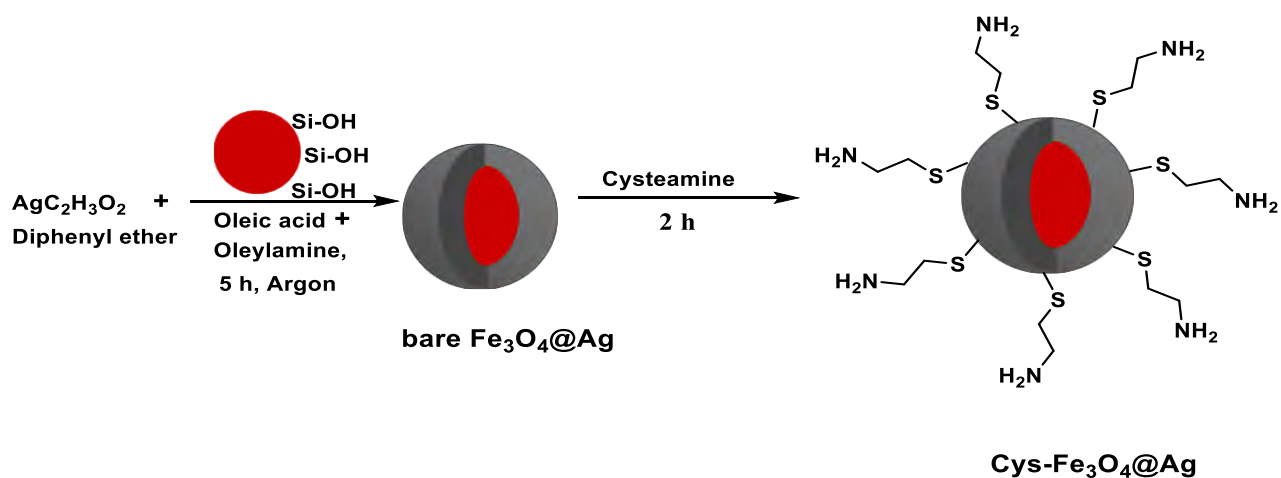
As demonstrated in **Scheme 3.5**, magnetic NPs were synthesised through the co-precipitation of  $\text{Fe}^{2+}$  and  $\text{Fe}^{3+}$  salts, surface stabilisation with TEOS to yield  $\text{Si-Fe}_3\text{O}_4$  NPs and finally, functionalisation with APTES to yield  $\text{NH}_2\text{-Fe}_3\text{O}_4$  NPs.





**Scheme 3.5:** Synthesis of amine functionalised Fe<sub>3</sub>O<sub>4</sub> NPs (NH<sub>2</sub>-Fe<sub>3</sub>O<sub>4</sub> NPs).

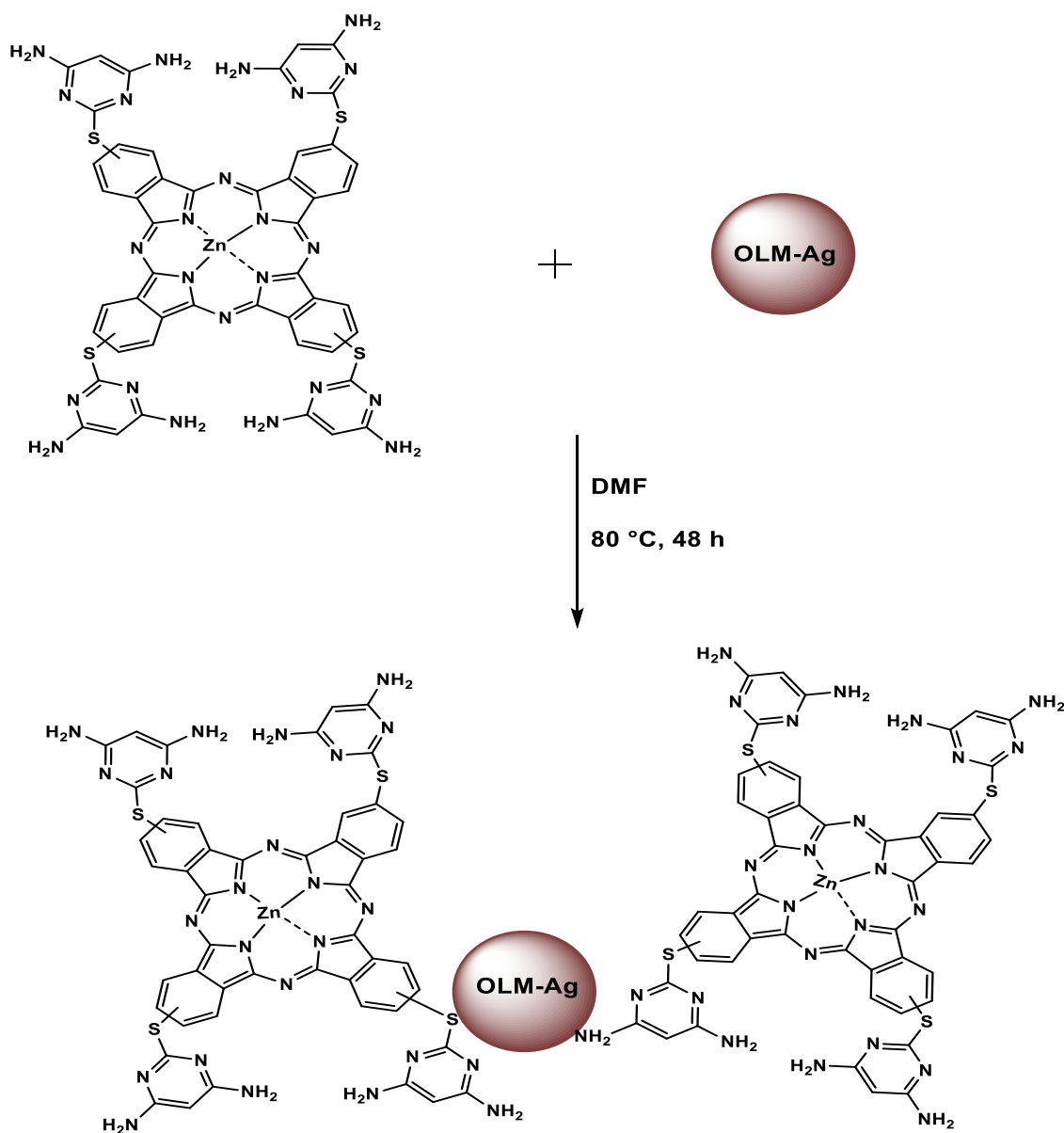
With the aim of adopting properties from both the Ag NPs and magnetic NPs, composite NPs were synthesised. As demonstrated in **Scheme 3.6**, the TEOS stabilised magnetic NPs (Si-Fe<sub>3</sub>O<sub>4</sub>) were used as a canvas for making of the Ag NPs which were then further functionalised with amine groups using cysteamine.



**Scheme 3.6:** Synthesis of cysteamine capped core-shell composite (Cys-Fe<sub>3</sub>O<sub>4</sub>@Ag NPs).

### 3.2.2 Chemisorption of complexes 1-3 to OLM-Ag NPs

The method of conjugation of complexes **1-3** to the OLM-Ag NPs *via* chemisorption is depicted in **Scheme 3.7** (using complex **1** as an example). The chemisorption method takes advantage of the loosely bound OLM being replaced by the Pc through Ag-S and Ag-N bond formation.



**Scheme 3.7:** Chemisorption of complex **1** on OLM-Ag NPs.

### 3.2.2.1 Transmission Electron Microscopy (TEM)

The sizes, dispersion and shapes of the NPs and their respective conjugates were analysed using TEM. As shown in **Figure 3.7**, the OLM-Ag NPs are well dispersed spheres while the conjugates (using **3-Ag** as an example) show slight aggregation. This can be attributed to the interaction of Pcs on neighbouring NPs through  $\pi - \pi$  bonding. The sizes of the NPs and conjugates are listed in **Table 3.2** and they show that the conjugates are bigger in size than the individual NPs, which is proof of efficient anchoring of the Pcs on the surface of the NPs.

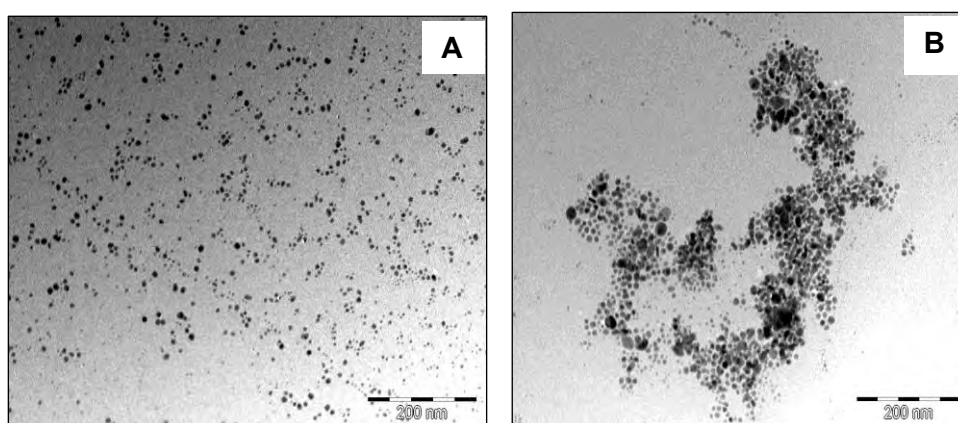


**Figure 3.7:** TEM images of (A) OLM-Ag NPs and (B) **3-Ag**.

### 3.2.2.2 X-ray Diffraction (XRD)

As shown in **Figure 3.8**, the diffraction pattern of the OLM-Ag NPs shows crystalline behaviour with characteristic diffraction peaks at  $2\theta$  values of  $38.03^\circ$ ,  $44.27^\circ$ ,  $64.42^\circ$ ,  $77.16^\circ$  and  $81.44^\circ$  corresponding to hkl Miller indices of (111), (200), (220), (311) and (222), respectively. The diffraction pattern therefore corresponds to the faced-centred cubic structure of metallic silver [188]. Using **3-Ag** as an example, the crystalline nature of the OLM-Ag NPs is maintained in the conjugates with an additional broad peak at  $2\theta = 26.13^\circ$  attributed to the amorphous character of Pcs as reported before [189].

The results therefore show that the conjugates possess combined amorphous and crystalline character. The same patterns were observed for **1-Ag** and **2-Ag** (not shown).

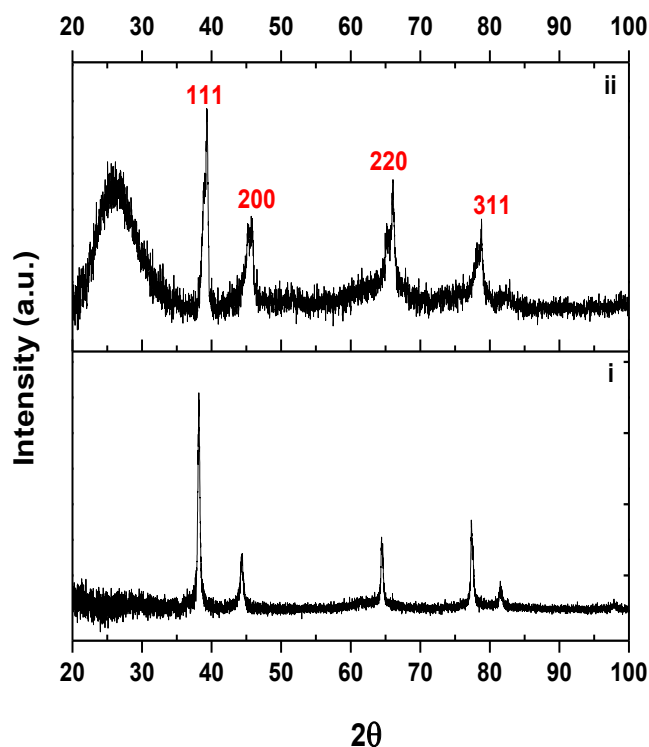


**Figure 3.8:** XRD pattern of (i) OLM-Ag and (ii) **3-Ag**.

### 3.2.2.3 Ground state UV-vis spectroscopy

As shown in **Figure 3.9 A (insert)**, the spectrum of the OLM-Ag NPs shows a distinct absorption band at 410 nm (**Table 3.2**) due to the surface plasmon resonance (SPR) of the metallic silver. Using the conjugates of the novel complexes **2** and **3** as examples, the absorption spectra of **2-Ag** and **3-Ag** are shown in **Figures 3.9 A** and **B**, respectively alongside those of their respective Pcs for comparison. The spectra reveal that conjugation of the Pcs to the Ag NPs does not affect their Q band maxima but the spectra of the conjugates do show an enhancement in absorption in the SPR

band region. A similar spectrum was observed for 1-Ag (not shown). The Q band maxima of the conjugates are listed in **Table 3.1**.

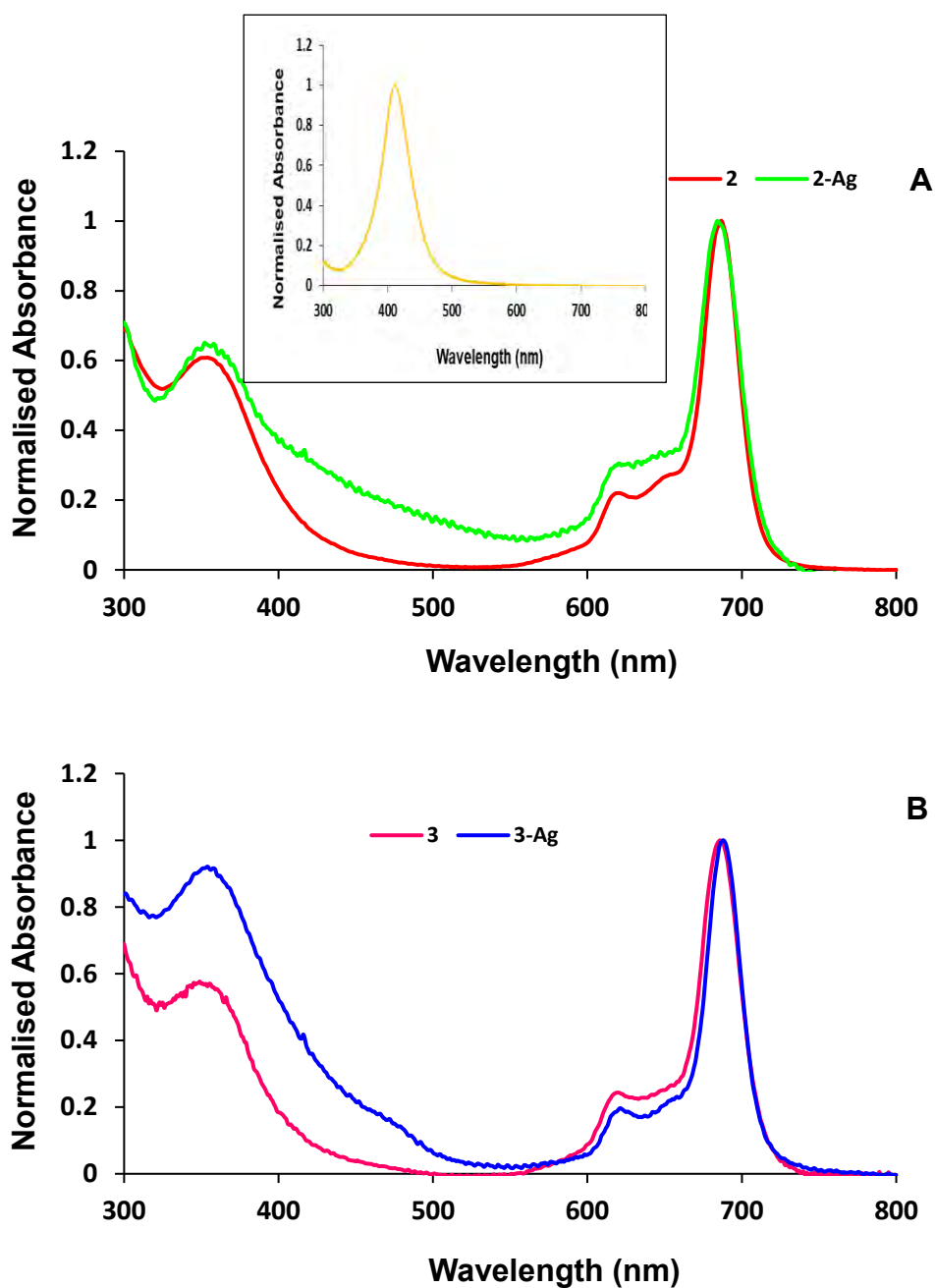


**Figure 3.9:** Ground state UV-vis spectra of (A) complexes 2 and 2-Ag (Insert = Absorption spectra of OLM-Ag NPs) as well as (B) complexes 3 and 3-Ag in DMSO.

### 3.2.2.4 X-ray photoelectron spectroscopy (XPS)

X-ray photoelectron spectroscopy (XPS) analysis was conducted to validate efficient anchoring of the Pcs on the surface of the OLM-Ag NPs. Complex **2** has both nitrogen and sulfur atoms available for bonding with the Ag NPs, hence it was used as an example.

As shown in **Figure 3.10**, the deconvoluted N 1s spectrum of complex **2** shows three peaks at 397.4 eV (N-C), 399.0 eV (N-H) and 399.8 eV (N-Zn). The deconvolution of the N1s spectrum of **2**-Ag however shows four peaks at 387.9 eV (N-C), 390.9 eV (N-H), 394.9 eV (N-Zn) and 399.5 eV (N-Ag). The shift in the binding energies of the various peaks in the conjugate relative to the Pc as well as the appearance of a new peak in the conjugate is an indication that the lone pair electrons of the nitrogen atoms in the terminal amine groups of the Pc take part in the chemisorption of the Pc onto the Ag NPs.

To prove that the sulfur atoms also interact with the Ag NPs, deconvolution of the S 2p spectra of complexes **2** and **2**-Ag was conducted. The spectrum of complex **2** was deconvoluted to two peaks at 161.4 eV (S-C) and 162.6 eV (S) while that of **2**-Ag was deconvoluted to three peaks 161.7 eV (S-C), 162.9 eV (S) and 165.9 eV (S-Ag). The emergence of the new peak in **2**-Ag relative to complex **2** alone is an indication of successful interaction of the Pc with the NPs using the sulfur atom.

Similar results were obtained for complexes **1** and **3** (not shown) where the former was found to interact using both nitrogen and sulfur atoms with the OLM-Ag NPs while the latter only interacts using sulfur due to quaternization of all of its nitrogen atoms.

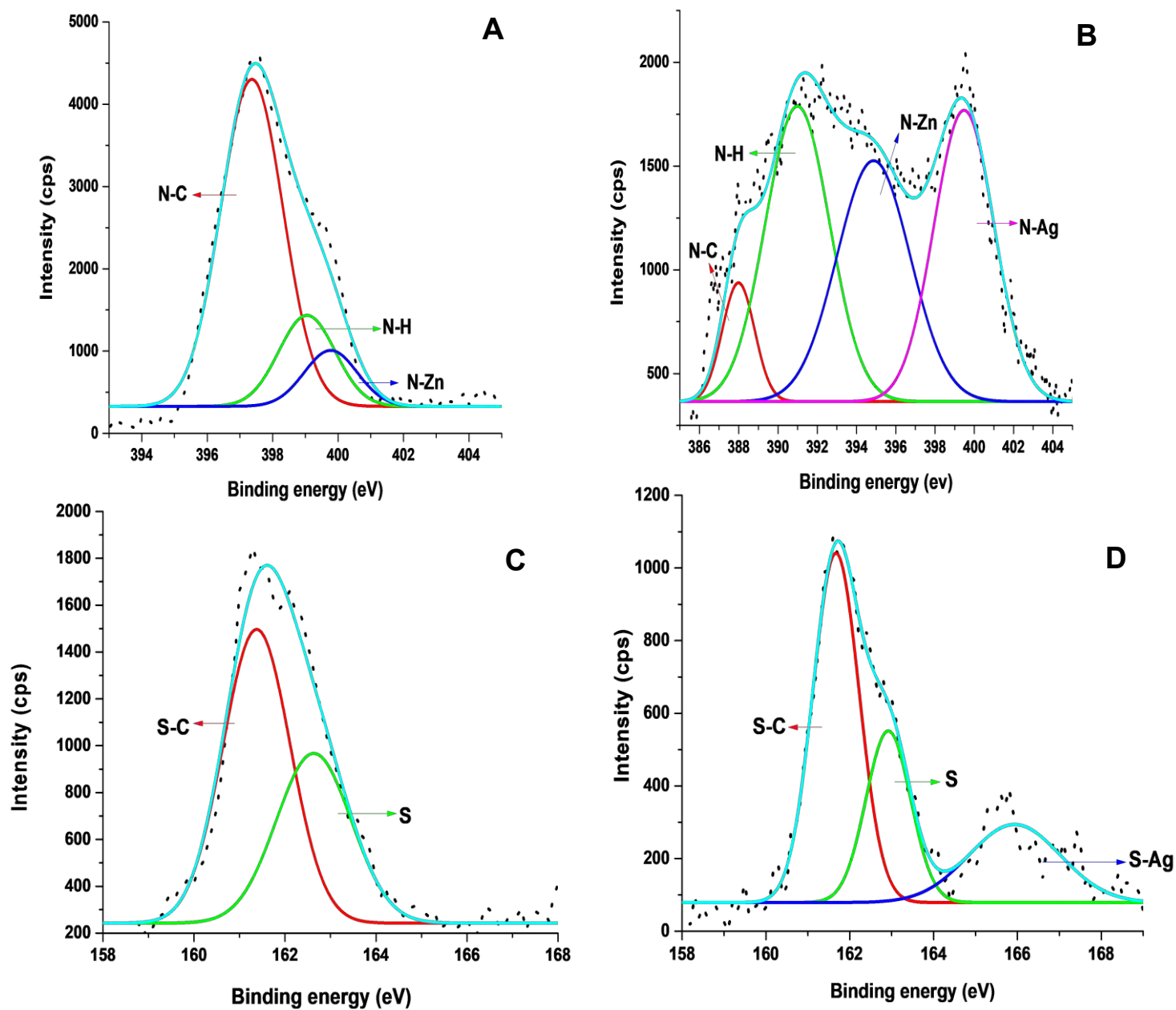


**Figure 3.10:** XPS High resolution N 1s spectra of (A) complex 2, (B) 2-Ag, and S 2p spectra of (C) complex 2, (D) 2-Ag.

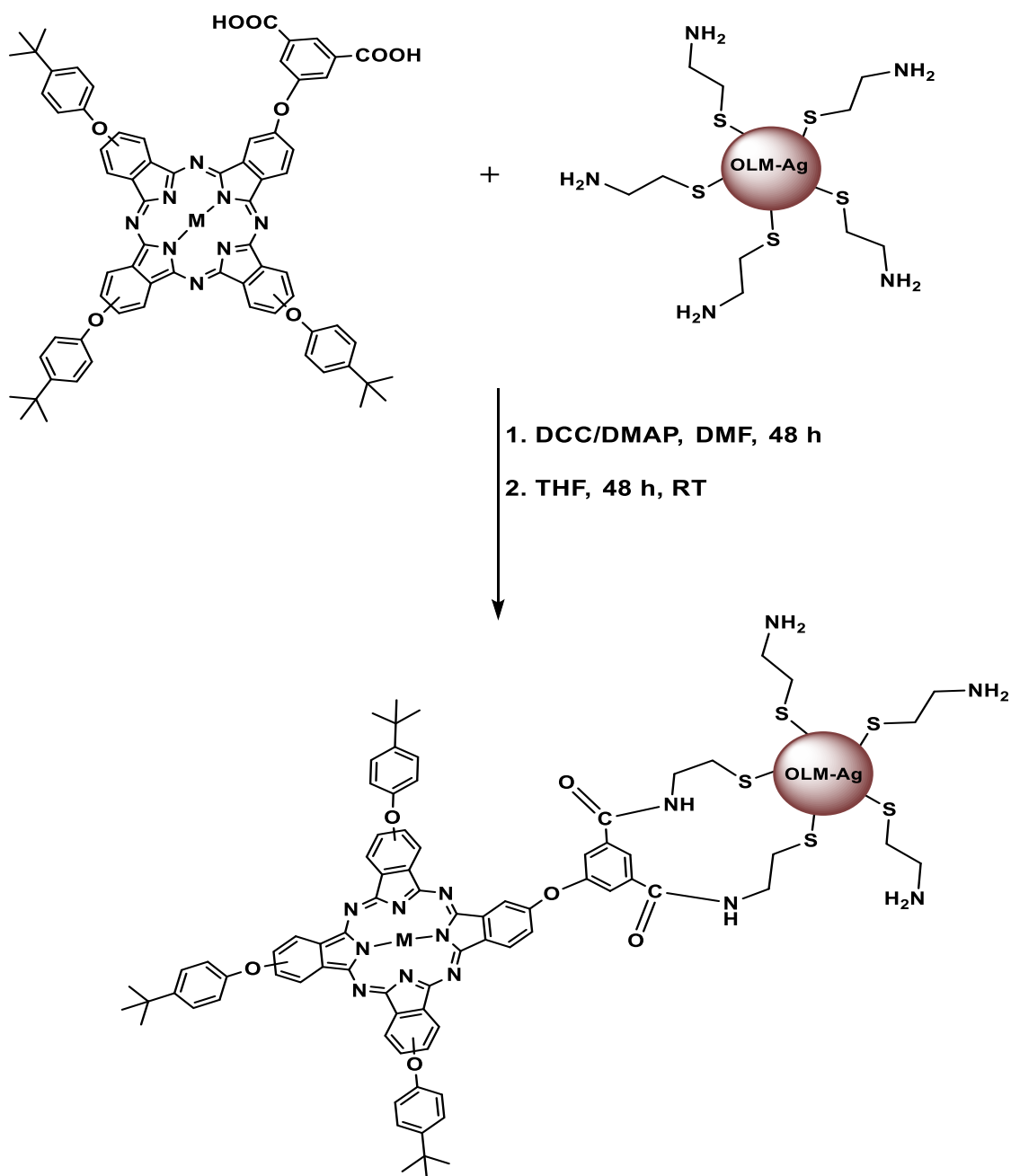
**Table 3.2:** Properties of NPs and their respective conjugates

<b>NPs/ nanoconjugate</b>	<b>TEM Sizes (nm)</b>	<b>Loading NP: Pc</b>	<b>NP Absorbance (nm)</b>
OLM-Ag NPs	12.08 ± 2.51	-	410
1-Ag	30.05 ± 3.52	1:7	-
2-Ag	26.01 ± 2.46	1:5	-
3-Ag	18.05 ± 1.56	1:3	-
Cys-Ag NPs	15.40 ± 1.29	-	430
4-Ag	20.40 ± 2.40	1:2	-
5-Ag	22.20 ± 1.65	1:3	-
6-Ag	21.90 ± 1.27	1:3	-
NH <sub>2</sub> -Fe <sub>3</sub> O <sub>4</sub> NPs	12.30 ± 3.25	-	-
4-Fe <sub>3</sub> O <sub>4</sub>	14.50 ± 1.75	1:2	-
5-Fe <sub>3</sub> O <sub>4</sub>	15.02 ± 1.02	1:4	-
6-Fe <sub>3</sub> O <sub>4</sub>	14.95 ± 2.02	1:3	-
Cys-Fe <sub>3</sub> O <sub>4</sub> @Ag NPs	17.10 ± 1.85	-	417
4-Fe <sub>3</sub> O <sub>4</sub> @Ag	22.50 ± 1.25	1:4	-
5-Fe <sub>3</sub> O <sub>4</sub> @Ag	26.50 ± 1.32	1:5	-
6-Fe <sub>3</sub> O <sub>4</sub> @Ag	25.95 ± 2.45	1:5	-



### 3.2.3 Covalent conjugation of complexes 4-6 to Cys-Ag, NH<sub>2</sub>-Fe<sub>3</sub>O<sub>4</sub> and Cys-Fe<sub>3</sub>O<sub>4</sub>@Ag NPs

The method of covalent conjugation of complexes 4-6 to the various amine functionalised NPs via amide bond formation is depicted in **Scheme 3.8** (using conjugation of complex 4 to the Cys-Ag NPs as an example).



**Scheme 3.8:** Amide bond linkage of complex 4 to Cys-Ag NPs resulting in 4-Ag.

### 3.2.3.1 Transmission Electron Microscopy (TEM)

The sizes, dispersion and shapes of the NPs and their respective conjugates were analysed using TEM. As shown in **Figure 3.11**, the Cys-Ag NPs are well dispersed spheres while the  $\text{NH}_2\text{-Fe}_3\text{O}_4$  NPs are aggregated spheres due to their superparamagnetic nature. The image of the Cys- $\text{Fe}_3\text{O}_4\text{@Ag}$  NPs shows that the NPs are also spherical and well dispersed. The larger size (**Table 3.2**) and good dispersion of the Cys- $\text{Fe}_3\text{O}_4\text{@Ag}$  NPs is an indication of efficient coating of the  $\text{Si-Fe}_3\text{O}_4$  NPs with Ag.

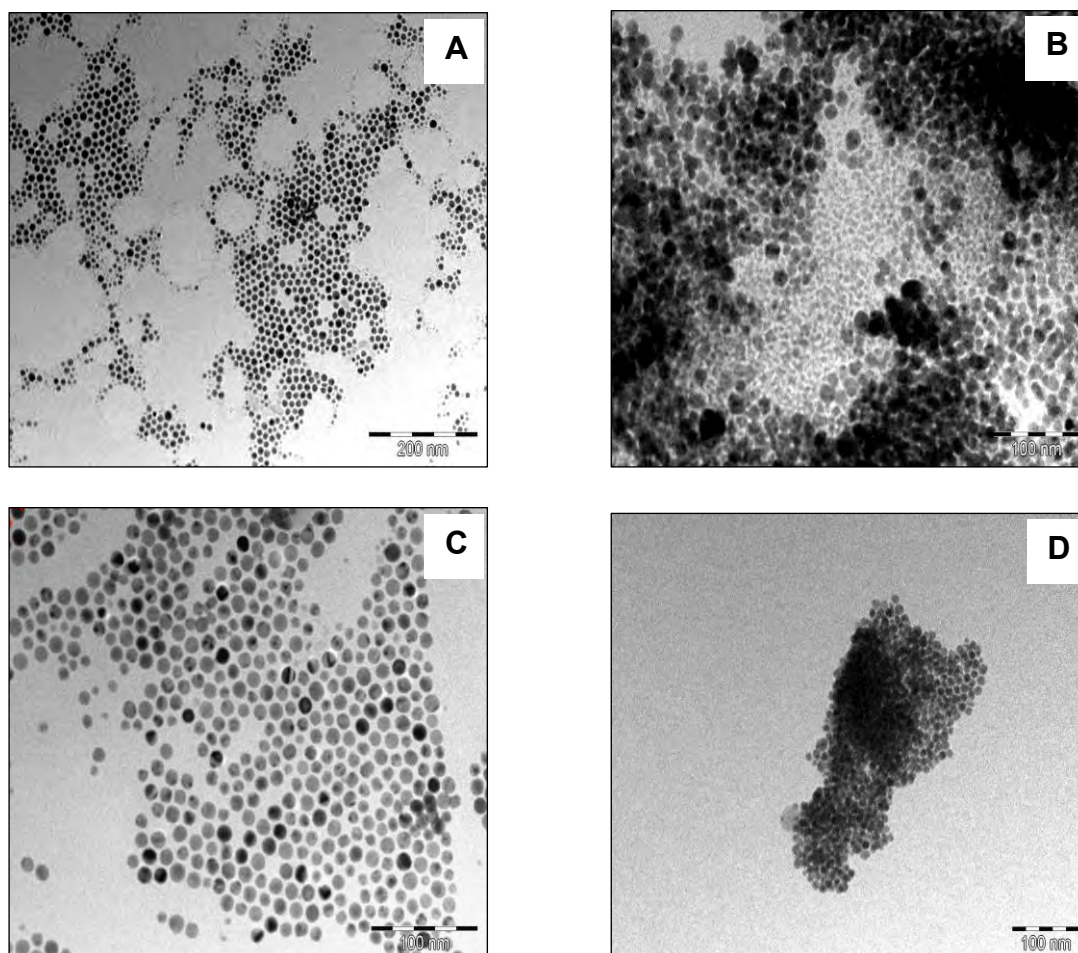


**Figure 3.11:** TEM images of (A) Cys-Ag NPs, (B)  $\text{NH}_2\text{-Fe}_3\text{O}_4$  NPs, (C) Cys- $\text{Fe}_3\text{O}_4\text{@Ag}$  NPs and (D)  $4\text{-Fe}_3\text{O}_4\text{@Ag}$ .

Amide bond linkage of the Pc to the NPs resulted in aggregated conjugates. This is shown in **Figure 3.11 D** (using 4-Fe<sub>3</sub>O<sub>4</sub>@Ag as an example) where the superparamagnetic nature of the NPs and interaction of Pcs on neighbouring NPs resulted in aggregates. The sizes of the NPs and their respective conjugates are listed in **Table 3.2**.

### 3.2.3.2 X-ray Diffraction (XRD)

The XRD patterns of the different NPs and conjugates (using NH<sub>2</sub>-Fe<sub>3</sub>O<sub>4</sub> NPs and 4-Fe<sub>3</sub>O<sub>4</sub> as examples) are shown in **Figure 3.12**.

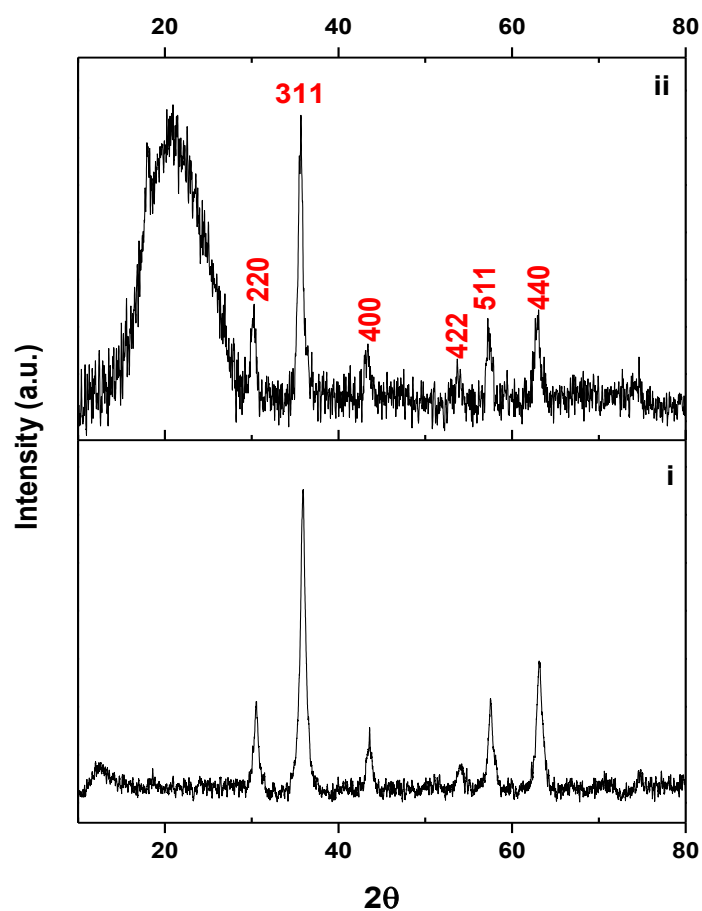


**Figure 3.12:** XRD patterns of (i) NH<sub>2</sub>-Fe<sub>3</sub>O<sub>4</sub> NPs and (ii) 4-Fe<sub>3</sub>O<sub>4</sub>.

The diffraction pattern of the  $\text{NH}_2\text{-Fe}_3\text{O}_4$  NPs shows a crystalline phase with a series of characteristic peaks at  $2\theta$  values of  $30.38^\circ$ ,  $35.77^\circ$ ,  $43.41^\circ$ ,  $54.20^\circ$ ,  $57.60^\circ$  and  $63.28^\circ$  corresponding to hkl Miller indices of (220), (311), (400), (422), (511), and (440), respectively. These peaks are in accordance with the inverse cubic spinel phase of magnetite [190]. For **4**- $\text{Fe}_3\text{O}_4$ , the crystalline peaks of the  $\text{NH}_2\text{-Fe}_3\text{O}_4$  NPs are preserved with an additional amorphous peak at  $2\theta = 22.30^\circ$  due to the Pc. Similar changes were observed for the other conjugates.

### 3.2.3.3 Ground state UV-vis spectroscopy

The normalised absorption spectra of the NPs are shown in **Figure 3.13 A**. The spectra reveal distinct absorption bands at 430 and 417 nm for the Cys-Ag and Cys- $\text{Fe}_3\text{O}_4\text{@Ag}$  NPs, respectively attributed to the SPR band of the metallic silver, **Table 3.2**. No distinct absorption band is observed for the  $\text{NH}_2\text{-Fe}_3\text{O}_4$  NPs. As shown in **Figure 3.13 B**, the spectra of the covalently bonded conjugates show an enhancement in the absorption below 600 nm relative to that of the Pc alone (using complex **4** as an example) due to the presence of the NPs which absorb around that region. The **4**-Ag and **4**- $\text{Fe}_3\text{O}_4\text{@Ag}$  conjugates show distinct peaks at  $\sim 420$  nm attributed to the SPR band of Ag, thereby proving that the conjugates are indeed composites of the NPs and Pcs. Similar spectra were observed for the conjugates of complexes **5** and **6** (not shown). As shown in **Table 3.1**, negligible changes in the Q band maxima of all the conjugates were observed relative to Pcs alone.

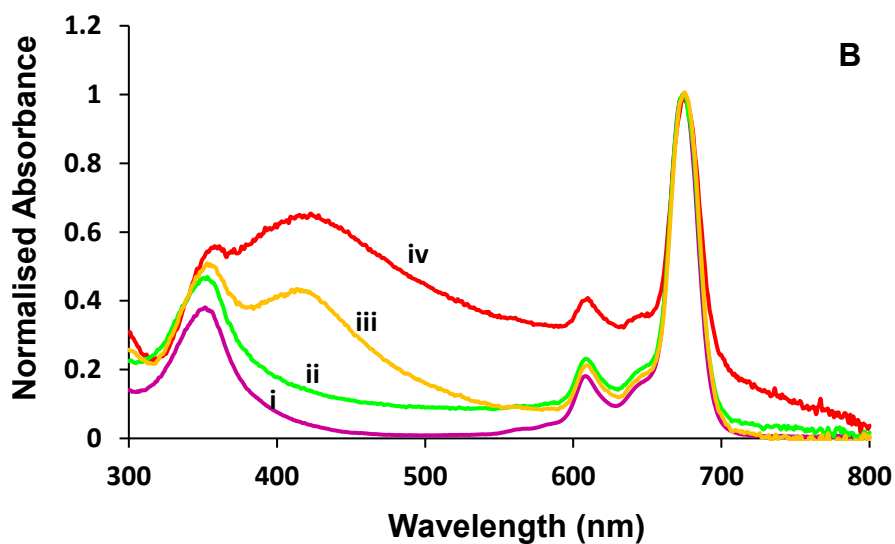
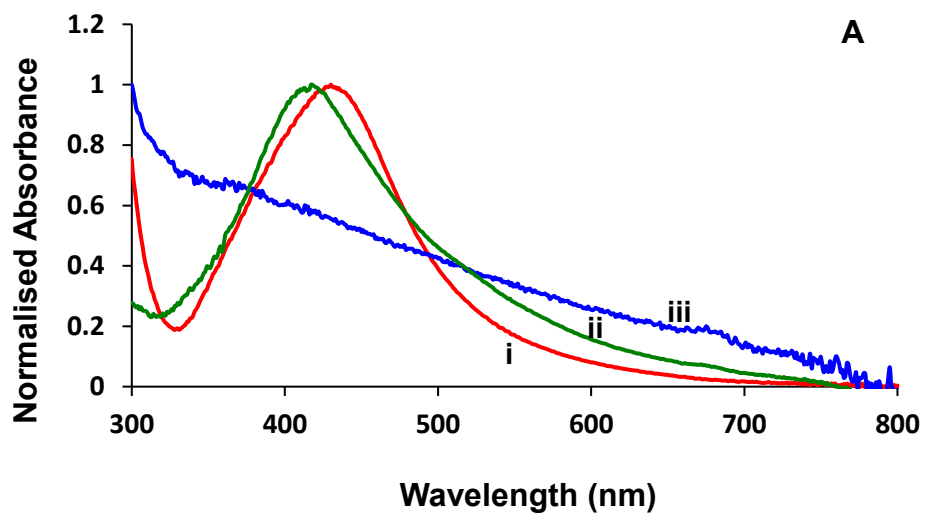


**Figure 3.13:** Ground state UV-vis spectra of (A) i. Cys-Ag NPs, ii. Cys-Fe<sub>3</sub>O<sub>4</sub>@Ag NPs and iii. NH<sub>2</sub>-Fe<sub>3</sub>O<sub>4</sub> NPs and (B) (i) complex **4**, (ii) **4**-Fe<sub>3</sub>O<sub>4</sub> (iii) **4**-Ag and (iv) **4**-Fe<sub>3</sub>O<sub>4</sub>@Ag in DMSO.

### 3.2.3.4 X-ray photoelectron spectroscopy (XPS)

Efficient amide bond formation between each of the Pcs and the different NPs was confirmed using XPS as shown in **Figure 3.14** (using complex **4** and its conjugates as examples).

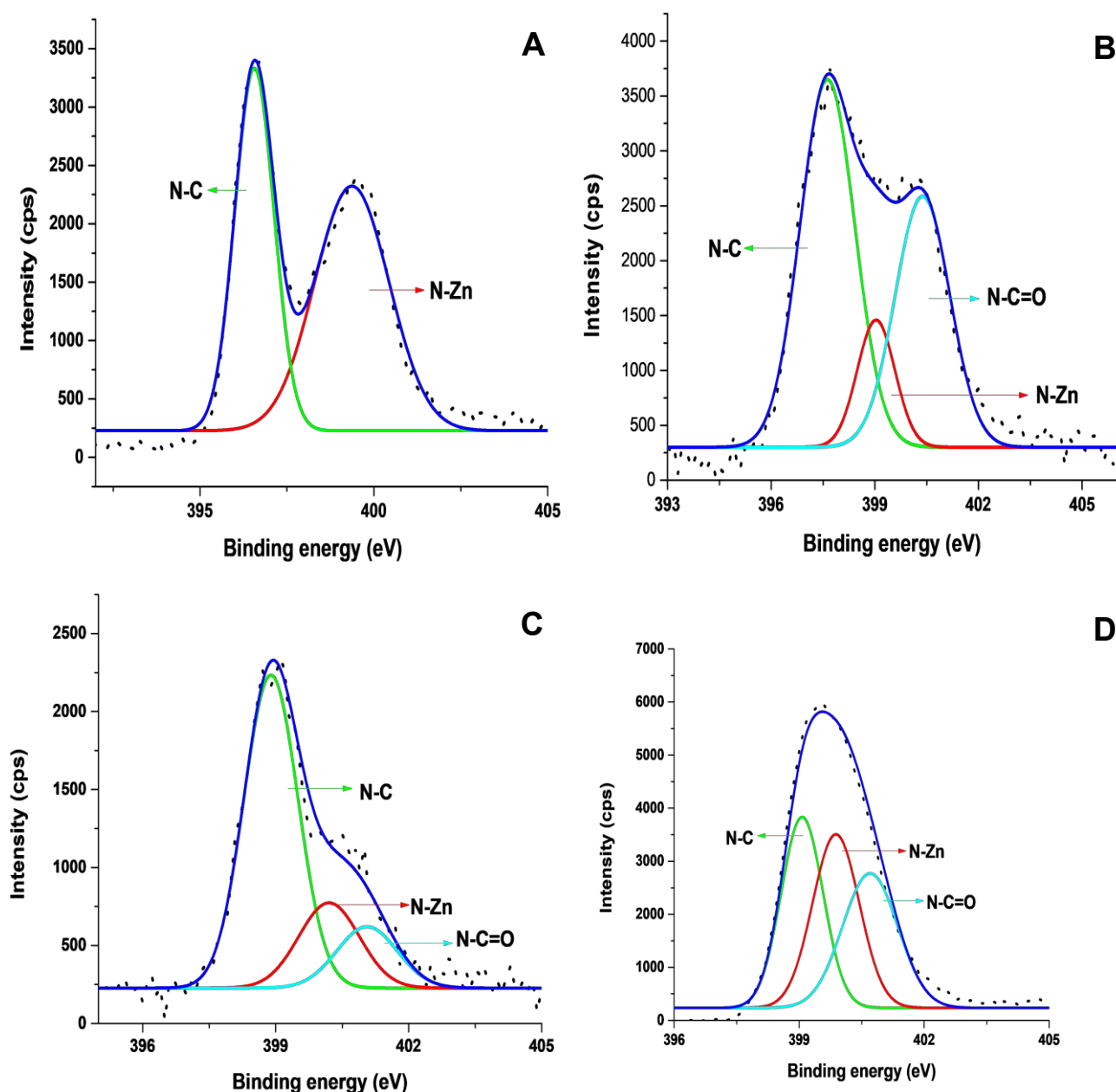


**Figure 3.14:** High resolution XPS (N1s) of (A) **4**, (B) **4-Ag** and (C) **4-Fe<sub>3</sub>O<sub>4</sub>** and (D) **4-Fe<sub>3</sub>O<sub>4</sub>@Ag**.

The deconvoluted N 1s spectrum of complex **4** shows two peaks at 397.4 eV (N-C) and 399.8 eV (N-Zn). The N 1s spectra of the conjugates however were deconvoluted to three components with the component at high binding energy (~401 eV) being representative of the N-C=O bond. This is proof of efficient amide bond formation between the Pc and each of the NPs. Similar spectra were observed for complexes **5** and **6** as well as their respective conjugates (not shown).

### 3.3 Loading of Pcs on NPs

Pcs have a size of ~1 nm while the NPs are all much bigger as shown in **Table 3.2**. It is therefore unlikely for more than one NP to be attached to a single Pc but it is possible for more than one Pc to be conjugated to a single NP. The ratio of Pc molecules bonded to each of the NPs were determined using absorption as reported before [191]. This entails comparing the Q band absorbance intensity of the Pc in the conjugates with that of the Pc alone using the same mass of the compounds. The NP: Pc ratios for the conjugates are listed in **Table 3.2**.

The loading of Pcs onto the OLM-Ag NPs was found to be higher for **1-Ag** than **2-Ag** and **3-Ag**. The higher loading of complex **1** onto Ag NPs compared to complex **2** could be due to the latter having less site of attachment to the Ag NPs as the quaternized nitrogen atoms are not available for coordination. This explains the even lower loading of the complex **3** on the OLM-Ag NPs as none of the nitrogen atoms are available and it is solely dependent on the sulfur for coordination to the OLM-Ag NPs.

The loadings of complexes **4-6** on each of the NPs shows that complex **4** has the lowest loading on all the NPs. This could be attributed to the bulky substituents of the Pc which can hinder efficient amide bond formation between numerous Pcs and the NPs unlike the less sterically challenged complexes **5** and **6**.

Since the *in situ* Ag NPs, Pd and Co NPs were made for modification of NFs and not conjugated to Pcs in solution, their characterisation is discussed together with that of the NFs in Chapter 4.

### 3.4 Closing Remarks

Novel cationic (complexes **2** and **3**) and asymmetrical (complexes **4** and **5**) Pcs were successfully synthesized and characterized by various microscopic and spectroscopic techniques. A variety of NPs (OLM-Ag, Cys-Ag, NH<sub>2</sub>-Fe<sub>3</sub>O<sub>4</sub> and Cys-Fe<sub>3</sub>O<sub>4</sub>@Ag) were also successfully synthesised and characterised. Complexes **1** to **3** were successfully conjugated to the OLM-Ag NPs *via* chemisorption while complexes **4-6** were covalently conjugated to the Cys-Ag, NH<sub>2</sub>-Fe<sub>3</sub>O<sub>4</sub> and Cys-Fe<sub>3</sub>O<sub>4</sub>@Ag NPs as proven with XPS.



# Chapter 4

This chapter discusses the optical and physical properties of the different electrospun nanofibers when bare and when modified with Pcs, NPs or both.

## 4. Characterisation of electrospun nanofibers

Characterisation of the NFs was conducted so as to elucidate their properties and compositions. The effect of modification of these NFs with Pcs, NPs and their conjugates is also explored. Comparison of the properties of bare SiO<sub>2</sub> NFs relative to their properties after modification with complexes **1-3** and *in situ* Ag NPs are discussed. The properties of semiconductor Hem, ZnO and TiO<sub>2</sub> NFs are also reported. The bare Hem NFs are modified with complexes **4-6** while the ZnO and TiO<sub>2</sub> NFs are modified with complex **6**. The properties of a second batch of TiO<sub>2</sub> NFs prepared at different calcination temperatures and modified with complex **7** as well as *in situ* Pd and Co NPs are also discussed.

### 4.1 SiO<sub>2</sub> NFs

Formation of inorganic SiO<sub>2</sub> NFs through the complete removal of PVP from the NFs by calcination was confirmed using FT-IR spectroscopy. As shown in **Figure 4.1**, the spectrum of the SiO<sub>2</sub> NFs (pre-calcination) shows a series of peaks at 460 (O-Si-O bending), 575 (N-C=O stretch), 958 (Si-OH stretch), 1026 (CH<sub>2</sub> rock), 1290 (C-N stretch), 1421 (C-H bend), 1639 (C=O stretch) and 2930 cm<sup>-1</sup> (C-H stretch) which serves as an indication that the NFs are comprised of both SiO<sub>2</sub> and PVP. In addition, there is a broad peak at 3250 cm<sup>-1</sup> which is due to the surface-adsorbed water and hydroxyl groups on the PVP [**192**].

Post-calcination however, the bare SiO<sub>2</sub> NFs only show peaks at 465 cm<sup>-1</sup> (O-Si-O bend), 810 (Si-O-Si symmetric stretch), 969 (Si-OH stretch), 1054 (Si-O-Si asymmetric stretch) and 3275 cm<sup>-1</sup> (OH stretch; surface water/hydroxyl groups)) as reported before [**193**]. This proves that the bare SiO<sub>2</sub> NFs are purely inorganic as no PVP peaks are observed.

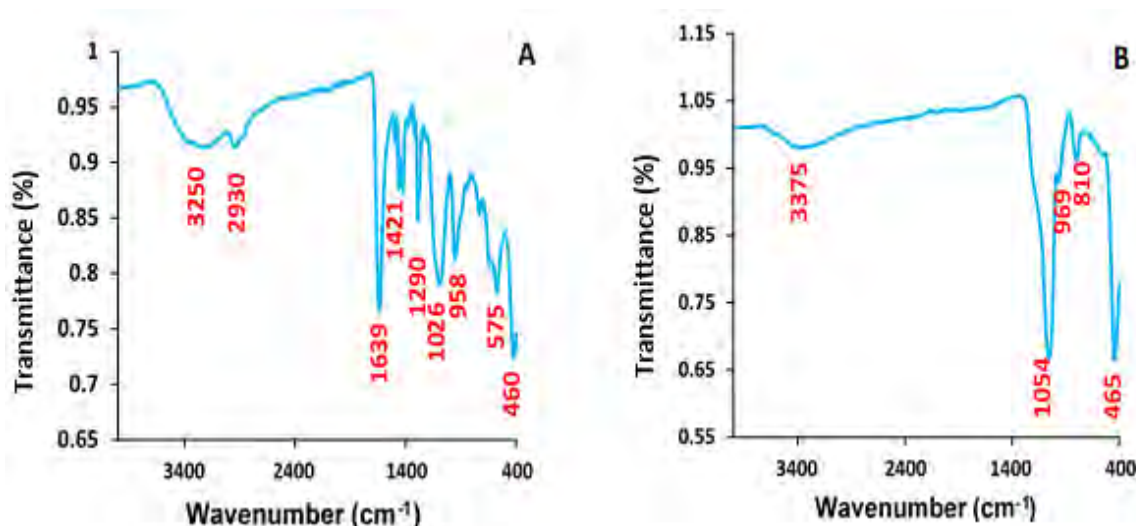


**Figure 4.1:** FT-IR spectra of (A) SiO<sub>2</sub> NFs (pre-calcination) and (B) bare SiO<sub>2</sub> NFs.

TOF-SIMS was used for characterizing the bare and modified SiO<sub>2</sub> NFs in order to confirm complete polymer removal, efficient modification of the NFs as well as distribution of the Pc and NPs on the NFs. Since TOF-SIMS uses a focused bismuth beam to dislodge species on the surface of the NFs, the particles produced closer to the site of impact tend to be dissociated ions (positive or negative) while those generated further from the impact site tend to be molecular compounds [194]. In this work, TOF-SIMS was run in positive ion mode so as to detect positive ions. The acquired secondary ion images are shown in **Figure 4.2** (using NFs modified with complex **1** as an example) depicting the chemical changes on the different NFs. The images reveal that the SiO<sub>2</sub> NFs (pre-calcination) show the dominance of a green colour with bits of red corresponding to mass locations of Si (red m/z 27.96) and PVP fragment (green m/z 93.99). These results therefore confirm that pre-calcination, the NFs are predominantly composed of the PVP. Post-calcination however, the bare SiO<sub>2</sub> NFs show only a red colour attributed to Si (red m/z 27.89) with no visible green PVP fragment representation.

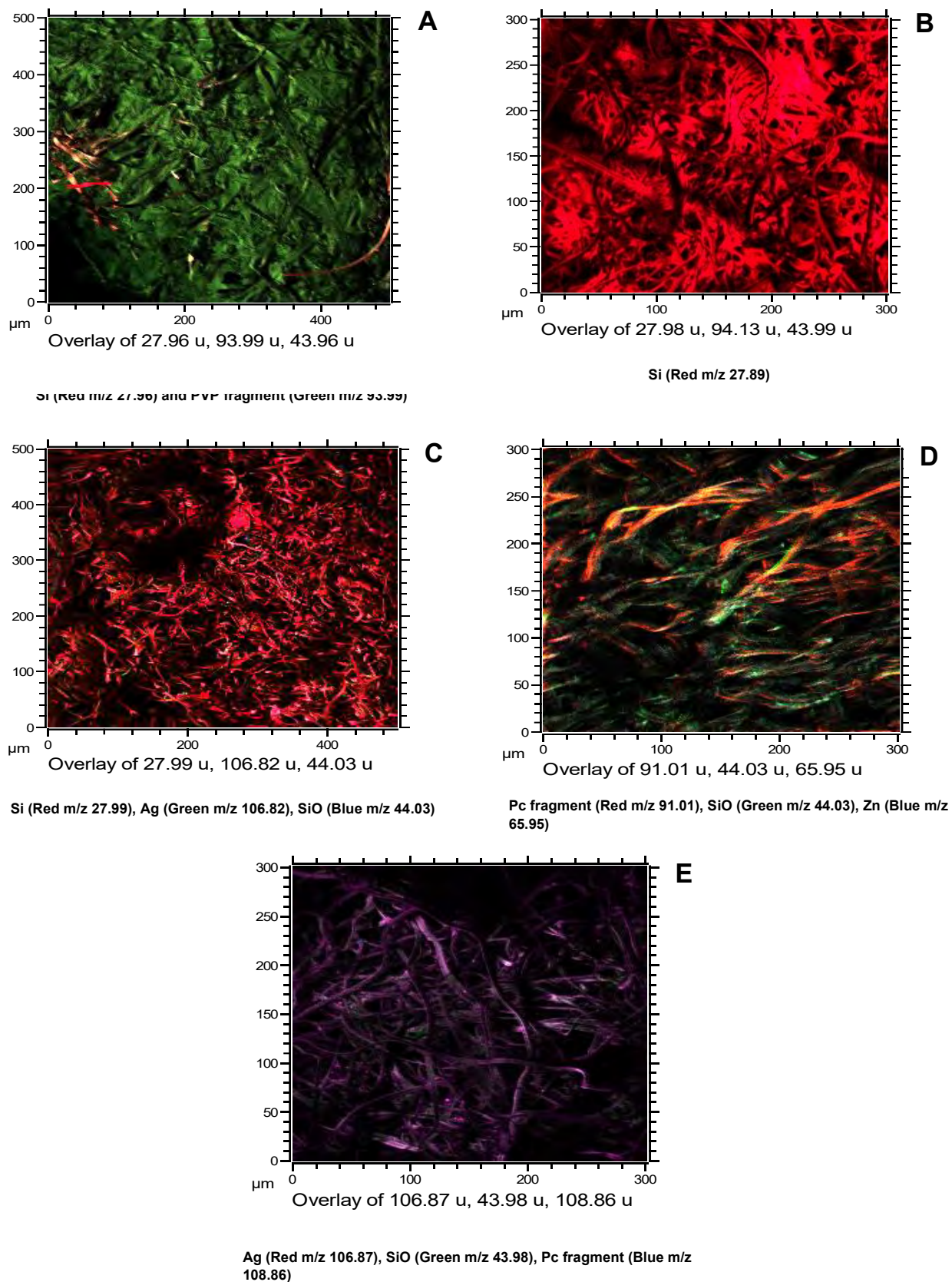


**Figure 4.2:** 2D TOF-SIMS ion images of (A) SiO<sub>2</sub> (pre-calcination), (B) bare SiO<sub>2</sub> (post-calcination), (C) Ag-SiO<sub>2</sub>, (D) 1-SiO<sub>2</sub> and (E) 1@Ag-SiO<sub>2</sub> NFs.

This is therefore confirmation that the bare SiO<sub>2</sub> NFs are purely inorganic as was observed with FT-IR. Efficient modification of the NFs with the Ag NPs is observed as shown in **Figure 4.2 C** which is predominantly red with green and blue specs attributed to mass allocations of Si (red m/z 27.99), Ag (green m/z 106.82) and SiO (blue m/z 44.03). Modification of the SiO<sub>2</sub> NFs with the Pcs was achieved as shown in **Figure 4.2 D** where mass allocations of the Pc fragment (red m/z 91.01), SiO (green m/z 44.03) and Zn (blue m/z 65.95) were observed for the **1**-SiO<sub>2</sub> NFs which is shown as an example. Modification of the NFs with the Pc and Ag NPs to yield the **1@Ag-SiO<sub>2</sub>** NFs was also proven as shown in **Figure 4.2 E** with mass allocations of Ag (red m/z 106.87), SiO (green m/z 43.98), and Pc fragment (blue m/z 108.86). The dominant violet colour on the acquired image is a result of red and blue mixing. This is therefore an indication that complex **1** and the Ag NPs coexist and thus occupy the same areas on the NFs. This is not surprising due to the affinity that Ag has for nitrogen and sulfur which are both present on the Pc. Similar results were obtained for **2**-SiO<sub>2</sub>, **3**-SiO<sub>2</sub>, **1@Ag-SiO<sub>2</sub>** and **2@Ag-SiO<sub>2</sub>** NFs (not shown).

The morphologies and topographies of the bare and modified NFs were determined using SEM as shown in **Figure 4.3** (using bare SiO<sub>2</sub>, Ag-SiO<sub>2</sub> NFs and **1@Ag-SiO<sub>2</sub>** NFs as examples). The images show that the bare NFs are flattened, narrow, coiled and have cylindrical shape. No significant change was observed upon modification of the NFs with the Pc due to the small size and low concentrations used for modification hence the images are not shown. The images of the Ag-SiO<sub>2</sub> and the conjugate NFs (using **1@Ag-SiO<sub>2</sub>** as an example) however show the presence of NPs which are dispersed throughout their surfaces (shown a few with arrows in **Figure 4.3**) due to the successful *in situ* reduction of the silver acetate in forming the NPs. Similar images were obtained for **2@Ag-SiO<sub>2</sub>** and **3@Ag-SiO<sub>2</sub>** NFs (not shown).

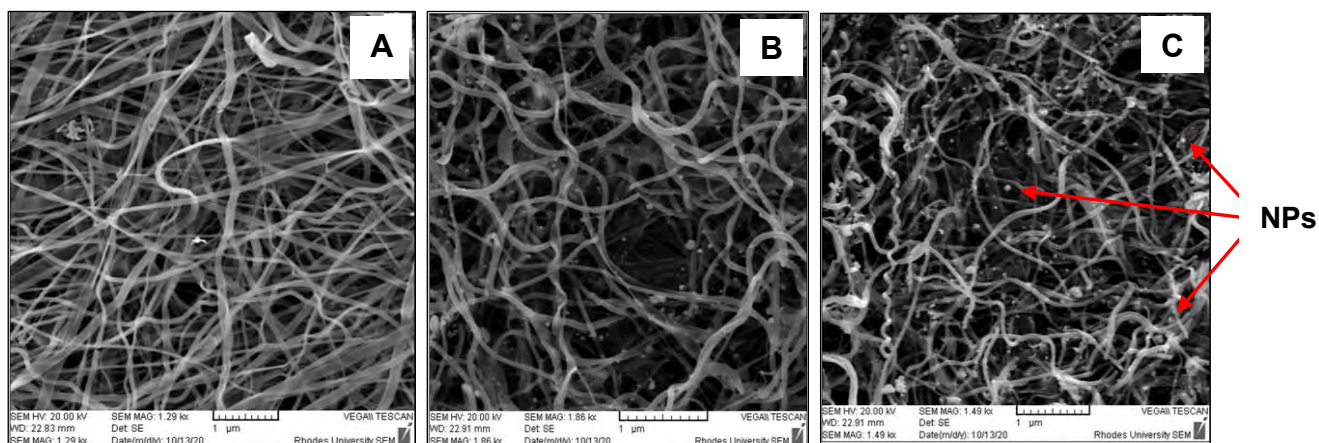


**Figure 4.3:** SEM images of (A) bare SiO<sub>2</sub>, (B) Ag-SiO<sub>2</sub> and (C) 1@Ag-SiO<sub>2</sub> NFs.

Studies of the optical properties of the bare and functionalized SiO<sub>2</sub> NFs were analysed using solid state UV-vis spectra as shown in **Figure 4.4** (using NFs modified with complex **1** as examples). The bare SiO<sub>2</sub> NFs show absorption in the UV region, consistent with results observed before for SiO<sub>2</sub> catalysts [195]. The UV-vis spectra of the 1-SiO<sub>2</sub>, Ag-SiO<sub>2</sub> and 1@Ag-SiO<sub>2</sub> NFs show that this peak is maintained even after modification. In addition, the spectra of the 1-SiO<sub>2</sub> and 1@Ag-SiO<sub>2</sub> NFs bands at ~ 600-750 nm which are attributed to the Q bands of the Pc. In solid state, the Pc Q band is broadened and split due to aggregation [196]. The NFs with Ag NPs (Ag-SiO<sub>2</sub> and 1@Ag-SiO<sub>2</sub> NFs) also show bands at ~ 515-560 nm attributed to the SPR band of Ag NPs [197]. The observed red shift of the SPR band relative to those observed for similar NPs that were analysed in solution (**Table 3.2**) is possibly due to the electronic coupling that occurs when the NPs are aggregated in solid state.

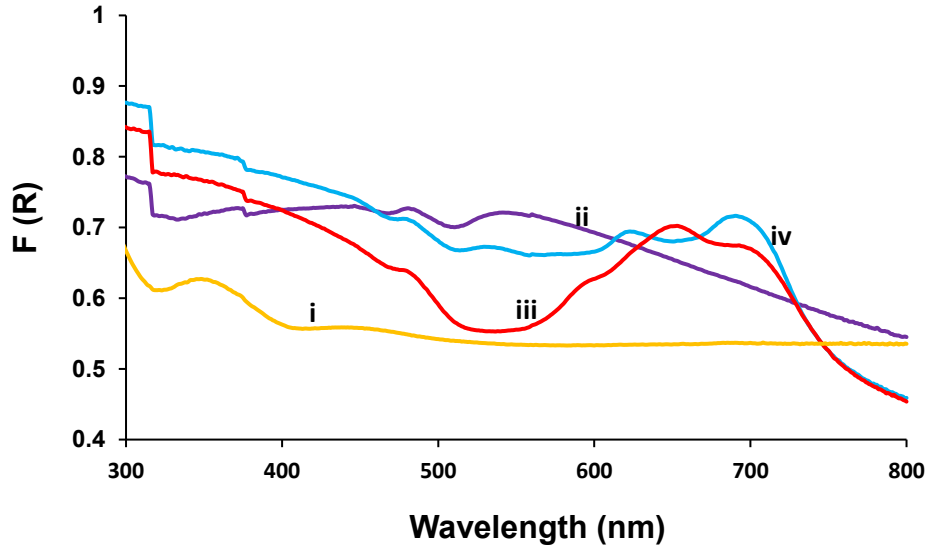


**Figure 4.4:** Solid state UV-vis spectra of i. bare SiO<sub>2</sub>, ii. Ag-SiO<sub>2</sub>, iii. **1**-SiO<sub>2</sub> and iii. **1**@Ag-SiO<sub>2</sub> NFs.

The band gap energies of the bare and modified SiO<sub>2</sub> NFs were calculated using Tauc's equation (4.1) as explained before [198,199].

$$(\alpha h\nu)^{1/n} = k(h\nu - E_g) \quad 4.1$$

where  $\alpha$  is the absorption coefficient,  $h$  is Planck's constant,  $\nu$  is the photon's frequency,  $E_g$  is the band gap and  $k$  is a proportionality constant. The value of  $n$  is the exponent is an indication of the nature of the electronic transition that occurs in the SiO<sub>2</sub> NFs [199]. In this case direct allowed transitions were studied so  $n=1/2$  [198].

The intercept of the linear fit of the Tauc plot as shown in **Figure 4.5** (using NFs modified with complex **1** as examples) gives  $E_g$ . The estimated  $E_g$  values for the bare and modified NFs are listed in **Table 4.1**. The results show that the estimated  $E_g$  for the bare SiO<sub>2</sub> NFs is  $\sim 3.92$  eV (316 nm), similar to values obtained before for amorphous SiO<sub>2</sub> nanowires [200]. The general trend is that upon modification, the  $E_g$

of the SiO<sub>2</sub> NFs is lowered due to the strong interaction between the Pc and/ or NPs with and SiO<sub>2</sub>. Similar Tauc plots were obtained for **2**-SiO<sub>2</sub>, **3**-SiO<sub>2</sub>, **2**@Ag-SiO<sub>2</sub> and **3**@Ag-SiO<sub>2</sub> NFs (not shown) and the obtained results are listed in **Table 4.1**.

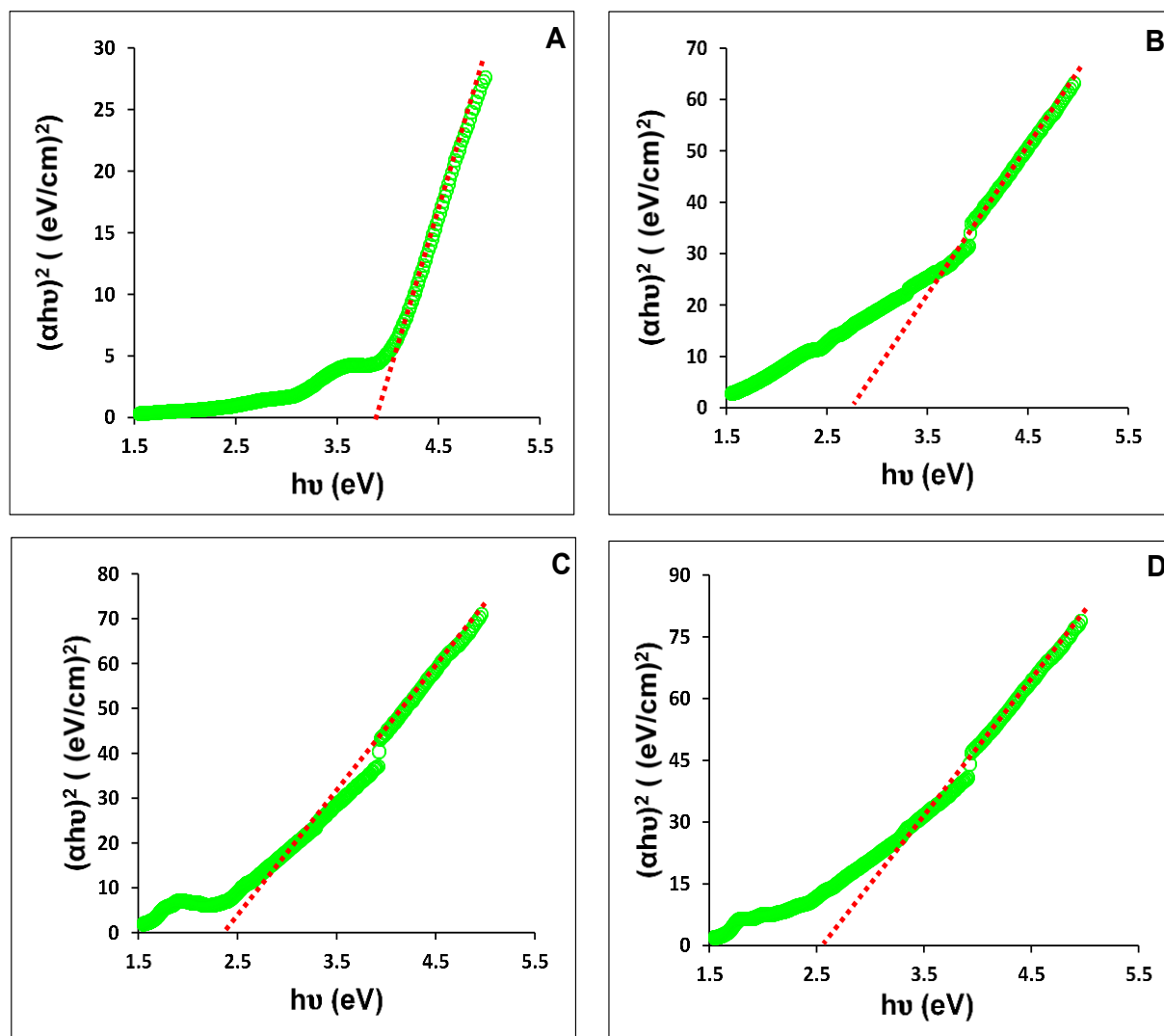


**Figure 4.5:** Tauc plots for the determination of the  $E_g$  of (A) bare SiO<sub>2</sub>, (B) Ag-SiO<sub>2</sub>, (C) 1-SiO<sub>2</sub> and (D) 1@Ag-SiO<sub>2</sub> NFs.



Phase identification of the bare and modified NFs was conducted using XRD as shown in **Figure 4.6** (using NFs modified with complex **1** as examples). The diffraction pattern of the bare SiO<sub>2</sub> NFs has a broad peak at  $\sim 2\theta = 22^\circ$  (**Figure 4.6 A**) which proves that the NFs are amorphous as reported before [28].

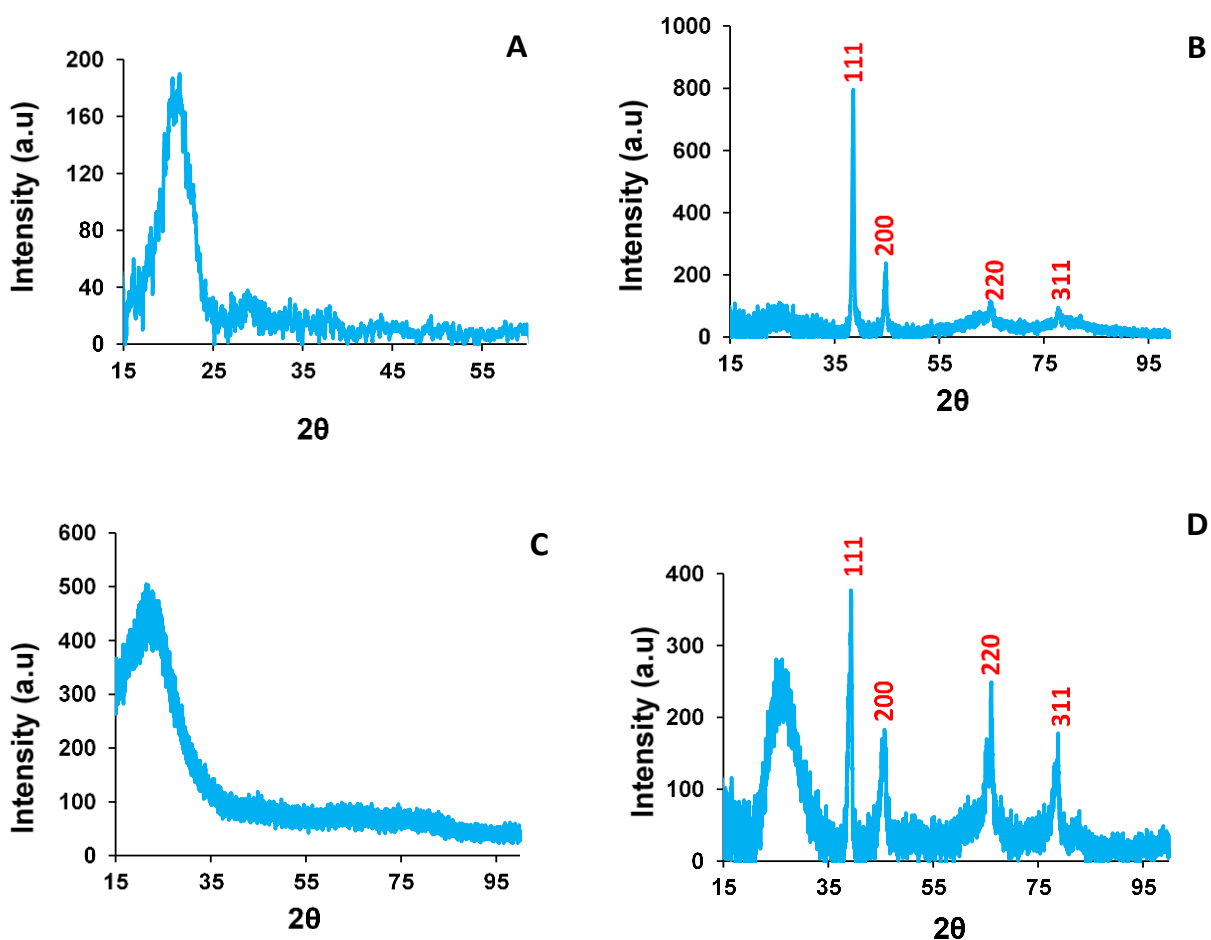


**Figure 4.6:** XRD patterns of (A) bare SiO<sub>2</sub>, (B) Ag-SiO<sub>2</sub>, (C) 1-SiO<sub>2</sub> and (D) 1@Ag-SiO<sub>2</sub> NFs.

The amorphous peak is maintained in the Ag-SiO<sub>2</sub> NFs with additional peaks of the crystalline faced-centred cubic structure of metallic silver (**Figure 4.6 B**). These results therefore prove efficient modification of the surface of the NFs with Ag NPs. Due to

the amorphous nature that Pcs tend to exist in as explained before, no phase changes were observed when the NFs were modified with complex **1** (**Figure 4.6 C**). The diffraction pattern of the **1@Ag-SiO<sub>2</sub>** NFs shows the peaks associated with the Ag NPs are maintained and there's a prominent amorphous peak that is observed due to the presence of both the SiO<sub>2</sub> and Pc (**Figure 4.6 D**). Similar results were observed with the NFs modified with complexes **2** and **3**.

**Table 4.1:** The optical and physical properties of the bare and modified SiO<sub>2</sub> NFs.

Nanofibers	Band gap (eV)	Surface Area m <sup>2</sup> g <sup>-1</sup>	Pore Volume cm <sup>3</sup> g <sup>-1</sup>
Bare SiO <sub>2</sub>	3.92 (316 nm)	301.6	0.1154
Ag-SiO <sub>2</sub>	2.83 (438 nm)	382.4	0.1140
<b>1</b> -SiO <sub>2</sub>	2.48 (500 nm)	365.5	0.0356
<b>1@Ag-SiO<sub>2</sub></b>	2.53 (486 nm)	719.0	0.0049
<b>2</b> -SiO <sub>2</sub>	2.40 (505 nm)	425.5	0.0420
<b>2@Ag-SiO<sub>2</sub></b>	2.50 (490 nm)	725.0	0.0052
<b>3</b> -SiO <sub>2</sub>	2.45 (501 nm)	395.5	0.0039
<b>3@Ag-SiO<sub>2</sub></b>	2.59 (484 nm)	780.0	0.0050

The pore sizes and surface areas of the bare and modified SiO<sub>2</sub> NFs were determined using BET and the obtained results are listed in **Table 4.1**. Modification of the SiO<sub>2</sub> NFs results in an increase in the surface area and decrease in the pore volume. Since rough surfaces have been reported to possess larger surface areas than smooth ones

[201], the observed increase in surface area could possibly suggest that modification of the SiO<sub>2</sub> NFs with the Pcs and NPs causes increased roughness of their surfaces.

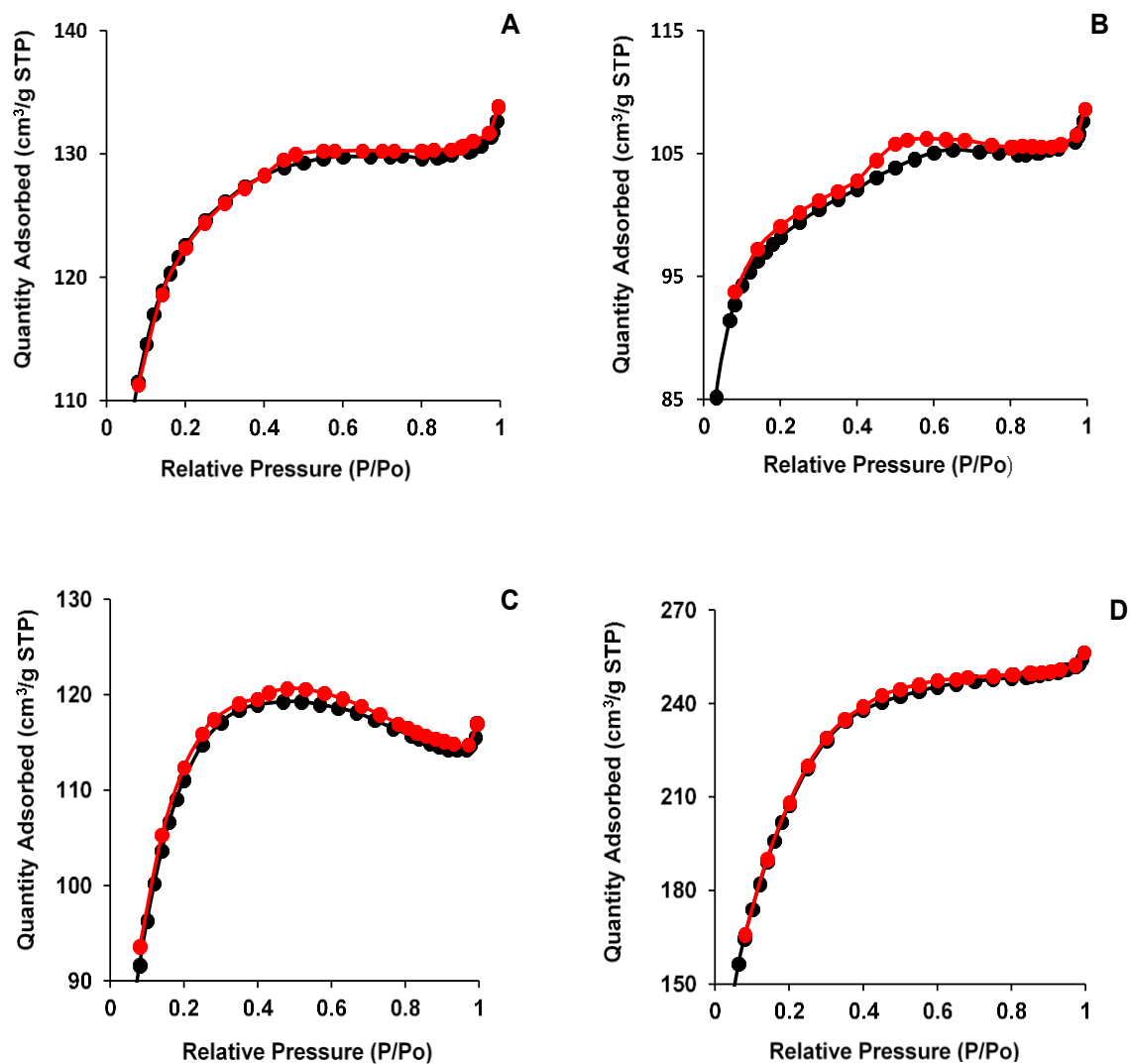


**Figure 4.7:** BET isotherms of (A) bare SiO<sub>2</sub>, (B) Ag-SiO<sub>2</sub>, (C) 1-SiO<sub>2</sub> and (D) 1@Ag-SiO<sub>2</sub> NFs.

The decrease in the pore volumes of the modified NFs can be attributed to the Pc molecules and Ag NPs being entrapped and filling the pores of the NFs.

The BET isotherms of the bare and modified SiO<sub>2</sub> NFs are shown in **Figure 4.7** (using NFs modified with complex **1** as examples).

The results show that all the NFs show type IV BET isotherms with a hysteresis loop consisting of adsorption and desorption branches. This is an indication of the existence of mesopores on the NFs. The type IV isotherms are also an indication of an indefinite multilayer formation after completion of the monolayer followed by a capillary condensation step associated with the hysteresis loop [202,203].

## 4.2 Semiconductor NFs

The Hem NFs were fabricated and modified with Pc complexes **4-6** while the ZnO and TiO<sub>2</sub> NFs were modified with complex **6** without NPs. The second batch of TiO<sub>2</sub> NFs were modified with complex **7** as well as *in situ* synthesised Pd and Co NPs.

### 4.2.1 Hem NFs

Just as with the SiO<sub>2</sub> NFs, formation of the inorganic Hem NFs through complete calcination and thus removal of PVP was confirmed using FT-IR spectroscopy as shown in **Figure 4.8 A**. The Hem NFs show a single peak at 560 cm<sup>-1</sup> correlating to the Fe-O stretch. The absence of polymer peaks is an indication of complete polymer removal resulting in purely inorganic Hem NFs.

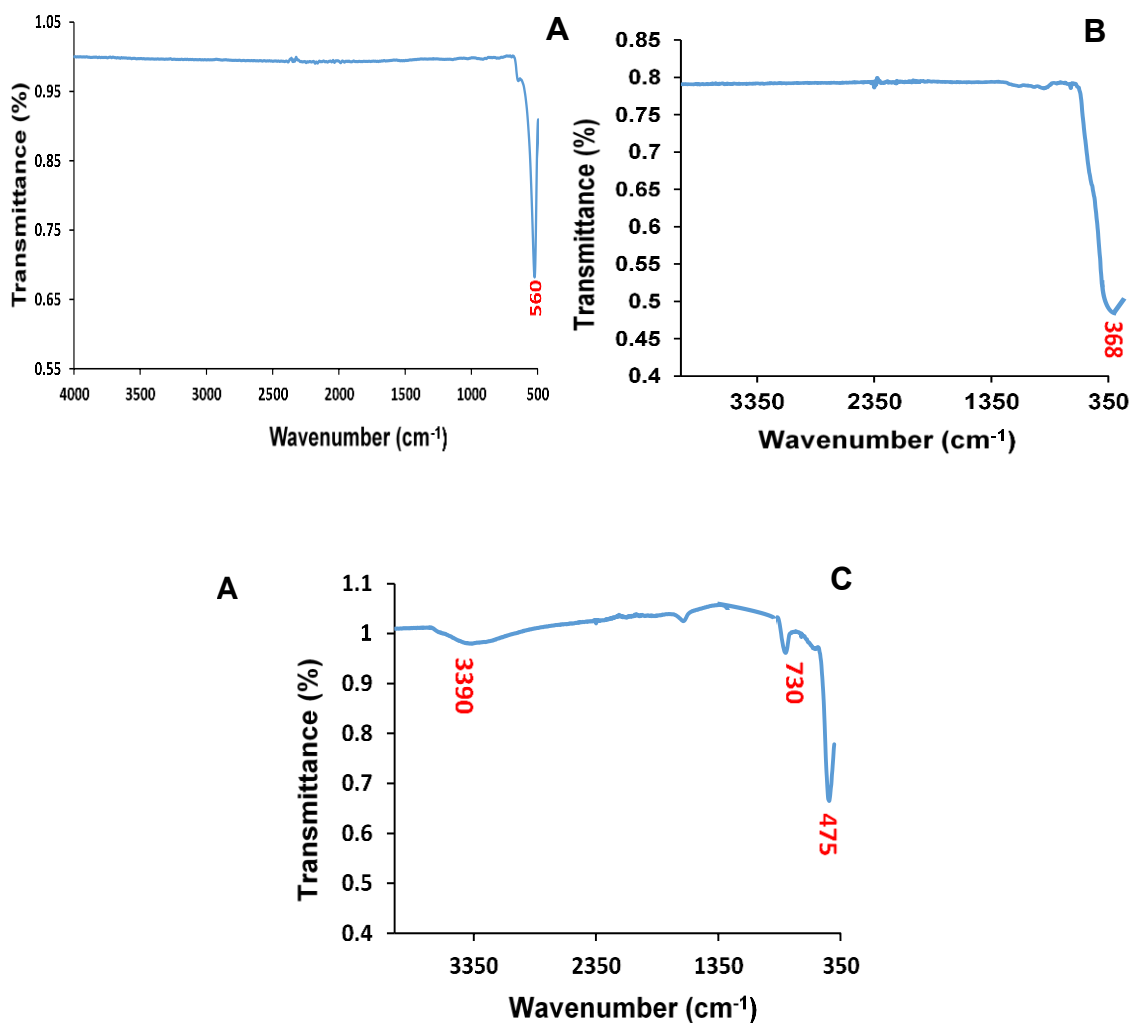


**Figure 4.8:** FT-IR spectra of bare (A) Hem, (B) ZnO and (C) TiO<sub>2</sub> NFs.

The elemental compositions of the bare and modified NFs were confirmed using EDX as shown in **Figure 4.9** (using NFs modified with complex **6** as an example). As expected the bare Hem NFs only show Fe and O peaks (**Figure 4.9 A**) while the **6**-Hem NFs have additional C, N and Zn peaks due to the presence of the Pc (**Figure 4.9 B**). Similar results were observed with the NFs modified with complexes **4** and **5** (not shown).

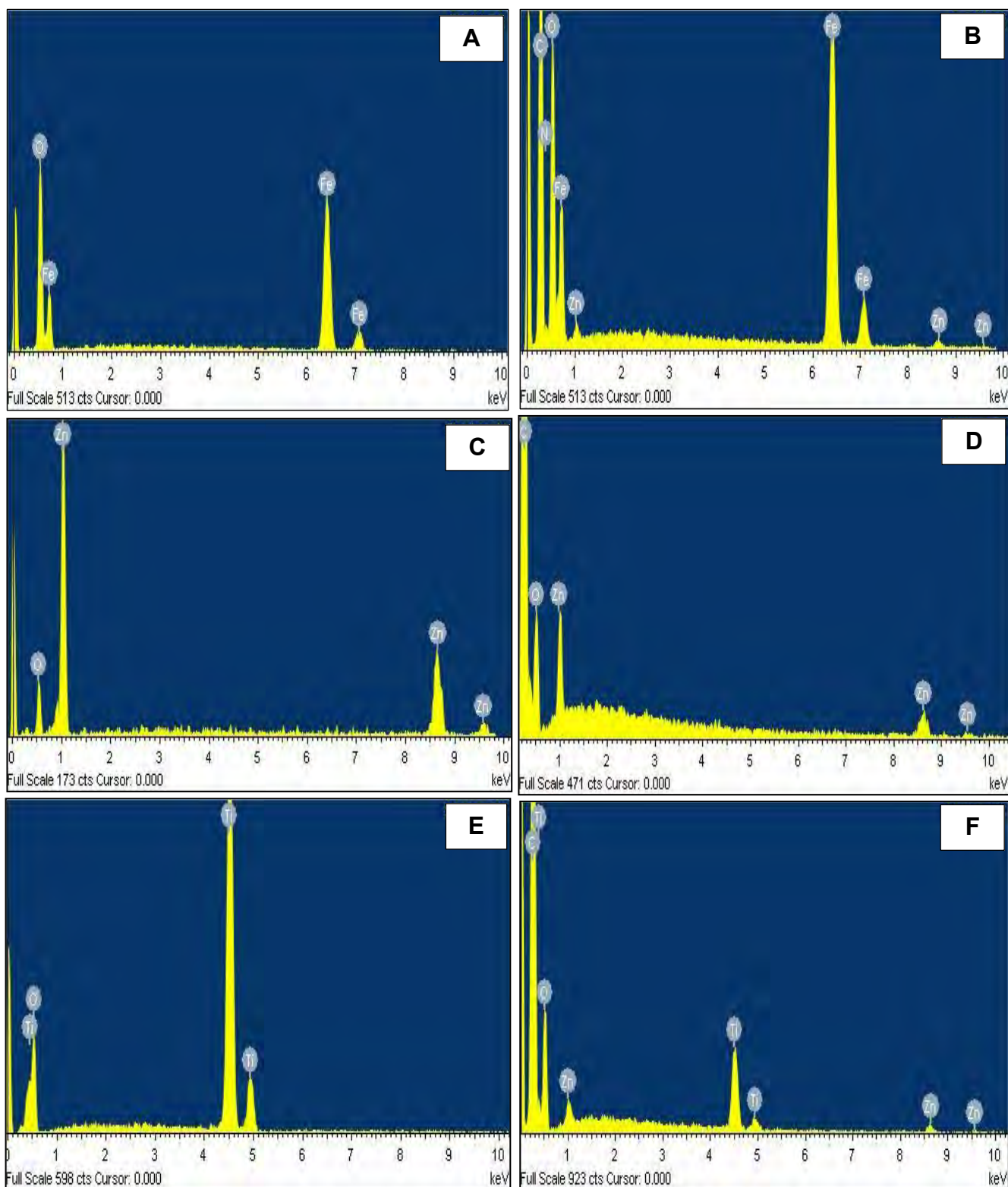


**Figure 4.9:** EDX spectra of (A) bare Hem, (B) **6**-Hem, (C) bare ZnO, (D) **6**-ZnO, (E) bare TiO<sub>2</sub> and (F) **6**-TiO<sub>2</sub> NFs.

The morphologies of the Hem NFs were studied using SEM as shown in **Figure 4.10**. **A**. The Hem NFs are coiled, elongated and cylindrical with smooth surfaces. Due to the small sizes of the Pcs and low concentrations used, no significant changes were observed for the morphologies of the NFs upon modification with complexes **4-6** hence their images are not shown.

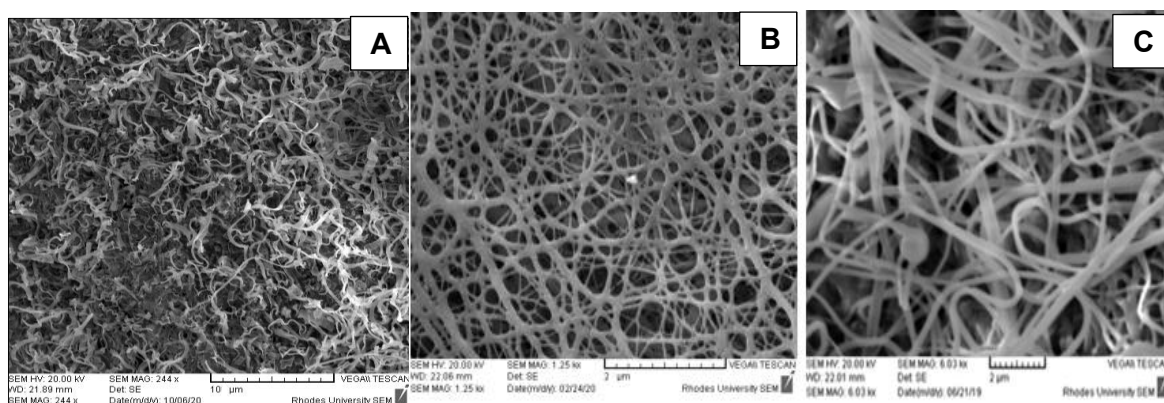


**Figure 4.10:** SEM image of the bare (A) Hem, (B) ZnO and (C) TiO<sub>2</sub> NFs.

The optical properties of the bare and Pc modified NFs were studied using solid state UV-vis spectroscopy as shown in **Figure 4.11** (using NFs modified with complex **6** as an example). The spectrum of the Hem NFs shows peaks at ~ 350, 480-550 and 650 nm, similar to those observed before for hematite NPs [204]. The absorption band at ~350 nm results from the ligand to metal charge transfer (LMCT) which is a direct transition of O<sup>2-</sup>→Fe<sup>3+</sup>. The bands at ~480-550 nm have been assigned to the double excitation processes [205]. The double excitation processes which give rise to the strong absorption band at ~550 nm are responsible for the red colour of Hem [204]. The band at ~650 nm is due to various ligand field transitions [206]. In addition, to the

Hem bands, the spectrum of the **6**-Hem NFs shows a peak at ~650-720 nm attributed to the Pc Q band which is broadened due to aggregation in the solid state [196].

The  $E_g$  of the bare and modified NFs was determined using Tauc's equation (4.1) as explained before for the SiO<sub>2</sub> NFs. Since the obtained Tauc's plots are similar to those observed for the SiO<sub>2</sub> NFs, they are not shown but the calculated band gap energies are listed in **Table 4.2**. For direct allowed transitions, the estimated  $E_g$  for the Hem NFs is 2.20 eV which is close to that observed before for other hematite materials [207,208]. Just as with the SiO<sub>2</sub> NFs, a reduction in the  $E_g$  of the Hem NFs was observed upon modification with the Pc complexes.

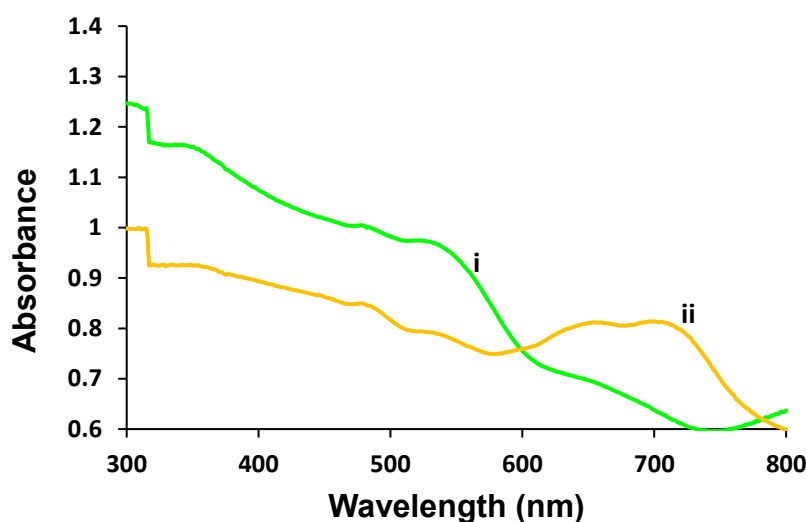


**Figure 4.11:** Solid state UV-vis spectrum of i. Hem NFs and ii. **6**-Hem NFs.

The XRD patterns of the bare and modified NFs are shown in **Figure 4.12** (using NFs modified with complex **6** as an example). The diffraction pattern of the Hem NFs show highly crystallinity with peaks at  $2\theta$  values of 24.74°, 33.59°, 36.11°, 41.34°, 50.02°, 54.53°, 58.13°, 62.83° and 64.46° corresponding to the (012), (104), (110), (113), (024), (116), (122), (214) and (300) rhombohedral (hexagonal) planes of hematite



[209,210]. The crystalline diffraction peaks are maintained in the modified NFs but there is an additional peak due to the presence of the amorphous Pc. The results therefore show that the **6**-Hem NFs have adopted properties from both the bare Hem NFs and complex **6**. Similar diffraction patterns were observed for **4**-Hem and **5**-Hem NFs.

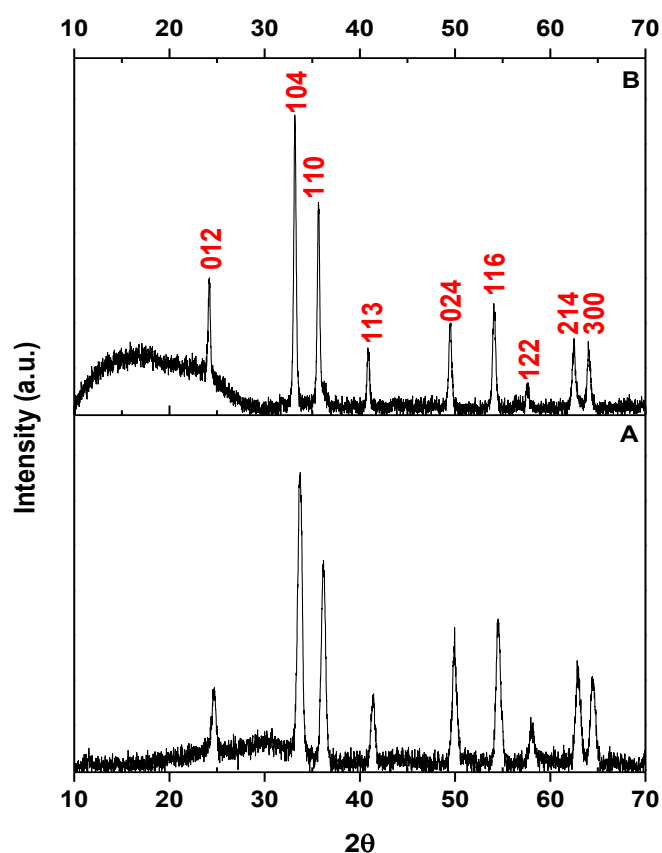


**Figure 4.12:** XRD patterns of (A) Hem and (B) **6**-Hem NFs.

Analyses of the BET isotherms of the bare and modified Hem NFs gave type IV BET isotherms as observed for the SiO<sub>2</sub> NFs hence they are not shown but the obtained surface area and porosity data is listed in **Table 4.2**. The results show a slight increase in surface area and decrease in porosity upon modification with the Pcs as observed for the modified SiO<sub>2</sub> NFs.

**Table 4.2:** The optical and physical properties of the semiconductor NFs

<b>Nanofibers</b>	<b>Band gap (eV)</b>	<b>Surface Area m<sup>2</sup>g<sup>-1</sup></b>	<b>Pore Volume (cm<sup>3</sup>g<sup>-1</sup>)</b>	<b>NP loading</b>
Bare Hem	2.20	18.25	0.185	-
<b>4</b> -Hem	1.92	29.36	0.142	-
<b>5</b> -Hem	1.90	28.45	0.095	-
<b>6</b> -Hem	1.87	22.65	0.0050	-
Bare ZnO	3.28	11.36	0.240	-
<b>6</b> -ZnO	3.00	10.45	0.080	-
Bare TiO <sub>2</sub>	3.19	13.40	0.190	-
<b>6</b> -TiO <sub>2</sub>	2.90	12.70	0.110	-
Bare TiO <sub>2</sub> -500	3.21	12.66	0.167	-
Bare TiO <sub>2</sub> -750	3.05	3.31	0.0013	-
Bare TiO <sub>2</sub> -950	3.01	-	-	-
<b>7</b> @TiO <sub>2</sub> -500	2.87	10.60	0.082	-
<b>7</b> @TiO <sub>2</sub> -750	2.75	1.12	0.003	-
<b>7</b> @TiO <sub>2</sub> -950	2.70	-	-	-
Pd@TiO <sub>2</sub> -500	2.90	60.96	0.069	3.26
Pd@TiO <sub>2</sub> -750	2.95	49.50	0.002	1.37
Pd@TiO <sub>2</sub> -950	2.80	-	-	1.31
Co@TiO <sub>2</sub> -500	3.18	27.60	0.180	2.50
Co@TiO <sub>2</sub> -750	3.00	13.21	0.013	2.50
Co@TiO <sub>2</sub> -950	2.96	-	-	2.50

#### 4.2.2 ZnO NFs

The ZnO NFs were characterised with FT-IR spectroscopy to confirm complete removal of the PVP from the NFs post calcination. As shown in **Figure 4.8 B**, the spectrum shows a single peak at  $368\text{ cm}^{-1}$  corresponding to the vibration of hexagonal ZnO [211], thereby proving the NFs are purely inorganic.

The elemental compositions of the bare and Pc modified NFs were confirmed using EDX as shown in **Figures 4.9 C** and **D**. As expected the bare ZnO NFs only show Zn and O peaks while the **6**-ZnO NFs have an additional C peak due to the presence of the Pc.

Analysis of the surface topography of the NFs was conducted using SEM. As shown in **Figure 4.10 B**. The NFs are branched and connected with uneven and smooth surfaces. Just as with other reported NFs, no changes in the morphologies of the NFs were observed upon modification with the Pc due to the small concentrations used hence the image is not shown.

The solid state UV–vis spectra of the bare and Pc functionalised NFs are shown in **Figure 4.13**. The spectrum of the bare ZnO NFs only exhibit absorption in the UV region, while the **6**-ZnO NFs exhibit additional absorption bands at 550–750 nm due to the presence of the Pc.

The  $E_g$  of the bare and modified NFs were determined using Tauc's equation (4.1) and the obtained results are listed in **Table 4.2**. The estimated  $E_g$  for the ZnO NFs is 3.28 eV, similar to values reported before for ZnO catalysts [179]. Just as with the other NFs, the interaction of the Pc lowered its  $E_g$  wherein the **6**-ZnO NFs were found to have a  $E_g$  of 3.00 eV.

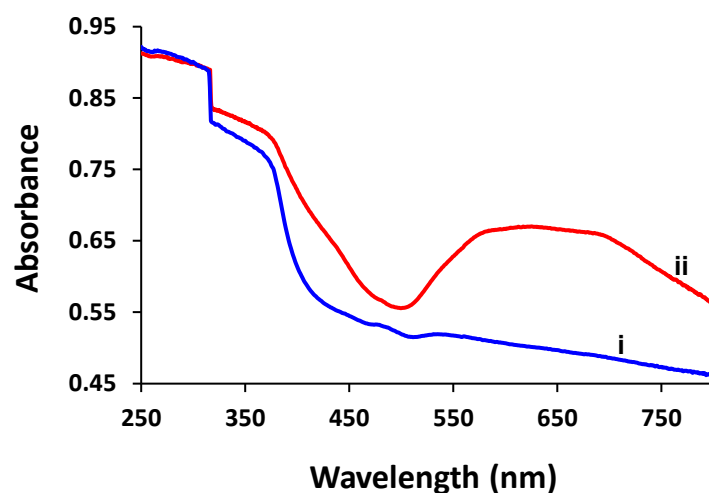


**Figure 4.13:** Solid state UV-vis spectra of i. bare ZnO and ii. **6**-ZnO NFs.

Phase identification of the NFs was conducted using XRD as shown in **Figure 4.14**.

The ZnO NFs show diffraction peaks at  $2\theta$  values of  $31.72^\circ$ ,  $34.46^\circ$ ,  $36.94^\circ$ ,  $47.86^\circ$ ,  $56.78^\circ$ ,  $63.76^\circ$ ,  $68.96^\circ$  and  $69.70^\circ$ , corresponding to the (100), (002), (101), (102), (110), (103), (112) and (201) planes of hexagonal wurzite of crystalline ZnO [212].

This means that there is a close packing of oxygen and zinc atoms in tetrahedral sites, which gives rise to the typical crystal habit of ZnO [179]. Upon modification with complex **6**, there is an additional amorphous peak at due to the presence of the Pc.

Analyses of the BET isotherms of the bare and modified ZnO NFs gave type IV isotherms as observed for the SiO<sub>2</sub> NFs hence they are not shown but the obtained surface area and porosity data is listed in **Table 4.2**. Interestingly, the results show a slight decrease in surface area and porosity upon modification with the Pcs. This can therefore suggest that the roughness of the NFs is reduced in the presence of the Pc as rough surfaces have been reported to possess larger surface areas than smooth ones [201].

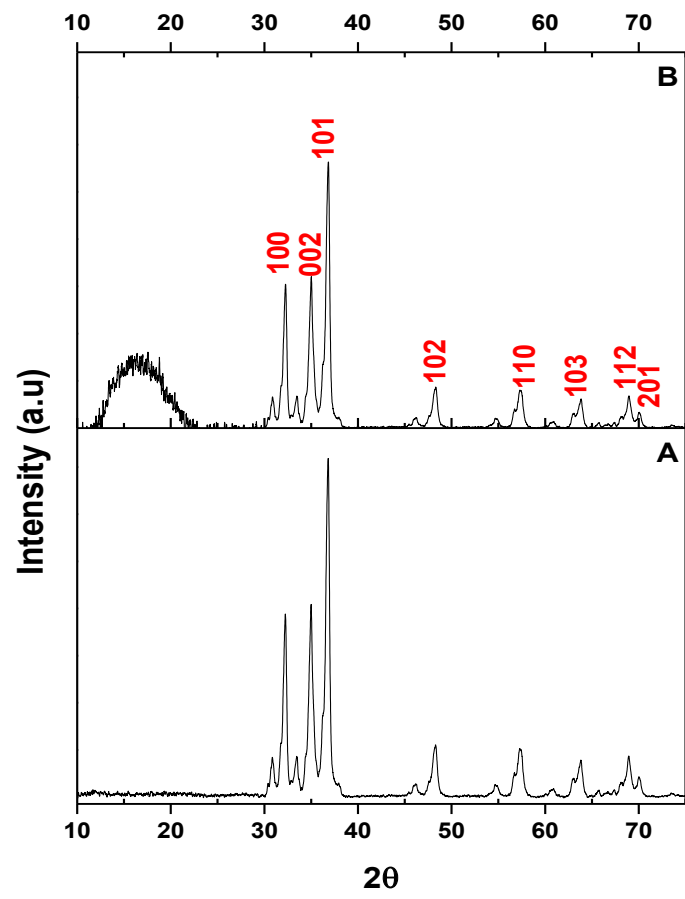


**Figure 4.14:** XRD patterns of (A) bare ZnO and (B) 6-ZnO NFs.

### 4.2.3 TiO<sub>2</sub> NFs

The FT-IR spectrum of the TiO<sub>2</sub> NFs is shown in **Figure 4.8 C**. No polymer peaks are observed, instead the TiO<sub>2</sub> NFs show peaks at 475 and 730 cm<sup>-1</sup> attributed to the O–Ti–O bonding thereby proving the TiO<sub>2</sub> NFs are purely inorganic [213]. The peak at 3390 cm<sup>-1</sup> can be attributed to the OH stretch of surface water.

The elemental compositions of the bare and Pc modified NFs were confirmed using EDX as shown in **Figure 4.9**. As expected the bare TiO<sub>2</sub> NFs only show Ti and O peaks (**Figure 4.9 E**) while the 6-TiO<sub>2</sub> NFs have additional C and Zn peaks (**Figure 4.9 F**) due to the presence of the Pc.

The morphologies of the bare and Pc modified TiO<sub>2</sub> NFs were analysed using SEM as shown in **Figure 4.10 C**. The NFs are cylindrical with smooth surfaces and broken edges. Just as with other reported NFs, no changes in the morphologies of the NFs were observed upon modification with the Pc due to its small sizes hence the image is not shown.

The spectra of the bare TiO<sub>2</sub> NFs only exhibit absorption in the UV region, while the 6-TiO<sub>2</sub> NFs exhibit additional absorption bands at 550–750 nm due to the presence of the Pc (**Figure 4.15**). The E<sub>g</sub> of the bare and modified NFs were determined using Tauc's equation (4.1) and the obtained results are listed in **Table 4.2**. The estimated E<sub>g</sub> for the bare TiO<sub>2</sub> NFs is 3.19 eV, similar to values reported before for anatase TiO<sub>2</sub> catalysts [214].

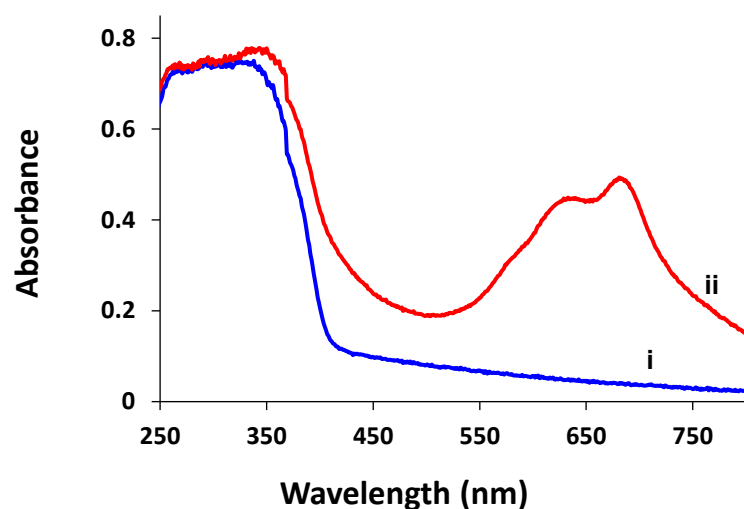


**Figure 4.15:** Solid state UV-vis spectra of i. bare TiO<sub>2</sub> and ii. **6**-TiO<sub>2</sub> NFs.

The anatase nature of the TiO<sub>2</sub> NFs was confirmed using XRD as shown in **Figure 4.16**. The bare TiO<sub>2</sub> NFs show diffraction peaks at  $2\theta$  values of 25.39°, 37.93°, 48.26°, 54.13°, 55.28°, 62.88°, 69.21°, 70.50° and 75.30° corresponding to the (101), (004), (200), (105), (211), (204), (116), (220) and (215) tetragonal planes of anatase TiO<sub>2</sub> as reported before [215]. In addition, an amorphous peak was observed for the **6**-TiO<sub>2</sub> NFs due to the presence of the Pc.

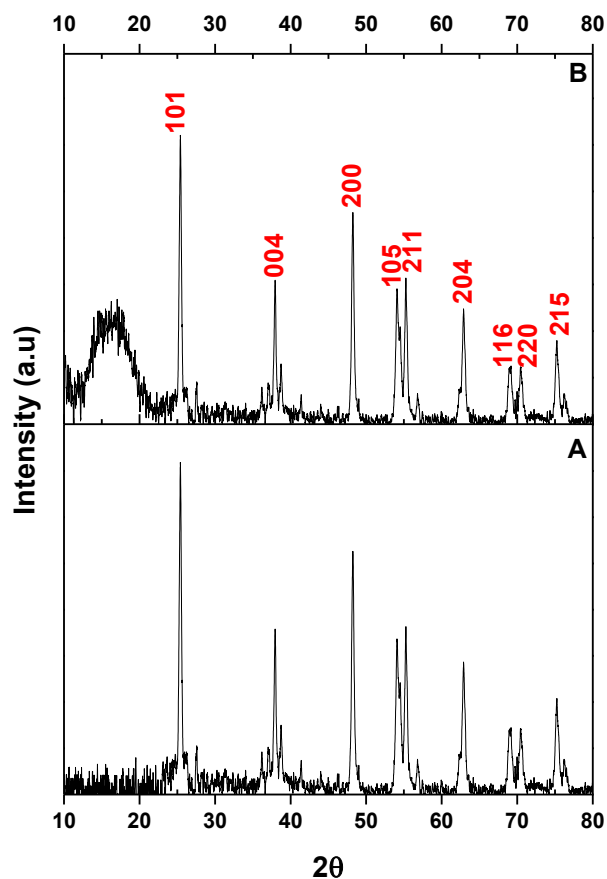


**Figure 4.16:** XRD patterns of (A) TiO<sub>2</sub>-500 and (B) **6**-TiO<sub>2</sub> NFs.

Analyses of the BET isotherms of the bare and modified TiO<sub>2</sub> NFs also gave type IV isotherms as observed for the SiO<sub>2</sub> NFs hence they are not shown but the obtained surface area and porosity data is listed in **Table 4.2**. Just as with the ZnO NFs, the TiO<sub>2</sub> NFs show a slight decrease in surface area and porosity upon modification with the complex **6**.

Characterisation of the second batch of TiO<sub>2</sub> NFs which were calcined at different temperatures (500,750 and 950 °C) and modified with complex **7** as well as Pd and Co NPs are discussed next.



Just as discussed before with the FT-IR spectra of the first batch of TiO<sub>2</sub> NFs, complete removal of the PVP was observed for the second batch too to obtain purely inorganic TiO<sub>2</sub> NFs (spectrum not shown).

The crystalline phases of the TiO<sub>2</sub> NFs calcined at different temperatures were analysed using XRD as shown in **Figure 4.17**. The peak positions of the TiO<sub>2</sub>-750 and TiO<sub>2</sub>-950 NFs are the same, suggesting that they have the same phase while those of TiO<sub>2</sub>-500 are different. The TiO<sub>2</sub>-500 NFs planes are characteristic of the tetragonal anatase phase as observed before [215]. For TiO<sub>2</sub>-750 and TiO<sub>2</sub>-950 on the other hand, the main peaks were observed at 2 $\theta$  values of 27.90, 36.63, 41.83, 54.63 and 57.03° corresponding to the (110), (101), (111), (211) and (220) planes of tetragonal rutile phase as reported before [216].

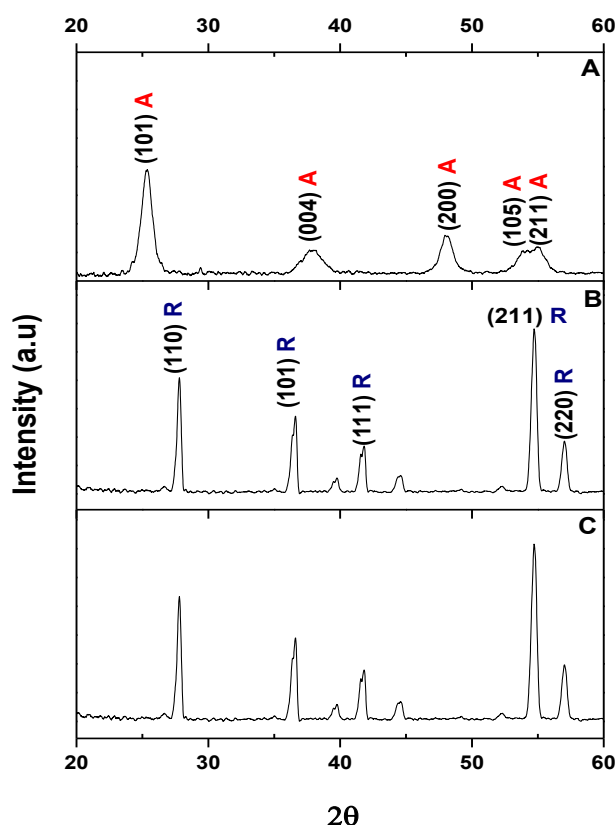


**Figure 4.17:** XRD patterns of (A) TiO<sub>2</sub>-500, (B) TiO<sub>2</sub>-750 and (C) TiO<sub>2</sub>-950 NFs where R = rutile and A = anatase.

Since the NFs calcined at 750 °C have been reported to give a mixture of anatase and rutile phases [217], confirmation of the data obtained from XRD was then conducted using Raman spectroscopy as shown in **Figure 4.18** as it is sensitive enough to distinguish between the different TiO<sub>2</sub> phases. The TiO<sub>2</sub>-500 NFs were found to have active vibrations located at 144 cm<sup>-1</sup> (E<sub>g</sub>), 396 cm<sup>-1</sup> (B<sub>1g</sub>), 518 cm<sup>-1</sup> (A<sub>1g</sub>) and 637 cm<sup>-1</sup> (E<sub>g</sub>) while for TiO<sub>2</sub>-750 and TiO<sub>2</sub>-950, vibrations at 134 cm<sup>-1</sup> (B<sub>1g</sub>), 236 cm<sup>-1</sup> (broad band), 442 cm<sup>-1</sup> (E<sub>g</sub>), and 605 cm<sup>-1</sup> (A<sub>1g</sub>) were observed, corresponding to those reported before [218]. The results prove that each of the calcined NFs are pure phase where TiO<sub>2</sub>-500 is purely anatase while TiO<sub>2</sub>-750 and TiO<sub>2</sub>-950 are purely rutile.

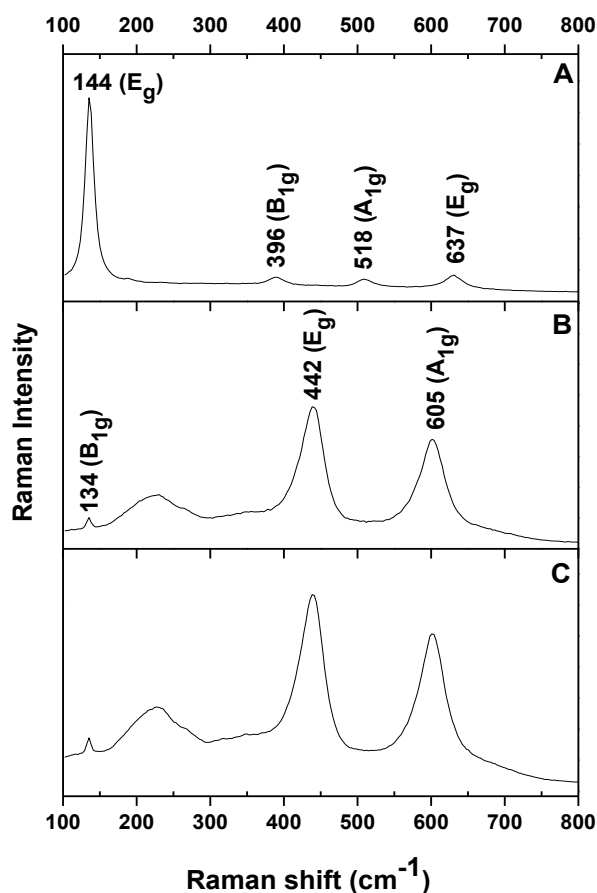


**Figure 4.18:** Raman spectra of (A) TiO<sub>2</sub>-500, (B) TiO<sub>2</sub>-750 and (C) TiO<sub>2</sub>-950.

The UV-vis spectra of the modified NFs are shown in **Figure 4.19** (using the NFs calcined at 500 °C as examples). The spectra of the bare TiO<sub>2</sub> NFs show a broad peak in the UV region (<400) which was maintained even post-modification. Surprisingly, the NFs decorated with the Pd NPs exhibit slight red shift and broadening in the spectral band which is not observed for the NFs decorated with the Co NPs. The 7@TiO<sub>2</sub>-500 NFs have an additional peak in the visible region due to the Pc Q band. The obtained spectra are an indication of efficient fabrication and modification of the NFs. Similar spectra were obtained for TiO<sub>2</sub>-750 and TiO<sub>2</sub>-950 as well as their decorated counterparts (not shown).

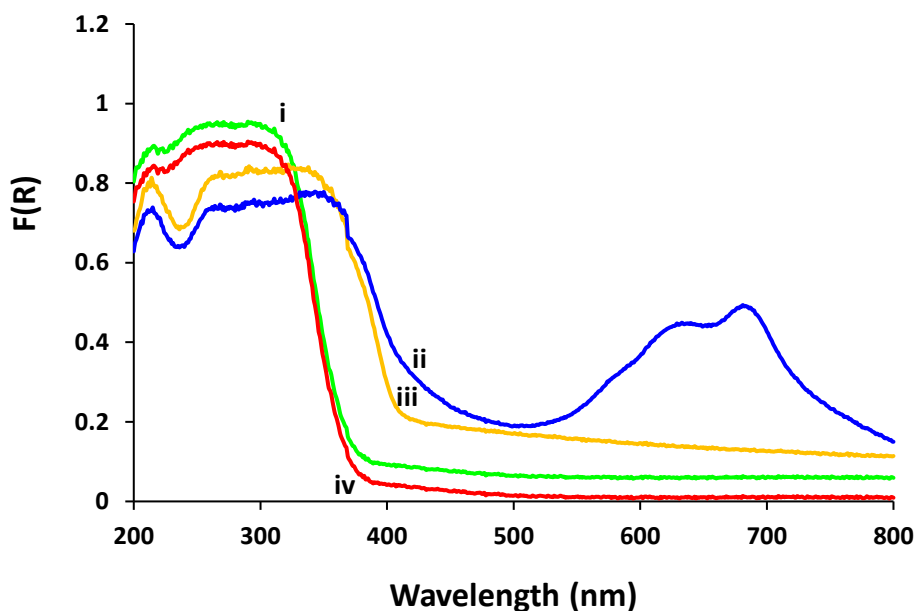


**Figure 4.19:** (A) Solid state UV-vis spectra of (i) TiO<sub>2</sub>-500, (ii) 7@TiO<sub>2</sub>-500 (iii) Pd@TiO<sub>2</sub>-500 and (iv) Co@TiO<sub>2</sub>-500 NFs.

Using Taucs equation as explained before, the E<sub>g</sub> of the bare and modified TiO<sub>2</sub> NFs were determined and listed in **Table 4.2**. Important to note is that increased calcination temperature resulted in slightly reduced direct band gap energies. This is not

surprising as anatase TiO<sub>2</sub> materials have been reported to have larger band gaps than rutile [219]. Modification of the NFs with the Pc and NPs has also resulted in reduced E<sub>g</sub>.

Confirmation of efficient photoreduction of Pd(II) and Co(II) to form the NPs on the surface of each of the bare NFs was conducted with XPS as shown in **Figure 4.20** (showing Pd@TiO<sub>2</sub>-500 and Co@TiO<sub>2</sub>-500 as examples). A Pd 3d core level spectrum consisting of two components i.e. Pd 3d<sub>5/2</sub> and Pd 3d<sub>3/2</sub> (separated by approximately 5.4 eV) was obtained as observed before [220]. The Pd 3d spectrum of Pd@TiO<sub>2</sub>-500 was deconvoluted to four peaks at 336.9 (Pd<sup>0</sup>), 337.7 (Pd<sup>2+</sup>), 342.3 (Pd<sup>0</sup>) and 343.9 eV (Pd<sup>2+</sup>). The Pd<sup>0</sup> peaks are of higher intensity than those of Pd<sup>2+</sup> which could be an indication that although there are still traces of Pd<sup>2+</sup> in the NFs but the NPs in the form of Pd<sup>0</sup> are in abundance. For the Co NPs, the Co 2p core level spectrum was performed by using two spin-orbit split components i.e. Co 2p<sub>3/2</sub> and Co 2p<sub>1/2</sub> (separated by 15.5 eV) as observed before [221]. The Co 2p spectrum of Co-TiO<sub>2</sub>-500 was deconvoluted to two peaks at 778.1 (Co<sup>0</sup>) and 793.6 eV (Co<sup>0</sup>). This serves as proof of complete reduction of Co<sup>2+</sup> to Co<sup>0</sup> as no Co<sup>2+</sup> peaks were observed.

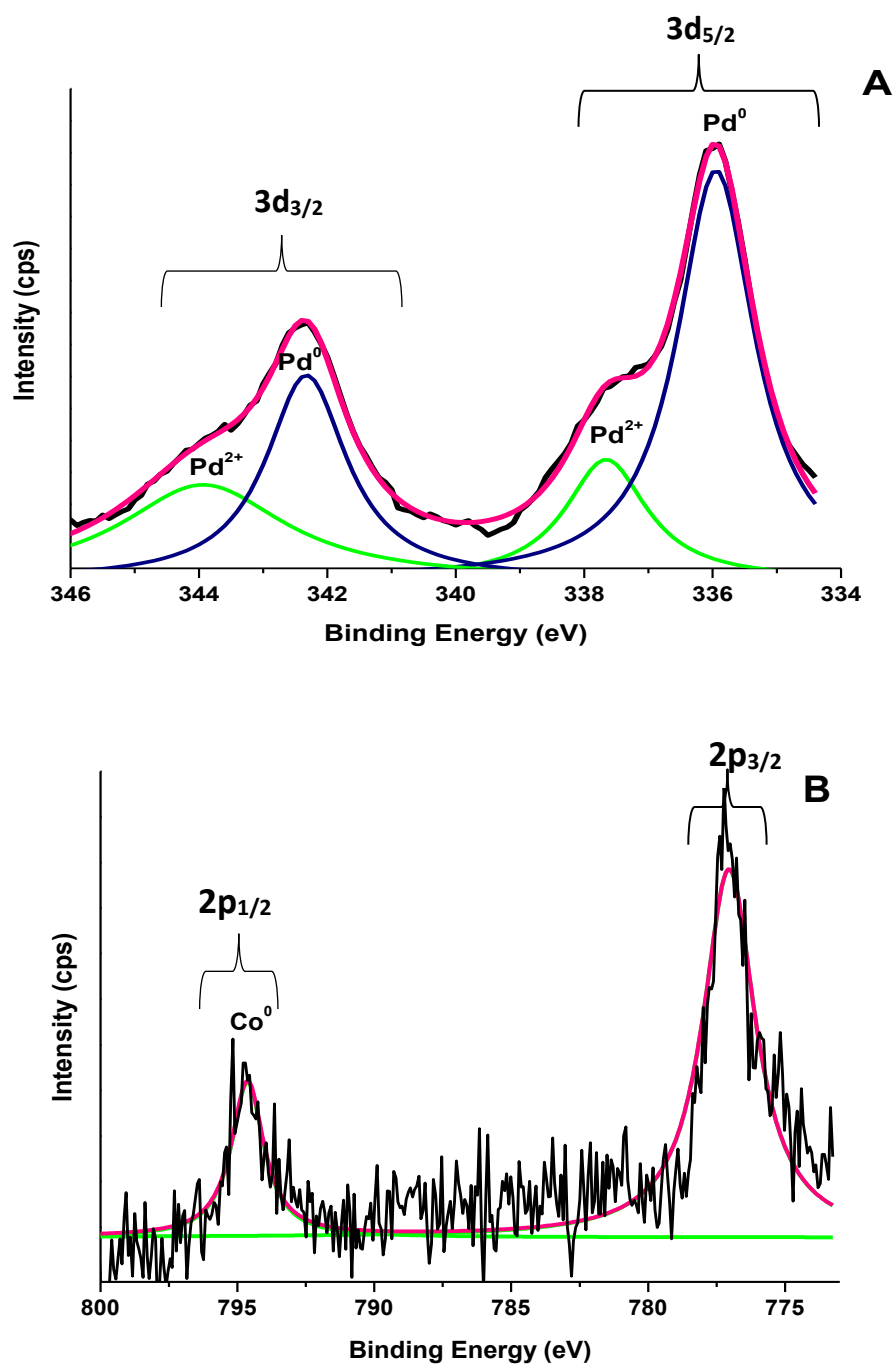


**Figure 4.20:** Deconvoluted XPS spectra of (A) Pd@TiO<sub>2</sub>-500 NFs highlighting the Pd 3d photoemission and (B) Co@TiO<sub>2</sub>-500 NFs highlighting the Co 2p photoemission.

SEM was conducted for analyses of the topography of the calcined NFs before and after deposition of the NPs and the obtained images are shown in **Figure 4.21**. The images reveal that some of the calcined NFs are porous which is a good attribute as it has been reported that porous nanostructured materials are more efficient semiconductor photocatalysts [127].

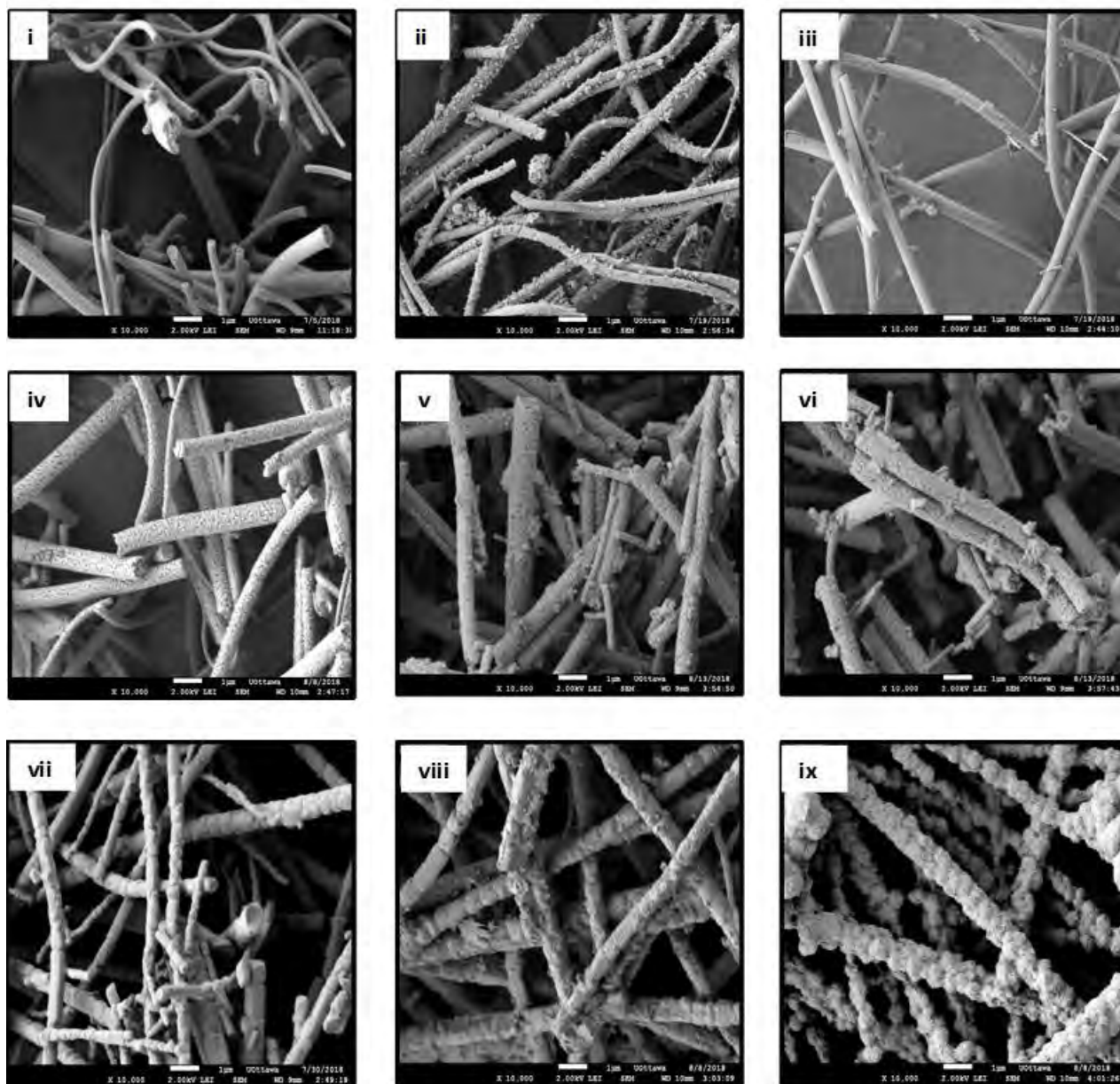


**Figure 4.21:** SEM images of (i)  $\text{TiO}_2$ -500, (ii)  $\text{Pd@TiO}_2$ -500, (iii)  $\text{Co@TiO}_2$ -500, (iv)  $\text{TiO}_2$ -750, (v)  $\text{Pd@TiO}_2$ -750 (vi)  $\text{Co@TiO}_2$ -750, (vii)  $\text{TiO}_2$ -950 (viii)  $\text{Pd@TiO}_2$ -950 and (ix)  $\text{Co@TiO}_2$ -950 NFs.

This is because porous materials generally have better mass transport of reactants and radiation, large specific surface area and abundant active sites for the reactions [222]. Even though the TiO<sub>2</sub>-750 and TiO<sub>2</sub>-950 NFs have both been proven to be rutile (XRD and Raman spectra), their SEM images show that they have different morphologies. The TiO<sub>2</sub>-750 NFs are more cylindrical and porous while TiO<sub>2</sub>-950 has a more distorted surface with grain like structures which are sintered. The distortion of the NFs with increased calcination temperature is possibly due to the breakage of the Ti–O bonds in the anatase structure, permitting the rearrangement of Ti–O to form the rutile phase. Thus phase transformation can lead to the disruption of the lattice of TiO<sub>2</sub> [223]. There are no notable differences in the images of NFs decorated with complex 7 because of the small concentrations that are used hence their images are not shown. The surfaces of the NFs modified with the Pd and Co NPs appear rough thereby confirming successful formation of the NPs.

The surface area and porosity data that was obtained upon analysis of the NFs is listed in **Table 4.2**. No BET surface area/porosity data was obtained upon analysis of the bare and decorated TiO<sub>2</sub>-950 NFs, this is probably due to their brittle nature and distorted structure. Analyses of the bare TiO<sub>2</sub>-500 and TiO<sub>2</sub>-750 NFs shows that increased heating temperature caused a decrease in the surface area and pore volume of the NFs. Decoration of the bare NFs with the NPs resulted in an increased surface area with the anatase NFs being larger than the rutile NFs.

Analyses of the loading of the NPs on each of the calcined TiO<sub>2</sub> NFs was conducted using ICP-OES and the obtained results are shown in **Table 4.2**. It is important to note that the loadings of the Pd NPs on the three NFs (Pd@TiO<sub>2</sub>-500, Pd@TiO<sub>2</sub>-750 and Pd@TiO<sub>2</sub>-950) are different, but are the same for the Co NPs. In order for the NPs to

form,  $\text{Pd}^{2+}$  is reduced to  $\text{Pd}^0$ , a process that is catalysed by the NFs. The  $\text{Pd@TiO}_2$ -500 NFs have a greater Pd loading ( $\sim 3.26$  wt %), presumably as a result of a higher photoreduction efficiency, while the  $\text{Pd@TiO}_2$ -750 and  $\text{Pd@TiO}_2$ -950 NFs have comparable loadings ( $\sim 1.3$  wt %). This is not surprising as the pore volume of the  $\text{Pd@TiO}_2$ -500 NFs is larger ( $0.069 \text{ cm}^3/\text{g}$ ) than that of the  $\text{Pd@TiO}_2$ -750 NFs ( $0.002 \text{ cm}^3/\text{g}$ ) and porosity has been reported to increase the activity of a catalyst [127]. In addition, anatase phase  $\text{TiO}_2$  has been reported to possess better photocatalytic activity than rutile [219]. In the case of the Co NPs, the photoreduction of  $\text{Co}^{2+}$  to  $\text{Co}^0$  occurs but this is driven by the use of a photoinitiator hence the same loading was obtained. In the case of the Pc decorated fibers, no activity of the fibers is used, they are dyed in the same manner hence the loading is also the same.

### 4.3 Closing Remarks

The fabrication and modification of  $\text{SiO}_2$ , Hem, ZnO and  $\text{TiO}_2$  NFs has been achieved and their physical as well as optical properties have been reported. The photophysicochemical properties of the bare and modified NFs together with those of the Pcs and NPs in solution are discussed in the next chapter.



# Chapter 5

This chapter gives details on the photophysical and photochemical properties of the Pcs reported herein. It also discusses how these parameters are influenced in the presence of NPs and NFs in different solvents.

## 5.1 Fluorescence studies

### 5.1.1 Spectra

The absorption, emission and excitation spectra of the Pcs and Pc-NP conjugates were analysed and that of complex **3** is shown **Figure 5.1** as an example. The emission spectrum is a mirror image of the excitation and absorption spectra, as is normally expected for monomeric planar  $\pi$ -conjugated dyes. The Q band absorption maxima is close to that of the excitation, thereby showing that the absorbing molecule is the same as the emitting molecule. Small Stokes shifts of 11-13 nm were obtained for the Pcs and their respective conjugates. This is typical for Pcs as it confirms that the nuclear configurations of the ground and excited states are similar due to the rigidity of the structure.

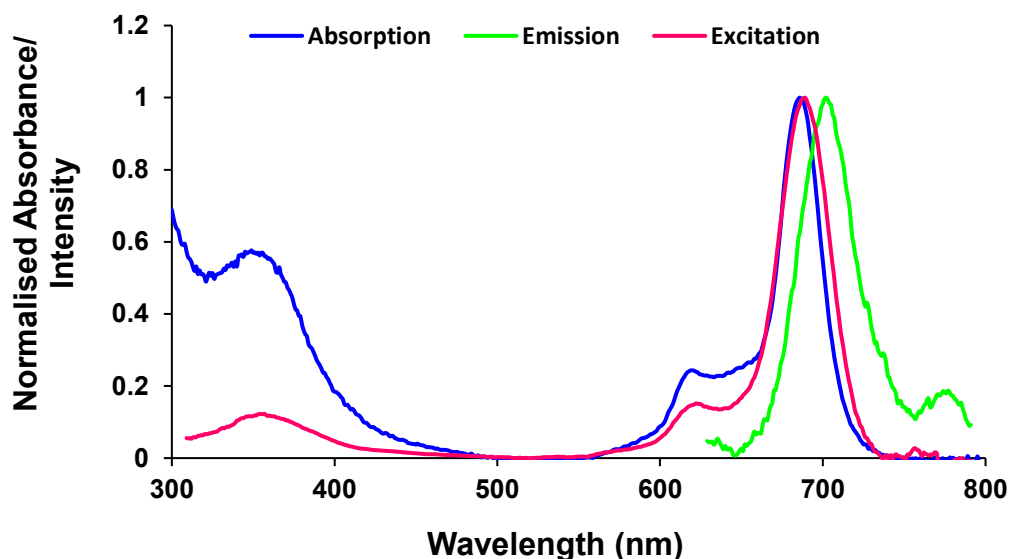


**Figure 5.1:** Absorption, emission and excitation spectra of complex **3** in DMSO at an excitation wavelength of 620 nm.

The slight differences between the absorbance and excitation spectra can be attributed to the use of different equipment to generate the data. Similar fluorescence behaviour was observed for the rest of the Pc complexes as well as their respective conjugates.

### 5.1.2 Quantum yields ( $\Phi_F$ ) and lifetimes ( $\tau_F$ )

Using the comparative method, the fluorescence quantum yields ( $\Phi_F$ ) of all the Pcs and their respective conjugates were calculated using **Equation 1.1** and listed in **Table 5.1**. For studies conducted in DMSO, unsubstituted ZnPc ( $\Phi_F = 0.20$  [224]) was used as the standard. Due to the aggregation in 2% DMSO (in PBS), low  $\Phi_F$  values of  $<0.01$  were obtained for the Pcs and their conjugates, thus they are not shown nor discussed.

The fluorescence lifetime values ( $\tau_F$ ) of the Pc complexes as well as their respective conjugates were measured in DMSO using TCSPC (time correlated single photon counting) method and the obtained results are listed in **Table 5.1**. The extrapolated fluorescence decay curve from the TCSPC for complex **3** is shown in **Figure 5.2** as an example with its accompanying residual graph. It is a representative of the decay curves obtained for the rest of the Pcs and their conjugates.

With the exception of some conjugates (**5-Ag**, **5-Fe<sub>3</sub>O<sub>4</sub>** and **5-Fe<sub>3</sub>O<sub>4</sub>@Ag**), the Pc complexes and the rest of the conjugates show mono-exponential fluorescence decay. The **5-Ag**, **5-Fe<sub>3</sub>O<sub>4</sub>** and **5-Fe<sub>3</sub>O<sub>4</sub>@Ag** conjugates showed bi-exponential decays and the lifetimes with the greatest percentage occupancy are reported on **Table 5.1**. This type of decay may occur for Pcs due to the formation of aggregates which are non-fluorescent, but which can quench the monomer [225]. Different orientations of the Pc

on the NPs could also be a contributing factor in observing two lifetimes [226]. Complex **5** has less substituents and thus minimal steric hindrance unlike the more bulky complexes **4** and **6**.

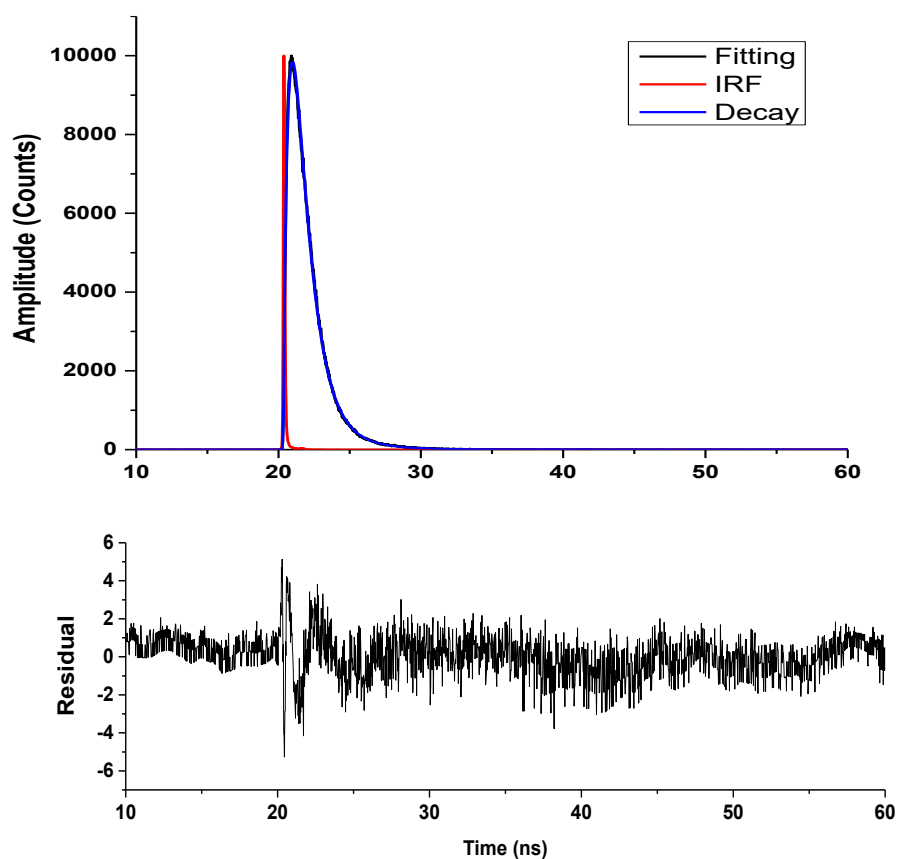


**Figure 5.2:** Fluorescence decay curve of complex **3** in DMSO.

As shown in **Table 5.1**, the cationic complexes **2** and **3** have slightly lower  $\Phi_F$  values than the neutral complex **1**, showing that quaternization does not improve fluorescence. Complexes **4-6** are all asymmetrical and have isophthalic acid moieties. Asymmetry introduces distortions on the Pc macrocycle which in turn affect their photophysical properties [114]. The results show that complex **5** which is monosubstituted has the highest  $\Phi_F$  relative to the tetrasubstituted complexes **4** and

6. A similar behaviour has been observed before for similarly substituted Pcs [227,228].

In addition, **Table 5.1** shows that all the conjugates have lower  $\Phi_F$  relative to the Pcs alone. This is because the NPs impose a heavy atom effect on the Pc, which encourages intersystem crossing to the triplet state thereby suppressing the relaxation of the excited photosensitisers to the ground state through fluorescence. As expected, the reduction in the  $\Phi_F$  due to the presence of the NPs results in shortened  $\tau_F$ .

The fluorescence properties of complex **7** are also listed on **Table 5.1** but because its substituents do not permit it to be conjugated to any NPs or to be compared to any other Pc, the properties are just listed and not discussed.

## 5.2 Triplet Quantum yields ( $\Phi_T$ ) and triplet lifetimes ( $\tau_T$ )

The triplet quantum yield is an indication of the fraction of molecules that undergo intersystem crossing to the excited triplet state. The triplet quantum yield is inversely proportional to the fluorescence quantum yield hence when the former is large, it suggests a high intersystem crossing efficiency of the Pc. A high triplet quantum yield is attractive as it influences the singlet oxygen generation.

**Table 5.1:** Fluorescence and triplet state parameters of the Pcs and their respective conjugates in DMSO.

Complex	Loading NP:Pc	$\Phi_F$	$\tau_F$ (ns)	$\Phi_T$	$\tau_T$ ( $\mu$ s)
Complex 1	-	0.110 <sup>a</sup>	2.53 <sup>a</sup>	0.83 <sup>a</sup>	351 <sup>a</sup>
1-Ag	1:7	0.080	1.44	0.90	358
Complex 2	-	0.077	2.01	0.73	260
2-Ag	1:5	0.039	1.82	0.80	241
Complex 3	-	0.100	2.04	0.85	360
3-Ag	1:3	0.074	1.75	0.87	348
Complex 4	-	0.095	3.68	0.58	287
4-Ag	1:2	0.048	3.46	0.71	203
4-Fe <sub>3</sub> O <sub>4</sub>	1:2	0.055	3.50	0.78	176
4-Fe <sub>3</sub> O <sub>4</sub> @Ag	1:4	0.073	3.52	0.62	181
Complex 5	-	0.190	2.95	0.75	305
5-Ag	1:3	0.110	1.60	0.78	227
5-Fe <sub>3</sub> O <sub>4</sub>	1:2	0.150	1.79	0.80	220
5-Fe <sub>3</sub> O <sub>4</sub> @Ag	1:5	0.110	1.25	0.88	185
Complex 6	-	0.140	7.60	0.82	129
6-Ag	1:3	0.100	3.05	0.85	122
6-Fe <sub>3</sub> O <sub>4</sub>	1:2	0.080	4.85	0.88	118
6-Fe <sub>3</sub> O <sub>4</sub> @Ag	1:5	>0.01	3.87	0.85	125
Complex 7	-	0.067 <sup>b</sup>	9.07 <sup>b</sup>	0.71 <sup>b</sup>	69.0 <sup>b</sup>

<sup>a</sup>Values extrapolated from [118], <sup>b</sup>Studies conducted in toluene.

Using laser flash photolysis, the triplet state parameters ( $\Phi_T$ ,  $\tau_T$ ) were determined and quantified. For studies conducted in DMSO, unsubstituted ZnPc ( $\Phi_T = 0.65$  [229]) was used as the standard and **Equation 1.2** was employed in the calculations.

A representation of the mono-exponential triplet decay curve of the Pcs and their conjugates is shown in **Figure 5.3** (using complex **3** as an example). Fitting the decay curve at the absorption maxima gave the triplet lifetimes and the obtained values together with the triplet quantum yields are listed in **Table 5.1**.

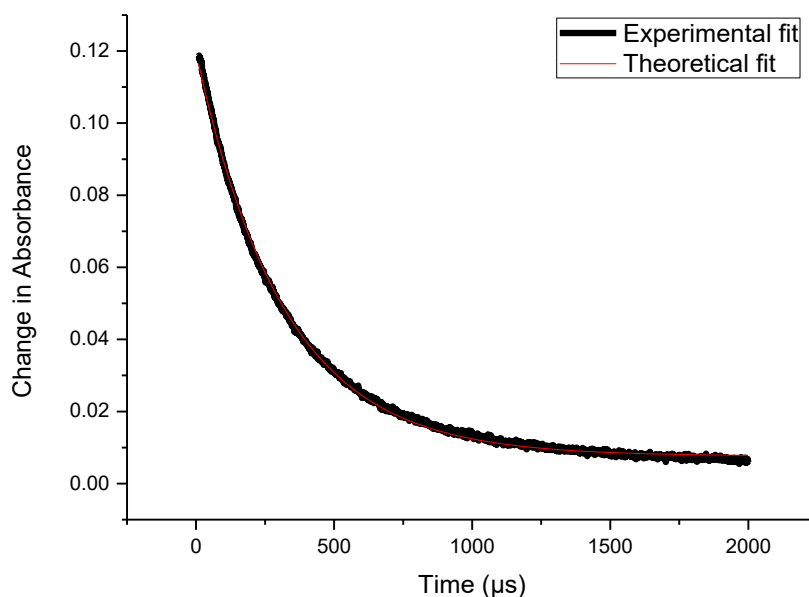


**Figure 5.3:** Triplet absorption decay curve of complex **3** in DMSO.

The general observation is that all the Pc complexes have high  $\Phi_T$  due to the presence of the heavy Zn central metal. In most cases, conjugation of the Pcs to the different NPs resulted in increased  $\Phi_T$  and a decrease in the  $\tau_T$  values. This is due to the heavy atom effect, which enhances intersystem crossing and thus triplet state population.

Comparison of complexes **1-3** shows that the hexadecacationic complex **3** has the highest  $\Phi_T$  followed by the neutral complex **1** and then the octacationic complex **2**. Showing there is no particular trend in the  $\Phi_T$  that is followed by the Pcs based on the number of charges that they possess.

Complexes **4-6** have  $\Phi_T$  values of 0.58, 0.75 and 0.82, respectively. No particular trend was observed for these values. The triplet state parameters of complex **7** are also just listed in **Table 5.1** and not discussed. This is due to the Pc not having the appropriate substituents for its conjugation to NPs.

### 5.3 Singlet oxygen quantum yields ( $\Phi_\Delta$ )

Using the comparative and absolute methods, the singlet oxygen quantum yields were determined for the Pcs (and their conjugates) in solution and when supported on NFs, respectively.

#### 5.3.1 Comparative method

One of the characteristics of a good photosensitiser is its ability to generate high singlet oxygen [230]. This is because singlet oxygen is the main active species in photosensitiser mediated photocatalytic oxidation and microbial photoinactivation [12,13]. Its production is highly dependent on the triplet state population and effectiveness of energy transfer process between the excited triplet state Pc and molecular oxygen [231].

The comparative method was implemented in the quantification of the singlet oxygen generated by the Pc complexes and their conjugates using **Equation 1.5**. For studies conducted in DMSO, unsubstituted ZnPc ( $\Phi_\Delta = 0.67$  [232]) was used as the standard



and for studies conducted in aqueous media (2% DMSO), AlPcSmix ( $\Phi_{\Delta} = 0.42$  [233]) was used as the standard.

By spectroscopically monitoring the degradation of DPBF and ADMA (singlet oxygen quenchers in organic solvents and aqueous media, respectively), quantification of the  $\Phi_{\Delta}$  was achieved. As shown in **Figure 5.4 A** (using studies conducted with complex **3** as an example), there was an observed DPBF degradation at  $\sim 417$  nm while the Q band of the Pc remained unchanged. This demonstrates the photostability of the Pc. Similar results were obtained for the rest of the Pcs and their conjugates.

The degradation of ADMA in 2% DMSO solution is shown in **Figure 5.4 B** (using complex **3** as an example). The spectrum shows degradation of the ADMA bands and a broadened, split Q band for the Pc due to its aggregation in aqueous media. Similar spectra were observed for other Pcs and their respective conjugates (not shown).

The calculated  $\Phi_{\Delta}$  values for all the reported Pcs and their respective conjugates are listed in **Table 5.2**. The results show that conjugation of the Pcs to the NPs results in increased  $\Phi_{\Delta}$  due to the heavy atom effect imposed by the latter.

Comparison of the singlet oxygen generation efficiencies of complexes **1-3** in DMSO shows that complexes **1** and **2** have lower  $\Phi_{\Delta}$  values, possibly due to the inhibition of the intramolecular charge transfer (ICT) effect due to their amino groups [124]. Even though **3-Ag** has the highest  $\Phi_{\Delta}$  of 0.68 relative to **2-Ag** and **1-Ag**, the greatest enhancement in the  $\Phi_{\Delta}$  was however observed for **1-Ag** which is not surprising as it has the highest loading of Pcs (**Table 3.2**) on the NPs which could possibly cause stronger energy transfer processes.

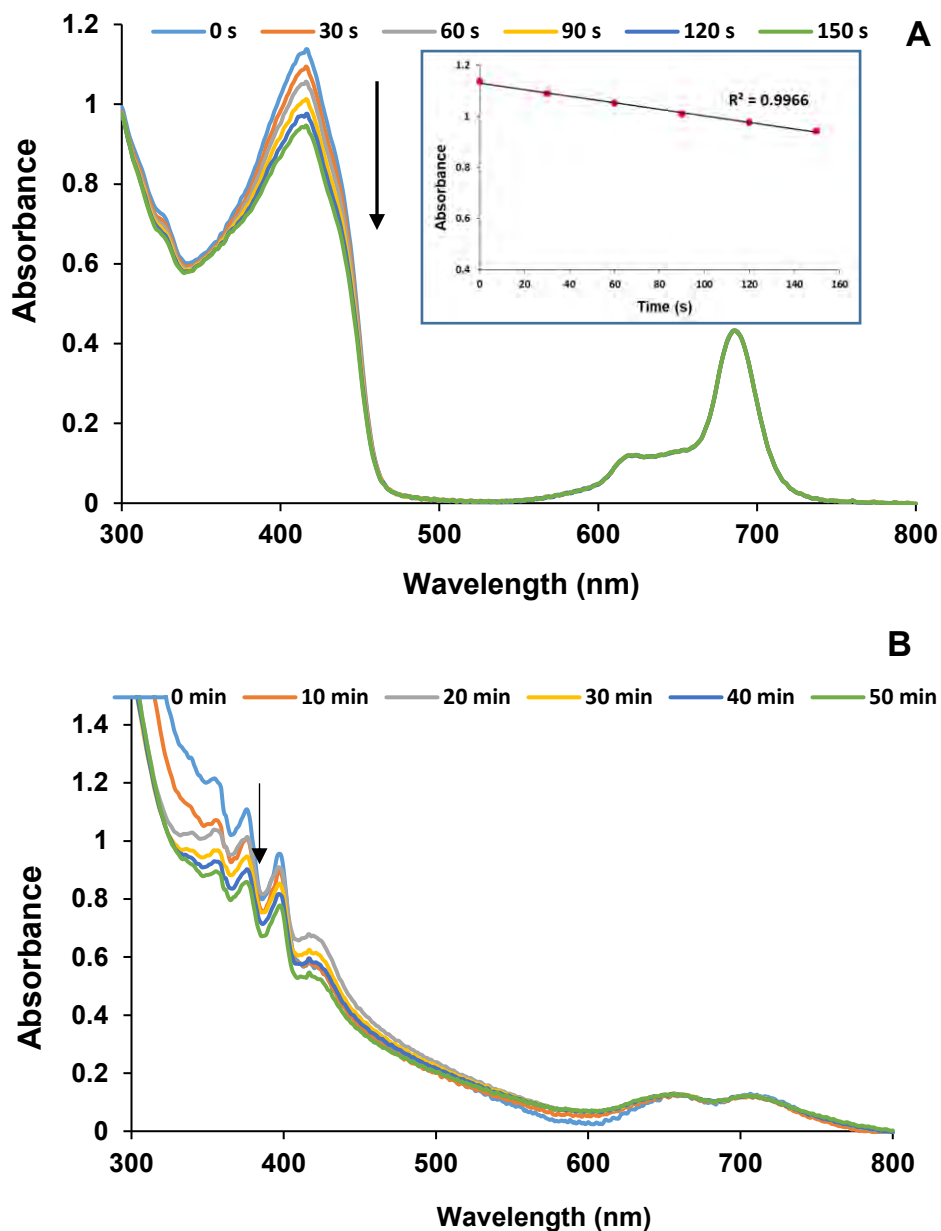


**Figure 5.4:** Ground state UV-vis spectrum demonstrating the photodegradation of (A) DPBF (in DMSO) where inset = plot showing the relationship between absorbance of quencher and time and (B) ADMA (in 2% DMSO) in the presence of complex **3**.

Comparison of the  $\Phi_{\Delta}$  values of complexes **4-6** shows that the asymmetrical tetrasubstituted complex **6** has the highest  $\Phi_{\Delta}$  of 0.57 relative to complexes **4** and **5** with  $\Phi_{\Delta}$  values of 0.29 and 0.42, respectively. Although all three Pcs have the greatest

loading on the Fe<sub>3</sub>O<sub>4</sub>@Ag NPs, these NPs induce the lowest enhancement of the  $\Phi_{\Delta}$  of the Pcs relative to the Cys-Ag and NH<sub>2</sub>-Fe<sub>3</sub>O<sub>4</sub> NPs. This could possibly be attributed to the large Cys-Fe<sub>3</sub>O<sub>4</sub>@Ag NPs shielding the Pc from energy transfer processes through the screening effect [231].

Complex **7** does not have the required substituents for conjugation to NPs hence its  $\Phi_{\Delta}$  is just listed in **Table 5.2** and not discussed.

There is an observed reduction of the  $\Phi_{\Delta}$  values in aqueous media relative to DMSO alone due to oxygen having a higher solubility in many organic solvents compared to water [234]. Water molecules also induce a quenching effect on singlet oxygen generation [224]. In addition, aggregation of Pcs tends to reduce their photoactivity [235]. This is because aggregation can cause conversion of the electronic energy to vibrational energy thereby reducing the excited state population [236].

Quantification of the  $\Phi_{\Delta}$  of complex **7** in aqueous media was not possible due to its degradation in the 2% DMSO solvent mixture attributed to instability and hence degradation of the Pc.

**Table 5.2:** The singlet oxygen quantum yields of the Pc and their respective conjugates in different solvents.

<b>Complex</b>	<b>Loading NP:Pc</b>	<b>DMSO</b>	<b>2% DMSO</b>
Complex 1	-	0.30 <sup>a</sup>	0.12
1-Ag	1:7	0.65	0.28
Complex 2	-	0.44	0.25
2-Ag	1:5	0.55	0.32
Complex 3	-	0.58	0.36
3-Ag	1:3	0.68	0.40
Complex 4	-	0.29	0.08
4-Ag	1:2	0.44	0.15
4-Fe <sub>3</sub> O <sub>4</sub>	1:2	0.50	0.11
4-Fe <sub>3</sub> O <sub>4</sub> @Ag	1:4	0.40	0.18
Complex 5	-	0.42	0.11
5-Ag	1:3	0.65	0.16
5-Fe <sub>3</sub> O <sub>4</sub>	1:4	0.60	0.22
5-Fe <sub>3</sub> O <sub>4</sub> @Ag	1:5	0.55	0.18
Complex 6	-	0.57	0.16
6-Ag	1:3	0.75	0.22
6-Fe <sub>3</sub> O <sub>4</sub>	1:3	0.79	0.25
6-Fe <sub>3</sub> O <sub>4</sub> @Ag	1:5	0.62	0.28
Complex 7	-	0.39 <sup>b</sup>	-

<sup>a</sup>Values extrapolated from [118], <sup>b</sup>Studies conducted in toluene.

### 5.3.2 Absolute method

The photochemical properties of Pc-functionalised NFs have been reported to be maintained within the solid polymeric matrix [237]. In this work, the singlet oxygen generating abilities of Pc functionalised polymer-free NFs were evaluated and reported for the first time.

Due to lack of standards, the absolute method [238] (Equations 1.8 and 1.9) was implemented for  $\Phi_{\Delta}$  quantifications of the NFs wherein ADMA (singlet oxygen quencher) was degraded in unbuffered aqueous media. The obtained degradation spectra are shown in **Figure 5.5** (using 1-SiO<sub>2</sub> NFs as an example).

The calculated  $\Phi_{\Delta}$  values for the modified NFs are listed in **Table 5.3**. The low  $\Phi_{\Delta}$  values for the NFs relative to when in solution are due to enhanced charge transfer interactions in water which retard singlet oxygen formation efficiency [239].

In addition, the used absorbance values when quantifying the  $\Phi_{\Delta}$  values of the NFs are those of the Pcs in the NFs and the measured light intensity is that of the light reaching the spectrophotometer cells which may be scattered, hence the  $\Phi_{\Delta}$  values of the Pcs in the NFs are estimates.

The obtained results show that the trends observed in solution are sustained in the NFs i.e. the NFs with both NPs and Pcs have greater  $\Phi_{\Delta}$  than the NFs with Pcs only.

Although singlet oxygen is not a necessity for hydrogen generation which is what the NFs modified with complex **7** were used for, it was still quantified so as to evaluate and compare the photoactivities of the different TiO<sub>2</sub> NFs. Interestingly the **7**@TiO-500 NFs have a higher  $\Phi_{\Delta}$  relative to **7**@TiO-750 and **7**@TiO-950 NFs, possibly due to the Pc and anatase TiO<sub>2</sub> having a greater synergy relative to the rutile. Based on

the ability of the synthesised Pcs, conjugates and NFs to generate singlet oxygen, they were then applied for photocatalytic applications as discussed in the upcoming chapters.

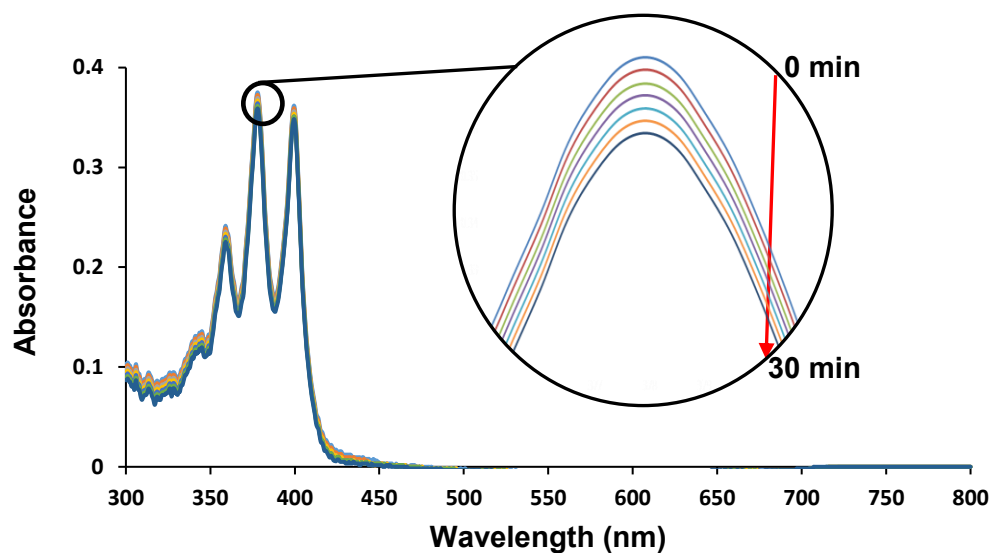


**Figure 5.5:** Photodegradation of ADMA in the presence of 1-SiO<sub>2</sub> NFs. Insert = picture of the NFs in the ADMA solution.

**Table 5.3:** The singlet oxygen quantum yields of the Pcs and their respective conjugates supported on different NFs.

<b>Nanofibers</b>	<b><math>\Phi_{\Delta}</math></b>
<b>1-SiO<sub>2</sub></b>	0.08
<b>1@Ag-SiO<sub>2</sub></b>	0.12
<b>2-SiO<sub>2</sub></b>	0.18
<b>2@Ag-SiO<sub>2</sub></b>	0.22
<b>3-SiO<sub>2</sub></b>	0.15
<b>3@Ag-SiO<sub>2</sub></b>	0.25
<b>4-Hem</b>	0.28
<b>5-Hem</b>	0.25
<b>6-Hem</b>	0.26
<b>6-ZnO</b>	0.16
<b>6-TiO<sub>2</sub></b>	0.22
<b>7-TiO-500</b>	0.25
<b>7-TiO-750</b>	0.12
<b>7-TiO-950</b>	0.09

## 5.4 Closing Remarks

The photophysical properties of the Pcs and their conjugates were successfully determined and so were those of the NFs modified with Pcs. Conjugation of the Pcs to the NPs resulted in suppressed fluorescence and enhanced singlet oxygen generation. Aggregation of the Pcs and their conjugates when supported on NFs and when dissolved in water resulted in them having lower singlet oxygen quantum yields in aqueous solutions relative to organic solvents. The ability of the reported Pcs to generate the highly active singlet oxygen makes them viable candidates for photocatalysis as discussed in the upcoming chapters



# Chapter 6

This chapter gives details on the use of Pcs, NPs and their respective conjugates as antimicrobial agents. It also explores the antimicrobial properties of bare as well as modified SiO<sub>2</sub> and Hem NFs.

## 6.1 Antimicrobial activity of Pcs and Pc-NP conjugates in solution

Due to the ability of the Pc complexes and their respective conjugates to generate singlet oxygen, all their antimicrobial activities were evaluated with the exception of complex **7**. A comparative study on the antimicrobial efficiencies of complexes **1-3** (and their respective conjugates with OLM-Ag NPs) against *S. aureus*, *E. coli* and *C. albicans* was conducted as depicted in **Figure 6.1** (using **3-Ag** as an example).

The antimicrobial activity of the solvent mixture alone (2% DMSO, control) was also evaluated and found to have no effect on the cells. An optimum concentration of 5  $\mu\text{M}$  was determined for complexes **1-3** against *S. aureus* as well as *C. albicans* while 10  $\mu\text{M}$  was applied for *E. coli*.

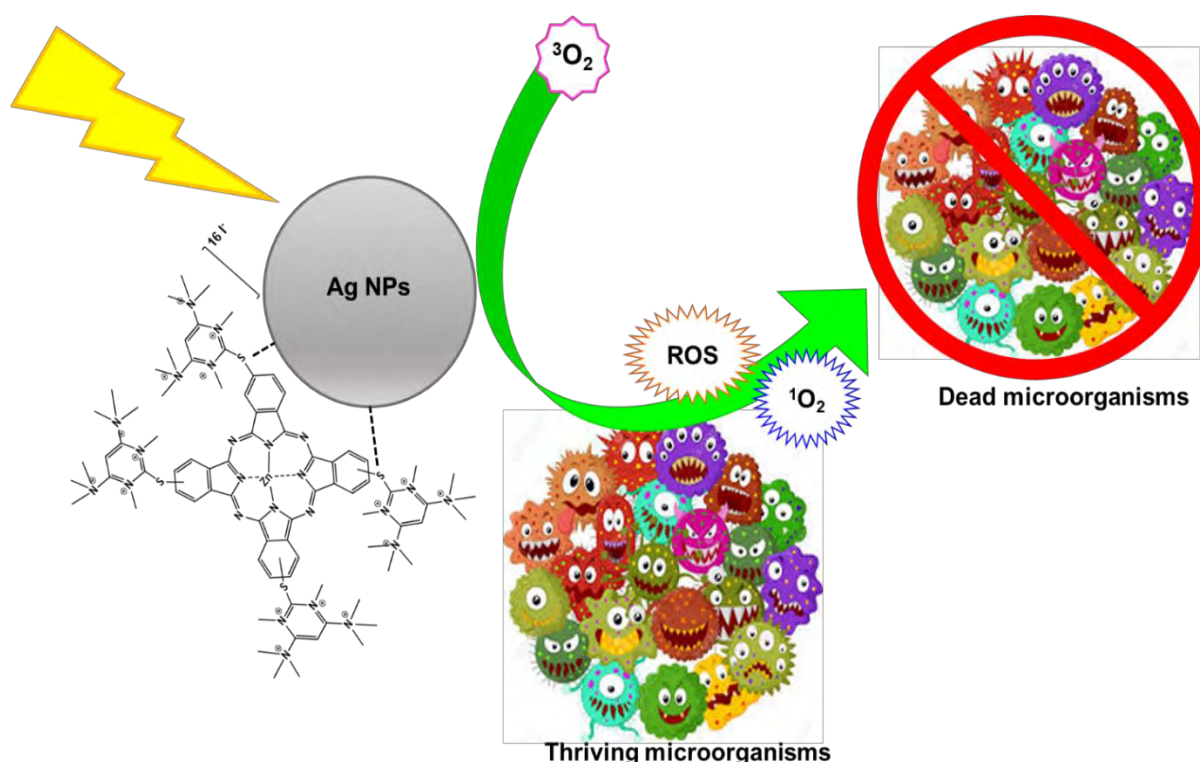


**Figure 6.1:** Illustration of the antimicrobial activity of Pc-NP conjugates against *S. aureus*, *E. coli* and *C. albicans*.

Negligible dark toxicity was observed for complexes **1-3** at elongated exposure times for all the microorganisms (**Figure 6.2**, using studies conducted on *S. aureus* as an example). Increased dark toxicity was however observed for their respective conjugates. This can be attributed to the presence of the Ag NPs which disrupt the integrity of the bacterial cell wall, an act that is not necessarily light-driven but can be light-enhanced [240]. A similar trend was observed for the other microorganisms (not shown).

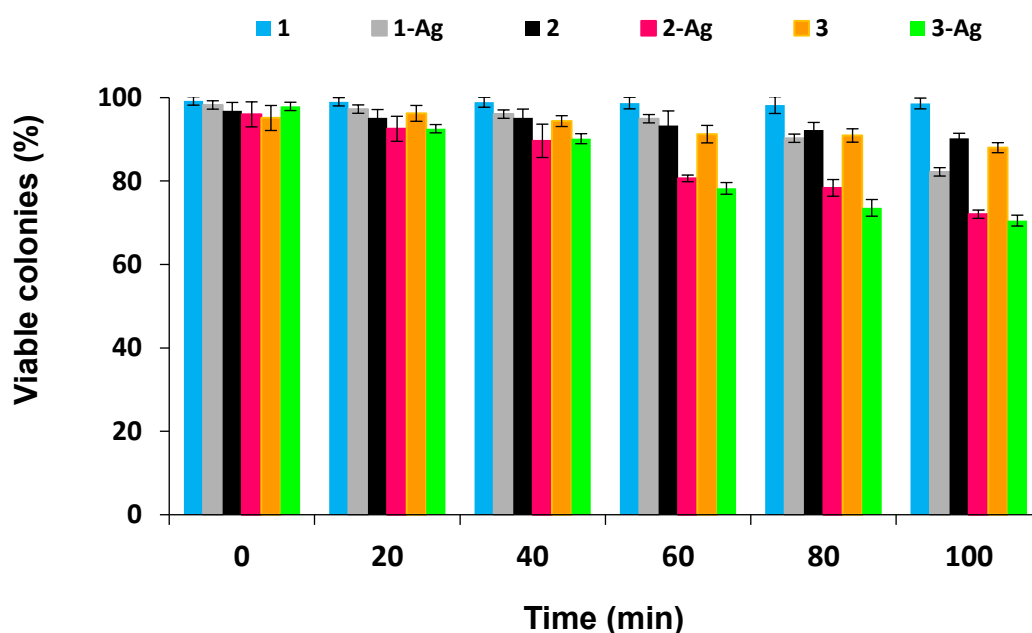


**Figure 6.2:** Dark toxicity studies of complexes **1-3** (5  $\mu$ M) as well as their respective conjugates (**1-Ag**, **2-Ag** and **3-Ag**) against *S. aureus*.

The photo-toxicity studies of the Pcs and their conjugates were conducted as depicted in **Figure 6.3** (using studies conducted with complex **3** and **3-Ag** as examples). The bar graphs depict the survival percentage (viable colonies) of the microorganisms post-treatment with light and the Pcs/conjugates.

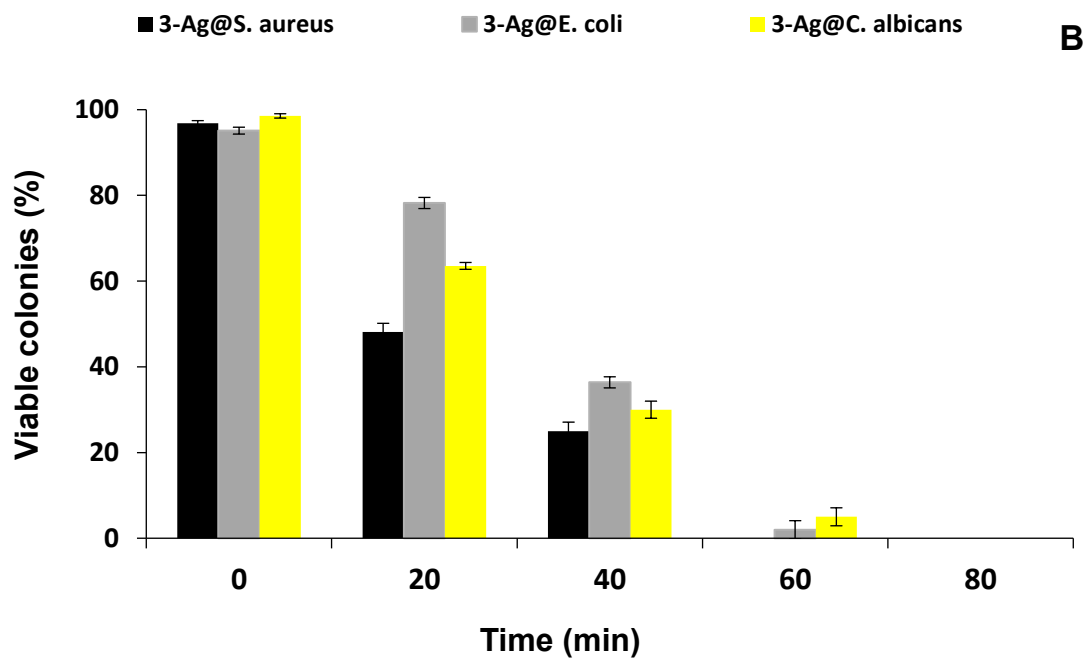
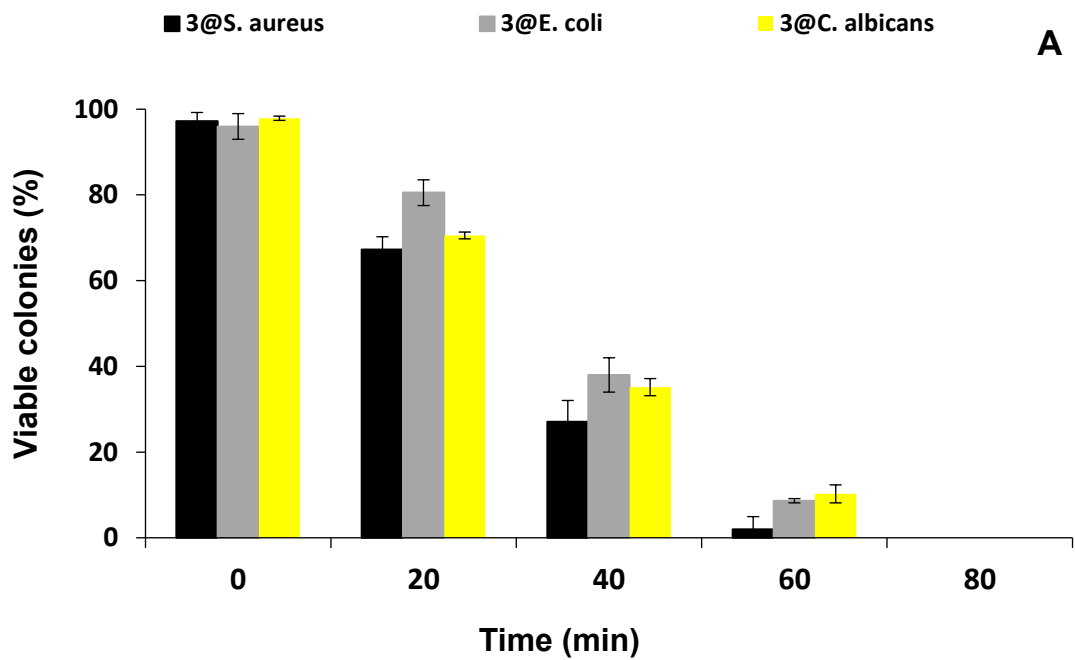


**Figure 6.3:** Graphs showing the percentage reduction of viable colonies of *S. aureus*, *E. coli* and *C. albicans* using (A) **3** and (B) **3-Ag**.

The graphs show a gradual decrease in the percentage of viable microorganisms at elongated irradiation times with *S. aureus* being the quickest to be depleted. This is

expected due to the easily penetrable cell wall of the gram-positive bacteria. The results also show that the conjugation of the Pcs to the Ag NPs enhances their antimicrobial efficiencies. This can be attributed to enhanced singlet oxygen generation. In addition, the conjugation of Pcs to NPs can improve the retention and permeability effect [241]. Similar results were observed for complexes **1** and **2** as well as their respective conjugates (Figures not shown).

The survival curves of *E. coli* (shown as an example) treated with the different Pcs and their respective conjugates are shown in **Figure 6.4**. The plots depict the reduction of the microorganism CFU's using a logarithmic scale. The greatest reduction was observed when complex **3** and its conjugate were applied against *E. coli* unlike the complex **1** which demonstrated little to no activity. A similar trend was observed for *S. aureus* and *C. albicans* (Figures not shown).

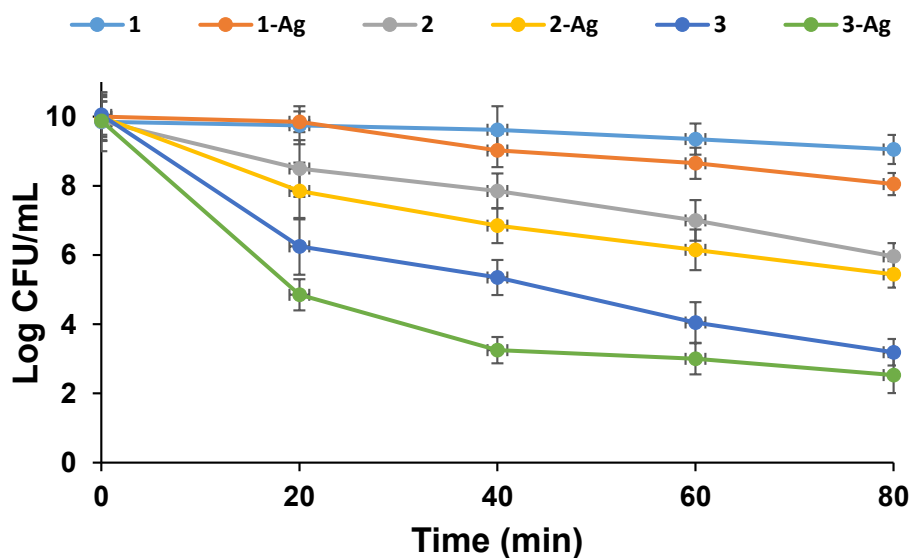


**Figure 6.4:** Survival curves of *E. coli* using the Pc complexes and their respective conjugates in the presence of light.

Quantification of viable bacteria in this work was conducted with log reductions using equation (6.1):

$$\text{log reduction} = \log_{10} (A) - \log_{10} (B) \quad (6.1)$$

where A is the number of viable bacteria pre-treatment and B is the number of viable bacteria post-treatment.

The calculated log reductions for complexes **1-3** as well as their conjugates are listed in **Table 6.1**.

The results show that all Pcs and conjugates have the highest log values for *S. aureus*. This is expected as it is gram-positive and can thus easily take up photosensitisers and undergo photoinactivation. This is due to it only having a capsule and peptidoglycan layer unlike gram-negative bacteria with thicker cell walls [242], hence lower log values were obtained for *E. coli*. Complexes **1** and **2** have particularly low log values against *E. coli*, this can be attributed to them having amino groups. Amino containing Pcs have been reported to show poor PACT activity against *E. coli* [150]. Even though *E. coli* has a low permeability, its log values are higher than those of *C. albicans*. This is not surprising as it has been reported that some bacteria including *E. coli* tend to have an affinity for sulfur containing compounds [243,244].

The obtained log values are in agreement with the  $\Phi_{\Delta}$  values wherein the Pc with the highest  $\Phi_{\Delta}$  was found to possess the highest activity against all the microorganisms. This trend was observed in their respective conjugates too. The higher activity of complex **3** relative to complexes **1** and **2** could also be attributed to it having more positively charged groups which help in orientating the Pc towards destabilizing cell function and cell organization of the microbial cell [245].

**Table 6.1:** Values of log reductions based on the photo-treatment of the microorganisms using complexes **1-6** and their respective conjugates

Sample	$\Phi_{\Delta}$ (2% DMSO)	Loading NP:Pc	log reduction		
			<i>S. aureus</i>	<i>E. coli</i>	<i>C. albicans</i>
Complex 1	0.12	-	3.60	0.80	0.29
1-Ag	0.28	1:7	4.20	1.95	1.01
Complex 2	0.25	-	6.70	3.91	2.50
2-Ag	0.32	1:5	8.10	4.55	3.35
Complex 3	0.36	-	7.38	6.86	5.20
3-Ag	0.40	1:3	8.70	7.35	6.80
Complex 4	0.08	-	1.35	-	-
4-Ag	0.15	1:2	4.15	-	-
4-Fe <sub>3</sub> O <sub>4</sub>	0.11	1:2	4.00	-	-
4-Fe <sub>3</sub> O <sub>4</sub> @Ag	0.18	1:4	6.81	-	-
Complex 5	0.11	-	2.05	-	-
5-Ag	0.16	1:3	4.85	-	-
5-Fe <sub>3</sub> O <sub>4</sub>	0.22	1:2	4.50	-	-
5-Fe <sub>3</sub> O <sub>4</sub> @Ag	0.18	1:5	7.15	-	-
Complex 6	0.16	-	1.55	-	-
6-Ag	0.22	1:3	4.35	-	-
6-Fe <sub>3</sub> O <sub>4</sub>	0.25	1:2	4.25	-	-
6-Fe <sub>3</sub> O <sub>4</sub> @Ag	0.28	1:5	6.85	-	-

In addition, the cationic charges can play an important role in targeting both the extracellular and intracellular components where the photocytotoxic activity occurs [241]. Lastly, the varying extent of aggregation of each of the complexes in the 2% DMSO solution could also be a contributing factor in the activities of the Pc complexes as the highly aggregated form of photosensitisers is quite large and may cause difficulty with penetration into the microbial membrane and wall, resulting in the reduction of its phototoxicity [246].

Since the neutral complex **1** is not effective in the treatment of *E. coli* and *C. albicans* due to their less permeable cell walls, the neutral complexes **4-6** and their respective conjugates were therefore only applied for the photoinactivation of *S. aureus*. Just as with complexes **1-3**, PACT studies were performed in 2% DMSO as complexes **4-6** are not soluble in water alone. The optimisations of the concentrations of the Pcs for PACT activity against *S. aureus* was conducted. A concentration of 5  $\mu$ M of complexes **4-6** was applied in all the solutions including the conjugates.

Just as with complexes **1-3** (and their conjugates), both dark and light studies were conducted for complexes **4-6** (and their conjugates) so as to elucidate whether their activities are light triggered or not. Only the conjugates of Cys-Ag and Cys-Fe<sub>3</sub>O<sub>4</sub>@Ag possessed slight activity in the dark due to antimicrobial activity of Ag as explained before. Phototoxicity studies at different time intervals were however found to show activity for all the catalysts. The photoactivities of the catalysts are demonstrated in **Figure 6.5** (using **4-Fe<sub>3</sub>O<sub>4</sub>@Ag** as an example) wherein significant reduction in bacterial colonies is observed post-irradiation relative to pre-irradiation.



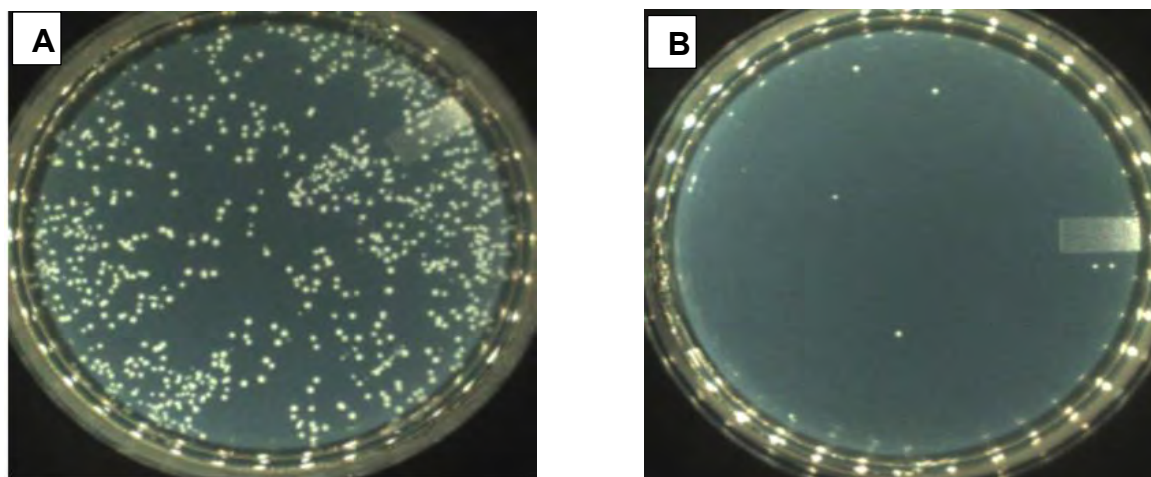


**Figure 6.5:** Image of the bacterial culture (A) before irradiation and (B) after 60 min irradiation during PACT studies using  $4\text{-Fe}_3\text{O}_4\text{@Ag}$ .

Comparison of the log values of the Pcs and their conjugates shows that as expected, there is an increase in activity upon conjugation of the Pcs to each of the NPs (**Table 6.1**). This is due to increased singlet oxygen generation due to the heavy atom effect of the NPs on the Pc. In addition the synergistic interaction of the Pcs to the NPs involves photoactivity from both constituents and in this case  $\text{Fe}_3\text{O}_4$  and Ag NPs are both known catalysts against bacteria [247,248]. For all three Pcs, the conjugates of the  $\text{Fe}_3\text{O}_4\text{@Ag}$  NPs give the best activities. This could be due to the greater loading of Pcs on these NPs and hence higher singlet oxygen generation relative to the other NPs. In addition conjugates of the  $\text{Fe}_3\text{O}_4\text{@Ag}$  NPs are a concoction of three catalysts i.e. a Pc,  $\text{Fe}_3\text{O}_4$  and Ag NPs, hence their great activity.

Comparison of the activities of complexes **4-6** shows that the monosubstituted complex **5** has better activity than the asymmetrical tetrasubstituted complexes **4** and **6** as observed before [249]. This is regardless of complex **6** having a slightly higher  $\Phi_\Delta$  than complexes **4** and **5**, thereby proving that other factors including the extent of aggregation and nature of substituents can influence the PACT activity of Pcs.

## 6.2 Antimicrobial activity of Pc/NP modified electrospun NFs

The antimicrobial efficiencies of the Pcs when supported on NFs were evaluated. This is because antimicrobial studies conducted in solution are only efficient on low microbial concentrations, the Pcs/conjugates have low surface areas and they cannot be effectively retrieved post application (with the exception of the magnetic conjugates).

A comparative study on the antimicrobial efficiencies of complexes **1-3** when supported on SiO<sub>2</sub> NFs was conducted against *S. aureus*, *E. coli* and *C. albicans*. The effect of the presence of Ag NPs on their activities is also reported. The applied NFs were cut to dimensions of 1.3 cm × 1.3 cm. In addition, comparison of the antibacterial activities of the bare and Pc (complexes **4-6**) modified Hem NFs with no incorporated NPs are reported based on their activities against *S. aureus*. Due to their lower yields upon fabrication, the applied NFs were cast to dimensions of 0.8 cm × 0.8 cm.

### 6.2.1 Antimicrobial activity on SiO<sub>2</sub> NFs

The antibacterial activities of the bare and modified SiO<sub>2</sub> NFs with light irradiation and in the dark are shown in **Figures 6.6** and **6.7**, respectively (using bare SiO<sub>2</sub>, Ag-SiO<sub>2</sub>, **1**-SiO<sub>2</sub> and **1@Ag**-SiO<sub>2</sub> NFs against *S. aureus* as examples). A summary of the zones of inhibition i.e. the extent of antimicrobial activities around each of the SiO<sub>2</sub> NFs is listed in **Tables 6.2-6.4** for NFs modified with complexes **1-3**, respectively. The images show that the bare SiO<sub>2</sub> NFs do not exhibit any antimicrobial activity for both light and dark toxicity studies. This is judged by the *S. aureus* colony growing over and around the NFs. Upon irradiation however, all the modified NFs (Ag-SiO<sub>2</sub>, **1**-SiO<sub>2</sub> and **1@Ag**-SiO<sub>2</sub> NFs) demonstrated antibacterial properties as a zone of bacterial inhibition was observed around each of the NFs (**Figure 6.6**). This is because as the NFs are placed

onto the plates, the generated  $\text{Ag}^+$  ions and various ROS (including singlet oxygen) diffuse out thereby preventing the growth of bacteria close to the NFs. As shown on **Table 6.2** and from the images in **Figure 6.6**, the conjugates of the Pc and Ag NPs on the  $\text{SiO}_2$  NFs have the highest zone of inhibition in the light and thus possess the greatest activity against the microorganisms. The lower zones of inhibition of the Ag- $\text{SiO}_2$  and **1**- $\text{SiO}_2$  NFs is indication of the efficiency of the synergistic interaction between the Ag NPs and Pc on the **1**@Ag- $\text{SiO}_2$  NFs. Similar results were observed for the  $\text{SiO}_2$  NFs modified with complexes **2** and **3**. As shown in **Figure 6.7**, the agar plates that were kept in the dark for the modified NFs show that the **1**- $\text{SiO}_2$  NFs do not show any antimicrobial activity in the absence of light as bacterial growth was observed on and around the NFs. The Ag- $\text{SiO}_2$  and **1**@Ag- $\text{SiO}_2$  NFs did however demonstrate dark toxicity against the *S. aureus*, similarly to when the Ag containing NPs were applied for PACT in solution. Comparison of light and dark toxicity studies of these NFs shows that they are more active in the presence of light. This is not surprising because as mentioned before, Ag NPs tend to display light-enhanced antimicrobial activity [240]. In addition, the stabilisation the NPs on the surface of the  $\text{SiO}_2$  NFs may enhance the release and toxicity of the highly reactive  $\text{Ag}^+$  ion in response to irradiation as observed before for substrate and surfactant stabilised Ag NPs [240,250].

As shown in **Table 6.2**, the NFs modified with complex **1** are not active against *E. coli* and *C. albicans* due to their less permeable cell walls as observed before for studies conducted in solution. This shows that the trends of activity observed in solution are the same when the catalysts are supported on NFs. The cationic complexes **2** and **3** show more or less the same behaviour. This shows that the number of charges do not necessarily affect the antimicrobial activities of the Pcs when they are supported on

SiO<sub>2</sub> NFs. Pictorial representations of the different activities of complexes **1-3** against the more resistant *E. coli* are shown in **Figure 6.8** as an example.

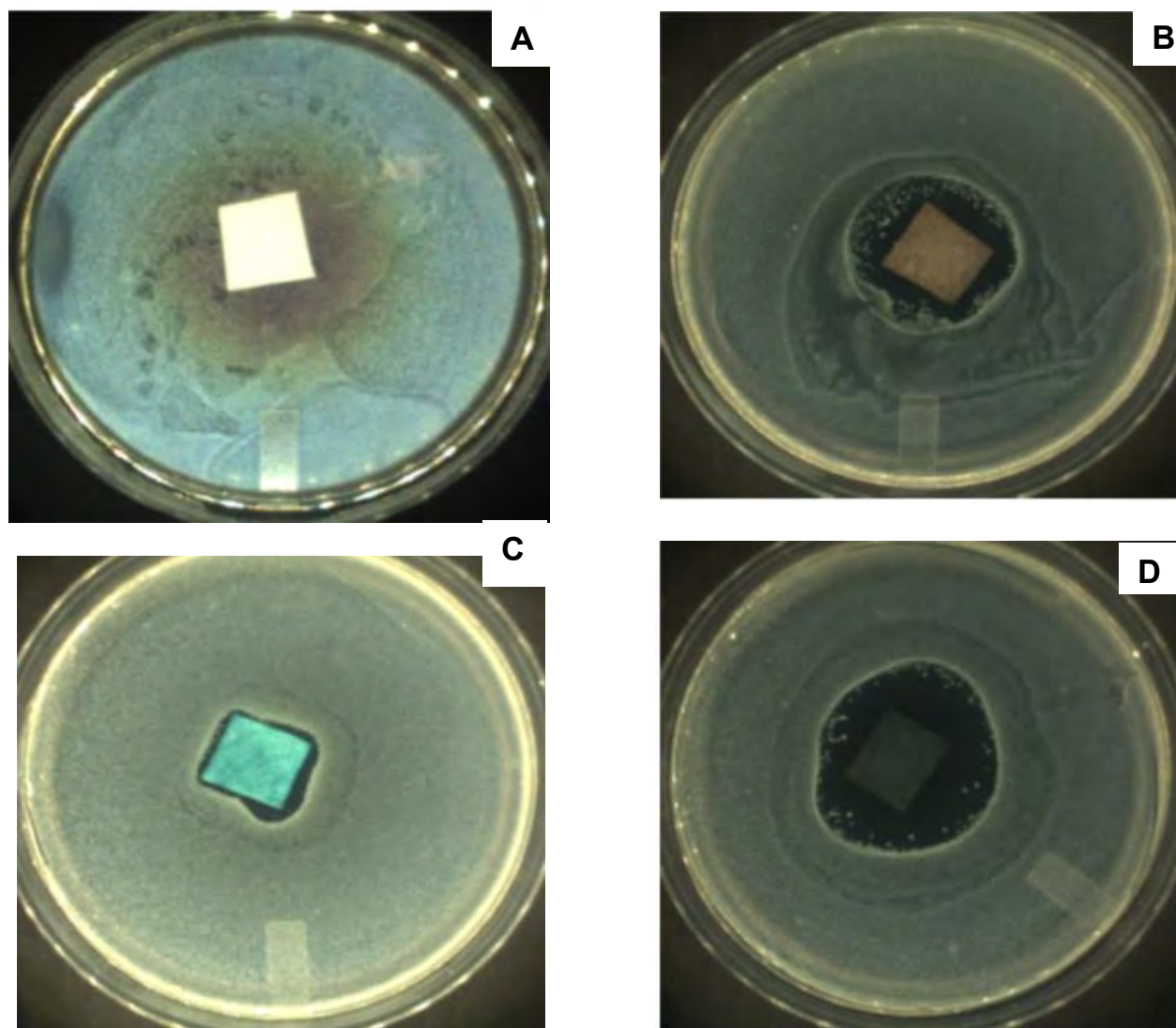


**Figure 6.6:** Images of agar plates showing the antimicrobial effect of: (A) Bare SiO<sub>2</sub> NFs (B) Ag-SiO<sub>2</sub> NFs, (C) **1**-SiO<sub>2</sub> NFs and (D) **1**@Ag-SiO<sub>2</sub> NFs on *S. aureus* after 30 min of irradiation.

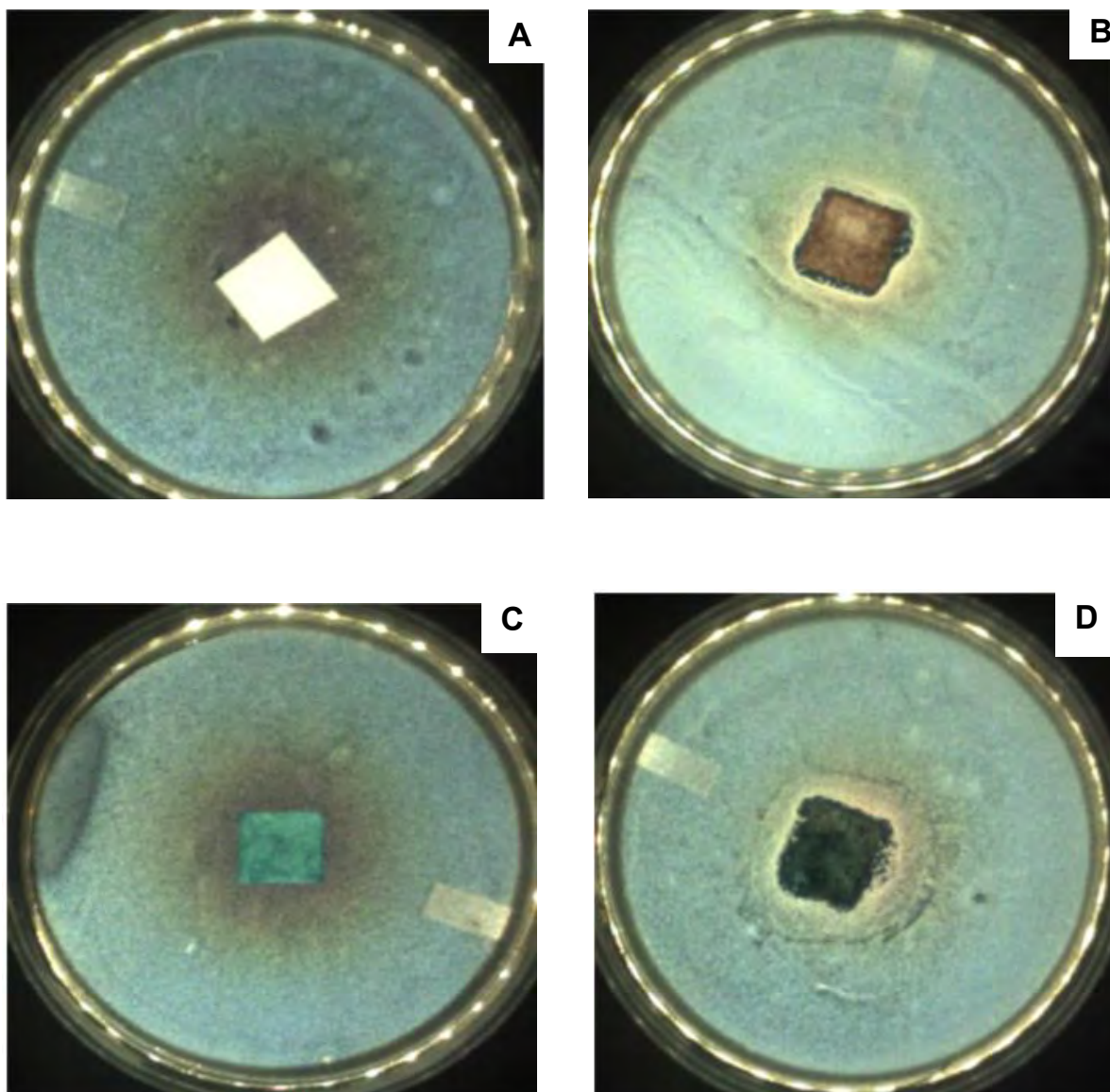


**Figure 6.7:** Images of agar plates showing the antimicrobial effect of: (A) Bare SiO<sub>2</sub> NFs, (B) Ag-SiO<sub>2</sub> NFs, (C) 1-SiO<sub>2</sub> NFs and (D) 1@Ag-SiO<sub>2</sub> NFs on *S. aureus* after 30 min of being kept in the dark.

The obtained results in **Tables 6.2-6.4** also show that regardless of the microorganism, the Pc-Ag NPs supported on the SiO<sub>2</sub> NFs give better results than the Pcs alone or the Ag NPs alone. Unlike 1-SiO<sub>2</sub> which only has antimicrobial activity against *S. aureus*, 2-SiO<sub>2</sub> and 3-SiO<sub>2</sub> are active against all the microorganisms with

the best activity being against the easily penetrable *S. aureus*, followed by the more complex *E. coli* and *C. albicans*.

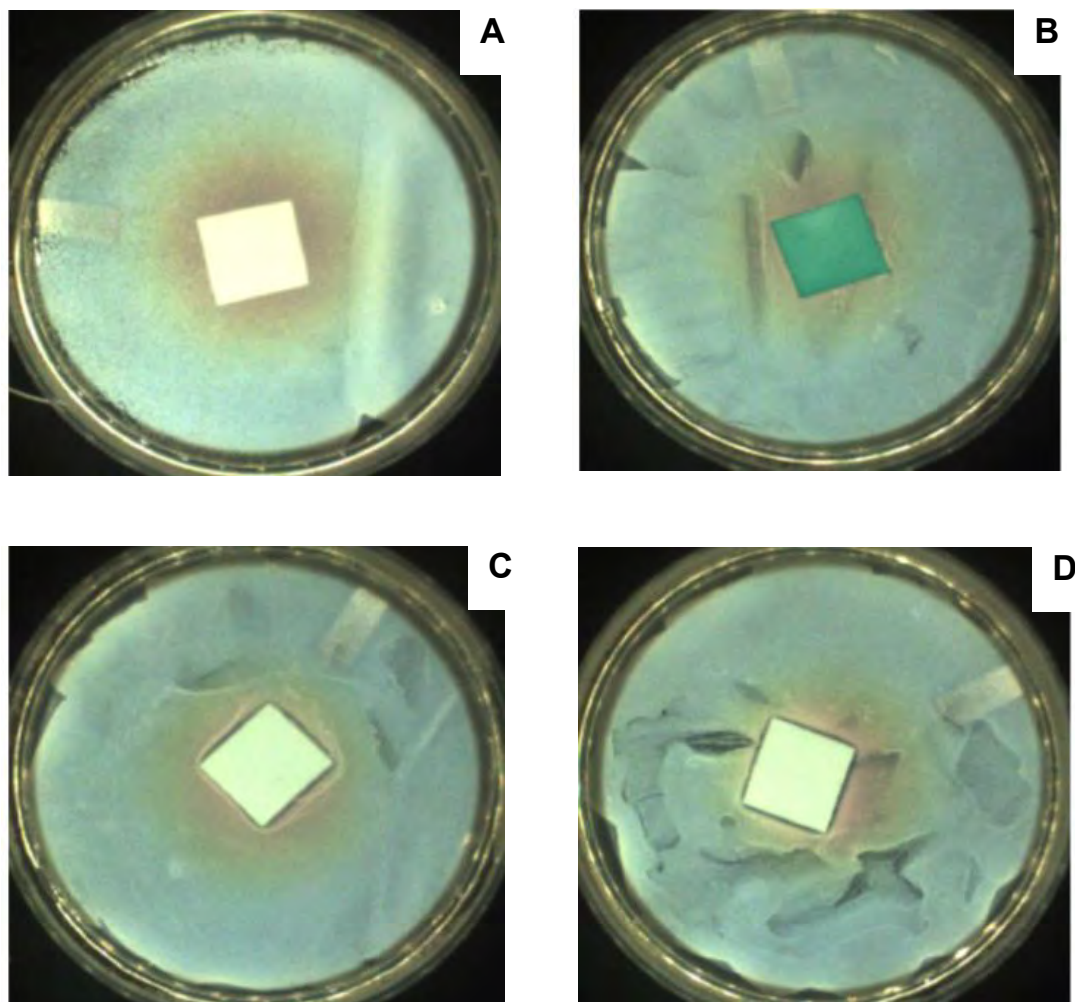


**Figure 6.8:** Images of agar plates showing the antimicrobial effect of: (A) Bare SiO<sub>2</sub> (B) 1-SiO<sub>2</sub>, (C) 2-SiO<sub>2</sub> and (D) 3-SiO<sub>2</sub> NFs on *E. coli* after 30 min of irradiation.

Since the 1-SiO<sub>2</sub> NFs alone do not possess any activity against *E. coli* and *C. albicans*, the activity of the 1@Ag-SiO<sub>2</sub> NFs against these microbes can be attributed to the presence of the Ag NPs which have been reported be active against both of them [251,252].

**Table 6.2:** Antibacterial efficiencies of the bare and complex **1** modified SiO<sub>2</sub> NFs

<b>Microorganisms</b>	<b>Nanofibers</b>	<b>Zone of inhibition (Light) mm</b>	<b>Zone of inhibition (Dark) mm</b>
<b>S. aureus</b>	Bare SiO <sub>2</sub> NFs	-	-
	Ag-SiO <sub>2</sub> NFs	9.50	6.50
	<b>1</b> -SiO <sub>2</sub> NFs	7.00	-
	<b>1</b> @Ag-SiO <sub>2</sub> NFs	17.0	6.00
<b>E. coli</b>	Bare SiO <sub>2</sub> NFs	-	-
	Ag-SiO <sub>2</sub> NFs	7.50	6.50
	<b>1</b> -SiO <sub>2</sub> NFs	-	-
	<b>1</b> @Ag-SiO <sub>2</sub> NFs	8.50	8.00
<b>C. albicans</b>	Bare SiO <sub>2</sub> NFs	-	-
	Ag-SiO <sub>2</sub> NFs	7.00	6.00
	<b>1</b> -SiO <sub>2</sub> NFs	-	-
	<b>1</b> @Ag-SiO <sub>2</sub> NFs	8.50	8.00

**Table 6.3:** Antimicrobial efficiencies of the bare and complex **2** modified SiO<sub>2</sub> NFs

<b>Microorganisms</b>	<b>Nanofibers</b>	<b>Zone of inhibition (Light) mm</b>	<b>Zone of inhibition (Dark) mm</b>
<b>S. aureus</b>	Bare SiO <sub>2</sub> NFs	-	-
	Ag-SiO <sub>2</sub> NFs	9.50	6.50
	<b>2</b> -SiO <sub>2</sub> NFs	12.0	-
	<b>2</b> @Ag-SiO <sub>2</sub> NFs	19.5	8.00
<b>E. coli</b>	Bare SiO <sub>2</sub> NFs	-	-
	Ag-SiO <sub>2</sub> NFs	7.50	6.50
	<b>2</b> -SiO <sub>2</sub> NFs	6.00	-
	<b>2</b> @Ag-SiO <sub>2</sub> NFs	9.00	7.50
<b>C. albicans</b>	Bare SiO <sub>2</sub> NFs	-	-
	Ag-SiO <sub>2</sub> NFs	7.00	6.00
	<b>2</b> -SiO <sub>2</sub> NFs	7.50	-
	<b>2</b> @Ag-SiO <sub>2</sub> NFs	9.50	7.00



**Table 6.4:** Antimicrobial efficiencies of the bare and complex **3** modified SiO<sub>2</sub> NFs

Microorganisms	Nanofibers	Zone of inhibition (Light) mm	Zone of inhibition (Dark) mm
<b>S. aureus</b>	Bare SiO <sub>2</sub> NFs	-	-
	Ag-SiO <sub>2</sub> NFs	9.50	6.50
	<b>3</b> -SiO <sub>2</sub> NFs	11.0	-
	<b>3</b> @Ag-SiO <sub>2</sub> NFs	20.0	8.00
<b>E. coli</b>	Bare SiO <sub>2</sub> NFs	-	-
	Ag-SiO <sub>2</sub> NFs	7.50	6.50
	<b>3</b> -SiO <sub>2</sub> NFs	6.00	-
	<b>3</b> @Ag-SiO <sub>2</sub> NFs	9.00	7.00
<b>C. albicans</b>	Bare SiO <sub>2</sub> NFs	-	-
	Ag-SiO <sub>2</sub> NFs	7.00	6.00
	<b>3</b> -SiO <sub>2</sub> NFs	7.50	-
	<b>3</b> @Ag-SiO <sub>2</sub> NFs	9.00	7.50

Unlike in studies conducted in solution, the obtained results show that increased charges on the Pcs have no consistent effect on the photoinactivation efficiencies of the NFs as the **2**-SiO<sub>2</sub> and **3**-SiO<sub>2</sub> NFs have similar activities.

### 6.2.2 Antimicrobial activity on Hem NFs

The antimicrobial properties of the bare and Pc modified Hem NFs were evaluated against *S. aureus* with light irradiation as shown in **Figure 6.9** (using the bare Hem and 4-Hem NFs as examples). A summary of the zones of inhibition is listed in **Table 6.5**. The bare and modified Hem NFs do not exhibit any dark toxicity hence no results are reported. Upon irradiation however, the bare and modified NFs (4-Hem, 5-Hem and 6-Hem demonstrated antibacterial properties as a zone of bacterial inhibition was observed around each of the NFs.

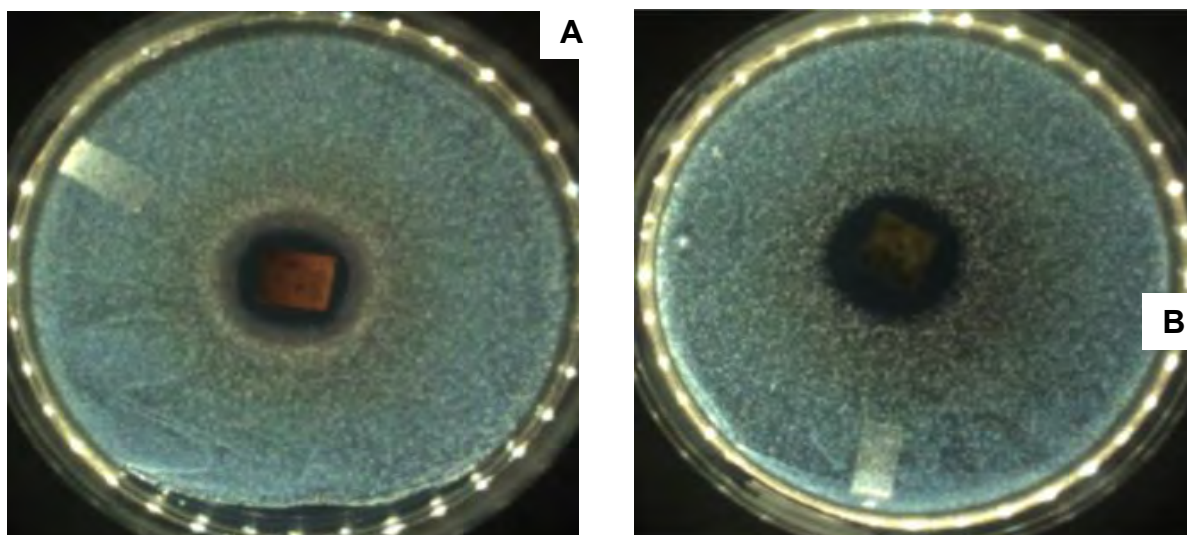


**Figure 6.9:** Images of agar plates showing the antimicrobial effect of: (A) Bare Hem NFs and (B) 4-Hem NFs on *S. aureus* after 30 min of irradiation.

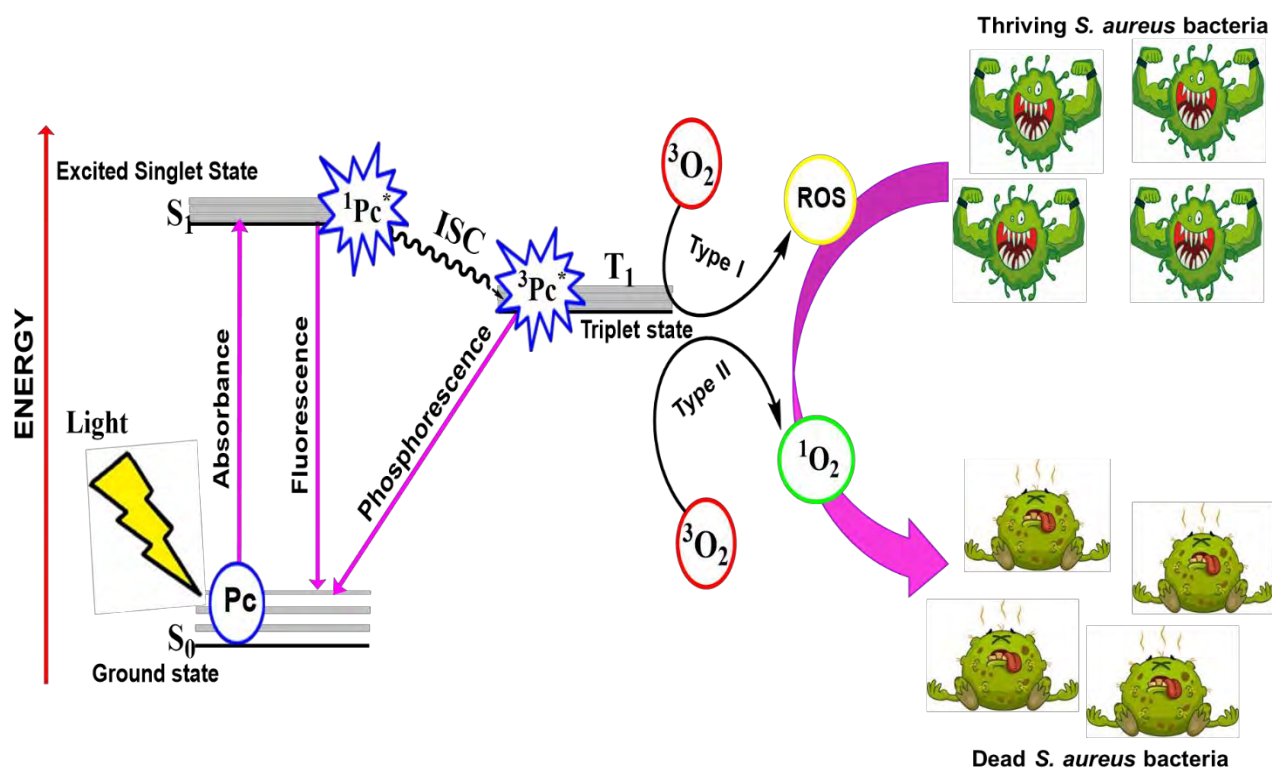
The obtained results show that although the Hem NFs demonstrate antibacterial activities, it is enhanced in the presence of the Pcs. Comparison of the degree of enhancement between the Pcs shows that they all have more or less the same extent of enhancement with complex **5** being slightly better. Interesting to note is that unlike the SiO<sub>2</sub> NFs, the Bare Hem also possess significant dark toxicity which is not enhanced in the presence of any of the Pcs.

**Table 6.5:** Antibacterial efficiencies of the bare and the Hem NFs modified with complexes **4-6**

Microorganisms	Nanofibers	Zone of inhibition (Light) mm	Zone of inhibition (Dark) mm
<b>S. aureus</b>	Bare Hem NFs	6.50	6.00
	<b>4</b> -Hem NFs	8.00	6.00
	<b>5</b> -Hem NFs	8.50	6.20
	<b>6</b> -Hem NFs	8.00	6.10

### 6.3 Mechanism of PACT activity

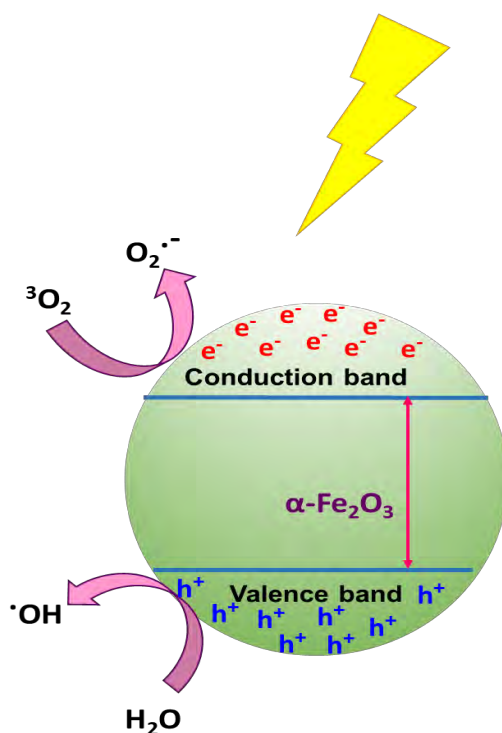
From the obtained results, it is evident that the trend observed for the antimicrobial activities of the Pc and NP based catalysts is the same in solution and when supported on NFs. The mechanism of the antimicrobial activity of the reported catalysts is demonstrated in **Scheme 6.1**. The excitation of a Pc with visible light to its excited singlet state causes intersystem crossing to its forbidden excited triplet state. In the presence of molecular oxygen, electron and energy transfer processes occur leading to the formation of ROS (Type I mechanism) and singlet oxygen (Type II mechanism), respectively. The generated ROS (and singlet oxygen) can be lethal to microorganisms [253]. The antimicrobial activity of the Ag NPs in particular in solution and when supported on SiO<sub>2</sub> NFs is attributed to their ability to trigger membrane leakage and cell death or other physiological disturbances by Ag<sup>+</sup> ions generation [240].



**Scheme 6.1:** Mechanism of microbial photoinactivation of Pcs/ Pc-NP conjugates in solution and when supported on NFs. ISC = intersystem crossing, ROS = reactive oxygen species.

The antimicrobial activity of the Pc-NP conjugates in solution and when supported on  $SiO_2$  NFs is as a result of the synergistic interaction between the Pc and NPs resulting in combination therapy against the microorganisms using properties adopted from both the Pc and NPs. The enhanced antimicrobial efficiency of the conjugates can therefore be attributed to the heavy atom effect that the NPs impose on the Pc. This results in enhanced triplet state population and thus ROS (including singlet oxygen) production leading to enhanced antimicrobial efficiencies. In addition, the modified NFs are able to kill microbes on contact by a disruptive action on their cell membranes [254].

Additional mechanisms for the antibacterial activities of hematite nanocatalysts involve damaging the cell membranes via disturbance in metal/metal ion homeostasis, protein and enzyme dysfunction, genotoxicity and photokilling [255,256]. Another explanation is depicted in **Scheme 6.2** and highlights the formation of electron–hole pairs upon activation of the Hem NFs with light irradiation. The generated positive holes are direct oxidants and essential for the creation of reactive hydroxyl radicals from water. The electrons on the other hand reduce dissolved oxygen molecules into superoxide anion radicals. The generated radicals during this process can react with organic substances inside bacterial cells which cause DNA rupture of bacterial cell and inactivation of enzymes leading to bacterial death [204].



**Scheme 6.2:** Mechanism of antimicrobial activity of the Hem NFs.

## 6.4 Closing Remarks

The antimicrobial properties of Pcs and Pc-NP conjugates in solution and when supported on electrospun NFs have been proven. The synergistic interaction of Pcs and NPs results in enhanced activity relative to the Pcs alone in solution and when supported on NFs. Unlike the bare SiO<sub>2</sub> NFs, the Hem NFs possess slight antibacterial activity which is enhanced in the presence of the Pcs. Modification of the electrospun NFs with Pcs and NPs therefore alters their photophysicochemical and thus antimicrobial properties.

# Chapter 7

This chapter gives details on the photodegradation efficiencies of bare as well as Pc modified Hem, TiO<sub>2</sub> and ZnO NFs. Comparative studies and kinetics calculations are described.

## 7.1 Photodegradation of Methyl Orange (MO)

Chapter 6 demonstrated that Hem NFs possessed antibacterial activity even when unmodified. This chapter therefore explores the versatility of the Hem NFs by reporting on their photodegradation efficiencies against MO and compares them to those of other semiconductor NFs i.e. ZnO and TiO<sub>2</sub>. The conducted studies also report on the effect that modification of Hem NFs with a monosubstituted (complex **5**) vs a tetrasubstituted Pc (complex **6**) has on their photocatalytic activity. For comparison, the photodegradation efficiencies of the ZnO and TiO<sub>2</sub> NFs when modified with complex **6** are also reported as an example. Spectral changes that occurred upon exposure of MO to the NFs are shown in **Figure 7.1** (using **6**-TiO<sub>2</sub> NFs as an example).

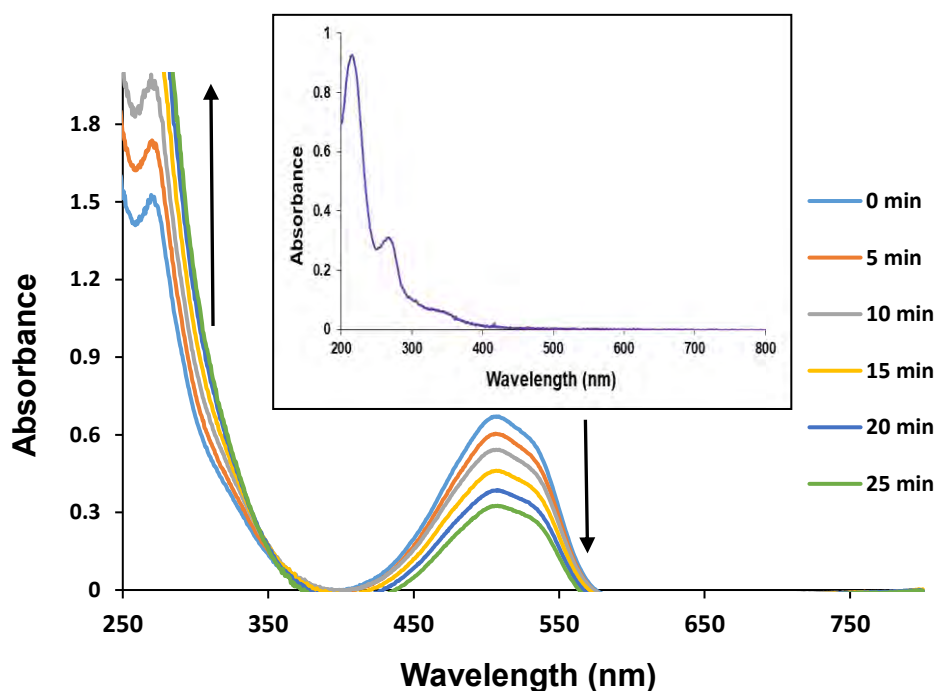


**Figure 7.1:** UV/Vis spectral changes in the photodegradation of  $1.44 \times 10^{-5}$  M MO using **6**-TiO<sub>2</sub> NFs at pH 2.5 with 5 minute irradiation intervals. Insert = Spectrum of degradation product(s) of  $1.44 \times 10^{-5}$  molL<sup>-1</sup> MO after 60 min of irradiation in the presence of **6**-TiO<sub>2</sub> NFs.



The observed spectral changes prove that indeed the pollutant does not just adsorb on the surface of the NFs but is degraded instead. There is an observed decrease in the intensity of the absorption peaks at 506 nm which is attributed to the azo bond. This explains the observed fading in the colour of the MO solution with increased irradiation time. The azo bond determines the colour of the dyes and is very reactive, usually undergoing oxidation hence leading to fading of the dye colour [157]. The spectrum also shows an increase the peaks below 330 nm which have been attributed to the presence of benzene rings [257]. This therefore suggests that the benzene rings remain intact and are not degraded during the photodegradation of MO. This is verified in the spectrum of the final degradation product(s) which is shown in **Figure 7.1** (insert) and reveals that the product(s) only absorbs light in the UV-region of the spectrum.

The photodegradation of MO using Pc based catalysts has been reported to yield poly(catechol) and 2-amino-5(3-hydroxy-4-oxo-cyclohexa-2,5-dienylideneamino)-benzene sulphonic acid as degradation products [258]. No spectral changes were observed when studies were conducted in the absence of irradiation and oxygen (i.e. nitrogen purged solutions). This is an indication that light and molecular oxygen are prerequisites for the photodegradation process. Similar spectral changes were observed in the degradation of MO using the other NFs (not shown).

The photocatalytic degradation of MO was conducted on five different concentrations:  $1.44 \times 10^{-5}$ ,  $2.80 \times 10^{-5}$ ,  $3.70 \times 10^{-5}$ ,  $4.45 \times 10^{-5}$  and  $6.6 \times 10^{-5} \text{ molL}^{-1}$ . A selection of kinetics plots for the degradation of MO are shown in **Figure 7.2** (using studies conducted with 6-TiO<sub>2</sub> NFs as examples).

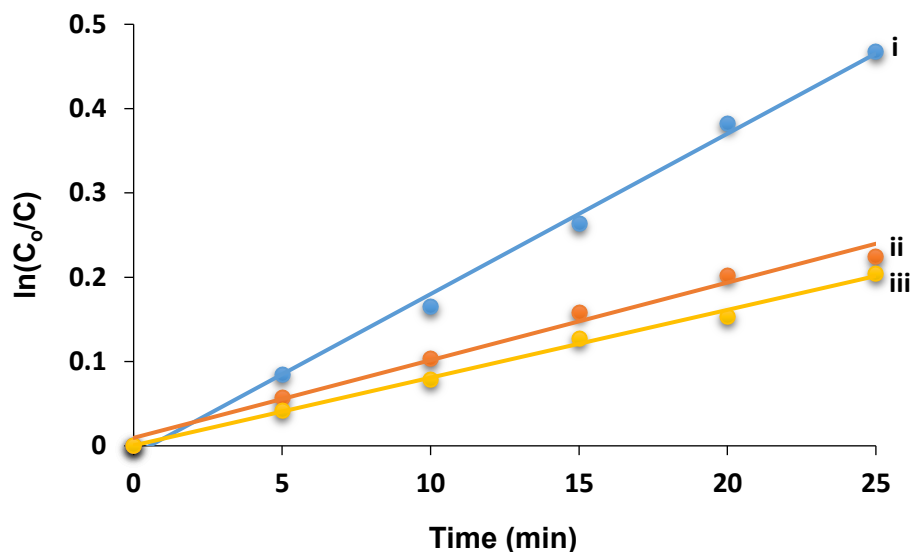


**Figure 7.2:** Pseudo first order kinetics plot for the degradation of i.  $1.44 \times 10^{-5}$ , ii.  $3.70 \times 10^{-5}$  and iii  $4.45 \times 10^{-5}$  mol L<sup>-1</sup> MO using **6**-TiO<sub>2</sub> NFs at pH 2.5.

The plots are well fitted by a mono-exponential curve, suggesting that degradation using the NFs follows pseudo first order kinetics as observed before in the degradation of MO with semiconductor based catalysts [259,260].

The tabulated results (**Tables 7.1-7.3**) show that the kinetic rate constant ( $k_{obs}$ ) decreases with increase in the concentration while the half-lives ( $t_{1/2}$ ) and rates of degradation increased. This basically means that for the same illumination time, the relative amount of MO decomposed is less for the more concentrated solutions due to the elongated  $t_{1/2}$  [261].

Due to the easy retrievability of the NFs post application, they were rinsed with water followed by ethanol, dried in a high vacuum fumehood overnight and then reused. The reused NFs showed a slight reduction in the photodegradation efficiencies of the NFs, possibly be due to the adsorption of species on the photocatalyst surface resulting in the blocking of some active sites [261].

As shown in **Tables 7.1-7.3**, comparison of the degradation efficiencies of the bare NFs shows that the Hem NFs have better activity than ZnO and TiO<sub>2</sub> NFs as they have greater rates of degradation. This can be attributed to the bare TiO<sub>2</sub> and ZnO NFs having band gap energies of 3.19 and 3.28 eV, respectively showing their limited range of light absorption relative to the Hem with a band gap energy of 2.20 eV. In addition, the surface area of the Hem NFs (18.25 m<sup>2</sup>g<sup>-1</sup>) is higher than that of the TiO<sub>2</sub> (13.40 m<sup>2</sup>g<sup>-1</sup>) and ZnO (11.36 m<sup>2</sup>g<sup>-1</sup>) NFs (**Table 4.2**) and it has been reported that increased catalyst surface area can enhance its photocatalytic activity [**194**]. The poor activity of the ZnO NFs relative to the other NFs can be attributed to the dissolution and photodissolution of ZnO under acidic conditions [**262,263**].

Comparison of the degradation efficiencies of the bare relative to the Pc modified NFs on the other hand depicts that the modified NFs are better photocatalysts than the bare ones. This is because the modified NFs are able to generate singlet oxygen as shown in **Table 5.3**. Furthermore the modified NFs have two light absorbers and have band gap energies that extend into the visible region. Comparison of the effect of the type of used Pc (i.e. monosubstituted (**5**) and tetrasubstituted (**6**)) for the modification of the NFs was conducted by supporting complexes **5** and **6** on Hem NFs. The results show that the **6**-Hem NFs have slightly better activity than the **5**-Hem NFs (**Table 7.1**). Since the singlet oxygen quantum yields of the NFs are more or less the same (**Table 5.3**), the better enhancement of complex **6** on the activity of the Hem NFs can be attributed to the nature of its substituents. The induced directionality through the “push” (electron donating) and “pull” (electron withdrawing) functional groups on the Pc ring could make for better interaction between the Pc and Hem NFs as reported before [**264**]. Complex **6** contains three *tert*-butyl and two carboxylic acid groups that act as “push” and “pull” groups, respectively while complex **5** only has carboxylic acid groups.

**Table 7.1:** Kinetic data for the degradation of MO using the bare Hem, 5-Hem and 6-Hem NFs

[MO] × 10 <sup>-5</sup> (mol L <sup>-1</sup> )	k <sub>obs</sub> (min <sup>-1</sup> )			Rate (10 <sup>-7</sup> mol L <sup>-1</sup> min <sup>-1</sup> )			t <sub>1/2</sub> (min)		
	bare Hem	5-Hem	6-Hem	bare Hem	5-Hem	6-Hem	bare Hem	5-Hem	6-Hem
1.44	0.013 (0.010)	0.015 (0.014)	0.016 (0.015)	1.87 (1.44)	2.16 (2.06)	2.33 (2.22)	53.31 (69.30)	46.20 (48.46)	42.78 (45.00)
2.80	0.0083 (0.0068)	0.0095 (0.0093)	0.010 (0.010)	2.32 (1.90)	2.66 (2.60)	2.83 (2.80)	84.51 (101.9)	72.95 (74.52)	68.61 (69.30)
3.70	0.0065 (0.0052)	0.0075 (0.0064)	0.0078 (0.0070)	2.41 (1.92)	2.78 (2.37)	2.89 (2.59)	106.6 (133.2)	92.40 (108.3)	88.85 (99.00)
4.45	0.0058 (0.0045)	0.0067 (0.0057)	0.0074 (0.0063)	2.58 (2.00)	2.98 (2.54)	3.29 (2.80)	119.5 (154.0)	103.4 (121.6)	93.65 (110.0)
6.60	0.0039 (0.0030)	0.0045 (0.0034)	0.0050 (0.0037)	2.57 (1.98)	2.97 (2.24)	3.30 (2.44)	177.7 (231.0)	154.0 (203.8)	138.6 (187.3)

Values in brackets are the results obtained for the reused catalysts.

**Table 7.2:** Kinetic data for the degradation of MO using bare ZnO and 6-ZnO NFs

[MO] $\times 10^{-5}$ (mol L <sup>-1</sup> )	k <sub>obs</sub> (min <sup>-1</sup> )		Rate (10 <sup>-7</sup> mol L <sup>-1</sup> min <sup>-1</sup> )		t <sub>1/2</sub> (min)	
	Bare ZnO	6-ZnO	Bare ZnO	6-ZnO	Bare ZnO	6-ZnO
<b>1.44</b>	0.0089 (0.0083)	0.016 (0.015)	1.28 (1.20)	2.30 (2.16)	77.87 (83.49)	43.31 (46.20)
<b>2.80</b>	0.0056 (0.0052)	0.0099 (0.0094)	1.57 (1.46)	2.77 (2.63)	123.8 (133.3)	70.00 (73.72)
<b>3.70</b>	0.0047 (0.0045)	0.0080 (0.0076)	1.74 (1.67)	2.96 (2.81)	147.4 (154.0)	86.63 (91.18)
<b>4.45</b>	0.0041 (0.0037)	0.0070 (0.0067)	1.82 (1.65)	3.12 (2.98)	169.0 (187.3)	99.00 (103.4)
<b>6.60</b>	0.0028 (0.0027)	0.0050 (0.0048)	1.85 (1.78)	3.30 (3.17)	247.5 (256.7)	138.6 (144.4)

Values in brackets are the results obtained for the reused catalysts.

**Table 7.3:** Kinetic data for the degradation of MO using bare TiO<sub>2</sub> and 6-TiO<sub>2</sub> NFs

[MO] × 10 <sup>-5</sup> (mol L <sup>-1</sup> )	k <sub>obs</sub> (min <sup>-1</sup> )		Rate (10 <sup>-7</sup> mol L <sup>-1</sup> min <sup>-1</sup> )		t <sub>1/2</sub> (min)	
	Bare TiO <sub>2</sub>	6-TiO <sub>2</sub>	Bare TiO <sub>2</sub>	6-TiO <sub>2</sub>	Bare TiO <sub>2</sub>	6-TiO <sub>2</sub>
<b>1.44</b>	0.0099 (0.0090)	0.019 (0.018)	1.43 (1.30)	2.73 (2.59)	70.00 (77.00)	36.47 (38.50)
<b>2.80</b>	0.0069 (0.0063)	0.012 (0.011)	1.93 (1.76)	3.36 (3.08)	100.4 (110.0)	57.75 (63.00)
<b>3.70</b>	0.0054 (0.0051)	0.0092 (0.0087)	2.00 (1.89)	3.40 (3.22)	128.3 (135.9)	75.32 (79.66)
<b>4.45</b>	0.0046 (0.0041)	0.0080 (0.0073)	2.05 (1.82)	3.65 (3.25)	157.5 (169.0)	86.63 (94.93)
<b>6.60</b>	0.0032 (0.0029)	0.0057 (0.0051)	2.11 (1.91)	3.76 (3.37)	216.6 (239.0)	121.6 (135.9)

Values in brackets are the results obtained for the reused catalysts.

**Table 7.4:** Summary of the rates of degradation of MO using the semiconductor NFs

[MO]	Rate of degradation ( $10^{-7} \text{ molL}^{-1}\text{min}^{-1}$ )					
	Bare Hem	<b>6</b> -Hem	Bare ZnO	<b>6</b> -ZnO	Bare TiO <sub>2</sub>	<b>6</b> -TiO <sub>2</sub>
<b>1.44</b>	1.87 (1.44)	2.33 (2.22)	1.28 (1.20)	2.30 (2.16)	1.43 (1.30)	2.73 (2.59)
<b>2.80</b>	2.32 (1.90)	2.83 (2.80)	1.57 (1.46)	2.77 (2.63)	1.93 (1.76)	3.36 (3.08)
<b>3.70</b>	2.41 (1.92)	2.89 (2.59)	1.74 (1.67)	2.96 (2.81)	2.00 (1.89)	3.40 (3.22)
<b>4.45</b>	2.58 (2.00)	3.29 (2.80)	1.82 (1.65)	3.12 (2.98)	2.05 (1.82)	3.65 (3.25)
<b>6.60</b>	2.57 (1.98)	3.30 (2.44)	1.85 (1.78)	3.30 (3.17)	2.11 (1.91)	3.76 (3.37)

Values in brackets are the results obtained for the reused catalysts.

All the semiconductor NFs modified with complex **6** (**6**-Hem NFs, **6**-ZnO and **6**-TiO<sub>2</sub>) were compared to evaluate the extent of enhancement of the photocatalytic activities of the bare NFs upon modification and the rates of degradation are summarised in **Table 7.4**. The results show that the **6**-TiO<sub>2</sub> NFs have the greatest overall activity. The **6**-TiO<sub>2</sub> NFs also show the greatest enhancement of activity relative to their bare counterparts while the **6**-Hem and **6**-ZnO NFs show comparable photodegradation efficiencies.

The relationship between the concentration and rate of degradation of organic pollutants in heterogenous photocatalytic reactions such as those reported herein can be expressed using the Langmuir-Hinshelwood model. The model has been successfully employed to describe kinetics of solid-liquid reactions in the degradation of various pollutants using semiconductor based catalysts [44,259]. This model basically suggests that during the photocatalytic process, the reactants adsorb on the surface of catalyst in the first step followed by reactions between adsorbed reactants [265]. This basically entails the oxidation of the dye through attacks by the various reactive oxygen species (ROS) (including singlet oxygen) from the photocatalysts.

The Langmuir–Hinshelwood kinetic model [266], **Equation 7.1**:

$$\frac{1}{r_0} = \frac{1}{kK_A C_0} + \frac{1}{k} \quad (7.1)$$

where  $r_0$  is the initial photocatalytic degradation rate ( $\text{mol L}^{-1} \text{min}^{-1}$ ),  $C_0$  is the initial concentration of MO ( $\text{mol L}^{-1}$ ),  $k$  is the apparent reaction rate constant ( $\text{mol L}^{-1} \text{min}^{-1}$ ) and  $K_A$  is the adsorption coefficient ( $\text{mol}^{-1} \text{L}$ ) [266].

Plots of the reciprocal of the initial rate of degradation against the reciprocal of the concentration of MO for all the photocatalysts were found to be linear with non-zero intercepts as shown in **Figure 7.3** (using the fresh and reused 6-TiO<sub>2</sub> NFs as examples).



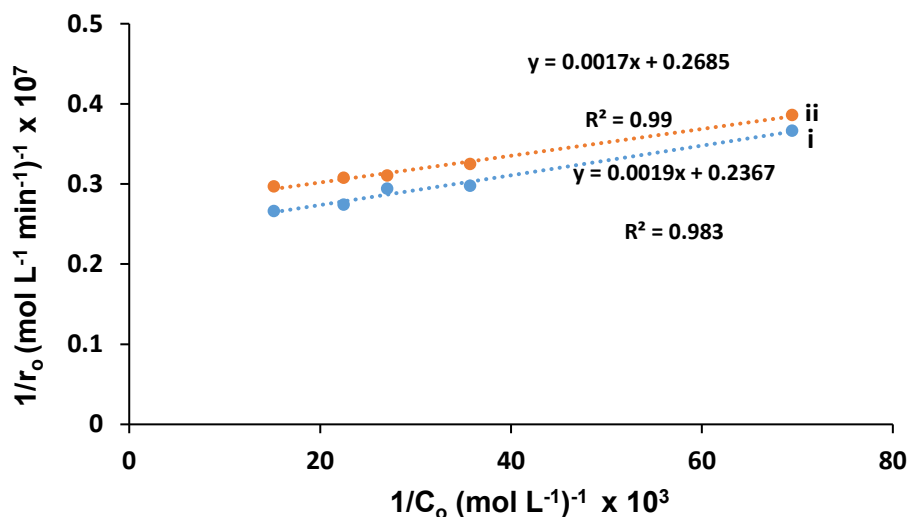


**Figure 7.3:** Plots of the reciprocal of the initial rate of degradation against the reciprocal of the concentration of MO using i. the fresh 6-TiO<sub>2</sub> NFs and ii. reused 6-TiO<sub>2</sub> NFs.

This is confirmation that the degradation of MO using semiconductor NFs under the reported conditions obeys the Langmuir-Hinshelwood kinetics model. The apparent rate constants ( $k$ ) and adsorption coefficient ( $K_A$ ) were obtained from the y-intercepts and slopes of the lines, respectively. As shown in **Table 7.5**, high  $K_A$  values are obtained for the nanocatalysts, possibly due to the  $\pi - \pi$  interaction between the Pc and MO.

The results show that the Hem based NFs have the highest  $K_A$  values relative to the TiO<sub>2</sub> and ZnO based NFs. This is an indication that the adsorption of MO favours the Hem based NFs, possibly due to their larger surface areas as explained before with BET and shown in **Table 4.2**.

**Table 7.5:** Langmuir-Hinshelwood kinetics for the bare and modified Hem, TiO<sub>2</sub> and ZnO NFs

Catalyst	k (10 <sup>-7</sup> ) molL <sup>-1</sup> min <sup>-1</sup>	K <sub>A</sub> (10 <sup>4</sup> ) mol <sup>-1</sup> L	R <sup>2</sup>
Bare Hem NFs	2.97 (2.25)	4.37 (4.20)	0.986 (0.991)
<b>5</b> -Hem NFs	3.44 (3.15)	4.36 (4.07)	0.995 (0.985)
<b>6</b> -Hem NFs	2.63 (2.55)	5.99 (6.02)	0.995 (0.980)
Bare ZnO NFs	2.18 (2.06)	4.08 (4.05)	0.986 (0.980)
<b>6</b> -ZnO NFs	3.71 (3.59)	4.30 (4.18)	0.994 (0.994)
Bare TiO <sub>2</sub> NFs	2.57 (2.34)	3.86 (3.85)	0.967 (0.941)
<b>6</b> -TiO <sub>2</sub> NFs	4.22 (3.72)	4.49 (4.83)	0.984 (0.993)

Values in brackets are the results obtained for the reused catalysts.

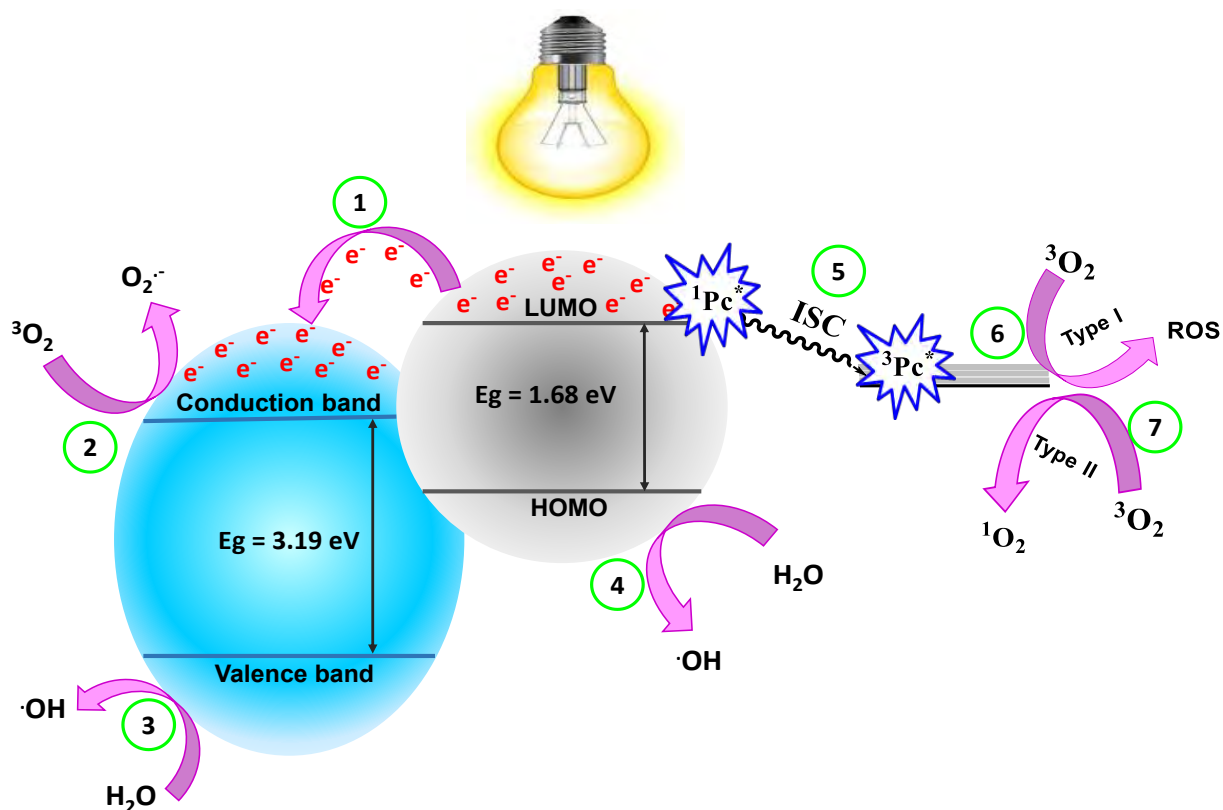
## 7.2 Mechanism of photodegradation

The general mechanism of degradation of MO using the reported NFs is similar and shown in **Scheme 7.1** (using the **6**-TiO<sub>2</sub> NFs as an example).

When the bare TiO<sub>2</sub> NFs are exposed to UV irradiation, electrons are transferred from the valence band (leaving holes behind) to the conduction band, thereby forming electron-hole pairs. The generated electrons and holes can reduce and oxidize the reactants which are adsorbed by the semiconductors, respectively [267]. The photogenerated holes facilitate the formation of hydroxyl radicals by the oxidation of

OH<sup>-</sup> and H<sub>2</sub>O molecules which are absorbed on the surfaces of the semiconductor. These photo-produced hydroxyl radicals in turn oxidize and degrade organic materials such as MO [268].

Modification of the NFs with a Pc however yields a system wherein the semiconductor primarily acts as an electron transfer agent and the Pc acts as a photosensitizer [269]. As shown in **Scheme 7.1**, degradation of MO using a halogen lamp with **6**-TiO<sub>2</sub> NFs is initiated by the excitation of the complex **6** thereby generating electrons and photogenerated holes in the LUMO and HOMO of the Pc, respectively. The electrons in the LUMO are then injected into the conduction band of TiO<sub>2</sub> (path 1). The electrons in the conduction band of TiO<sub>2</sub> react with molecular oxygen to generate reactive superoxide anion radicals (path 2). The holes in the valence band of TiO<sub>2</sub> react with the adsorbed water molecules on the surface of the photocatalyst to generate hydroxyl radicals (path 3). Simultaneously, the radical cation of the Pc that is formed during its excitation, reacts with water that is present on the surface of the photocatalysts to generate strongly oxidizing hydroxyl radicals (path 4) [266,269]. In another process, the photosensitizer in its singlet excited state undergoes intersystem crossing to the forbidden triplet excited state (path 5). Subsequent reactions result in the formation of ROS (path 6) and singlet oxygen (path 7) through electron and energy transfer processes, respectively [270]. The generated ROS, singlet oxygen and hydroxyl radicals from the interaction of the catalysts are strong oxidizing agents that can decompose organic pollutants [271].



**Scheme 7.1:** Mechanism of degradation of Methyl Orange using **6**-TiO<sub>2</sub> NFs. ISC = Intersystem crossing, LUMO = Lowest Unoccupied Molecular Orbital, HOMO = Highest Unoccupied Molecular Orbital and ROS = Reactive Oxygen Species.

### 7.3 Closing Remarks

The semiconductor NFs possess photocatalytic activity against MO with the bare Hem NFs being the best followed by the TiO<sub>2</sub> NFs and then the ZnO NFs. Modification of the Hem NFs with Pcs resulted in enhanced activity, even more so when the asymmetrical tetrasubstituted complex **6** was used rather than the asymmetrical monosubstituted complex **5**. Modification of all of the semiconductor NFs with complex **6** showed that the **6**-TiO<sub>2</sub> NFs showed the best degradation efficiency while the **6**-Hem and **6**-ZnO NFs showed comparable activity.

# Chapter 8

This chapter gives details on the hydrogen generation studies that were conducted using the bare and modified TiO<sub>2</sub> NFs.

### 8.1 Photo-induced hydrogen generation

Due to the high activity, good yield and attractive physical properties of the TiO<sub>2</sub> NFs, they were modified and applied in the sacrificial electron donor (SED) assisted hydrogen generation using 1% methanol as the SED. The photocatalytic activity of the commercially available P25-TiO<sub>2</sub> NFs was also evaluated and discussed. Bare TiO<sub>2</sub> NFs calcined at different temperatures (500, 750 and 950 °C) were used as well as NFs modified with complex **7**, Pd and Co NPs. As shown in **Figure 8.1** (showing TiO<sub>2</sub>-500 and Pd@TiO<sub>2</sub>-500 as examples), the utilised TiO<sub>2</sub> have a macroscopic thin-paper-like appearance which remains intact even post modification. This enormously facilitates their separation and/or future potential in flow system applications hence their attractiveness for hydrogen generation from polluted water.

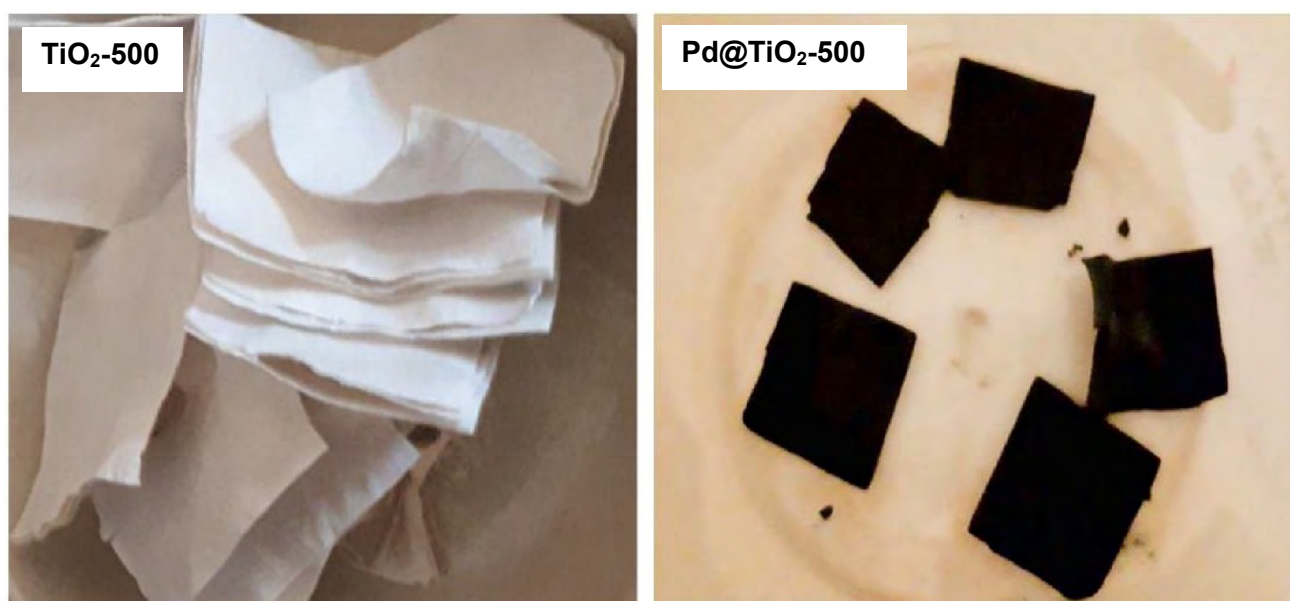


**Figure 8.1:** Macroscopic appearance of bare TiO<sub>2</sub> NFs and Pd@TiO<sub>2</sub>-500 showing their paper-thin appearance and the change in color post-synthetic Pd decoration.

As mentioned before, the studies were conducted using UV and visible light and the photocatalytic properties of the bare and modified NFs were compared under both light sources.

The results obtained for the H<sub>2</sub> generation experiments are depicted in **Figure 8.2**. The H<sub>2</sub> generation from the bare NFs showed that the pure anatase NFs (TiO<sub>2</sub>-500 NFs) have better photoactivity compared to rutile counterparts (TiO<sub>2</sub>-750 and TiO<sub>2</sub>-950 NFs), as previously observed [223]. The high activity of anatase relative to rutile has been ascribed to the former having slower charge recombination kinetics than the latter [272,273]. The P25-TiO<sub>2</sub> (comprised by >70% anatase and small amounts of rutile and amorphous phase [274,275]) showed poorer activity than the TiO<sub>2</sub>-500 NFs, but better activity than the TiO<sub>2</sub>-750 and TiO<sub>2</sub>-950. None of the bare NFs showed any activity upon exposure to visible light, which was expected as TiO<sub>2</sub> does not absorb visible light [276].

Under UV irradiation excitation, the NFs with the Pd NPs showed a 35-fold increase in activity relative to the bare ones while the Co NPs showed an enhancement of ~5-fold. This correlates to what has been observed before where Pd NPs were found to be good at enhancing SED assisted H<sub>2</sub> generation while Co NPs only enhance true water splitting (in the absence of a SED) [168].

Decoration of the NFs with complex **7** showed a decrease in H<sub>2</sub> generation using UV excitation. Thus, although a zinc Pc has been reported to be effective in H<sub>2</sub> generation [127], the obtained results showed lower H<sub>2</sub> generation for catalysts decorated with complex **7** relative to the bare TiO<sub>2</sub> NFs under UV irradiation.

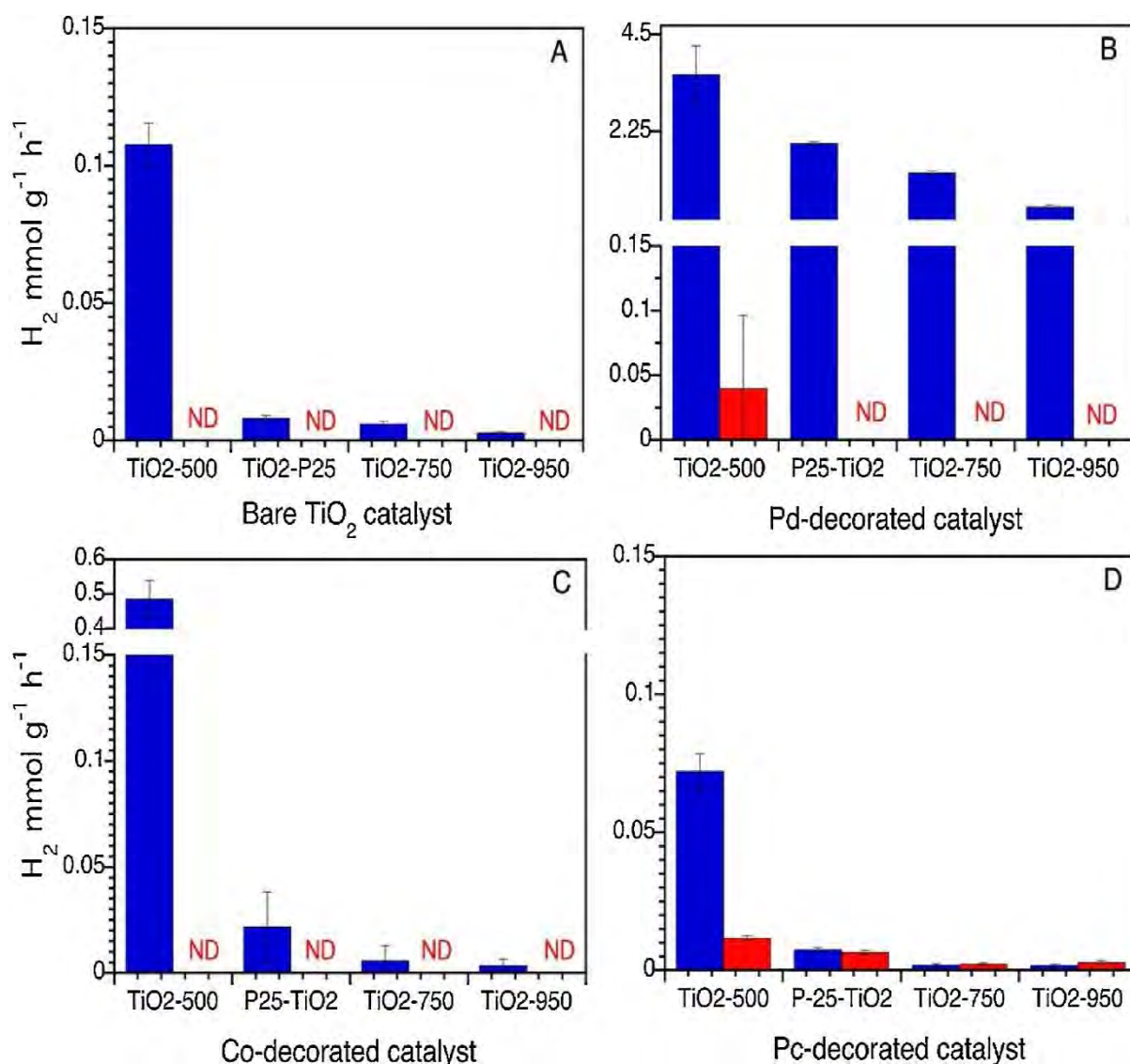


**Figure 8.2:** H<sub>2</sub> generation rates with (A) bare NFs, (B) NFs decorated with Pd NPs, (C) NFs decorated with Co NPs and (D) NFs decorated with complex **7**. Tests were conducted using an irradiance of 16 W m<sup>-2</sup> at 368 nm (blue) and 630 nm (red) in the presence of 1% methanol. ND: not detected.

However, under visible light irradiation the Pc-decorated NFs with the best reproducible H<sub>2</sub> generation ability is the anatase **7**@TiO<sub>2</sub>-500. There are some indications that Pd@TiO<sub>2</sub>-500 may also generate some H<sub>2</sub>, but the results were not



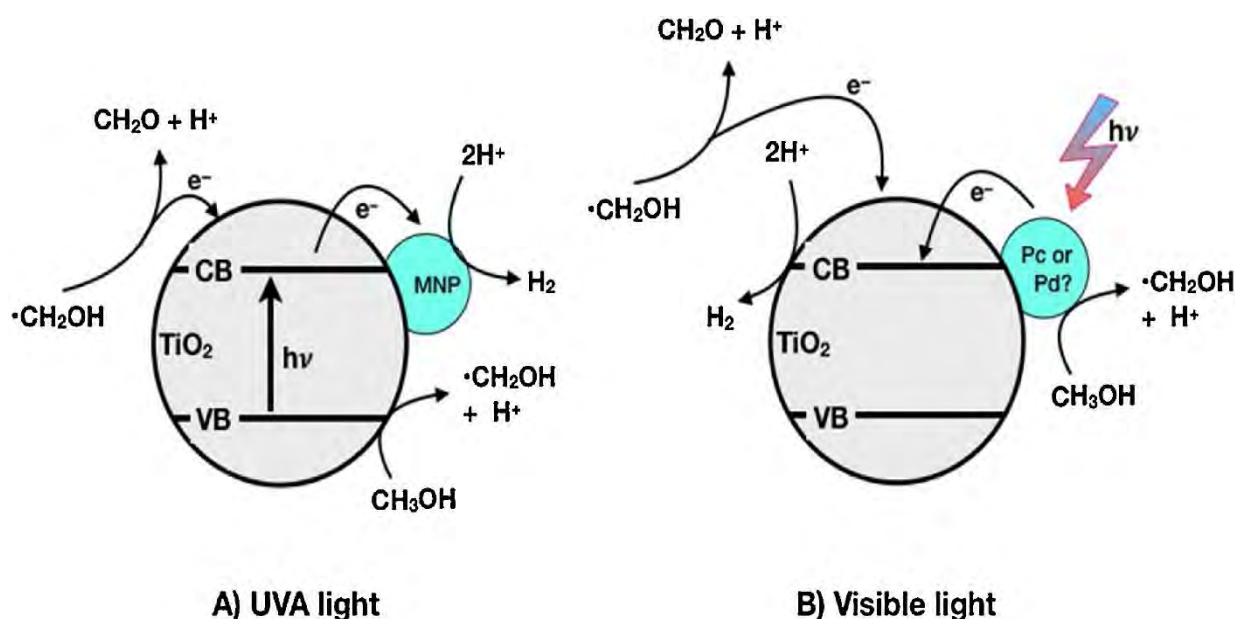
reproducible to claim that this material is a reliable H<sub>2</sub> source with visible light (note error bars in **Figure 8.2B**).

From results reported here, it is clear that regeneratable electrospun TiO<sub>2</sub> NFs are good catalysts for metal reduction (as shown in the *in situ* synthesis of Co and Pd NPs) as well as H<sub>2</sub> generation in the presence of organic compounds, a characteristic that is attractive for water purification strategies in flow systems.

## **8.2 Mechanism of sacrificial electron donor (SED) assisted hydrogen generation**

Based on the obtained results, a possible mechanism of H<sub>2</sub> evolution using the decorated NFs is proposed and shown in **Scheme 8.1**.

Under UV irradiation excitation, the photogenerated electrons in the TiO<sub>2</sub> conduction band are trapped by the Pd or Co, thereby delaying the electron-hole recombination process and thus favouring H<sub>2</sub> production **Scheme 8.1A**. In the case of the NFs decorated with a complex **7**, the Pc has a dual role wherein it acts as a photosensitiser and donates electrons to TiO<sub>2</sub> following the absorption of visible light and leaving behind photogenerated vacancies in the HOMO. Thus the excited dye and possibly Pd NPs inject electrons into the conduction band of the TiO<sub>2</sub> thus enabling hydrogen formation. Methanol acts as a SED thus forming formaldehyde as part of the same process. The •CH<sub>2</sub>OH radical can donate an electron to the conduction band and contribute to the H<sub>2</sub> generation. Given the exceptional electrophilic properties of the TiO<sub>2</sub> hole [277], the assumption is that many molecules that are present in water streams as contaminants can be degraded while simultaneously generating H<sub>2</sub> as shown when methanol acts as a surrogate contaminant in this work.



**Scheme 8.1:** Mechanism of photoactivity of the decorated TiO<sub>2</sub> fibers under (A) UVA and (B) visible irradiation in the presence of methanol as a SED. CB = Conduction band, VB = Valence band, MNP = metal nanoparticle i.e. Co/ Pd NPs.

### 8.3 Closing Remarks

Modified TiO<sub>2</sub> NFs proved to be efficient photocatalysts in SED assisted hydrogen generation with the anatase (TiO<sub>2</sub>-500) NFs being even better than the commercially available P25-TiO<sub>2</sub>. The good activity and retrievable nature of the fabricated photocatalysts post-application makes them ideal candidates for real-life flow systems where water decontamination is achieved simultaneously with hydrogen generation.

# Chapter 9

This chapter summarizes the results obtained in the characterisation and application of the nanomaterials reported in thesis. It also gives recommendations on future work that could be conducted to enhance the reported studies.

## 9.1 Conclusions

The conjugation of complexes **1-3** to OLM-Ag NPs resulted in enhanced singlet oxygen generation and thus antimicrobial activity. The cationic complexes **2** and **3** show better activity than the neutral complex **1** in solution and when anchored onto SiO<sub>2</sub> NFs with the hexadecacationic complex **3** being the best.

The conjugation of complexes **4-6** to different NPs (Cys-Ag, NH<sub>2</sub>-Fe<sub>3</sub>O<sub>4</sub> and Cys-Fe<sub>3</sub>O<sub>4</sub>@Ag NPs) showed that the bimetallic Cys-Fe<sub>3</sub>O<sub>4</sub>@Ag NPs best enhanced the singlet oxygen quantum yields and thus antibacterial properties of the Pcs. Anchoring these Pcs onto Hem NFs also resulted in enhanced antibacterial activities relative to the bare NFs. For pollutant versatility, the bare and Pc modified NFs were also effectively applied in the photodegradation of MO.

Comparison of the effect of the type of asymmetrical Pc (i.e. monosubstituted (**5**) and tetrasubstituted (**6**)) used for the modification of the NFs was conducted by supporting complexes **5** and **6** on Hem NFs wherein the **6**-Hem NFs showed slightly better activity than the **5**-Hem NFs.

Comparison of the bare semiconductor NFs showed that the bare Hem NFs exhibited better photocatalytic ability against MO relative to TiO<sub>2</sub> and ZnO NFs. Studying the effect of complex **6** on each of the semiconductor NFs however showed that there was a greater enhancement of activity for the TiO<sub>2</sub> NFs relative to the Hem NFs and ZnO NFs thus the **6**-TiO<sub>2</sub> NFs have the best activity.

Fabrication and characterisation of the bare and modified anatase and rutile TiO<sub>2</sub> NFs showed that the NFs have different optical and physical properties. The anatase TiO<sub>2</sub> NFs showed better photocatalytic activity than the rutile NFs or the commercially available P25-TiO<sub>2</sub> even more so when modified with Pd NPs.

## 9.2 Future work

Due to the good antibacterial properties of the reported Pc-NP conjugates, they could be evaluated for more complex antigens like prominent viruses. The reported physical properties and antimicrobial activities of the reported NFs also makes them good candidates for other real life applications including wound dressing, protective clothing and tissue engineering. In addition, with the current pandemic, antibacterial (and possibly anti-viral) masks could be fabricated and evaluated with the use of Pc and NP modified NFs.

In addition to exploring different types of NPs and their effect on the photoactivities of Pcs and NFs, varying their shapes, sizes and capping agents would make for an interesting study.

Enhancing the photoactivities of the NFs using various other types of photosensitisers including porphyrins and chlorins could also be explored when they are supported on these nanomaterials.

Based on the promising activities of the NF based heterogenous catalysts reported herein, future work could entail applying them for other water related problems such as the photoreduction of heavy metals and desulfurization of crude oils. The obtained results would be an indication of the specificity of the NFs on the type of pollutant and the mechanisms behind it.

Various other polymer free NFs including alumina and cyclodextrin NFs could be fabricated and employed for the different water purification applications so as to determine the best NFs for the each of the different applications.

## References

1. A. Formhals, Process and Apparatus for Preparing Artificial Threads, U.S. Patent 1,975,504.
2. J. -S. Park, *Adv. Nat. Sci: Nanosci. Nanotechnol.* 1 (2010) 043002.
3. J. Huang, T. You, *Electrospun Nanofibers: From Rational Design, Fabrication to Electrochemical Sensing Applications*, R. Maguire (Ed.), *Advances in Nanofibers*, IntechOpen, London, 2013.
4. S. Maghsoodlou, B. Noroozi, A. K. Hagh, *Nano.* 12 (2017) 1.
5. Z. M. Huang, Y. Z. Zhang, M. Kotaki, S. Ramakrishna, *Compos. Sci. Technol.* 63 (2003) 2223.
6. D. Li, Y. N. Xia, *Adv. Mater.* 16 (2004) 1151.
7. T. J. Sill, H. A. von Recum, *Biomaterials* 29 (2008) 1989.
8. S. Lee, S. K. Obendorf, *Text. Res. J.* 77 (2007) 696.
9. X. Qin, S. Wang, *J. Appl. Polym. Sci.* 102 (2006) 1285.
10. M. Liu, X. -P. Duan, Y. -M. Li, D. -P. Yang, Y. -Z. Long, *Mater. Sci. Eng.: C* 76 (2017) 1413.
11. A. Sindelo, T. Nyokong, *Heliyon* 5 (2019) 02352.
12. R. Zuggle, E. Antunes, S. Khene, T. Nyokong, *Polyhedron* 33 (2012) 74.
13. O. L. Osifeko, T. Nyokong, *Dyes Pigm.* 111 (2014) 8.
14. P. Modisha, T. Nyokong, *J. Mol. Catal. A: Chem.* 381 (2014) 132.
15. S. Mapukata, F. Chindeka, K. E. Sekhosana, T. Nyokong, *J. Mol. Catal.* 439 (2017) 211.
16. X. Guo, X. Zhou, X. Li, C. Shao, C. Han, X. Li, Y. Liu, *J. Colloid Interface Sci.* 525 (2018) 187.

17. N. Masilela, P. Kleyi, Z. Tshentu, G. Priniotakis, P. Westbroek, T. Nyokong, *Dyes Pigm.* 96 (2013) 500.
18. J. -H. Kim, S. -J. Yoo, D. -H. Kwak, H. -J. Jung, T. -Y. Kim, K. -H. Park, J. -W. Lee, *Nanoscale Res. Lett.* 9 (2014) 44.
19. A. Celebioglu, T. Uyar, *Langmuir* 27 (2011) 6218.
20. J. P. Santos, M. J. Fernández, J. L. Fontecha, D. Matatagui, I. Sayago, M. C. Horrillo, I. Gracia, *Sensors* 14 (2014) 24231.
21. N. Dharmaraj, H. C. Park, C. H. Kim, P. Viswanathamurthi, H. Y. Kim, *Mater. Res. Bull.* 41 (2006) 612.
22. N. Tahmasbi, S. Madmoli, P. Farahnak, S. Barzegar, H. Moayeri, *Russ. J. Appl. Chem.* 90 (2017) 1488.
23. M. Wu, Y. Liang, J. Jiang, J. S. Tse, *Sci. Rep.* 2 (2012) 1.
24. R. Fan, Y. Wu, D. Li, M. Yue, A. Majumdar, P. Yang, *J. Am. Chem. Soc.* 125 (2003) 5254.
25. A. Liberman, N. Mendez, W.C. Trogler, A. C. Kummel, *Surf. Sci. Rep.* 69 (2014) 132.
26. X. Zong, Y. Cai, G. Sun, Y. Zhao, F. Huang, L. Song, Y. Hu, H. Fong, Q. Wei, *Sol. Energy Mater. Sol. Cells* 132 (2015) 183.
27. A. Almasian, G. C. Fard, L. Maleknia, *Environ. Prog. Sustain. Energy* 36 (2017) 1390.
28. S. Wen, M. Liang, R. Zou, Z. Wang, D. Yue, L. Liu, *RSC Adv.* 5 (2015) 41513.
29. M. -J. Chang, W. N. Cui, J. Liu, *J. Nanomater.* 2017 (2017) 1.
30. A. O. Ibhaddon, P. Fitzpatrick, *Catalysts* 3 (2013) 189.
31. S. Gosh, V. S. Goudar, K. G. Padmalekha, S. V. Bhat, S. S. Indi, H. N. Vasan, *RSC Adv.* 2 (2012) 930.

32. H. Yin, P. S. Casey, M. J. McCall, M. Fenech, *Langmuir* 19 (2010) 15399.
33. J. Tang, J. R. Durrant, D. R. Klug, *J. Am. Chem. Soc.* 130 (2008) 13885.
34. D. J. Mowbray, J. I. Martinez, J. M. García Lastra, K. S. Thygesen, K. W. Jacobsen, *J. Phys. Chem. C* 113 (2009) 12301.
35. M. Willander, Q. X. Zhao, Q. -H. Hu, P. Klason, V. Kuzmin, S. M. Al-Hillib, O. Nur, Y. E. Lozovik, *Superlattice. Microstruct.* 43 (2008) 352.
36. S. Hernández, D. Hidalgo, A. Sacco, A. Chiodoni, A. Lamberti, V. Cauda, E. Tresso, G. Saracco, *Phys. Chem. Chem. Phys.* 17 (2015) 7775.
37. S. V. Fridrikh, J. H. Yu, M. P. Brenner, G. C. Rudledge, *Phys. Rev. Lett.* 90 (2003) 1.
38. D. H. Reneker, I. Chun, *Nanotechnology* 7 (1996) 216.
39. X. Yu, T. Hou, Y. Li, X. Sun, S. -T. Lee, *Int. J. Quantum Chem.* 113 (2013) 2546.
40. U. S. Nur, F. C. Thye, Y. K. Kuan, R. Y. Mohd, K. N. G. Inn, *Mater. Sci. Forum* 888 (2016) 309.
41. P. Fageria, S. Gangopadhyay, S. Pande, *RSC Adv.* 4 (2014) 24962.
42. P. Modisha, E. Antunes, T. Nyokong, *J. Nanosci. Nanotechnol.* 15 (2015) 3688.
43. G. G. Matlou, D. O. Oluwole, E. Prinsloo, T. Nyokong, *J. Photochem. Photobiol. B.* 186 (2018) 216.
44. P. Khoza, T. Nyokong, *J. Coord. Chem.* 68 (2015) 1117.
45. K. P. Priyanka, S. Sankararaman, K. M. Balakrishna, T. Varghese, *J. Alloys Compd.* 720 (2017) 541.
46. P. Kumar, U. Burman, R. K. Kaul, *Ecological Risks of Nanoparticles: Effect on Soil Microorganisms*, D. K. Tripathi, P. Ahmad, S. Sharma, D. K. Chauhan, N. K. Dubey (Eds.), *Nanomaterials in Plants, Algae, and Microorganisms*, Academic Press, USA, 2018.



47. I. Khan, K. Saeed, I. Khan, Arab. J. Chem. 12 (2019) 908.
48. S. R. Mudshinge, A. B. Deore, S. Patil, C. M. Bhalgat, Saudi Pharma. J. 19 (2011) 129.
49. C. Buzea, I. Pacheco, K. Robbie, Biointerphases 2 (2007) 17.
50. A. Singh, M. Y. Dar, B. Joshi, B. Sharma, S. Shrivastava, S. Shukla, Toxicol. Rep. 5 (2018) 333.
51. F. U. Khan, Y. Chen, N. U. Khan, Z. U. H. Khan, A. U. Khan, A. Ahmad, K. Tahir, L. Wang, M. R. Khan, P. Wan, J. Photochem. Photobiol. B: Biol. 164 (2016) 344.
52. F. Paladini, M. Pollini, Materials (Basel) 12 (2019) 2540.
53. M. M. Zaman, M. A. S. Karal, M. N. I. Khan, A. R. M. Tareq, S. Ahammed, M. Akter, A. Hossain, A. K. M. A. Ullah, ChemistrySelect 4 (2019) 7824.
54. A. Moslehi, M. Zarei, New J. Chem. 43 (2019) 12690.
55. Y. Pang, C. Wang, J. Wang, Z. Sun, R. Xiao, S. Wang, Biosens. Bioelectron. 79 (2016) 574.
56. Y. -J. Ko, J. -Y. Kim, K. -S. Lee, J. -K. Park, Y. -J. Baik, H. -J. Choi, W. -S. Lee, Int. J. Hydrog. Energy 43 (2018) 19029.
57. E. K. Dann, E. K. Gibson, R. H. Blackmore, C. R. A. Catlow, P. Collier, A. Chutia, T. E. Erden, C. Hardacre, A. Kroner, M. Nachtegaal, A. Raj, S. M. Rogers, S. F. R. Taylor, P. Thompson, G. F. Tierney, C. D. Zeinalipour-Yazdi, A. Goguet, P. P. Wells, Nat. Catal. 2 (2019) 157.
58. S. M. Ansari, R. D. Bhor, K. R. Pai, D. Sen, S. Mazumder, K. Ghosh, Y. D. Kolekar, C. V. Ramana, Appl. Surf. Sci. 414 (2017) 171.
59. F. Michalek, A. Lagunas, C. Jimeno, M. A. Pericàs, J. Mater. Chem. 18 (2008) 4692.
60. N. Masilela, E. Antunes, T. Nyokong, J. Porphyr. Phthalocya. 17 (2013) 417.

61. G. G. Matlou, T. Nyokong, *Dyes Pigm.* 176 (2020) 108237.
62. P. Modisha, T. Nyokong, E. Antunes, *J. Mol. Catal. A: Chem.* 380 (2013) 131.
63. A. Magadla, D. O. Oluwole, M. Managa, T. Nyokong, *Polyhedron* 162 (2019) 30.
64. X. -F. Zhang, Z. -G. Liu, W. Shen, S. Gurunathan, *Int. J. Mol. Sci.* 17 (2016) 1534.
65. W. R. Li, X. B. Xie, Q. S. Shi, H. Y. Zeng, Y. S. Ou-Yang, Y. B. Chen, *Appl. Microbiol. Biotechnol.* 8 (2010) 1115.
66. A. A. Menazea, *Radiat. Phys. Chem.* 168 (2020) 108616.
67. Y. S. Soliman, *Radiat. Phys. Chem.* 102 (2014) 60.
68. Y. Li, Y. N. Kim, E. J. Lee, W. P. Cai, S. O. Cho, *Nucl. Instrum. Methods Phys. Res. B* 251 (2006) 425.
69. S. Joseph, B. Mathew, *J. Mol. Liq.* 204 (2015) 184.
70. M. Guilger-Casagrande, T. Germano-Costa, T. Pasquoto-Stigliani, L. F. Fraceto, R. de Lima, *Sci. Rep.* 9 (2019) 14351.
71. K. Gudikandula, S. C. Maringanti, *J. Exp. Nanosci.* 11 (2016) 714.
72. D. A. Mosselhy, H. Granbohm, U. Hynönen, Y. Ge, A. Palva, K. Nordström, S. P. Hannula, *Nanomater.* 7 (2017) 261.
73. P. Jeevanandam, C. K. Srikanth, S. Dixit, *Mater. Chem. Phys.* 122 (2010) 402.
74. S. Majidi, F. Z. Sehrig, S. M. Farkhani, M. S. Goloujeh, A. Akbarzadeh, *Artif. Cells Nanomed. Biotechnol.* 44 (2016) 722.
75. A. Radoń, A. Drygał, Ł. Hawelek, D. Łukowiec, *Mater. Charact.* 131 (2017) 148.
76. X. Liang , X. Jia , L. Cao , J. Sun, Y. Yang, *J. Dispers. Sci. Technol.* 31 (2010) 1043.
77. W. Glasgow, B. Fellows, B. Qi, T. Darroudi, C. Kitchens, L. Ye, T. M. Crawford, O. T. Mefford, *Particuology* 26 (2016) 47.
78. W. Zhang, F. Shen, R. Hong, *Particuology* 9 (2011) 179.

79. S. Aliramaji A. Zamanian Z. Sohrabijam, *Procedia Materials Science* 11 (2015) 265.
80. T. K. Indira, P. K. Lakshmi, *Int. J. Pharm. Sci. Nanotechnol.* 3 (2010) 1035.
81. Z. Xu, Y. Hou, S. Sun, *J. Am. Chem. Soc.* 129 (2007) 8698.
82. V. Leso, I. Iavicoli, *Int. J. Mol. Sci.* 19 (2018) 503.
83. R. Narayanan, M. A. El-Sayed, *J. Phys. Chem. B* 109 (2005) 12663.
84. A. R. Siamaki, A. E. R. S. Khder, V. Abdelsayed, M. S. El-Shall, B. F. Gupton, *J. Catal.* 279 (2011) 1.
85. C. –C. Wang, D. –H. Chen, T. –C. Huang, *Colloids Surf. A Physicochem. Eng. Asp.* 189 (2001) 145.
86. A. Bankar, B. Joshi, A. R. Kumar, S. Zinjarde, *Mater. Lett.* 64 (2010) 1951.
87. A. Nemamcha, J. -L. Rehspringer, D. Khatmi, *J. Phys. Chem. B* 110 (2006) 383.
88. Y. Yu, A. Mendoza-Garcia, B. Ning, S. Sun, *Adv. Mater.* 25 (2013) 3090.
89. J. Schällibaum, F. H. D. Torre, W. R. Caseri, J. F. Löffler, *Nanoscale* 1 (2009) 374.
90. I. C. Kong, K. –S. Ko, D. –C. Koh, C. –M. Chon, *Int. J. Mol. Sci.* 21 (2020) 6767.
91. Y. Song, H. Modrow, L. L. Henry, C. K. Saw, E. E. Doomes, V. Palshin, J. Hormes, C. S. S. R. Kumar, *Chem. Mater.* 18 (2006) 2817.
92. J. Ahmed, S. Sharma, K. V. Ramanujachary, S. E. Lofland, A. K. Ganguli, *J. Colloid Interface Sci.* 336 (2009) 814.
93. A. S. Vijayanandan, R. M. Balakrishnan, *J. Environ. Manage.* 218 (2018) 442.
94. D. D. Li, R. S. Thompson, G. Bergmann, J. G. Lu, *Adv. Mater.* 20 (2008) 4575.
95. R. P. Linstead, A. R. Lowe, *J. Chem. Soc.* (1934) 1022.

96. G. de la Torre, M. Nicolau, T. Torres, Phthalocyanines: Synthesis, Supramolecular Organization, and Physical Properties, H. S. Nalwa (Ed.), Supramolecular Photosensitive and Electroactive Materials, Academic Press, New York, 2001.
97. R. P. Linstead, J. Chem. Soc. (1934) 1016.
98. P. Gregory, J. Porphyr. Phthalocya. 4 (2000) 432.
99. S. Mgidlana, D. O. Oluwole, T. Nyokong, Polyhedron 159 (2019) 102.
100. G. G. Matlou, M. Managa, T. Nyokong, Spectrochim. Acta A Mol. Biomol. Spectrosc. 214 (2019) 49.
101. F. Chindeka, P. Mashazi, J. Britton, G. Fomo, D. O. Oluwole, A. Sindelo, T. Nyokong, Synth. Met. 246 (2018) 236.
102. B. Yıldız, E. Güzel, D. Akyüz, B. S. Arslan, A. Koca, M. K. Şener, Sol. Energy 191 (2019) 654.
103. O. J. Achadu, T. Nyokong, Talanta 166 (2017) 15.
104. B. Tawiah, B. K. Asinyo, W. Badoe, L. Zhang, S. Fu, Int. J. Ind. Chem. 8 (2017) 17.
105. N. Nnaji, N. Nwaji, G. Fomo, J. Mack, T. Nyokong, Electrocatalysis 10 (2019) 445.
106. B. I. Kharisov, U. Ortiz Me´ndez, J. L. Almaraz Garza, J. R. Almaguer Rodríguez, New J. Chem. 29 (2005) 686.
107. P. Yiru, H. Fenghua, L. Zhipeng, C. Naisheng, H. Jinling, Inorg. Chem. Commun. 7 (2004) 967.
108. F. Dumoulin, M. Durmuş, V. Ahsen, T. Nyokong, Coord. Chem. Rev. 254 (2010) 2792.

109. W. M. Sharman, J. E. Van Lier, Phthalocyanines: Synthesis, K. Kadish, K. Smith, R. Guillard (Eds.), The Porphyrin Handbook, Academic Press, New York, 2003.
110. N. B. McKeown, Phthalocyanine Materials: Synthesis, Structure and Function, Cambridge University Press, New York, 1998.
111. M. Hanack, D. Meng, A. Beck, M. Sommerauer, L. R. Subramanain, J. Chem. Soc. Chem. Commun. 58 (1993) 58.
112. J. Yang, T. C. Rogers, M. R. Van De Mark, J. Heterocycl. Chem. 30 (1993) 571.
113. J. V. Bakboord, M. J. Cook, E. J. Hamuryudan, J. Porphyr. Phthalocya. 4 (2000) 510.
114. V. N. Nemykin, S. V. Dudkin, F. Dumoulin, C. Hirel, ARKIVOC 2014 (2014) 142.
115. V. Novakova, J. Roh, P. Gela, J. Kuneš, P. Zimcik, Chem. Commun. 48 (2012) 4326.
116. N. Nwaji, B. Jones, J. Mack, D. O. Oluwole, T. Nyokong, J. Photochem. Photobiol. A Chem. 346 (2017) 46.
117. J. Obirai, T. Nyokong, Electrochim. Acta 50 (2005) 5427.
118. O. L. Osifeko, T. Nyokong, Dyes Pigm. 131 (2016) 186.
119. S. Mapukata, N. Kobayashi, M. Kimura, T. Nyokong, J. Photochem. Photobiol. A Chem. 379 (2019) 112.
120. M. S. Ağırtaş, C. Karataş, S. Özdemir, Spectrochim. Acta A Mol. Biomol. Spectrosc. 135 (2015) 20.
121. R. A. Bell, J. R. Kramer, Environ. Toxicol. Chem. 18 (1999) 9.
122. M. Li, B. Mai, A. Wang, Y. Gao, X. Wang, X. Liu, S. Song, Q. Liu, S. Wei, P. Wang, RSC Adv. 7 (2017) 40734.

123. P. Sen, A. Sindelo, D. M. Mafukidze, T. Nyokong, *Synth. Met.* 258 (2019) 116203.
124. B. –D. Zheng, S. –L. Li, Z. –L. Huang, L. Zhang, H. Liu, B. –Y. Zheng, M. –R. Ke, J. –D. Huang, *J. Photochem. Photobiol. B: Biol.* 213 (2020) 112086.
125. D. Wöhrle, A. Hirth, T. Bogdahn-Rai, G. Schnurpfeil, M. Shopova, *Russ. Chem. Bull.* 47 (1998) 807.
126. D. O. Oluwole, S. L. Manoto, R. Malabi, C. Maphanga, S. Ombinda-Lemboumba, P. Mthunzi-Kufa, T. Nyokong, *Dyes Pigm.* 150 (2018) 139.
127. A. Tiwari, N. V. Krishna, L. Giribabu, U. Pal, *Phys. Chem. C* 122 (2018) 495.
128. T. Fukuda, K. Ono, S. Homma, N. Kobayashi, *Chem. Lett.* 32 (2003) 736.
129. N. Kobayashi, H. Ogata, N. Nonaka, E. A. Luk'yanets, *Chem. Eur. J.* 9 (2003) 5123.
130. J. Mack, M. J. Stillman, *J. Am Chem. Soc.* 116 (1994)1292.
131. A. J. McHugh, M. Gouterman, J. C. Weiss, *Theor. Chim. Acta* 24 (1972) 346.
132. A. M. Schaffer, M. Gouterman, E. R. Davidson, *Theor. Chim. Acta* 30 (1973) 9.
133. C. G. Claessens, U. Hahn, T. Torres, *Chem. Rec.* 8 (2008) 75.
134. D. Frackowiak, *J. Photochem. Photobiol. B* 2 (1988) 399.
135. D. Phillips, *Proc. Math. Phys. Eng. Sci.* 472 (2016) 20160102.
136. D. Mondal, S. Bera, *Adv. Nat. Sci.: Nanosci. Nanotechnol.* 5 (2014) 1.
137. C. Würth, M. Grabolle, J. Pauli, M. Spieles, U. Resch-Genger, *Nat. Protoc.* 8 (2013) 1535.
138. E. T. Saka, C. Göl, M. Durmus, H. Kantekin, Z. Biyiklioglu, *J. Photochem. Photobiol. A Chem.* 241 (2012) 67.
139. A. G. Ryder, S. Power, T. J. Glynn, J. J. Morrison, *Proc. SPIE* 4529 (2001) 102.
140. S. M. Bachilo, R. B. Weisman, *J. Phys. Chem. A* 104 (2000) 7711.

141. J. H. Brannon, D. Magde, *J. Am. Chem. Soc.* 102 (1980) 62.
142. C. Schweitzer, R. Schmidt, *Chem. Rev.* 103 (2003) 1685.
143. E. Díez-Mato, F. C. Cortezón-Tamarit, S. Bogialli, D. García-Fresnadillo, M. D. Marazuela, *Appl. Catal. B: Environ.* 160 (2014) 445.
144. M. Wainwright, *J. Antimicrob. Chemother.* 42 (1998) 13.
145. L. V. Lutkus, S. S. Rickenbach, T. M. McCormick, *J. Photochem. Photobiol. A: Chem.* 378 (2019) 131.
146. A. Ogunsipe, T. Nyokong, *J. Photochem. Photobiol. A: Chem.* 173 (2005) 211.
147. E. A. Morell, D. M. Balkin, *Yale J. Biol. Med.* 83 (2010) 223.
148. M. S. Baptista, M. Wainwright, *Braz. J. Med. Biol. Res.* 44 (2011) 1.
149. M. R. Hamblin, T. Hasan, *Photochem. Photobiol. Sci.* 3 (2004) 436.
150. A. Sindelo, O. L. Osifeko, T. Nyokong, *Inorg. Chim. Acta* 476 (2018) 68.
151. F. F. Sperandio, Y. Y. Huang, M. R. Hamblin, *Recent. Pat. Antiinfect. Drug Discov.* 8 (2013) 108.
152. L. Brown, J. M. Wolf, R. Prados-Rosales, A. Casadeval, *Nat. Rev. Microbiol.* 13 (2015) 620.
153. Z. Malik, H. Ladan, Y. Nitzan, *J. Photochem. Photobiol. B* 14 (1992) 262.
154. T. Mthethwa, T. Nyokong, *Photochem. Photobiol. Sci.* 14 (2015) 1346.
155. D. M. Mafukidze, A. Sindelo, T. Nyokong, *Spectrochim. Acta A Mol. Biomol. Spectrosc.* 219 (2019) 333.
156. A. Pandey, P. Singh, L. Iyengar, *Int. Biodeterior. Biodegradation* 59 (2007) 73.
157. C. Zhu, L. Wang, L. Kong, X. Yang, L. Wang, S. Zheng, F. Chen, F. Maizhi, H. Zong, *Chemosphere* 41 (2000) 303.

158. X. Lu, R. Liu, Treatment of Azo Dye-Containing Wastewater Using Integrated Processes, H. Erkurt Atacag (Eds.), Biodegradation of Azo Dyes. The Handbook of Environmental Chemistry, Springer, Berlin, 2010.
159. L. Young, J. Yu, *Wat. Res.* 31 (1997) 1187.
160. N. Puvaneswari, J. Muthukrishnan, P. Gunasekaran, *Indian J. Exp. Biol.* 44 (2006) 618.
161. P. Cui, Y. Chen, G. Chen, *Ind. Eng. Chem. Res.* 50 (2011) 3947.
162. A. Szyguła, E. Guibal, M. Ruiz, A. M. Sastre, *Colloids Surf. A Physicochem. Eng. Asp.* 330 (2008) 219.
163. C. Galindo, P. Jacques, A. Kalt, *Chemosphere* 48 (2002) 1047.
164. T. Ohashi, A. M. T. Jara, A. C. L. Batista, L. O. Franco, M. A. B. Lima, M. Benachour, C. A. A. da Silva, G. M. Campos-Takaki, *Molecules* 17 (2012) 14219.
165. D. Wang, J. Huang, X. Li, P. Yang, Y. Du, C. M. Goh, C. Lu, *J. Mater. Chem. A* 3 (2015) 4195.
166. S. Y. Tee, K. Y. Win, W. S. Teo, L. D. Koh, S. H. Liu, C. P. Teng, M. Y. Han, *Adv. Sci.* 4 (2017) 1600337.
167. H. Pan, *Renewable Sustainable Energy Rev.* 57 (2016) 584.
168. A. S. Hainer, J. S. Hodgins, V. Sandre, M. Vallieres, A. E. Lanterna, J. C. Scaiano, *ACS Energy Lett.* 3 (2018) 542.
169. L. Zhou, E. Chen, W. Jin, Y. Wang, J. Zhou, S. Wei, *Dalton Trans.* 45 (2016) 15170.
170. P. Matlaba, T. Nyokong, *Polyhedron* 21 (2002) 2463.
171. M. Ambroz, A. Beeby, A. J. McRobert, M. S. C. Simpson, R. K. Svensen, D. Phillips, *Photochem. Photobiol. B* 9 (1991) 87.
172. H. Hiramatsu, F. E. Osterloh, *Chem. Mater.* 16 (2004) 2509.



173. D. O. Oluwole, E. Prinsloo, T. Nyokong, *Polyhedron* 119 (2016) 434.
174. S. Liu, G. Chen, P. N. Prasad, M. T. Swihart, *Chem. Mater.* 23 (2011) 4098.
175. W. Mekseriwattana, S. Srisuk, Y. Tantiapibalkun, K. Prapainop, *ScienceAsia* 45 (2019) 60.
176. S. Santra, R. Tapeç, N. Theodoropoulou, J. Dobson, A. Hebard, W. Tan, *Langmuir* 17 (2001) 2900.
177. Z. Ma, H. Ji, D. Tan, Y. Teng, G. Dong, J. Zhou, J. Qiu, M. Zhang, *Colloids Surf. A: Physicochem. Eng. Aspects* 387 (2011) 57.
178. K. -H. Na, W. -T. Kim, D. -C. Park, H. -G. Shin, S. -H. Lee, J. Park, T. -H. Song, W. -Y. Choi, *Thin Solid Films* 660 (2018) 358.
179. A. Di Mauro, M. Zimbone, M. E. Fragalà, G. Impellizzeri, *Mater. Sci. Semicond. Process* 42 (2016) 98.
180. B. Caratão, E. Carneiro, P. Sá, B. Almeida, S. Carvalho, *J. Nanotechnol.* 2014 (2014) 1.
181. D. Li, Y. Xia, *Nano Lett.* 3 (2003) 555.
182. A. Elhage, A. E. Lanterna, J. C. Scaiano, *ACS Catal.* 7 (2017) 250.
183. J. C. Scaiano, K. G. Stamplecoskie, G. L. Hallett-Tapley, *Chem. Commun.* 48 (2012) 4798.
184. T. J. Beveridge, *J. Bacteriol.* 181 (1999) 4725.
185. N. A. Youssef, S. A. Shaban, F. A. Ibrahim, A. S. Mahmoud, *Egypt. J. Petr.* 25 (2016) 317.
186. S. Al-Qaradawi, S. R. Salman, *J. Photochem. Photobiol. A* 148 (2002) 161.
187. T. F. M. de Souza, F. C. T. Antonio, M. Zanotto, P. Homem-de-Mello, A. O. Ribeiro, *J. Braz. Chem. Soc.* 29 (2018) 1199.

188. F. Heidarpour, W. A. Wan, A. B. Karim Ghani, F. R. Bin Ahmadun, S. Sobri, M. Zargar, M. R. Mozafari, *Dig. J. Nanomater. Bios.* 5 (2010) 787.
189. B. B. Topuz, G. Gündüz, B. Mavis, Ü. Çolak, *Dyes Pigm.* 96 (2013) 31.
190. O. M. Lemine, K. Omri, B. Zhang, L. El Mir, M. Sajjeddine, A. Alyamanie, M. Bououdina, *Superlattice Microst.* 52 (2012) 793.
191. L. Li, J. Zhao, N. Won, N. H. Jin, S. Kim, J. Y. Chen, *Nanos. Res. Lett.* 7 (2012) 386.
192. K. Hadjiivanov, *Adv. Catal.* 57 (2014) 99.
193. S. Musić, N. Filipović-Vinceković, L. Sekovanić, *Braz. J. Chem. Eng.* 28 (2011) 89.
194. H. Cheng, J. Wang, Y. Zhao, X. Han, *RSC Adv.* 4 (2014) 47031.
195. T. Tański, W. Matysiak, Ł. Krzemiński, P. Jarka, K. Gołombek, *Appl. Surf. Sci.* 424 (2017) 184.
196. L. Alagna, A. Capobianchi, M. P. Casaletto, G. Mattogno, A. M. Paoletti, G. Pennesi, G. Rossi, *J. Mater. Chem.* 11 (2001) 1928.
197. X. Xu, M. Wang, Y. Pei, C. Ai, L. Yuan, *RSC Adv.* 4 (2014) 64747.
198. A. Rawat, H. K. Mahavar, S. Chauhan, A. Tanwar, P. J. Singh, *Indian J. Pure Appl. Phys.* 50 (2012) 100.
199. B. D. Vierzicke, S. Patel, B. E. Davis, D. P. Birnie, *Phys. Status Solidi B* 252 (2015) 1700.
200. W. Matysiak, T. Tański, *Appl. Surf. Sci.* 489 (2019) 34.
201. S. Xu, S. Hartvickson, J. X. Zhao, *ACS Appl. Mater. Interfaces* 3 (2011) 1865.
202. M. Managa, J. Britton, E. Prinsloo, T. Nyokong, *J. Coord. Chem.* 69 (2016) 3491.
203. S. K. Bhatia, C. G. Sonwane, *Stud. Surf. Sci. Catal.* 128 (2000) 187.

204. A. Rufus, N. Sreeju, D. Philip, RSC Adv. 6 (2016) 94206.
205. L. A. Marusak, R. Messier, W. B. White, J. Phys. Chem. Solids 41 (1980) 981.
206. D. A. Wheeler, G. Wang, Y. Ling, Y. Li, J. Z. Zhang, Energy Environ. Sci. 5 (2012) 6682.
207. G. Ren, Y. Sun, M. Sun, Y. Li, A. Lu, H. Ding, Minerals 7 (2017) 230.
208. X. Zong, S. Thaweesak, H. Xu, Z. Xing, J. Zou, G. Lua, L. Wang, Phys. Chem. Chem. Phys. 15 (2013) 12314.
209. A. Lassoued, B. Dkhil, A. Gadri, S. Ammar, Results Phys. 7 (2017) 3007.
210. M. Zainuri, IOP Conf. Ser. Mater. Sci. Eng. 196 (2017) 012008.
211. A. K. Zak, R. Razali, W. H. A. Majid, M. Darroudi, Int. J. Nanomed. 6 (2011) 1399.
212. W. Muhammad, N. Ullah, M. Haroon, B. H. Abbasi, RSC Adv. 9 (2019) 29541.
213. G. Soler-Illia, A. Louis, C. Sanchez, Chem. Mater. 14 (2002) 750.
214. C. Dette, M. A. Pérez-Osorio, C. S. Kley, P. Punke, C. E. Patrick, P. Jacobson, F. Giustino, S. J. Jung, K. Kern, Nano Lett. 14 (2014) 6533.
215. V. Loryuenyong, N. Jarunsak, T. Chuangchai, A. Buasr, Adv. Mater. Sci. Eng. 2014 (2014) 1.
216. K. Sakurai, M. Mizusawa, Anal. Chem. 28 (2010) 3519.
217. A. K. Alves, F. A. Berutti, F. J. Clemens, T. Graule, C. P. Bergmann, Mater. Res. Bull. 44 (2009) 312.
218. M. Lubas, J. J. Jasinski, M. Sitarz, L. Kurpaska, P. Podsiad, J. Jasinski, Spectrochim. Acta A. 133 (2014) 867.
219. T. Luttrell, S. Halpegamage, J. Tao, A. Kramer, E. Sutter, M. Batzill, Sci. Rep. 4 (2014) 1.

220. E. F. Smith, I. J. Villar Garcia, D. Briggs, P. Licence, *Chem. Commun.* 2005 (2005) 5633.
221. P. Bazylewski, D. W. Boukhvalov, A. I. Kukhareno, E. Z. Kurmaev, A. Hunt, A. Moewes, Y. H. Lee, S. O. Cholakh, G. S. Chang, *RSC Adv.* 5 (2015) 75600.
222. Y. Li, Z. Y. Fu, B. L. Su, *Adv. Funct. Mater.* 22 (2012) 4634.
223. S. Madhugiri, B. Sun, P. G. Smirniotis, J. P. Ferraris, K. J. Balkus, *Micropor. Mesopor. Mat.* 69 (2004) 77.
224. A. Ogunsipe, J. Y. Chen, T. Nyokong, *New J. Chem.* 28 (2004) 822.
225. M. Bouchoucha, C. René, M. Fortin, F. Kleitz, *Adv. Funct. Mater.* 24 (2014) 5911.
226. S. Vukovic, S. Corni, B. Mennucci, *J. Phys. Chem. C* 113 (2009) 121.
227. D. O. Oluwole, T. Nyokong, *Polyhedron* 87 (2015) 8.
228. O. L. Osifeko, M. Durmuş, T. Nyokong, *J. Photochem. Photobiol. A: Chem.* 301 (2015) 47.
229. T. H. Tran-Thi, C. Desforge, C. Thiec, S. J. Gaspard, *Heterodimer. Phys. Chem.* 93 (1989) 1226.
230. A. B. Ormond, H. S. Freeman, *Materials (Basel)* 6 (2013) 817.
231. E. I. Sagun, E. I. Zenkevich, V. N. Knyukshuto, A. M. Shulga, D. A. Starukhin, C. von Borczyskowski, *Chem. Phys.* 275 (2002) 211.
232. N. Kuznetsova, N. Gretsova, E. Kalmykova, E. Makarova, S. Dashkevich, V. Negrimovskii, O. Kaliya, E. Lukyanets, *Russ. J. Gen. Chem.* 70 (2000) 133.
233. T. Nyokong, E. Antunes, *Photochemical and photophysical properties of metallophthalocyanines*, K. M. Kadish, K. M. Smith, R. Guilard (Eds.), World Scientific, London, 2010.

234. H. Ramesh, T. Mayr, M. Hobisch, S. Borisov, I. Klimant, U. Krühne, J. M. Woodley, *J. Chem. Technol. Biotechnol.* 91 (2016) 832.
235. J. Rak, P. Pouckova, J. Benes, D. Vetvicka, *Anticancer Res.* 39 (2019) 3323.
236. S. A. Majeed, K. E. Sekhosana, A. Tuhl, *Arab. J. Chem.* 13 (2020) 8848.
237. K. Lang, J. Mosinger, D. M. Wagnerova, *Coord. Chem. Rev.* 248 (2004) 321.
238. W. Spiller, H. Kliesch, D. Wöhrle, S. Hackbarth, B. Röder, G. Schnurpfeil, *J. Porphyr. Phthalocya.* 2 (1998) 145.
239. R. Schmidt, *Photochem. Photobiol.* 82 (2006) 1161.
240. M. Ratti, J. J. Naddeo, Y. Tan, J. C. Gripenburg, J. Tomko, C. Trout, S. M. O'Malley, D. M. Bubb, E. A. Klein, *Appl. Phys. A* 122 (2016) 346.
241. S. N. Nyamu, L. Ombaka, E. Masika, M. Ng'ang'a, *Adv. Chem.* 2018 (2018) 1.
242. A. Mai-Prochnow, M. Clauson, J. Hong, A. B. Murphy, *Sci. Rep.* 6 (2016) 38610.
243. J. Jadoun, A. Yazbak, S. Rushrush, A. Rudy, H. Azaizeh, *Evid.-Based Complementary Altern. Med.* 2016 (2016) 1.
244. I. Kushkevych, J. Cejnar, J. Trem, D. Dordevic, P. Kollar, M. Vitezová, *Cells* 9 (2020) 698.
245. X. Ragàs, X. He, M. Agut, M. Roxo-Rosa, A. R. Gonsalves, A. C. Serra, S. Nonell, *Molecules* 18 (2013) 2712.
246. J. Ghorbani, D. Rahban, S. Aghamiri, A. Teymouri, A. Bahador, *Laser ther.* 27 (2018) 293.
247. N. Tran, A. Mir, D. Mallik, A. Sinha, S. Nayar, T. J. Webster, *Int. J. Nanomedicine* 5 (2010) 277.
248. Y. Qing, L. Cheng, R. Li, G. Liu, Y. Zhang, X. Tang, J. Wang, H. Liu, Y. Qin, *Int. J. Nanomedicine* 13 (2018) 33117.

249. B. -Y. Zheng, M. -R. Ke, W. -L. Lan, L. Hou, J. Guo, D. -H. Wan, L. -Z. Cheong, J. -D. Huang, *Eur. J. Med. Chem.* 114 (2016) 380.
250. S. Mukherji, J. Ruparelia, S. Agnihotri, Antimicrobial activity of silver and copper nanoparticles: variation in sensitivity across various strains of bacteria and fungi, N. Cioffi, M. Rai (Eds.), *Nano-Antimicrobials: Progress and Prospects*, Springer, Berlin (2012) 225.
251. Y. Zhou, Y. Kong, S. Kundu, J. D. Cirillo, H. Liang, *J. Nanobiotechnol.* 10 (2012) 1.
252. D. Dhabalia, S. J. Ukkund, U. T. Syed, W. Uddin, M. A. Kabir, *Mater. Res. Express* 7 (2020) 125401.
253. M. Y. Memar, R. Ghotaslou, M. Samiei, K. Adibkia, *Infect. Drug Resist.* 11 (2018) 567.
254. S. Alfei, A. M. Schito, *Polymers (Basel)* 12 (2020) 1195.
255. A. Raghunath, E. Perumal, *Int. J. Antimicrob. Agents* 49 (2017) 137.
256. E. Alp, R. İmamoğlu, U. Savacı, S. Turan, M. K. Kazmanlı, A. Genç, *J. Alloys Compd.* 852 (2021) 157021.
257. S. -L. Chen, X. -J. Huang, Z. -K. Xu, *Cellulose* 18 (2011) 1295.
258. R. Zügler, T. Nyokong, *J. Mol. Catal. A: Chem.* 366 (2013) 247.
259. M. N. Rashed, A. A. El-Amin, *Int. J. Phys. Sci.* 2 (2007) 073.
260. J. Kaur, S. Bansal, S. Singhal, *Phys. B: Condens. Matter* 416 (2013) 33.
261. Y. Li, X. Li, J. Li, J. Yin, *Water Res.* 40 (2006) 1119.
262. M. U. D. Sheikh, G. A. Naikoo, M. Thomas, M. Banoa, F. Khan, *New J. Chem.* 40 (2016) 5483.
263. J. Z. Kong, A. D. Li, X. Y. Li, H. F. Zhai, W. Q. Zhang, Y. P. Gong, H. Li, D. Wu, *J. Solid State Chem.* 183 (2010) 1359.

264. L. Giribabu, C. V. Kumar, V. G. Reddy, P. Y. Reddy, C. S. Rao, S. -R. Jang, J. -H. Hum, M. K. Nazeeruddin, M. Grätzel, *Sol. Energ. Mat. Sol. C.* 91 (2007) 1611.
265. M. Saeed, S. Adeel, M. Ilyas, M. A. Shahzad, M. Usman, E. Haq, M. Hamayun, *Desalin. Water Treat.* 57 (2016) 12804.
266. M. A. Fox, M. T. Dulay, *Chem. Rev.* 93 (1993) 341.
267. J. Abhilasha, V. Dipti, *J. Chil. Chem. Soc.* 62 (2017) 3683.
268. J. L. Wang, L. J. Xu, *Crit. Rev. Environ. Sci. Technol.* 42 (2012) 251.
269. Z. Huang, B. Zheng, S. Zhu, Y. Yao, Y. Ye, W. Lu, W. Chen, *Mater. Sci. Semicond. Process.* 25 (2014) 148.
270. V. Raditoiu, A. Raditoiu, M. F. Raduly, V. Amariutei, I. C. Gifu, M. Anastasescu, *Coatings* 7 (2017) 229.
271. H. Kim, W. Kim, Y. Mackeyev, G. -S. Lee, H. -J. Kim, T. Tachikawa, S. Hong, S. Lee, J. Kim, L. J. Wilson, T. Majima, P. J. J. Alvarez, W. Choi, J. Lee, *Environ. Sci. Technol.* 46 (2012) 9606.
272. A. Fujishima, X. T. Zhang, D. A. Tryk, *Surf. Sci. Rep.* 63 (2008) 515.
273. A. Yamakata, T. Ishibashi, H. Onishi, *Chem. Phys.* 339 (2007) 133.
274. D. C. Hurum, A. G. Agrios, K. A. Gray, T. Rajh, M. C. Thurnauer, *J. Phys. Chem. B* 107 (2003) 4545.
275. B. Ohtani, O. O. Prieto-Mahaney, D. Li, R. Abe, *J. Photochem. Photobiol. A: Chem.* 216 (2010) 179.
276. S. P. Pitre, T. P. Yoon, J. C. Scaiano, *Chem. Commun.* 53 (2017) 4335.
277. A. Primo, T. Marino, A. Corma, R. Molinari, H. García, *JACS* 133 (2011) 6930.